SITE CHARACTERIZATION IN SHELBY COUNTY, TENNESSEE USING ADVANCED SURFACE WAVE METHODS

A Report
Presented to
The Mid-America Earthquake Center

by

Gregory L. Hebeler
&
Dr. Glenn J. Rix

Georgia Institute of Technology
February, 2001

Acknowledgements

We received generous assistance from a number of individuals who made the field testing in Memphis possible and who provided insight and comparative data regarding the results. Correspondence through email and/or data sets provided by Dr. Chris Cramer (CERI), Rob Williams (USGS), Professor Roy Van Arsdale (University of Memphis), Dr. Joan Gomberg (CERI), Dr. Paul Bodin (CERI), Professor Shahram Pezeshk (University of Memphis), Dr. Buddy Schweig (USGS), Professor Ron Street (University of Kentucky), Dr. Paul Mayne (Georgia Institute of Technology) and others at CERI and the MAE center have been helpful in providing additional perspective to the issues associated with this study.

This work was funded by the Mid-America Earthquake Center under a grant from the Earthquake Engineering Research Centers program of the National Science Foundation under Award No. EEC-9701785.

Abstract

The focus of the current study was to develop improved experimental and analytical methods to increase the applicability and accuracy of seismic surface wave testing for use in geotechnical site characterization. The recent research completed by Zywicki (1999) on the use of array-based techniques for use in active and passive surface wave testing was refined and expanded resulting in the development of the current surface wave testing procedures. The current developments focused on improving the procedures typically used in traditional engineering surface wave studies by implementing array-based testing and analysis procedures and improved signal processing techniques. An experimental testing program was conducted to evaluate the developed procedures and to provide near-surface shear wave velocity (V_S) data for the Memphis, Tennessee metropolitan region. This testing program consisted of 11 sites in Mid-America, ten within the Memphis, TN metropolitan area and one site in Northwest Arkansas. The testing program allowed for the comparison with previous data obtained using other in situ techniques, and with traditional surface wave data in order to validate the accuracy of the current methods and to highlight the improved capabilities over traditional surface wave methods. Additionally, active and passive procedures were combined in an effort to improve the range and capabilities of the individual methods allowing for more complete site characterization.

TABLE OF CONTENTS

LIST OF TABLES

LIST OF FIGURES

Chapter 1

Introduction

1.1 Introduction

The focus of the current study was to develop improved experimental and analytical methods to increase the applicability and accuracy of seismic surface wave testing for use in geotechnical site characterization. The recent research completed by Zywicki (1999) on the use of array-based techniques for use in active and passive surface wave testing was refined and expanded resulting in the development of the current surface wave testing procedures. The current developments focused on improving the procedures typically used in traditional engineering surface wave studies by implementing array-based testing and analysis procedures and improved signal processing techniques. An experimental testing program was conducted to evaluate the developed procedures and to provide near-surface shear wave velocity (V_S) data for the Memphis, Tennessee metropolitan region. This testing program consisted of 11 sites in Mid-America, ten within the Memphis, TN metropolitan area and one site in Northwest Arkansas. The testing program allowed for the comparison with previous data obtained using other in situ techniques, and with traditional surface wave data to validate the accuracy of the current methods and to highlight the improved capabilities over traditional surface wave methods. Additionally, active and passive procedures were combined in an effort to improve the range and capabilities of the individual methods allowing for more complete site characterization.

1.2 Dynamic Soil Properties

The response of soils to earthquake and other dynamic input motions is controlled by site-specific properties of the near-surface geomaterials. These properties have become commonly grouped into the term dynamic soil properties. Figure 1.1 shows the hysteric relationship between shear stress and shear strain. The value of the shear modulus changes nonlinearly with strain level and is maximum at zero strain. This value of the shear modulus at zero strain is known as the "initial tangent shear modulus" or G_{max}. The initial tangent shear modulus is often determined by measuring the shear wave velocity and using the relationship:

$$G_{max} = \rho V_S^2 \tag{1.1}$$

where ρ = density and V_S = shear wave velocity. The hysteric behavior of soils exists due to the dissipation of energy that occurs during cyclic loading known as material damping. The damping ratio is defined by Equation 1.2:

$$D = \Delta E/(4\pi E) \tag{1.2}$$

where D = the damping ratio, and ΔE and E are explained in Figure 1.1. Figures 1.2 and 1.3 show the effects of varying the initial tangent shear modulus and the initial shear damping ratio on the response of a 30 m homogeneous soil deposit using SHAKE91 (Lai, 1998). It can be clearly seen that the response is highly dependent on the shear modulus and damping ratio.

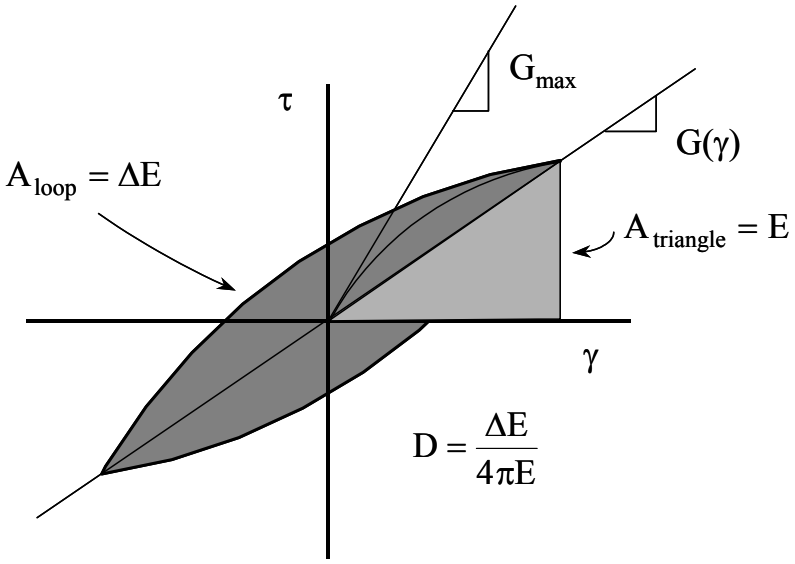

Figure 1.1 Hysteric Soil Model and Dynamic Material Properties (Adapted from Rix, 2000)

Dynamic soil properties are generally broken into two groups for convenient discussion, low- and high-strain properties. The transition between low- and high-strain behavior is known as the linear elastic threshold strain, below which soils behave approximately linear, and as a general rule this threshold strain is approximately 10^{-3} % for granular soils and 10^{-2} % for clays and silts as seen in the modulus reduction curves of Figure 1.4. Figure 1.5 shows similar curves sorted by plasticity index for the material damping ratio. At low levels of strain the dynamic response of soils is controlled by stiffness, damping, density, and Poisson's ratio, with stiffness and damping being the most important. Other factors, such as the number and rate of load cycles and volume change characteristics have a prominent impact on the large strain dynamic response. Most in situ seismic tests involve only low-strain levels. Since this report is focused on the use of Rayleigh wave propagation to measure in situ dynamic soil properties, all discussion of dynamic properties will be focused on low-strain properties unless otherwise stated. For a more detailed discussion of dynamic soil properties, including large strain effects, refer to, Kramer (1996).

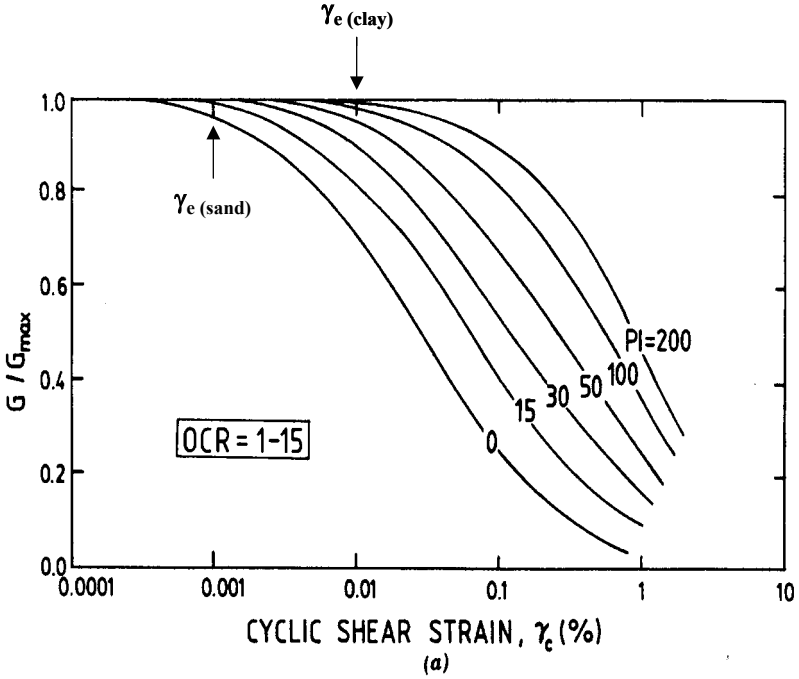

Figure 1.2 Dynamic Material Properties, Modulus Reduction Curves (Vucetic and Dobry, 1991)

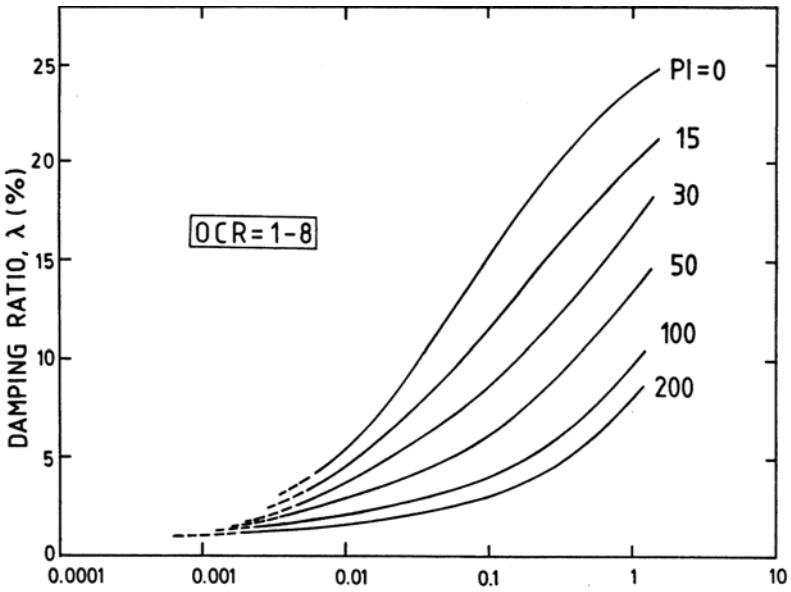

Figure 1.3 Dynamic Material Properties, Damping Ratio Curves (Vucetic and Dobry, 1991)

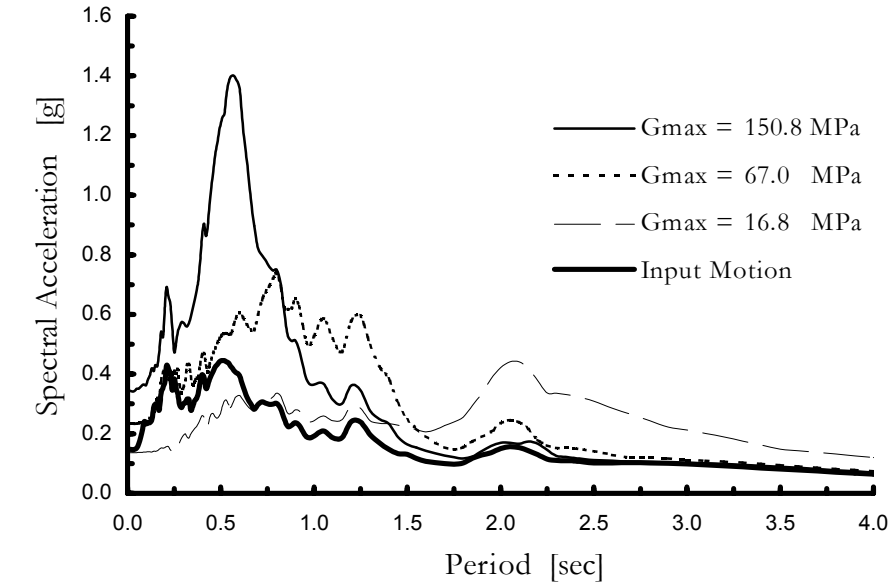

Figure 1.4 Influence of G_{max} on the Acceleration Response Spectrum (Lai, 1998)

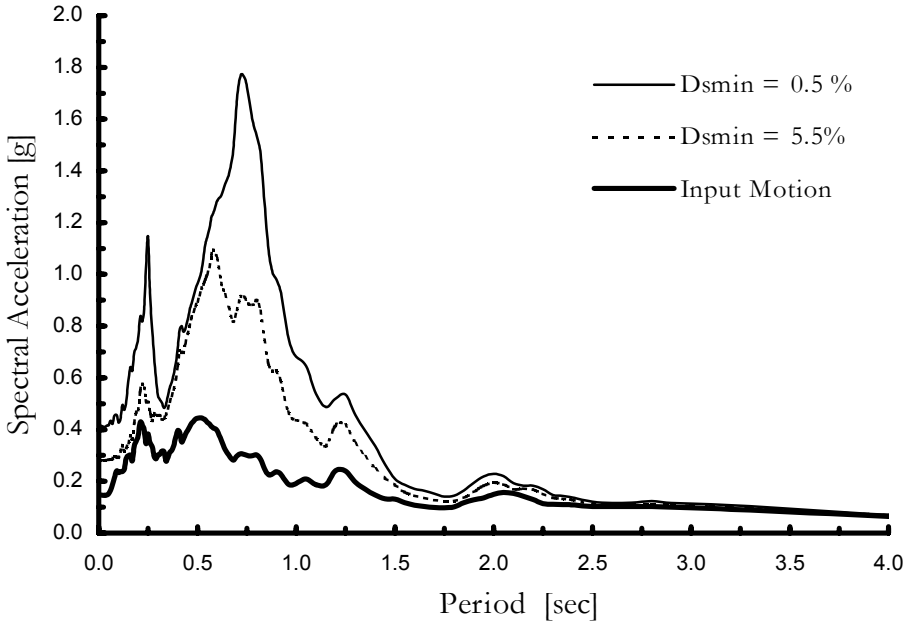

Figure 1.5 Influence of D_{min} on the Acceleration Response Spectra (Lai, 1998)

1.3 Measuring Dynamic Soil Properties

Dynamic soil properties can be measured both in situ and in the laboratory. The advantage of in situ techniques is that they test the soil in an undisturbed state and allow larger volumes of soil to be tested. However, in situ seismic methods are usually restricted to low-strain measurements. Laboratory tests can measure both large- and small-strain properties, and allow more control over stress path and drainage conditions. However, laboratory samples are almost always substantially disturbed, are expensive to obtain and test, and only represent a small fraction of the soil at a site. A combination of in situ and laboratory techniques is usually implemented to completely define the full range of dynamic soil properties as expressed in Figure 1.6.

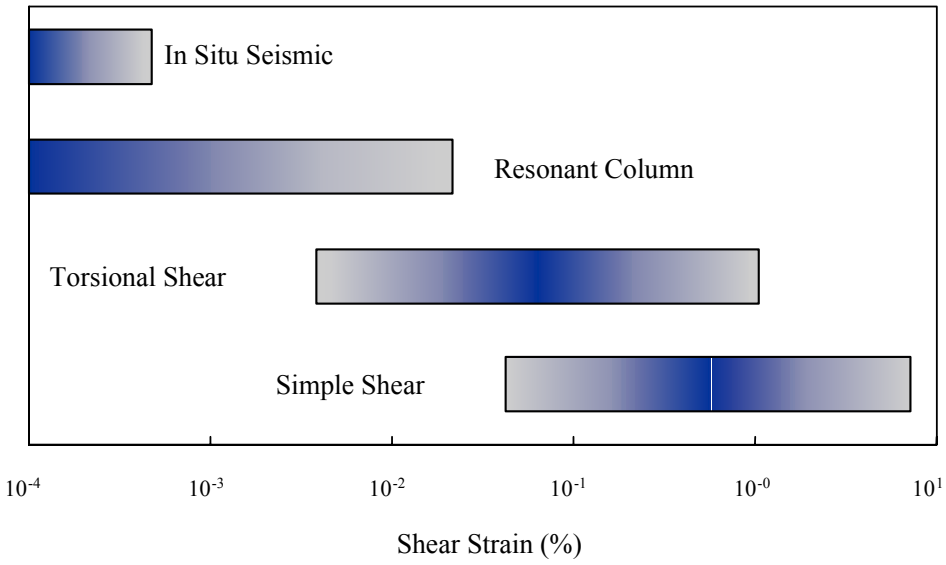

Figure 1.6 Range of Shear Strains Induced in Dynamic Tests (Adapted from Ishihara, 1996)

1.3.1 In situ Seismic Techniques

A wide variety of in situ seismic techniques are available to determine the dynamic material properties of a site. In situ methods can be grouped into two categories, invasive and noninvasive (surface) procedures. Common invasive procedures include crosshole, downhole, seismic cone penetration, and suspension logging, while the most common surface-based procedures include seismic refraction, seismic reflection, and surface wave testing. Invasive methods necessitate that either a borehole or probe be inserted into the ground, often resulting in higher costs and longer testing times than surface-based methods. These techniques typically measure the variability in wave travel times between small depth intervals to determine the shear wave velocity of a site with depth. Surface-based techniques use surface receivers to measure the travel times of seismic waves with distance along the surface. These techniques use the characteristics of wave propagation to infer the underlying material properties based on the measured surface recordings. Surface methods are usually less costly and more time effective, but resolution at depth is limited in some cases. Additionally, surface-based methods characterize the average site conditions over larger areas than typically measured using invasive procedures. Surface wave methods offer advantages over other surface-based in situ seismic techniques. These advantages include the ability to measure both shear wave velocity and material damping profiles with depth and the ability to detect low-velocity features underneath higher velocity layers, allowing for more accurate site characterization and the detection of susceptible liquefaction features. Moreover, surface wave procedures are highly adaptive to specific site conditions allowing for the testing of a wide range of geologic and topological conditions with the same experimental equipment.

1.3.2 Considerations for Mid-America

The seismic hazard of Mid-America is centered around the New Madrid seismic zone (NMSZ), the site of several large historic earthquakes. The soil and rock conditions of the region are such that in the event of a future damaging seismic event, the affected area would cover a large area spanning much of the Central and Eastern United States (Stover and Coffman, 1993). Subsequently, because local geologic and soil conditions strongly influence the ground motions resulting from an earthquake, it becomes important to determine the site-specific dynamic material properties over a large portion of Mid-America. Timely and cost effective procedures are necessary to efficiently conduct the large scale site characterization of the region. While site characterization has been conducted in some of the large metropolitan regions in Mid-America, there are still large portions of the region with high seismic risk that have not yet been characterized. As such, surface-based in situ seismic methods are conducive to the site characterization needs of Mid-America. Moreover, the improvement of these techniques would further aid in the widespread use of these methods and would allow for the site characterization of Mid-America to be conducted faster and more economically.

1.4 Geotechnical Surface Wave Testing

There are two fundamental wave types that exist in elastic media, body waves and surface waves. Body waves are possible in all media, while surface waves can only exist near the boundary of a medium. Body waves consist of compression (P) waves and shear (S) waves. While, the two most prominent types of surface waves are Rayleigh (R) waves and Love (L) waves. A thorough discussion of wave types and their propagation phenomena can be found in texts on wave propagation such as Graff (1975), Aki and Richards (1980), and Achenbach (1984).

1.4.1 Rayleigh Surface Waves

Lord Rayleigh conducted the first study on the propagation of surface waves at stress free surfaces in 1885, and the waves he discovered are now known as Rayleigh waves.

> "It is proposed to investigate the behavior of waves upon the plane free surface of an infinite homogeneous isotropic elastic solid, their character being such that the disturbance is confined to a superficial region, of thickness comparable with the wavelength."
>
> John William Strutt, Third Baron Rayleigh
> "On Waves Propagated Along the Plane
> Surface of an Elastic Solid", 1885.

Rayleigh waves are dispersive, meaning that waves of different frequency or wavelength propagate at different velocities. The dispersive nature of Rayleigh waves is due to the direct relationship between their wavelength and their zone of influence as shown for a homogenous half-space in Figure 1.7. Since soil stiffness usually increases with depth, Rayleigh waves of longer wavelengths tend to propagate faster than Rayleigh waves of shorter wavelength. The dispersive nature of Rayleigh waves enables their use in detecting changes in soil stiffness with depth by measuring the wavelength and velocity of propagating waves. The relationship between Rayleigh wave velocity and either frequency or wavelength is known as the dispersion relation. Determining the dispersion relation is an important component of in situ surface wave testing, and allows the soil stiffness to be characterized with depth.

Figure 1.8 shows the type and energy distribution of seismic waves produced from a vertically oscillating surface source. Through careful examination of this figure it can be seen that surface waves propagate radially outward in a cylindrical wave front, while body waves propagate radially outward and downward along a hemispherical wave front. As waves travel outward their energy is distributed over larger volumes of material, and consequently the energy in each unit of soil is reduced as the wave travels away from the source. Surface waves geometrically attenuate much slower than body waves along a free surface, at a rate of approximately $1/\sqrt{r}$ as compared to $1/r^2$. The slower attenuation of surface waves allows for the detection of Rayleigh waves over very large distances. The ability to measure Rayleigh wave displacements over large spatial distances allows the measurement of low-frequency, long-wavelength waves, which consequently allow deeper material properties to be inferred from the measured dispersion relation. These basic phenomena are the motivation for the use of surface waves in geophysical and geotechnical testing and provide the basis for the methods described in Chapters 3 and 4.

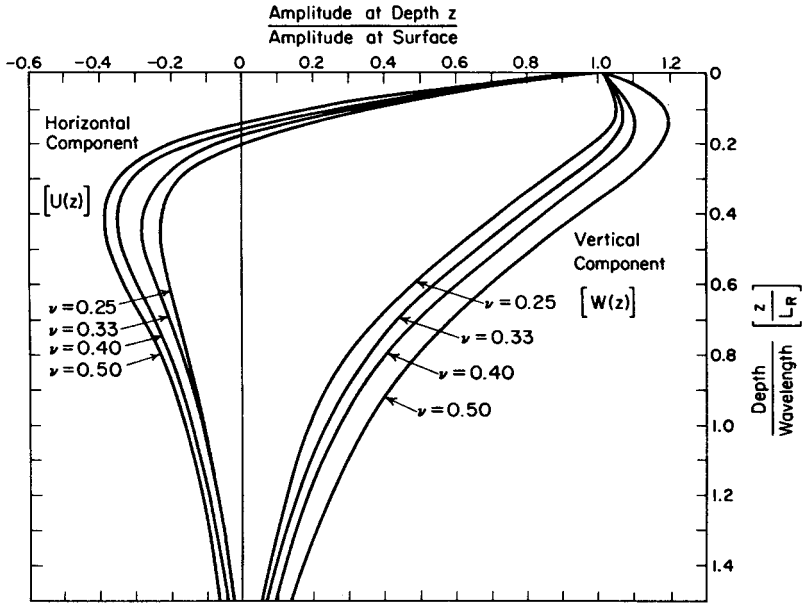

Figure 1.7 Amplitude Ratio vs. Dimensionless Depth for Rayleigh Waves in a Homogeneous Half-Space (Richart et al., 1970)

1.4.2 Traditional Limitations

Traditional engineering surface wave tests, otherwise known as the Spectral Analysis of Surface Waves (SASW), involves the generation and measurement of Rayleigh surface waves using two surface sensors and a digital signal analyzer. Multiple tests are conducted and combined at varying sensor spacings enabling the characterization of the shear wave velocity with depth. The traditional methods are hampered by several limitations that are discussed fully in Chapter 3. These limitations include inadequate signal processing methods, low noise removal capabilities, limited depth resolution, and the need to combine several tests introducing time dependent errors. The surface wave methods used in the current study decrease the effects of these limitations through the use of improved spatial and signal processing, frequency specific testing, the use of active and passive wave sources, and simultaneous array measurements. In depth discussions regarding traditional surface wave methods and the current surface wave procedures are presented in Chapters 3 and 4 respectively.

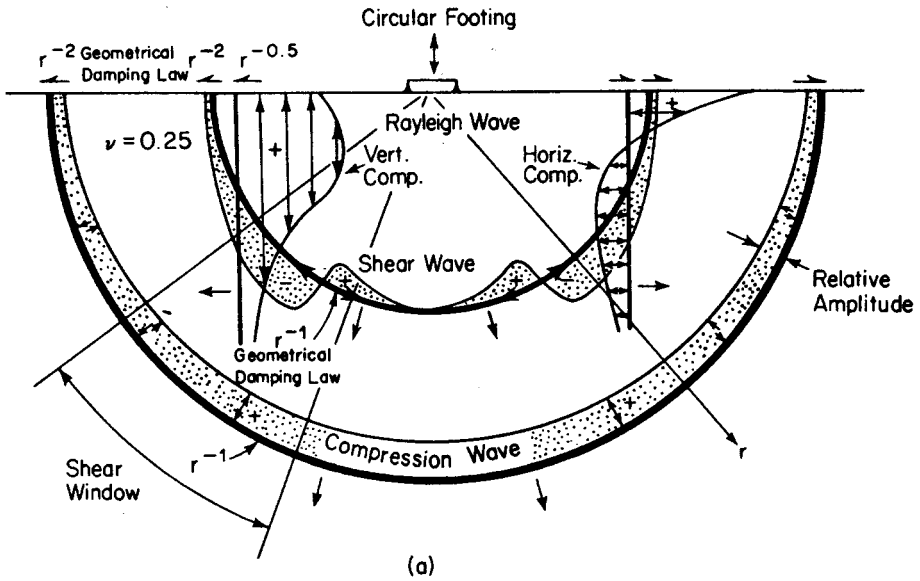

Wave Type	Per Cent of Total Energy
Rayleigh	67
Shear	26
Compression	7

(b)

Figure 1.8 Distribution of Displacement Waves from a Harmonic Surface source in an Isotropic Elastic Half-Space (Richart et al., 1970)

1.5 Report **Overview**

Chapter 2 introduces the motivations for the current study, focusing on the historic earthquakes and geologic conditions of Mid-America to provide an overview of the seismic conditions of the region. Chapter 3 presents an overview of the history of seismic surface wave testing and discusses the major past improvements that have been introduced into the field. This discussion summarizes each traditional testing method highlighting their limitations and brings the reader up to date with the present state of geotechnical surface wave testing.

The current surface wave methods are discussed in detail in Chapter 4. The chapter begins by discussing experimental considerations and the subsequent selection of the testing equipment. Next the choice of testing parameters for both active and passive testing is discussed, and the testing parameters used in the current study are presented. Dispersion calculations are discussed at length, and highlight a number of the improvements made regarding the collection and analysis of dispersion data. The chapter concludes with a discussion of the inversion procedures used, including some practical guidelines that directed their implementation.

Chapter 5 presents the results of the experimental testing program including active testing results conducted in Memphis, Tennessee in July of 2000, and passive measurements taken in October, 1999. The chapter presents the results from each site individually, including discussions on site-specific features that highlight the ability of the current procedures to resolve V_S profiles over a number of different site conditions. The results of previous V_S measurements are compared to the current results to evaluate the effectiveness of the current methods. Additionally, passive and active data were combined when possible in an effort to broaden the capabilities of conventional surface wave testing.

The results obtained through the use of the current surface wave methods are compared to the results of traditional SASW tests conducted at three of the test sites. These comparisons, shown in Chapter 6, clearly show the superior dispersion resolution attainable with the current methods and serve to further highlight the limitations of traditional engineering surface wave tests.

Chapter 7 summarizes the contributions of the current research, in particular the improvements made to enhance the seismic surface wave method. Some general recommendations regarding experimental testing procedures and parameters are presented as a result of the experiences gained through the current testing program. The report concludes with some general remarks and recommendations for future research that the author believes would further extend the capabilities and effective implementation of seismic surface wave testing.

Chapter 2

The Importance of Characterizing the Near Surface Dynamic Soil Properties of the New Madrid Seismic Zone

2.1 Introduction

The New Madrid Seismic Zone (NMSZ) spans Southeastern Missouri, Northeastern Arkansas, Northwestern Tennessee, Southwestern Kentucky, and Southern Illinois, as seen in Figure 2.1. While the NMSZ is not located above a tectonic plate boundary, it is still the most seismically active region in the United States east of the Rocky Mountains (Purser and Van Arsdale, 1998). The geologic features responsible for the seismicity in the region are shown in Figure 2.1. The NMSZ is the location of what is believed to be the largest earthquake sequence ever experienced within the contiguous 48 states, and has produced some of the largest intraplate earthquakes ever documented (Johnston and Kanter, 1990). Figure 2.2 shows the magnitude and epicenter of the measured seismic events within the NMSZ from 1974 to 1998.

Within the past twenty years research and studies have been conducted to understand the characteristics of the seismicity within the NMSZ, and the subsequent effects of possible future large magnitude events. However, because the NMSZ has not experienced a large magnitude event since technological advancements have made it possible to accurately measure and record large ground motions, there is no direct data to provide a basis for the seismic hazard analyses. Consequently, current research is focused on three main fronts: increasing awareness about the seismic risk present within the NMSZ and promoting structural retrofitting, developing theories and methods to accurately scale the well-defined methods for characterizing seismic events in "California-like" geologies for use in the NMSZ, and to accurately characterize the local geology and near surface dynamic material properties of the NMSZ in order to accurately predict the local site effects of future earthquakes.

In the event of another large event within the NMSZ, the geologic characteristics of the Memphis metropolitan area are estimated to result in significant losses of life and property, including the disruption of one of America's foremost transportation centers. The current research ties in with numerous other studies in the Memphis area, in efforts to better understand and document the dynamic soil behavior and characteristics of the region. These studies include the production of near surface dynamic material property databases (Center for Earthquake Research Institute, United States Geological Survey, and the Mid-America Earthquake Center), the formation of reference profiles depicting the generic geologic conditions present in the Memphis metropolitan area (Romero and Rix, 2001; Central United States Earthquake Consortium), as well as theoretical analyses regarding the unique characteristics of the geometry and geology of the Mississippi Embayment (ME) (Romero, 2001; Hashash 2001).

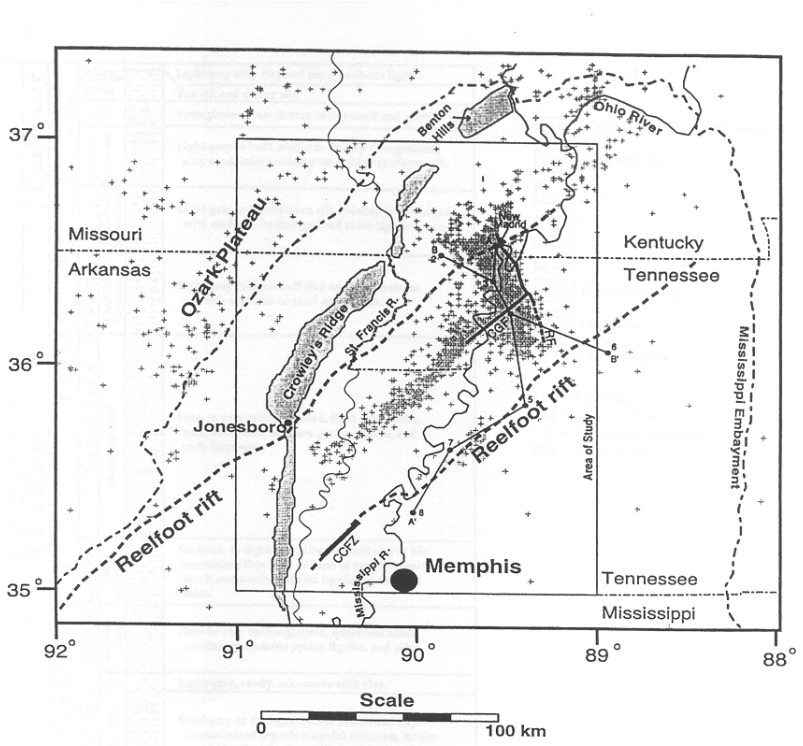

Figure 2.1 Major Physiographic and Structural Features of the Northern Mississippi Embayment. Crosses locate microearthquakes that define the New Madrid Seismic Zone. CCFZ, Crittenden County Fault Zone; CGF, Cottonwood Grove Fault; RF, Reelfoot Fault. (Van Arsdale and TenBrink, 2000)

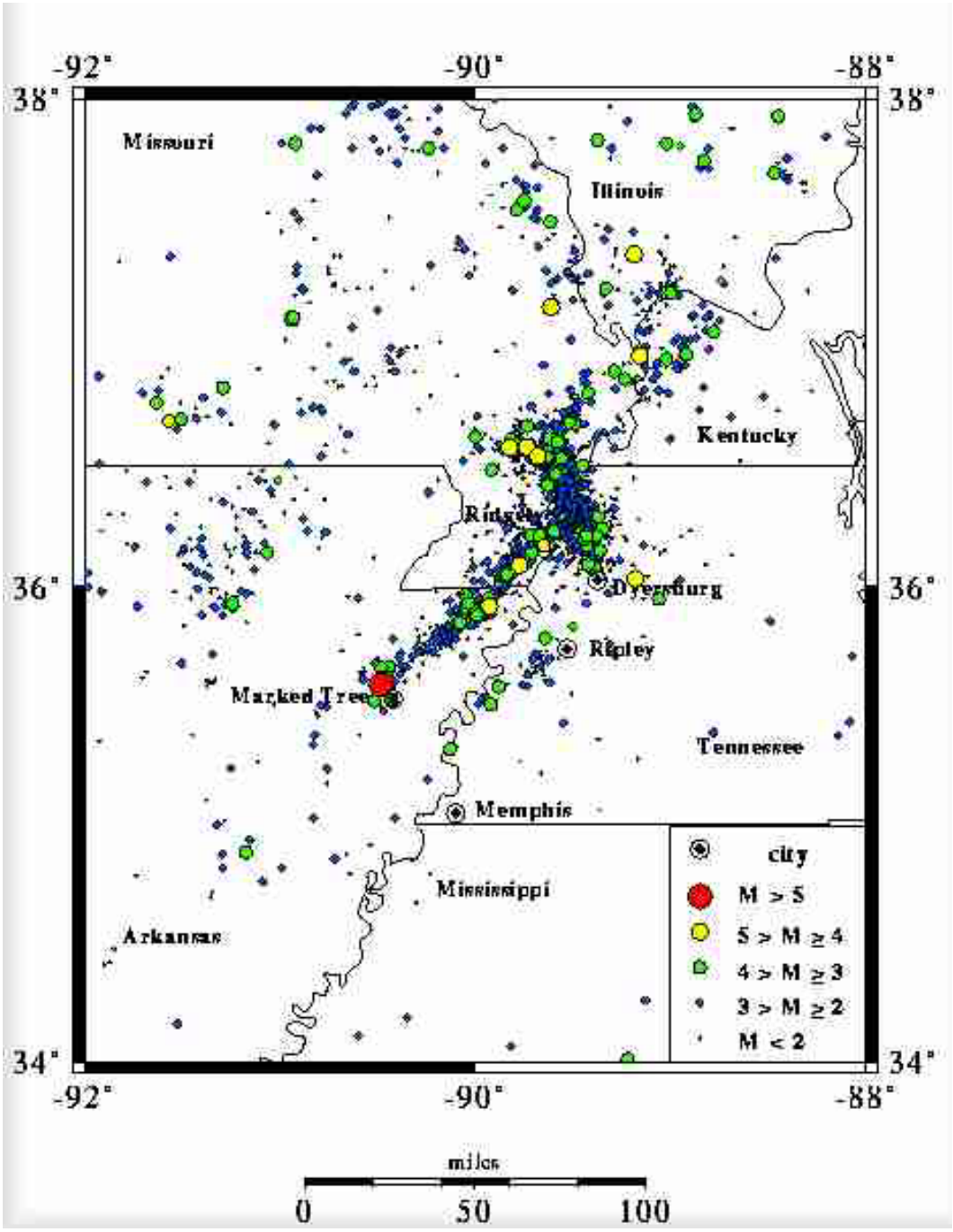

Figure 2.2 Measured Seismicity within the New Madrid Seismic Zone from 1974-1998 (4,387 locations). (CERI, 2000)

2.2 Historic Events

The sequence of three large earthquakes spanning the winter of 1811–1812 caused severe liquefaction and large ground subsidence throughout the NMSZ. The first and largest event, **M** 8.1 ± 0.3, occurred on December 16, 1811, with a projected epicenter Northwest of Blytheville Arkansas. The second event, **M** 7.8 ± 0.3, occurred on January 23, 1812, North of Caruthersville, Missouri, and the third event, **M** 8.0 ± 0.3, occurred on February 7, 1812, southwest of New Madrid, Missouri (Johnston, 1996). In addition to the sequence of 1811-1812, two other large magnitude earthquake sequences occurring within the NMSZ have been documented as a result of recent paleoliquefaction studies (Tuttle, 1999; Clarke, 2000). A sequence of three large earthquakes (**M** 8.1, 8.0, and 7.6) is believed to have occurred circa AD 900 ± 100 years, and a sequence of two large earthquakes (**M** 8.0 and 7.6) is believed to have occurred circa AD 1530 ± 130 years (Tuttle, 1999). Figure 2.3 shows the possible extent of the liquefaction caused by the large magnitude earthquakes in each of the three major sequences of the past 1200 years. Additionally two other earthquakes are known to have caused liquefaction within the NMSZ. Johnston and Schweig (1996) document a **M** 6.8 event in 1895, and Metzger (1996) documents a **M** 5.6 event in 1851 that both induced liquefaction. Unlike the major sequences mentioned earlier which caused wide spread liquefaction throughout the northern ME, these events are believed to have only induced liquefaction over small areas surrounding their epicenters. According to estimates by Tuttle (1999) and Clarke (2000), the return period for large magnitude, **M** > 7.0, events in the NMSZ is approximately 450 years, making the probability of a **M** > 7.0 event within the next 50 years 7-10 % (Clarke, 2000). Other studies have shown that the return period for damaging events, estimated as **M** > 6.3, is on the order of 70 ± 15 years. (Johnston and Nava, 1985)

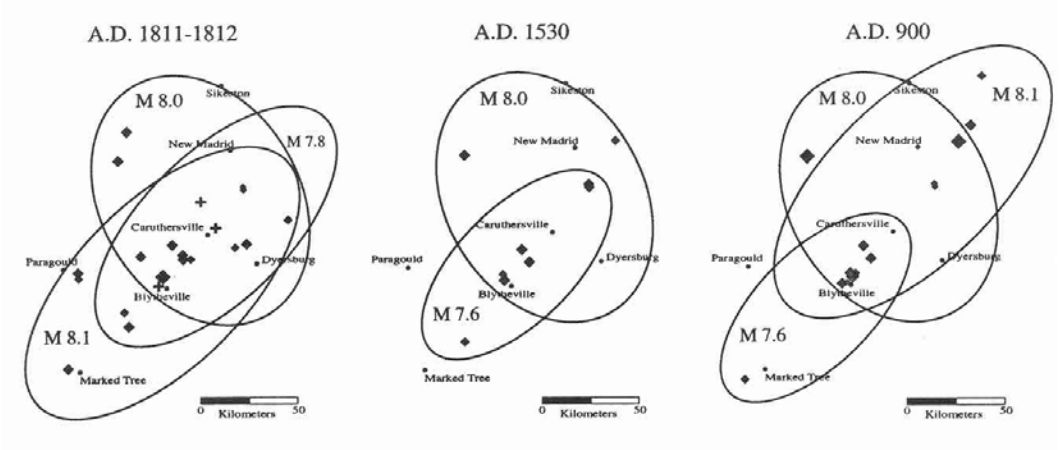

Figure 2.3 Interpretations of size distribution of liquefaction features attributed to earthquakes in 1811-1812, A.D. 1530, and A.D. 900. Ellipses outline proposed liquefaction fields for historic and prehistoric earthquakes. 1811-1812 earthquakes, for which locations, magnitudes, and rupture scenario have been estimated, serve as a model for interpreting distributions of prehistoric liquefaction features. Crosses mark possible epicentral locations and centers of liquefaction fields of 1811-1812 events. (Tuttle, 1999)

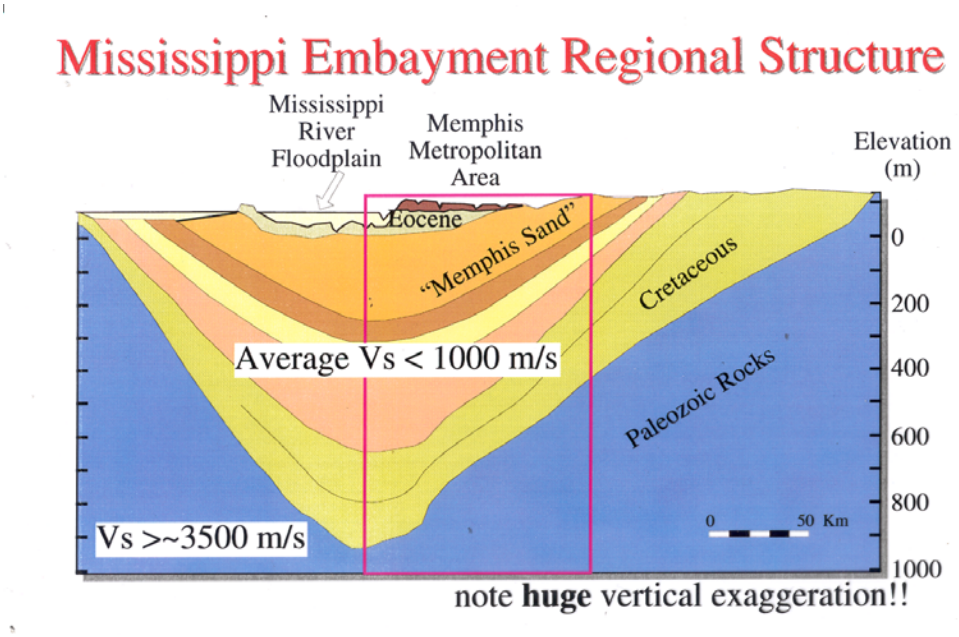

Figure 2.4 Cross Section of the Mississippi Embayment Taken at Memphis, Tennessee. (Bodin, 1999)

2.3 General Geology of the NMSZ

The seismic hazard of the NMSZ is largely attributed to the geologic conditions present within the area. The geology of the NMSZ is heavily influenced by the presence of the Mississippi River, which has created the large area of very deep sedimentary soil deposits known as the ME. The ME extends from southern Illinois to the Gulf of Mexico and extends to a maximum depth of 1,000 meters near Memphis, Tennessee (Romero, 2001). Figure 2.4 shows a cross section of the ME at its deepest point near Memphis, TN. In addition to the soft sedimentary nature of the ME, the entire NMSZ overlies stiff Paleozoic bedrock. The shear wave velocity of the crustal rocks underlying the NMSZ is approximately 3.5 km/sec. The shear wave velocities within the ME tend to be very low due to the young Holocene age and sedimentary nature of the deposits, and the average values in the surficial soils within the ME range from 0.1-1.5 km/sec (Romero and Rix, 2000).

2.4 Attenuation

The high V_S and low faulting of eastern bedrock corresponds to low attenuation of the seismic energy as it travels outward from the source. This allows crustal earthquake motions to spread laterally over very large areas. A repeat of any of the previously mentioned large earthquake sequences would cause severe damage to the major cities within and surrounding the NMSZ, and would be felt over a much larger area than equivalent earthquakes in California. Figure 2.5 depicts a general comparison of the felt areas for California and the New Madrid region based on similar magnitude events from 1994 and 1895 respectively. The darker areas in the figures depict geographic areas in which minor to major damage occurred to buildings, while the lighter outer regions represent the extent to which each event was felt. This figure shows both the large areas over which Mid-America earthquakes are felt and over which damage occurs. If events similar in magnitude to 1811-1812 sequence where to occur, this area would be

further extended to include almost all of the eastern United States as shown in Figure 2.6 which depicts the Modified Mercali Intensity (MMI) distribution estimated for the 1811-1812 events. Figure 2.6 is based on historical accounts that document the 1811-1812 sequence was felt as far away as Hartford, CT; Charleston, SC; and New Orleans, LA (Street and Nuttli, 1984).

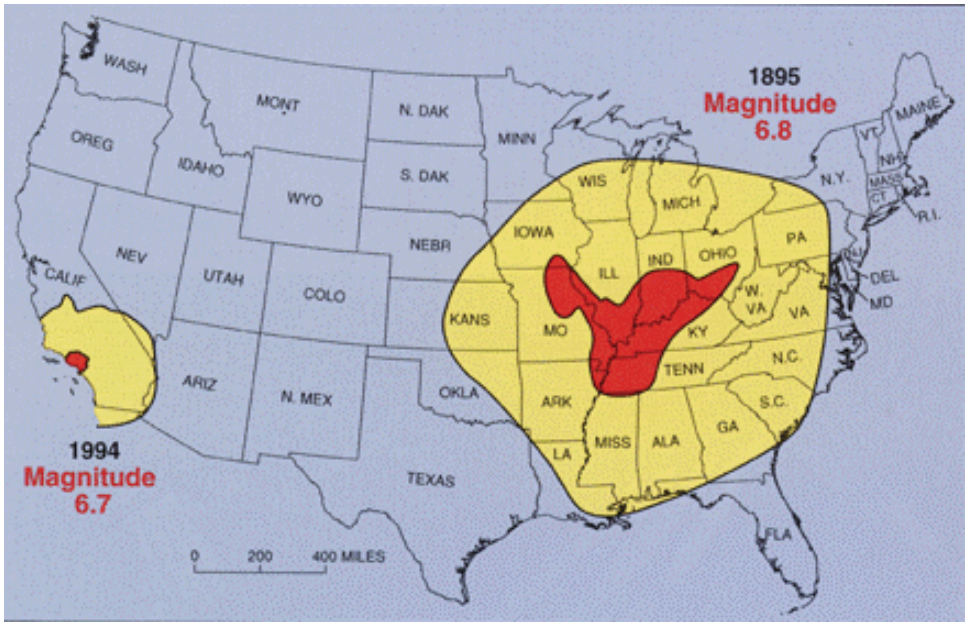

Figure 2.5 Areas affected by earthquakes of similar magnitude—the **M** 6.8 1895 Charleston, MO and the **M** 6.7 1994 Los Angeles earthquakes. Darker shading indicates minor- to-major damage to buildings and their contents. Outer, lighter shading indicates that shaking was felt, but objects received little or no damage. The NMSZ earthquake's substantially larger isoseismal areas reflect, in part, the combined effects of lower intrinsic attenuation and probably systematically higher eastern U.S. stress drops. The effect of river sediments is reflected in the shape of the New Madrid damage isoseismal. (From http://www.ceri.memphis.edu/usgs/hazmap_old/attenuation.html)

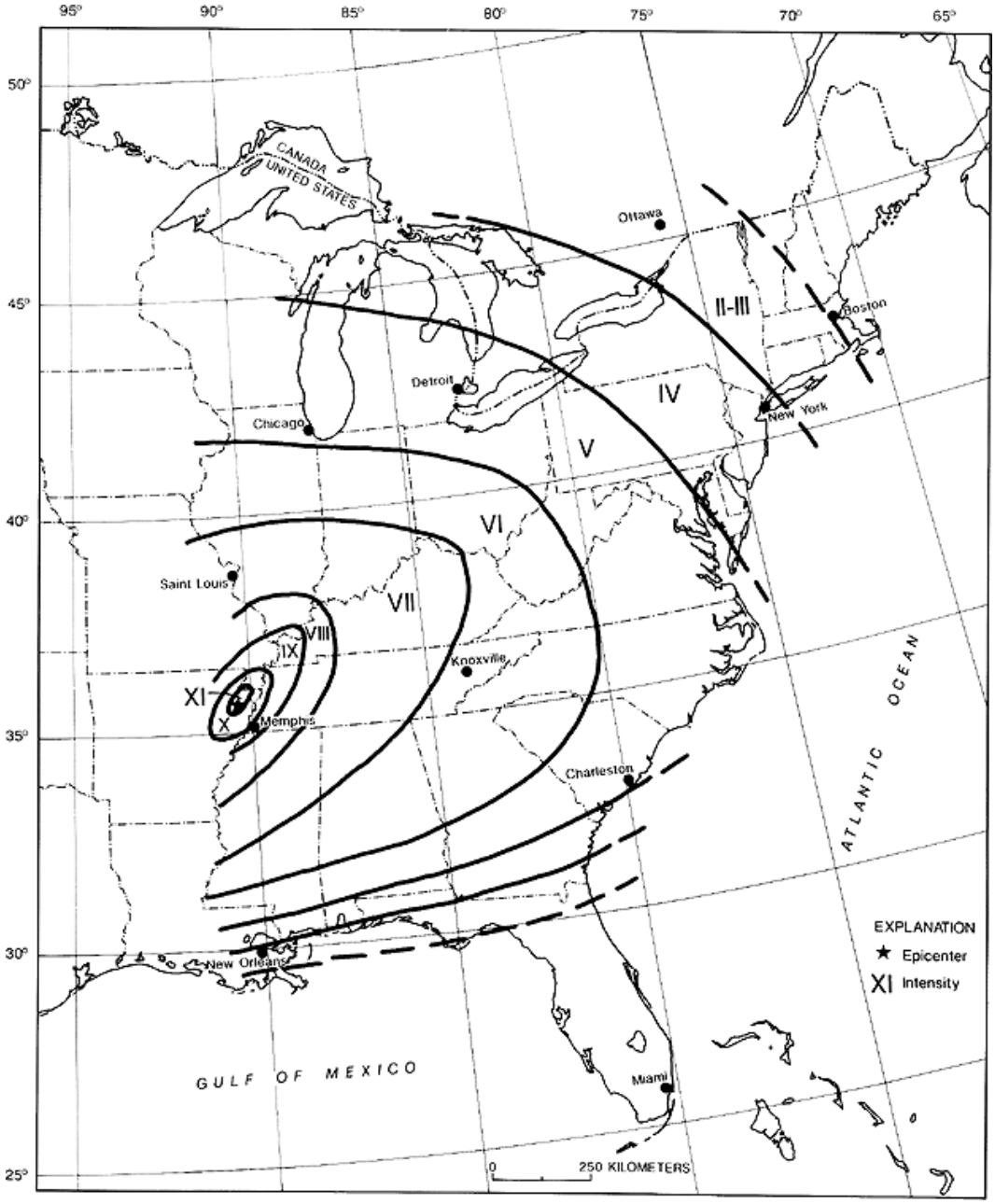

Figure 2.6 Isoseismal Map for the Arkansas Earthquake of December 16, 1811, 08:15 Utc (First of the 1811-1812 New Madrid Sequence), Showing the Estimated Modified Mercali Intensity Contours for the Populated Area of that Period. (Stover and Coffman, 1993.)

2.5 Site Amplification

Site amplification is a frequency dependent phenomena in which the characteristics of earthquake motions are influenced by a number of mechanisms related to the local soil and rock properties. At inception most earthquakes consist of a wide range of frequencies allowing the frequency content of the ground motions to be largely controlled by amplification mechanisms. Site amplification is typically quantified using the ratio presented in Equation 2.1, known as the amplification factor (Kramer, 1996):

$$Amplification\ Factor = F(\omega) = \frac{u_{(ground)}}{u_{(rock)}} \tag{2.1}$$

where u = vertical particle displacement. The stiff Paleozoic bedrock combined with the effects of the Mississippi River and its numerous tributaries present conditions that make the ground response to earthquake motions within the ME highly dependent on local site conditions and site amplification mechanisms . The effects of the local soil and rock conditions on earthquake ground motions are summarized well by Kramer (1996):

> "Local site conditions can profoundly influence all of the important characteristics – amplitude, frequency content, and duration – of strong ground motion."
>
> S. L. Kramer, 1996

2.5.1 Interface Effects

The large velocity gradient at the boundary between the Paleozoic bedrock and the soft overlying sedimentary soils within the ME produces large amplifications of the seismic energy at the soil/rock interface. Jacob (1991) notes that the bedrock of the eastern United States is typically harder and more crystalline than the softer rock conditions generally found in California. From this he states that amplification factors from the eastern United States tend to be on the order of 50% higher than amplification factors calculated using similar input motions for California bedrock conditions. The frequency content of site amplification is partially controlled by the magnitude of the velocity contrast, with larger contrasts corresponding to lower-frequency amplification. Figures 2.7 & 2.8 serve to show the effects of varying soil and rock properties on amplification. The softer soil, representing a large interface gradient, and shown in example (a), serves to accentuate the low-frequency motions. The stiffer material, representing a smaller interface gradient and shown in (b), serves to amplify motions at a higher-frequency.

2.5.2 Resonance

The effect of earthquakes are often quantified by the damage incurred to manmade structures in addition to the measured ground motions at a site. Consequently, to estimate the effect of a given earthquake one must assess the expected ground motion characteristics, and the subsequent response of both soil and structures to those ground motions. Amplification of earthquake motions is highly dependent on the frequency of excitation as seen in Figures 2.7 and 2.8. Soil deposits and structures will exhibit a natural or resonant frequency, i.e. a frequency of excitation that creates the largest resultant motions. As such, this natural frequency is often used to estimate the effects a particular level of ground motion can have on a given site or structure. While there are complex analysis procedures used to calculate these resonances exactly, e.g. laboratory structural and geotechnical testing, one can obtain an approximate value by using the simplified relationships presented in Equations 2.2 & 2.3:

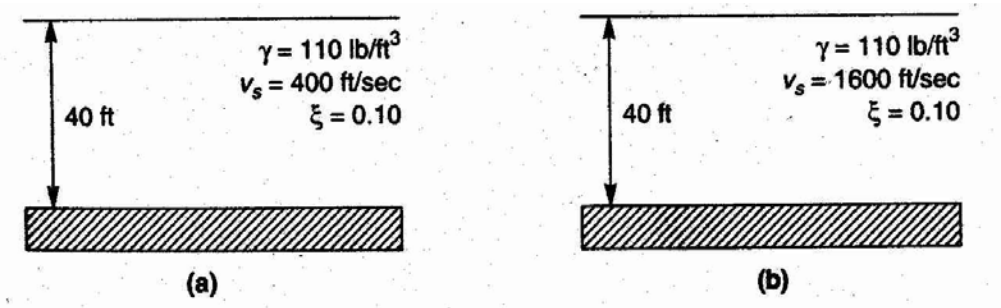

Figure 2.7 Two hypothetical soil deposits overlying rigid bedrock: (a) site A; 9b) site B. Soils are identical, except the s-wave velocity of the soil at site B is four times greater than that at site A. (Kramer, 1996)

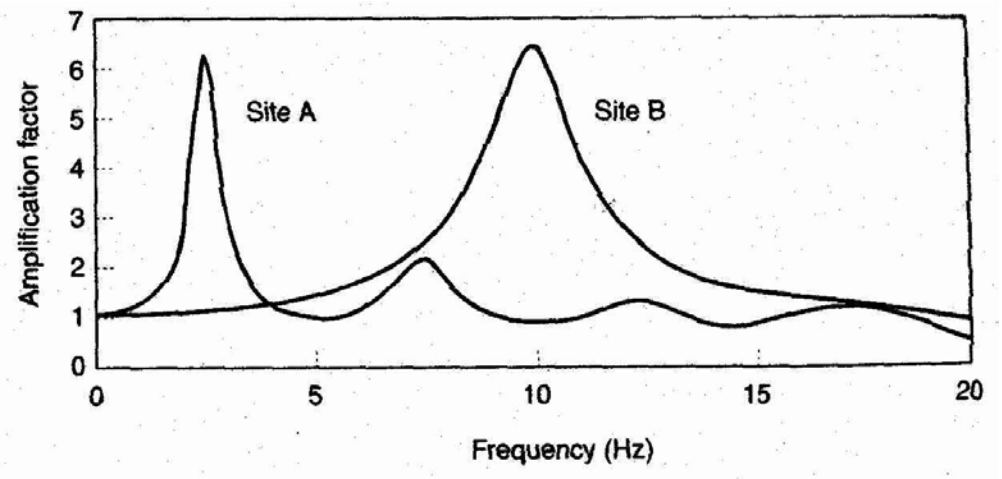

Figure 2.8 Amplification functions for sites A and B. Note that the softer soil at site A will amplify low-frequency input motions much more strongly than will the stiffer soils of site B. At higher frequencies, the opposite behavior would be expected. (Kramer, 1996)

$$Natural\ Frequency_{(Structure)} = \frac{N}{10\,\text{sec}} \tag{2.2}$$

$$Natural\ Frequency_{(Site)} = \frac{V_S}{4H} \tag{2.3}$$

where N = the number of stories in the structure, V_S = the shear wave velocity of the site, and H = the thickness of the soil deposit. Consequently, the response of a structure and its subsequent ability to withstand an applied harmonic load are directly related not only to the structural integrity, but also the height of the structure and the response of the underlying soil strata. It is common to only consider the effects of vertically propagating, horizontally polarized shear waves in site response analyses. This simplification is justified by the vertical orientation of earthquake motions near the surface and the poor response of most structures to lateral loading. The process of vertical orientation occurs according to Snell's theory of refraction and is due to the general decrease in wave propagation velocities towards the surface. Figure 2.9 depicts the typical course of seismic waves from their source deep within crustal rocks to the ground surface.

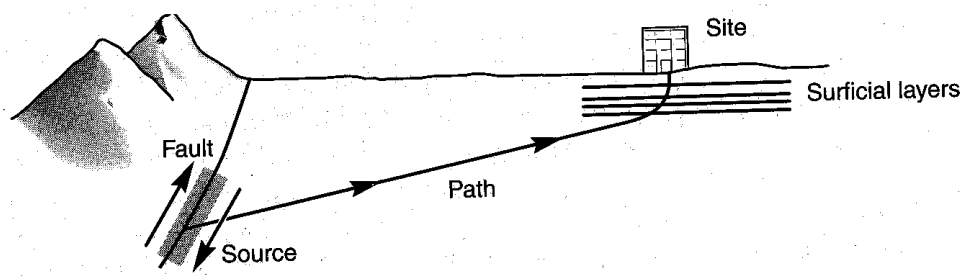

Figure 2.9 Refraction process that produces nearly vertical wave propagation near the ground surface. (Kramer, 1996)

2.5.3 Basin Geometry

The effects of an alluvial basin geometry on the magnitude and duration of ground motions can be significant. The velocity contrast between the soft alluvial soils within the basin and the hard bedrock forming the edge of the basin serves to trap body waves and causes some incident waves to travel through the basin soil as surface waves. The trapping of body waves and the creation of slowly attenuating surface waves results in stronger shaking and longer durations than would be experienced under typical one-dimensional conditions (Kramer, 1996). While the effects of geometry are limited towards the center of a large basin, they can be quite significant near the edges, where two- and three-dimensional site response analyses may be warranted. The Mississippi floodplain is estimated to be 57 km wide at Memphis; however, most of this width is located west of the Mississippi River (Street, 1999). As a result, Memphis sits near the eastern edge of the asymmetric ME basin. A cross section of the ME at Memphis was shown in Figure 2.4, and although the vertical scale is largely exaggerated, it serves to demonstrate the basin geometry responsible for the trapping of earthquake motions. A detailed discussion regarding topology and subsurface irregularities and the quantitative predictability of their effect on the amplitude and duration of earthquake motions is discussed in Silva (1988).

2.5.4 Energy Flux

Another significant ground motion amplification mechanism is related to the low near surface V_S values present throughout the ME. Without considering the added effects of scattering and material damping, the conservation of energy within an elastic solid requires that the flux rate of energy flow from the source to the ground surface remain constant. The energy flux can be simply defined by the relationship shown in Equation 2.4 (Aki and Richards, 1980):

$$Energy\ Flux = \rho V_S \dot{u}^2 \tag{2.4}$$

where ρ = the material density, and $\dot{u}$ = the particle velocity. Since both material density and V_S tend to decrease towards the surface, the particle velocity must increase to maintain constant energy flux transfer. The predominance of this site response mechanism in the near-surface allows seismic investigations conducted to depths of only 30 meters to provide good estimates of site response (NEHRP, 1997; Anderson et al., 1996; and Borcherdt, 1994). Low near-surface V_S values contributed to the destruction caused by the 1989 Loma Prieta earthquake (Seed et al., 1990) near San Francisco, and the 1985 Michoacan earthquakes (Seed et al., 1988) near Mexico City. San Francisco is underlain by loose Holocene age clayey silt, while Mexico City is built on brittle Holocene lacustrine deposits. The destruction caused in these areas was primarily due to the ground motion amplification of the young, loose soil deposits in the area. The geology of the ME, being constituted of very deep floodplains consisting of young, low-V_S alluvial deposits, presents a similar geologic condition.

2.6 Near Surface Geology of the Mississippi Embayment

The main geographic focus of the current testing was centered around Memphis, TN and included several other test sites throughout Tennessee's Shelby County, and one site in Arkansas. Memphis is the most populated metropolitan area in the vicinity of the NMSZ. Additionally, its unique geology can be generalized by three geologic profiles that characterize the soils of the region (Romero, 2001). For reference, a typical geologic column for the NMSZ is given in Figure 2.10, and a cross section of the ME at Memphis was given in Figure 2.4, with the soil conditions near Memphis highlighted in Figure 2.11. Two of the three profiles are defined by the two main geologic features of the Memphis region. The first is the alluvial floodplains of the Mississippi River and its tributaries (Wolf River, Nonconnah Creek, Loosahatchie River, and Big Creek), defined by Holocene-age loose sedimentary deposits. The other main geologic feature is the interfluve regions predominantly defined by a thick blanket of surficial loess and Pleistocene-Pliocene terrace deposits that consist of quartz sand, rounded chert, and some dispersed clay lenses (Romero, 2001; Street, 1999). The third generic profile is a special case of the above geologies for which the terrace deposits have become cemented creating a high velocity conglomerate layer between the surficial loess and the underlying Eocene Jackson Formation. The Jackson Formation is characterized by a bluish to greenish clay with lignite inclusions and increasing fine sand content with depth. The terrace formations have been eroded from most of the floodplain regions, for which the loess rests directly on the Jackson Formation (Street, 1999). Additionally, the terrace deposits disappear traveling east on the Gulf Coastal Plain into Western Tennessee, and are not found in the eastern sections of Shelby County (Van Arsdale 2000).

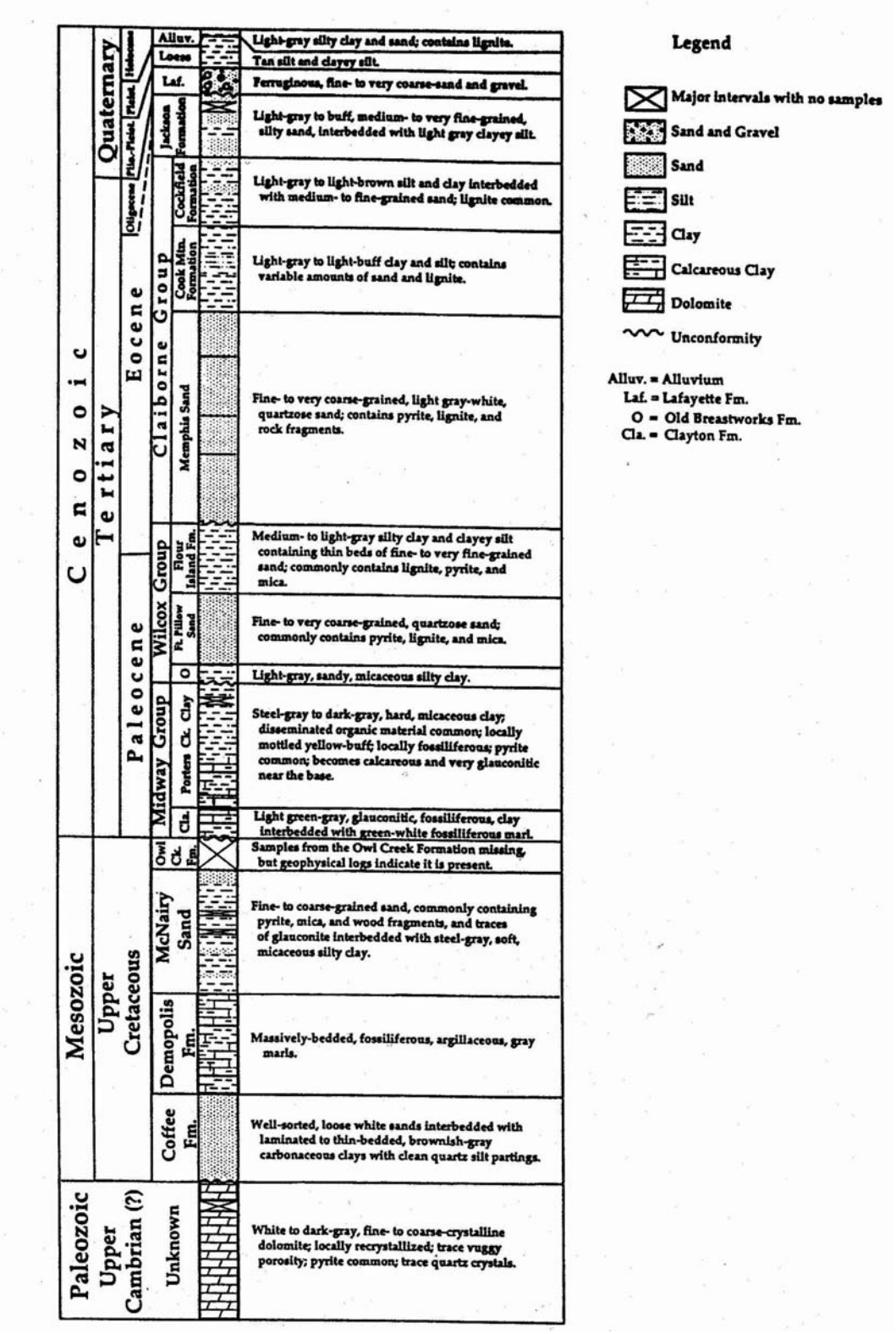

Figure 2.10 Geologic Column for the New Madrid Seismic Zone (Van Arsdale and TenBrink, 2000)

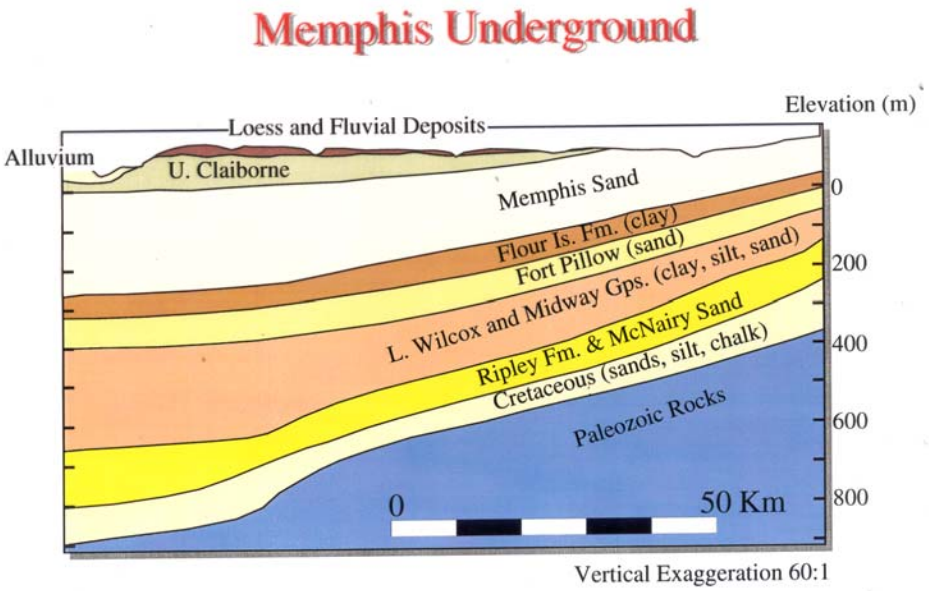

Figure 2.11 Generic Geology of the Mississippi Embayment for a Cross Section Taken at Memphis, Tennessee. (Bodin, 1999)

The current test sites represent all three of these typical geologies. The two sites located on Mud Island, as well as the two Shelby Farms sites are representative of the alluvial floodplains of the Mississippi and Wolf Rivers. Shelby Forest and the University of Memphis test site fall into the category defined by the interfluve terrace geology. While the remaining Memphis sites (W11, S16, Houston Levee Park, and Powell Road Park) were chosen to determine or substantiate the existence of the high velocity conglomerate layer at these locations. The W11 and S16 sites were chosen to determine the erosion of the conglomerate layer within the floodplains of Nonconnah Creek. While the two park sites were chosen to estimate the eastern extent of the distinguishing geologic features of the region. The Jackson County Landfill site located in northwest Arkansas is positioned on the outskirts of the Mississippi floodplain to the west.

2.7 Conclusions

The above considerations illustrate the seismic hazard present within Mid-America, namely the NMSZ and the Memphis metropolitan region. The large dependence of earthquake ground motions on V_S was also demonstrated through the discussion of site amplification. As a result, accurate near surface V_S data is needed to characterize local site conditions, providing the means for adequate measures to be implemented in preparation of future earthquakes. Further efforts should be focused on developing methods to accurately and cost effectively measure V_S data, and acquiring more V_S data for seismic zonation. The current study undertook both of these tasks by improving traditional engineering seismic surface wave testing and providing additional V_S data for the seismic zonation of the Shelby County, Tennessee.

Chapter 3

Surface Wave Techniques, A Historical Perspective

3.1 Introduction

Engineering analysis of surface waves to determine in situ dynamic soil properties dates back to the 1950's (Jones, 1955, 1958, and 1962). The US Army Corps of Engineers Waterways Experiment Station (WES) in Vicksburg, Mississippi also put forth a large effort to develop the use of surface waves for subsurface exploration (Ballard, 1964; Fry, 1963 and 1965). The first surface wave technique was called the Steady-State Vibration technique due to the harmonic excitation that was used to generate the surface waves. This first technique was cumbersome and time consuming and the Spectral-Analysis-of-Surface-Waves (SASW) technique was developed to alleviate some of the early deficiencies during work for the Texas Department of Transportation (DOT) by Heisey et al. (1982). In 1984, Nazarian and Stokoe established a standardized testing procedure for the SASW technique that has been used as the standard engineering surface wave testing procedure. Since its inception, the SASW technique has been improved both experimentally and theoretically. These improvements along with the introduction of several new surface wave methods in recent years have greatly increased the accuracy and breadth of application of surface wave testing.

This chapter will introduce the reader to the progression of surface wave testing throughout its brief history. The discussions will focus on three main topics: experimental procedures, determination of dispersion relations, and the inversion and forward modeling procedures used to determine the dynamic soil properties. This short discussion of the history of surface wave testing will provide the reader with a base knowledge that will allow for a better understanding of the current methods presented in Chapter 4. Throughout this background study the limitations of the various methods will be discussed, and the proposed improvements to overcome these problems will be presented. While current in situ surface wave tests still suffer from some theoretical and experimental shortcomings, the following presentation, as well as the discussion of the current methods in Chapter 4, should provide the reader with a clear understanding of the numerous subsurface exploration possibilities available through seismic surface wave testing.

3.2 Steady-State Vibration Method

The steady-state vibration technique, often call the steady-state Rayleigh wave method, was the precursor to present-day seismic surface wave tests. The concept behind the steady-state method is that by inputting a constant or "steady-state" sinusoidal input into the soil, the vertical displacements at any point along the surface would be sinusoidal. The test procedure consisted of moving two vertically oriented displacement sensors along the surface until they were in phase. Figure 3.1 shows an illustration of this concept, in which the outlying receiver was moved away from the source until the two receivers were in-

phase. Once an in-phase point was found, the outlying sensor would again be moved away from the source until the next in phase point was found. This process was repeated several times at each frequency producing a curve as shown in Figure 3.2 (a). The distance on the x-axis represents the distance between the two receivers and corresponds to a multiple of the wavelength (λ)when the receivers are in phase. The frequency of the Rayleigh waves was assumed to be equal to that of the source, which allowed the Rayleigh phase velocity to be determined from Equation 3.1:

$$V_R = f \cdot \lambda \tag{3.1}$$

This process is very time consuming and limits the number of frequencies used to determine the dispersion curve. A sample dispersion curve from a steady state test is shown in Figure 3.2 (b).

With the dispersion relationship determined, it was then necessary to invert the dispersion relation to determine a shear wave velocity profile, as shown in Figure 3.2 (c). The inversion procedure used in the steady-state technique was empirical. This procedure assumes that velocity of a Rayleigh wave of a particular wavelength is representative of a depth equal to one-half of the wavelength based on the particle motion in a homogenous half space shown in Figure 1.4. This empirical procedure then assumes the relation between Rayleigh and shear wave velocities for a homogeneous half-space:

$$V_S \approx 1.1 \cdot V_R \tag{3.2}$$

The ratio of V_S/V_R actually varies based on Poisson's ratio and other factors. However, the empirical nature of early inversion procedures makes the error involved with assuming a value of 1.1 minimal. This inversion procedure was shown to work well for homogenous and gradually changing sites, (Huekelom and Foster, 1960; Fry 1963; and Ballard, 1964). However, the method yields very poor results for other site conditions (Rix, 1988).

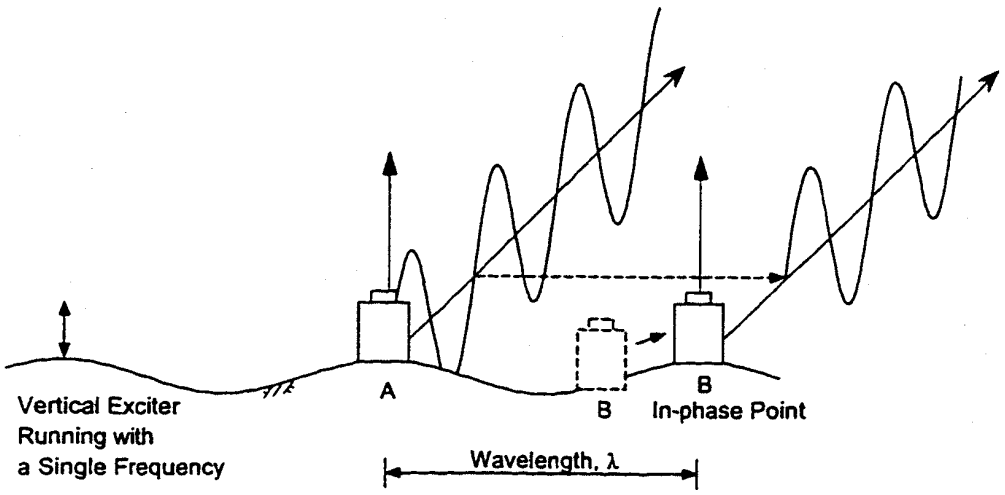

Figure 3.1 Illustration of Steady-State Rayleigh Wave Measurements. (Joh, 1996)

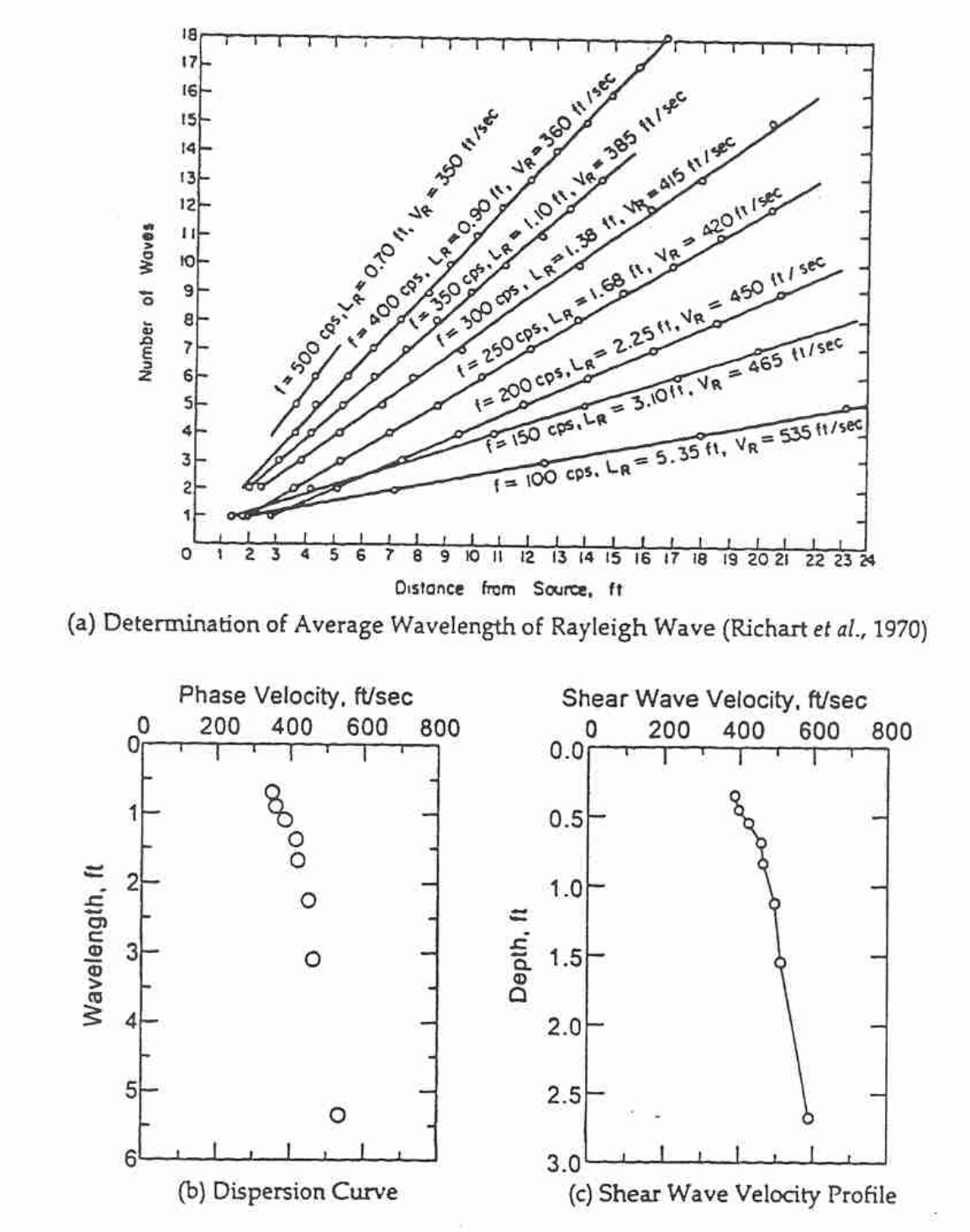

Figure 3.2 Determination of Phase Velocity from Steady-State Rayleigh Wave Measurements . (Joh, 1996)

3.3 The Spectral-Analysis-of-Surface-Waves (SASW) Method

Through advances in signal processing equipment and computers, the original steady-state surface wave method was improved into what is now known as the SASW technique. The SASW technique has undergone several developments since the 1980's, and a brief summary of those advances is presented here. The first standardized test procedure for conducting SASW measurements was developed by Nazarian and Stokoe (1984). This traditional SASW test setup uses two sensors to measure an actively produced Rayleigh wavefield at several receiver spacings. The active source may consist of either of an impulsive source, e.g. a sledge hammer or dropped weight, or a harmonic source. An impulsive source allows a range of frequencies to be tested in a single measurement, thus greatly decreasing the time required to complete a full set of measurements, while a sinusoidal source enables data to be collected within a large ambient noise field because the signal to noise ratio is increased. See Rix (1988) for a thorough discussion of the advantages of various input sources in SASW measurements.

3.3.1 Traditional Dispersion Calculations

A primary goal of in situ surface wave testing is to determine the dispersion relationship of the site being tested. This relationship is usually presented as a set of discrete points that represent the trend of Rayleigh phase velocity as a function of frequency known as a dispersion curve. In traditional dispersion calculations the Rayleigh surface wave particle motions generated at each spacing are measured by two sensors and recorded by a digital signal analyzer. Advances in dynamic digital signal processing in the 1980's allowed all of the necessary frequency-domain calculations to be made in real time through the use of a digital signal analyzer. In traditional two-sensor methods the following four calculations are made for each receiver spacing (Rix 1988).

$$G_{y1y1} = Y_1(f)^* \cdot Y_1(f) \quad \equiv \text{ Auto Power Spectrum of Receiver 1} \tag{3.3}$$

$$G_{y2y2} = Y_2(f)^* \cdot Y_2(f) \quad \equiv \text{ Auto Power Spectrum of Receiver 2} \tag{3.4}$$

$$G_{y1y2} = Y_1(f)^* \cdot Y_2(f) \quad \equiv \text{ Cross Power Spectrum of 2 Receivers} \tag{3.5}$$

$$\gamma^2_{y1y2} = \left|G_{y1y2}\right|^2 / \left(G_{y1y1} \cdot G_{y2y2}\right) \quad \equiv \text{ Coherence between 2 Receivers} \tag{3.6}$$

where Y_i = the Fourier spectra of the i^{th} receiver, * denotes complex conjugation, and | | represents the Euclidian mean operator. Examples of each calculation are shown in Figure 3.3. During SASW measurements the signal analyzer is usually set to display the two most informative calculations, the phase of the cross power spectrum and the coherence between the two receivers.

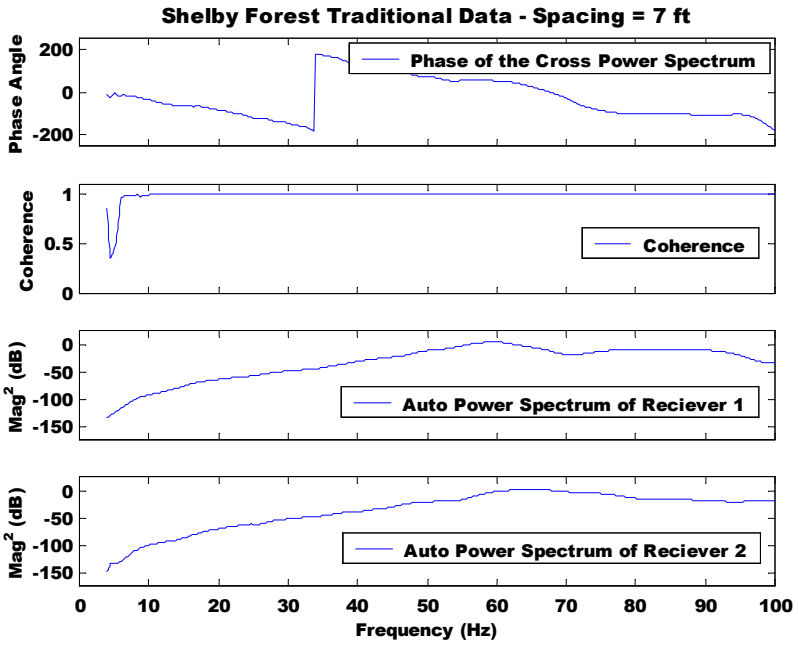

Figure 3.3 Illustration of the Typical Calculations Performed in Traditional SASW Tests

The cross power spectrum contains complex-valued terms composed of magnitude and phase data. The phase of the cross power spectrum, depicted in Equation 3.7, represents the phase shift measured between the two receivers as a function of frequency. Using this phase shift and the known distance between the receivers, an apparent wavenumber can be calculated for each frequency using Equation 3.8:

$$\Delta\phi(f) = \tan^{-1}\left(\frac{\mathrm{Im}(G_{y1y2})}{\mathrm{Re}(G_{y1y2})}\right) \tag{3.7}$$

$$k_{apparent}(f) = \frac{\Delta\phi(f)}{\Delta d} \tag{3.8}$$

where $\Delta\phi$ = the phase shift between receivers, and Δd = the spatial distance between receivers. The phase data from a traditional active test is shown in Figure 3.4. The coherence and the auto power spectra are used to determine what portions of the data may be corrupted. Coherence represents the portion of the signal measured at sensor 2 that is the direct result of the signal measured at sensor 1, i.e. the coherence represents the linearity of the relation between the two sensors. Coherence ranges in value from 0 to 1, with a value of 1.0 signifying a perfectly linear relation. Phase data with coherence values of more than 0.9 are then used in the subsequent dispersion calculations. Possible reasons for the deterioration of coherence include wave attenuation, body wave interference, spatial variability, and high levels of ambient noise. For a thorough discussion of these effects see (Sánchez-Salinero, 1987; Rix, 1988; Spang, 1995; and Zywicki, 1999).

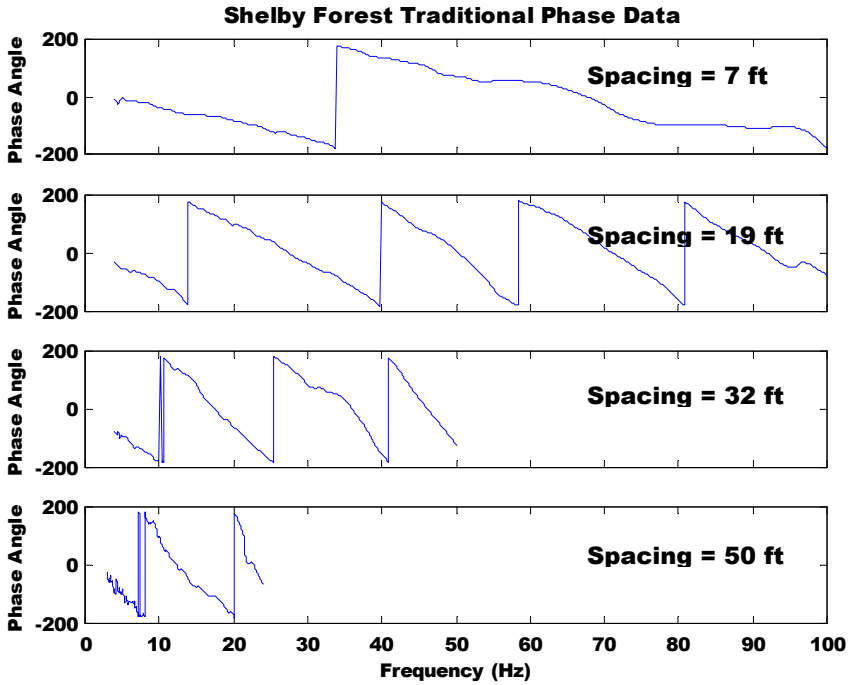

Figure 3.4 Illustration of the Typical Phase Records from a Traditional SASW Test

The apparent Rayleigh phase velocity can then be calculated using Equation 3.9:

$$V_R(f) = \frac{2\pi f}{k_{apparent}(f)} \tag{3.9}$$

Since traditional methods typically use sensor spacings that provide phase data over coincident resolvable frequency ranges, more than one value of V_R is calculated at most frequencies, as shown in the individual dispersion curves shown in Figure 3.5. Composite dispersion curves, consisting of all wavenumber calculations for each frequency, can be averaged to create a single average dispersion curve. An example of a composite dispersion curve and its subsequent average curve are shown in Figure 3.6. A primary drawback of traditional tests is that the entire range of phase data must be discernible in order to accurately estimate the phase shift of a receiver. That is, if the low-frequency data are indiscernible it becomes necessary to manually estimate the trend of the initial phase data in order to calculate the total phase shift at higher-frequencies.

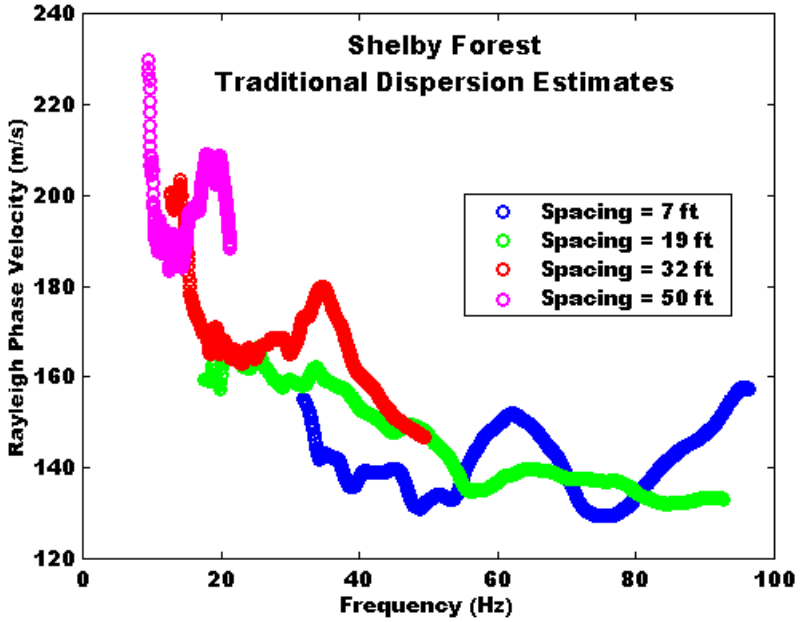

Figure 3.5 Individual Dispersion Curves from a Traditional SASW Test

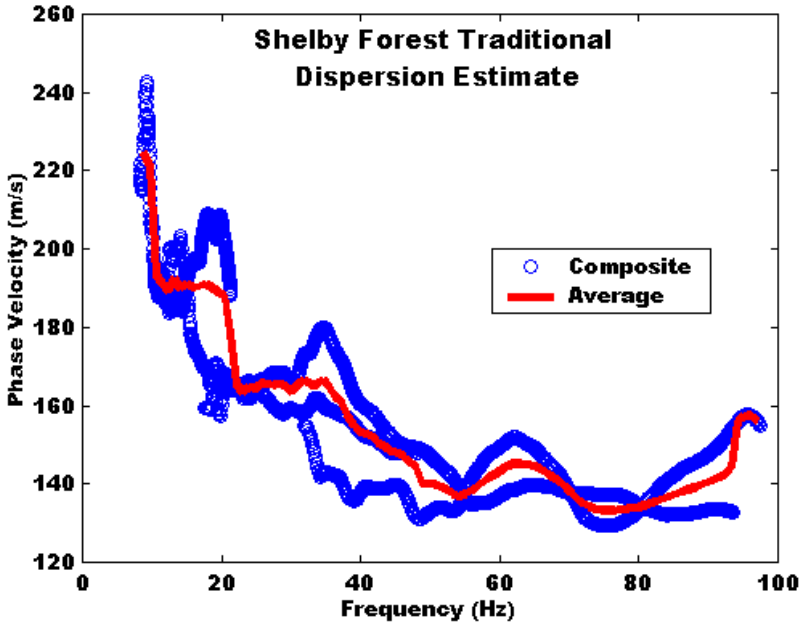

Figure 3.6 Composite and Average Dispersion Curves from a Traditional SASW Test

3.3.2 Cross Power Spectrum Method

The most common experimental setups used in the traditional SASW method are the Common Source Array and the Common Receiver Midpoint configurations, shown in Figures 3.8 and 3.9 respectively. The Common Source Array maintains equal spacing between the source and first receiver and between the first and second receivers throughout the testing. The spacing between the equipment is then typically doubled for each successive measurement to obtain phase data over a range of spatial lags. The Common Receiver Midpoint configuration moves both the source and the receivers for each spatial lag, and allows for the measurement of data from both the forward and reverse positions to enable the detection of sloped stratigraphy. As the spacings become larger, the sensors are able to measure longer wavelengths and thus measure deeper into the underlying soil strata. The spacing between the source and the first receiver is increased in an effort to minimize the near-field effects of body wave interference that occur when measuring long-wavelength surface waves. Sánchez-Salinero (1987) analyzed the effects of various source-receiver spacings and found that a ratio of ($d_2/d_1 = 2$) was a good compromise between the reduction of near-field effects and the practical consideration of measuring wavefronts at large distances due to attenuation.

3.3.3 Transfer Function Method

An alternative to the cross power spectrum SASW method is known as the transfer function method. This method traditionally uses two sensors, one of which is kept stationary either at a common point on the ground surface or on a harmonic source. The second sensor is then placed on the ground surface and moved in order to obtain several measurements across the desired range of spatial lags. (Sánchez-Salinero, 1987; and Lai and Rix, 1998). The transfer function between the two receivers is then calculated and used to determine the dispersion characteristics across a range of wavelengths. A transfer function, or frequency response function, normalizes the output of a system with respect to the input. Through this normalization, a transfer function emphasizes the characteristics and response of the system over the characteristics of the output or input (Rix, 1999). The complex-valued nature of transfer functions also allow for an elegant characterization of the magnitude and the phase of a system.

Once the transfer function between the two receivers is calculated, it can then be used to determine the phase velocity across a range of wavelengths. As with the previous traditional two-sensor methods, the transfer function method cannot resolve individual Rayleigh wave modes. However, the stationary position of the first receiver allows for much better attenuation estimates than the traditional cross power spectrum methods. This is achieved by using the first sensor as a reference point with respect to the various second receiver positions, thus combining an entire set of SASW measurements to more accurately define a single attenuation relationship. As with the V_R measurements, the dispersive nature of Rayleigh wave propagation makes the attenuation relationship a function of frequency, necessitating a combination of various spatial lag measurements to completely define the attenuation properties of the underlying soil strata. The common reference point of the first receiver also allows the wavefield model to theoretically account for geometric spreading (Lai and Rix, 1998), thus allowing the material damping to be separated from the geometry of the measuring array.

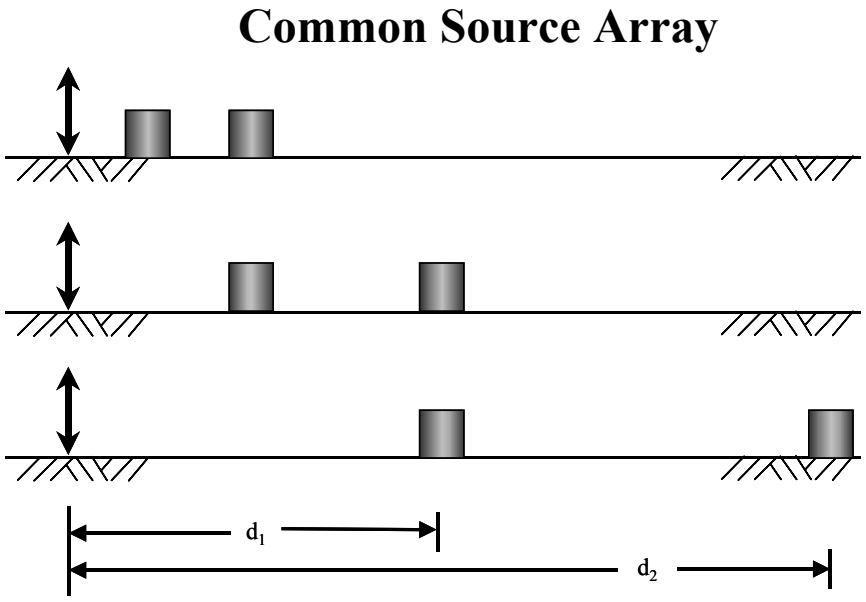

Figure 3.7 Traditional 2-station configuration, Common Receiver Midpoint Array (Adapted from Rix, 2000)

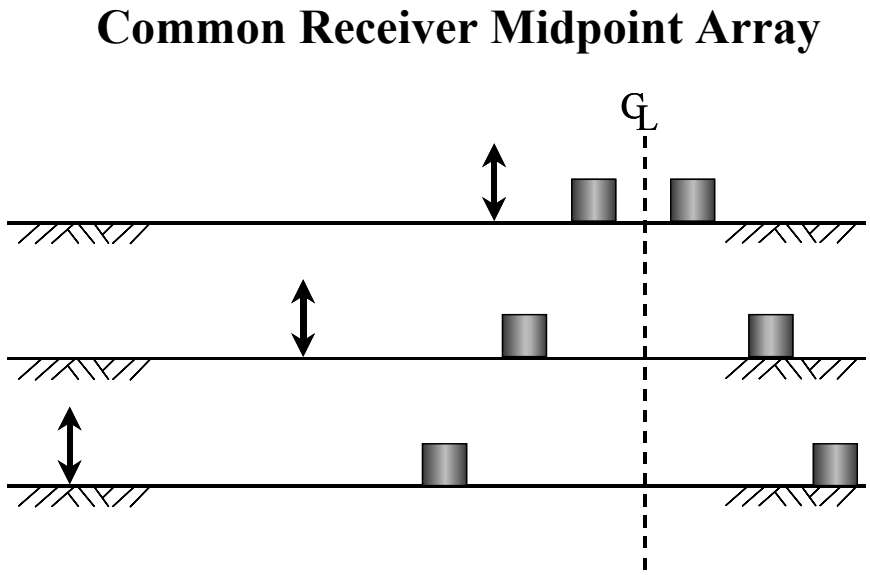

Figure 3.8 Traditional 2-station configuration, Common Receiver Midpoint Array (Adapted from Rix, 2000)

3.4 Multi-sensor Array Measurements

The next logical improvement to traditional surface wave measurements was to increase the number of sensors, enabling the measurements at all spatial lags to be computed simultaneously and consequently more efficiently. Not only is the simultaneous measurement and calculation of many spatial lags efficient, but it also allows for better attenuation estimates and provides the possibility of distinguishing multiple modes of propagation.

3.4.1 Linear Arrays

Active surface wave testing has been improved through the expansion of the technique to include array analysis techniques, making the dispersion calculations more robust. Recent surface wave studies using linear arrays include (Tokimatsu, 1995; Park et al., 1999; Zywicki, 1999; and Foti, 2000). Array measurements can be made by either increasing the number of sensors to measure all of the spatial lags simultaneously, or by combining several sensor measurements to form a synthetic array. However, if sensor measurements are to be combined to form a synthetic array, the source must be reproducible and remain stationary for each measurement so that the output measurements can be combined accurately.

The use of array analyses enables some of the drawbacks of traditional surface wave testing to be overcome. These drawbacks include: no multiple mode resolution, poor attenuation estimates, low ambient noise tolerance, and time intensive experimental procedures. Additionally, the phase shift between every sensor position can be calculated with array measurements, dramatically increasing the number of phase records available for use in the dispersion estimate. For example, consider a traditional receiver spacing, where sensors would be placed in pairs at the following distances from the source: (8, 16), (16, 32), (32, 64), and (64, 128) ft. This sensor arrangement allows for the measurement of 4 different spatial lags, and subsequently provides 4 phase records for use in the estimation of the dispersion relation, as illustrated in Figure 3.4. However, if multiple sensors are used in an array measurement a wide range of spatial lags can be measured resulting in the determination of phase records between every two-sensor combination in the array. The number of unique phase records obtained from an array of sensors is:

$$\text{\# of unique phase records} = \sum_{i=1}^{M} (i-1) \tag{3.10}$$

where M = the number of sensors in the array. For the current case of 15 sensors, this produces 105 unique sensor pairs, and as such 105 independent phase records available for use in defining the dispersion relation, as shown in Figure 3.9. This is a dramatic increase over the traditional two-sensor procedure, and not only allows for a larger distribution of spatial lags, but also allows the phase information at a number of spatial lags to be averaged over several spatial locations at a site. This averaging of multiple measures of the same spatial lag allows the measured dispersion relations to more accurately represent the global characteristics of the entire site rather than the specific area tested with a single spatial lag. The spacing of the receivers can be chosen to optimize the particular site and source characteristics. A more detailed discussion regarding the optimization of the spatial arrangement of receivers in multi-sensor arrays using array smoothing functions, is presented in Chapter 4.

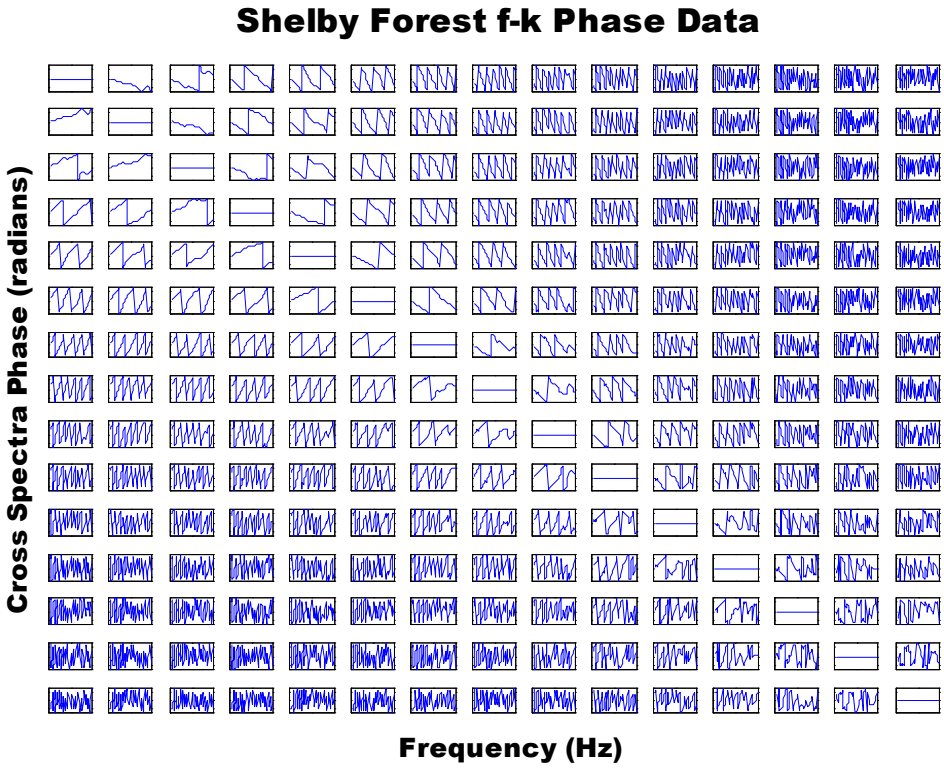

Figure 3.9 Phase Records generated using array-based f-k procedures, using a 15 sensor array.

3.4.2 Two-Dimensional Arrays

Several recent studies have used passive energy to conduct geotechnical and geophysical explorations, (Horike, 1985; Tokimatsu, 1995; and Zywicki, 1999). Two dimensional spatial arrays of receivers are required when conducting passive surface wave measurements since the direction of propagation of the surface wavefield(s) is not known as in the active case. The complexity of dispersion calculations is subsequently due to the added spatial dimension present in all calculations. Passive wavefronts may also have nonstationary frequency contents negating the use of Fourier techniques, and can also consist of multiple sources further complicating the dispersion calculations. However, the use of passive surface waves offers advantages over active surface wave testing in some cases. Passive wave sources, such as microtremors and cultural noise e.g. traffic vibrations, tend to generate low-frequency surface waves that can be measured as plane waves in the far-field. Thus enabling exploration to greater depths and eliminating previous near-field interference effects. A thorough discussion of passive surface wave testing using two-dimensional spatial arrays can be found in (Zywicki, 1999). Additionally, the passive procedures used in the current study are presented in Chapter 4.

3.4.3 Multisensor Dispersion Calculations

Numerous procedures have been used to determine the dispersion characteristics of surface wave measurements made with linear and spatial arrays. A thorough discussion of all of these methods is not warranted in this presentation of the historical developments of surface wave testing. However, if the reader is interested to gain a further understanding of this topic a sampling of these methods include: least squares fitting of wavenumber (Matthews et al., 1996; and Lai and Rix, 1998), instantaneous wavenumber estimation (Lai and Rix, 1998), multi-channel wavefield transformation (Park et al., 1999), and frequency-wavenumber spectrum methods (Tokimatsu, 1995; and Zywicki, 1999). The current research uses a frequency-wavenumber spectral technique to conduct the array-based dispersion calculations as described in Chapter 4.

3.5 Inversion Calculations

A main objective of in situ surface wave testing is to obtain the dynamic soil properties of the material, namely the shear wave velocity profile. Surface wave testing uses the dispersive nature of Rayleigh waves to "sample" the underlying soil strata. However, since the desired material properties are not measured directly they must be inferred from the measured dispersion curves through an inversion procedure. Almost all current inversion procedures used in surface wave analyses assume a media consisting of homogenous stacked layers of varying properties, as shown in Figure 3.10. It is intuitive that all site conditions cannot be accurately portrayed through this simplistic model. However, this discretization of a soil strata both simplifies the subsequent inversion and allows the calculated soil properties to be implemented into common site response programs such as SHAKE. These benefits make the model errors introduced by the assumption of horizontal, homogeneous layers acceptable in most cases.

Once a dispersion curve has been estimated from any of the above procedures, it can then be used in any number of inversion processes to determine a V_S profile. While numerous surface wave inversion algorithms have been developed, they all contain similar fundamental steps. A soil layering is determined based on either known geologic boundaries or other information. A theoretical dispersion curve is then calculated based on an initial estimate of the V_S profile for the given layering. The theoretical and

experimental dispersion curves are compared to determine the accuracy of the current V_S estimate. A curve fitting technique such as least squares updates the V_S values for the given profile layering to improve the agreement between the theoretical and experimental dispersion curves. This process is then repeated until the agreement between the theoretical and experimental dispersion curves falls within a preset error limit. While most inversion algorithms vary the V_S values while maintaining constant layering depths, it is possible to hold the V_S values constant and invert for the layer thicknesses.

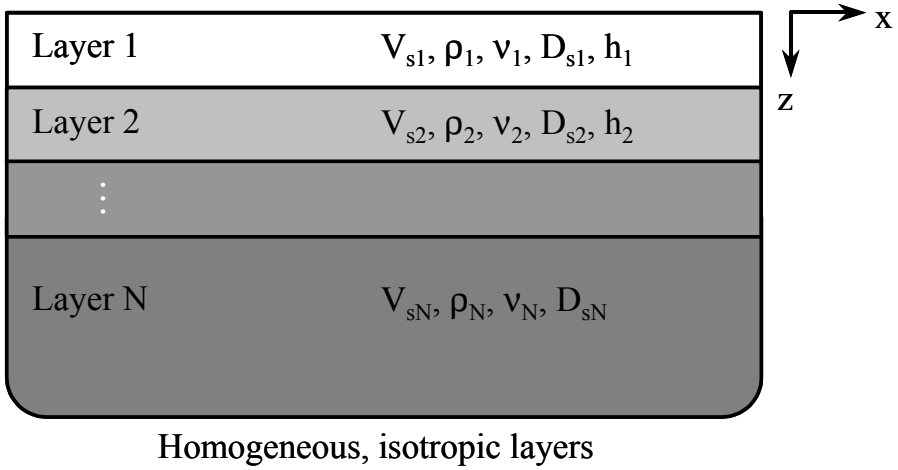

Figure 3.10 Stacked Layer Model (Adapted from Rix, 2000)

The inversion of surface wave data has received a great deal of attention in the last 20 years. However, the focus of this study is not based on inversion techniques and the reader is referred to the following references for more information on the evolution of inverse techniques used in surface wave tesing: (Thompson, 1950; Haskell, 1953; Nazarian, 1984; Horike, 1985; Yuan and Nazarian, 1993; Spang, 1995; Tokimatsu, 1995; Lai and Rix, 1998; Park et al., 1999; and Zywicki, 1999). The current study used the constrained least-squares algorithm developed by Lai and Rix (1998). The implementation of their procedures in the current testing will be covered in general in Chapter 4, and in detail regarding site specific considerations in Chapter 5.

3.6 Attenuation Estimates

Attenuation in particulate materials is composed of two main components that combine to form the global parameter of attenuation, geometric attenuation (spreading) and material attenuation (damping) (Kramer, 1996). The traditional attenuation model consists of the relationship shown in Equation 3.11:

$$A(\omega,r) = A_0(\omega)\, G\, e^{-\alpha(\omega)r} \tag{3.11}$$

where $A(\omega,r)$ is the magnitude of the experimentally measured particle displacements as a function of frequency (ω) and distance from the source (r), G is a function accounting for geometric spreading, and $\alpha(\omega)$ is the attenuation coefficient as a function of frequency. Unlike shear wave velocity measurements, which can be readily measured in situ, material damping has predominantly been measured in the laboratory using resonant column, torsional shear, and cyclic triaxial devices. This is primarily due to the dominance of global attenuation by the geometric portion of the phenomena. Laboratory testing allows for the isolation of material damping from the geometric components of global attenuation and allows material damping to be independently measured. Laboratory testing also allows the material damping to be measured over the full range of relevant strains, while in situ tests are predominantly conducted using seismic waves and are subsequently restricted to measuring low-strain properties. However, laboratory measurements of soil properties are compromised due to sample disturbance and spatial localization. Material damping is highly dependent on the effects of diagenesis and soil structure which are often destroyed in even the most careful sampling operations.

As such, methods used to measure the low-strain material damping of soils in situ can be extremely valuable. In addition to the calculation of the V_S profile for a site, surface wave measurements can also be used to measure the material damping ratio profile by measuring the spatial attenuation of surface waves (Jongmans and Demanet, 1993; and Rix et al., 2000). Additionally the same experimental procedures can be used to determine both the attenuation and velocity relations of a site, saving time and experimental resources. While velocity calculations are based primarily on the phase difference between receivers, attenuation calculations are based on the change in amplitude over distance. In order to accurately measure changes in amplitude over distance all measurements must be comparable. This requirement negates the use of testing procedures that do not contain either a fixed reference receiver or the use of a repeatable source. As with the V_S measurements, material damping measurements made with surface waves vary with frequency for non-homogeneous sites due to the dispersive nature of Rayleigh waves. Consequently, an inversion process similar to the one used to determine the velocity values must be undertaken to infer the desired material damping properties with depth. Lai and Rix (1998) developed a coupled inversion procedure that calculates both material damping and velocity values simultaneously. However, the main focus of this study is to determine shear wave velocity profiles in mid-America using surface wave measurements. As such, more detailed discussions of attenuation measurements using surface waves can be found in (Lai and Rix, 1998; Zywicki, 1999; and Rix et al., 2000).

Chapter 4

Current Surface Wave Methods

4.1 Introduction

Procedures for active and passive surface wave testing were developed to provide robust experimental methods that improved the capabilities of traditional testing methods. Specifically the current research focused on increasing the depth of resolution and the accuracy of dispersion estimates as well as eliminating previous testing limitations. This chapter presents the experimental and analytical techniques used in the current study and theoretical arguments for their superiority over traditional methods. Chapters 5 and 6 will validate the theoretical arguments made herein, with direct comparisons of results from the current surface wave techniques to both traditional surface wave measurements and other in-situ seismic methods.

4.2 Experimental Considerations

It is important to accurately define both the problem and the data necessary to solve that problem before embarking on the collection of experimental data. The main focus of this study was to determine the dispersion relation to allow the determination of V_S profiles. In order to completely characterize the dispersion of a propagating Rayleigh wavefield three dispersion parameters must be determined: phase velocity (V_R), temporal frequency (f), and spatial frequency (k). Spatial frequency, more commonly termed wavenumber, is defined as the number of cycles per unit length a wavefield exhibits in a particular direction:

$$\hat{k} = \frac{2\pi}{\lambda}\hat{\zeta} = \frac{\Delta\phi}{\Delta d}\hat{\zeta} \tag{4.1}$$

where λ = wavelength, $\hat{\zeta}$ = a unit vector in the direction of propagation, and $\Delta\phi / \Delta d$ = the change in phase with distance. These three parameters can be related to one another using Equation 4.2:

$$V_R = \frac{2\pi f}{\left|\hat{k}\right|} \tag{4.2}$$

Consequently, it is only necessary to determine two of the parameters experimentally, usually f and k, and the third parameter, V_R, can be calculated using Equation 4.2. For active measurements, for which the direction of wave propagation is known, the problem is simplified to the estimation of a single scalar wavenumber for each temporal frequency.

Several basic experimental considerations must be addressed to accurately measure the dispersion of a soil site. A number of measurement-specific criteria must also be considered prior to each test to

ensure that the most efficient experimental procedures are implemented. Experimental surface wave testing procedures vary with source type (impulsive, harmonic, or ambient), surface wave type (passive or active), measurement approach (two-sensor or array), sampling parameters (temporal and spatial), local site conditions (geology and topology), and most importantly the goal of the experiment. Extracting the desired information from a seismic wavefield offers several practical challenges as well. Electrical and cultural noise, multimode and diffractive wave propagation, spatial inhomogeneities of material properties, sensor coupling, and the unknown statistics of passive wave sources all interfere with the measurement process.

The equipment used in the current study was chosen to allow the flexibility to perform a number of different surface wave measurements, ranging from traditional procedures to active and passive f-k measurement methods. As such, the chosen equipment is not necessarily the optimum choice for use in practice or for any particular test; however, it provided the flexibility necessary to obtain high quality measurements and to vary a number of different testing parameters. A standard experimental procedure was developed that was modified to accommodate site-specific and test-specific characteristics when necessary. The selection and validation of the experimental procedures are discussed in detail below.

4.2.1 Source Selection

The first step in developing a surface wave testing program is to determine the source type. There are three common source types: active impulsive, active harmonic, and passive. One major advantage of active surface wave measurements is the ability to completely control the source, providing means for directing the measurement and analysis of the generated Rayleigh waves. While passive surface waves present the opportunity to sample to greater depths, their propagation characteristics are not known a priori, increasing the complexity of the post-measurement analyses. Impulsive sources allow an entire range of frequencies to be measured simultaneously; however, they are often not repeatable and limit the removal of external noise. Continuous harmonic sources allow each frequency to be tested individually by generating steady-state harmonic waveforms, permitting the analysis to be concentrated around a narrow frequency range which dramatically decreases the effects of external noise. The current procedures sought to limit the effects of external noise wherever possible in an effort to increase the accuracy of subsequent dispersion estimates. Consequently, a harmonic oscillator was chosen as the source for the current active testing. The source chosen was an electromagnetic shaker manufactured by APS Dynamics, Inc.

4.2.2 Sensor Selection

The number and type of sensors must be chosen to fit the needs of the testing program. The current study used array-based techniques to take advantage of the benefits provided by spatial array processing techniques described in Chapter 3. The number of sensors used in the array is governed by the capabilities of the data acquisition equipment. The current procedures use a 16-channel Hewlett Packard VXI-based digital signal analyzer that was chosen based on sampling and operational criterion described below. Seismic sensors must be chosen to fit the needs of the specific testing. The most important criterion when choosing seismic sensors is the frequency range over which they provide linear response. High sensitivity and resolution are also important characteristics, and sensors must also be durable and easily coupled to be implemented under field conditions. As such, testing was conducted using seismic accelerometers rather than the conventional choice of geophones. Accelerometers increase durability without sacrificing response, and their ease of calibration and robustness is advantageous for increased confidence in attenuation measurements (Zywicki, 1999). The present setup utilizes up to 16 Wilcoxon Research 731A Ultra-Quiet, Ultra Low Frequency seismic accelerometers and a source-mounted Wilcoxon Research Model 728T High Sensitivity, Low-Noise accelerometer used during active tests. Wilcoxon low

noise, R1-2-J93 coaxial cables were used with all 731A units while a Wilcoxon R1-2-J93-10 coaxial cable was used with the source mounted accelerometer. The source accelerometer was coupled to the source via a threaded mounting stud, while the surface accelerometers were meticulously gravity coupled to the soil surface by hand after removing surface vegetation.

4.2.3 Temporal Resolution

Before choosing a digital signal analyzer it is important to quantify the temporal sampling parameters, so that an appropriate analyzer can be specified. Two factors dominate the selection of test frequencies: the nature of Rayleigh wave propagation and the number of points to be used in the frequency-domain calculations. The dispersive propagation of Rayleigh waves, as seen in Figure 1.6, makes it necessary to obtain samples at smaller frequency intervals as frequency decreases. As such, the spacing of the discrete test frequencies narrows towards the lower end of the frequency spectrum. Secondly, since all of the dispersion analysis calculations are completed using a limited amount of discrete temporal data, there is an inherent limit to the frequency resolution of the calculations. Consequently, if the active source consists of waveforms generated at a series of discrete frequencies, it is necessary to test at frequencies that correspond to the exact values calculated in the Fourier dispersion analysis. As an example, the current testing parameters include 1,024 time domain data points obtained at a sampling frequency of 320 Hz for each discrete test frequency. The frequency resolution, or Δf, can be calculated using Equation 4.3:

$$\Delta f = \frac{f_s}{N} = \frac{320\ Hz}{1024\ pts} = 0.3125\ Hz \tag{4.3}$$

where f_s = the sampling frequency and N = the number of time domain data points collected at f_s for each sensor. In the above example, only frequencies equal to a multiple of Δf, 0.3125 Hz, can be exactly calculated in the frequency domain analysis. Consequently, the chosen test frequencies must all be multiples of Δf resulting in a minimum temporal spacing of Δf. Additionally, the upper limit of frequency resolution, known as the Nyquist frequency, is theoretically defined as half of the sampling frequency. However, because anti-aliasing filters are not ideal filters, the maximum frequency is less than one-half the sampling frequency in practice. The HP digital signal analyzer used in this study had a Nyquist criterion equal to $f_s/2.56$, corresponding to a maximum test frequency of 125 Hz for a sampling frequency of 320 Hz.

The series of discrete test frequencies was chosen based on the limitations of the source and the desired frequency distribution of the dispersion data. The chosen series of discrete frequencies ranged from the lower limit of the source, ~ 3.75 Hz, up to 100 Hz. The number of frequency measurements and the distribution of those frequencies is controlled by the amount of data that can be practically collected and analyzed, and the dispersive nature of Rayleigh wave propagation. As such, the current testing used frequency spacings of Δf ranging from 0.15625 to 2.5 Hz over preset frequency ranges that provided surface wave measurements at 60 individual frequencies per test site on average. The exact choice of the frequencies to be measured depends on site specific conditions and objectives, and was varied slightly throughout the testing. Consequently the engineer in charge of a particular test must use proper discretion and judgement to choose the appropriate frequency spacings for a particular test site.

4.2.4 Spatial Resolution

The ability to measure a surface wavefield is directly related to the geometry of the receiver configuration. For actively produced wavefields, the direction of propagation is known, so the problem of determining the wavefield characteristics simplifies to one of scalar wavenumber estimation. In an ideal case, spatial information would be collected at all spatial distances. However, practical constraints necessitate the use of a limited number of sensors placed in an optimum geometry. The upper limit of spatial resolution for a geometric array is controlled by the minimum spatial lag in the direction of propagation, as seen in Equation 4.4:

$$d_{\min}\left(\hat{\zeta}\right) \leq \frac{\lambda_{\min}\left(\hat{\zeta}\right)}{2} \Rightarrow k_{\max}\left(\hat{\zeta}\right) = \frac{2\pi}{\lambda_{\min}\left(\hat{\zeta}\right)} = \frac{\pi}{d_{\min}\left(\hat{\zeta}\right)} \tag{4.4}$$

where $d_{min}(\hat{\zeta})$ = the minimum spatial lag in the coarray direction $\hat{\zeta}$, $\lambda_{min}(\hat{\zeta})$ = the minimum wavelength contained in the wavefield in the direction $\hat{\zeta}$. Conversely, the minimum wavenumber resolution is controlled by two factors, the largest spatial lag contained in the sensor array and possible near-field effects. Near-field effects were described in Chapter 3, and are defined by the combination of body wave interference and the error caused by the incomplete development of long-wavelength surface waves measured close to their source. Traditionally, near-field effects limited measuring wavelengths greater than two times the distance from the first sensor to the source (Sanchez-Salinero, 1987). However, array measurements allow for more complete wavefront identification and allow the traditional criterion to be relaxed slightly. Common criteria used to quantify the minimum wavenumber resolution are the Rayleigh criterion, defined as half of the mainlobe width, or the full-width half-height defined as the width of the mainlobe at its mid-height (Zywicki, 1999). Insufficient minimum wavenumber resolution can cause multiple waves with closely spaced wavenumbers to become combined into a single peak, limiting the wavenumber resolution and accuracy of the analysis. This results in a superposition of modal energies and results in the estimate of an effective phase velocity. An example of this concept is shown in Figure 4.1 (Zywicki, 1999).

Every array geometry can be characterized by a smoothing kernel, or Array Smoothing Function (ASF). The ASF equals the Fourier transform of the weighted sensor array, as shown in Equation 4.5

$$W(k) = \sum_{i=1}^{S} w_i \exp\left(jk \cdot x_i\right) \tag{4.5}$$

where w_i = the weight applied to the i^{th} sensor, x_i = the spatial lag of the i^{th} sensor, S = the total number of sensors in the array, and $j = \sqrt{-1}$. An ideal ASF would be an impulse with zero side lobe height over the entire wavenumber spectrum. However, due to practical constraints, real ASF's have finite mainlobe width and sidelobe height. The width of the mainlobe in an ASF corresponds to its minimum wavenumber resolution. While the sidelobe height corresponds to an array's maximum spatial resolution and noise removal criterion. Optimization of an array geometry is achieved by minimizing side lobe height in conjunction with main lobe width. As such, there is an inherent trade off between numerical efficiency and the frequency and spatial resolution of the dispersion calculations. Figure 4.2 shows a comparison of the ASF for the current active test spacing, shown in Equation 4.6, to the ASFs of two linearly spaced geometries representing the minimum and maximum wavenumber resolution of the current array.

Active Sensor Geometry

$$\equiv \{8, 10, 12, 15, 18, 22, 28, 34, 42, 50, 60, 70, 80, 95, 110\} \text{ ft} \tag{4.6}$$

The large sidelobes of the ASF spaced uniformly to achieve the same maximum spatial lag (dashed line), occurring at a wavenumber of $2\pi/\Delta x_{min}$ = 2.82 1/m, correspond to the spatial aliasing limits of the array geometry and would lead to false peaks in the f-k spectrum plots. While the increased mainlobe width of the ASF spaced uniformly at the minimum spatial lag (dotted line), shows the loss of wavenumber resolution with decreased sensor spacing. Consequently, the ASF for the current array (solid line) was chosen to meet the sidelobe height and mainlobe width criteria of the current testing.

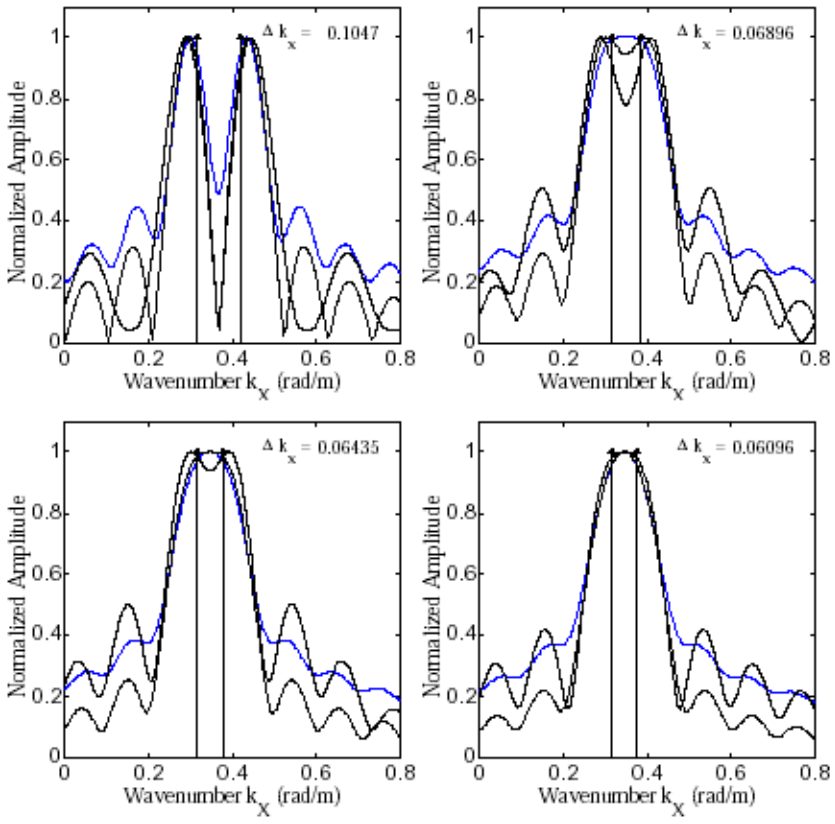

Figure 4.1 Array Resolution for Different Spatial Displacement Normalization Techniques. Two waves, with amplitudes equal to one, propagate past the array with progressively closer wavenumber spacing. The results from using no normalization technique (solid line), multiplying the wavefield by $x^{1/2}$ (dashed line), and normalizing the magnitude of displacements to one (dotted line) are shown. (Zywicki, 1999)

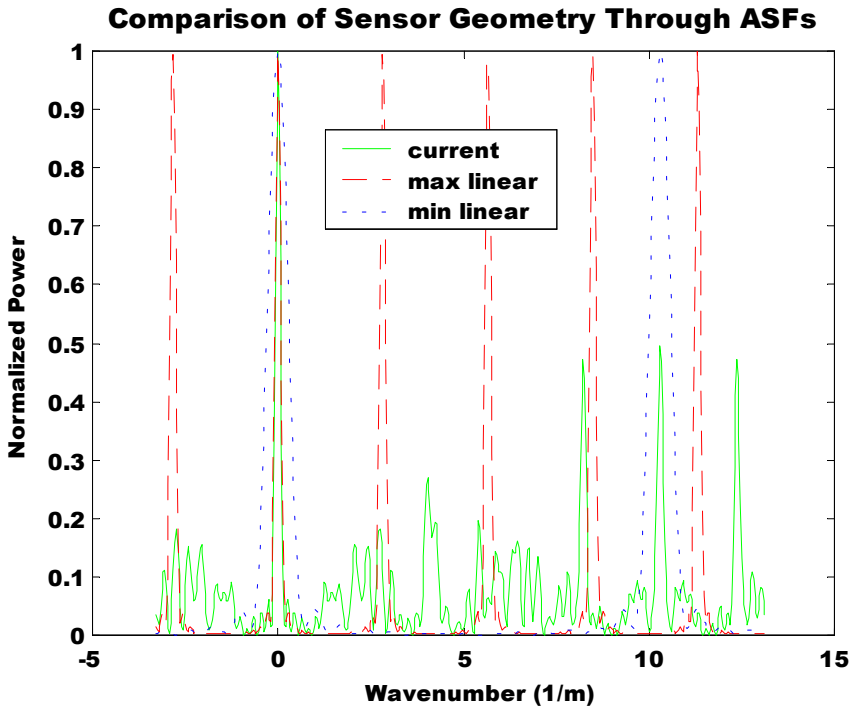

Figure 4.2 Comparison of the Spatial Resolution of Various Spatial Array Configurations using Array Smoothing Functions. All arrays are composed of 15 sensors, current active linear geometry (solid line), sensors placed evenly to achieve the maximum spatial lag of the current array (dashed line), sensors placed evenly at the minimum spatial lag of the current array (dotted line).

4.2.5 Data Acquisition and Signal Conditioning

Taking into account the above considerations: the number of sensors, the temporal sampling specifications, and the quality of measurements desired a means of acquiring data must be obtained. While surface wave measurements have traditionally been made using digital signal analyzers in order to allow for real time signal conditioning and Fourier analyses, it is possible to use other data acquisition methods. The current procedures utilized a Hewlett-Packard (HP) VXI digital signal analysis system. The HP VXI mainframe contains an embedded 133 MHz Pentium controller, 32 MB DRAM, an A/D converter, a dynamic signal analyzing module, and an HP E1562D throughput module. The 16-channel, 16-bit HP E1432A digitizer plus dynamic signal processor allows sampling of each channel at up to 51.2 kSamples/sec. Additionally, an external PCB Piezotronics 440 module provides signal conditioning with selectable gains of 1, 10, and 100 to 16 channels in four embedded 4-channel PCB 442A104 signal conditioners.

The Pentium controller and an external monitor allow the mainframe to operate in a Windows NT environment allowing easy access to data acquisition and system control files. For active measurements, a power amplifier was needed to operate the electromagnetic source. The source is currently controlled with the VXI's internal signal generator, although an external signal generator may be used. For all experimental measurements a computer script written in Matlab was used to control the test sequence. This script automated the active wavefield generation and data acquisition through the HP VXI signal analyzer and could be easily modified in the field to account for site-specific changes. By automating the test sequence, higher levels of precision and shorter test times were achieved. The matlab scripts used for both the active and passive procedures are included in Appendix A.

4.2.6 Active Testing Procedures

The active experimental setup used in the current study, as seen in Figures 4.3 and 4.4, included the HP VXI system, an external signal conditioner, an external monitor, a power amplifier, a harmonic source, a source mounted accelerometer, and 15 surface accelerometers. The electromagnetic harmonic source was programmed to oscillate at a predetermined series of discrete frequencies and specified temporal data acquisition parameters. The generated wavefield was then monitored with both a source-mounted accelerometer and a linear array of 15 ground-coupled accelerometers placed along a linear array originating at the source in the geometry stated in Equation 4.6. Each frequency was measured until 10,240 time domain data points, obtained at a sampling frequency of 320 Hz, were collected simultaneously at each of the 16 accelerometers. A plot of the time histories is displayed real time during the data collection to ensure the proper operation and coupling of all receivers. An example plot of time histories is shown in Figure 4.5 for a frequency of 10 Hz. The chosen number of 10,240 time domain points allowed for ten blocks to be averaged with a frequency resolution of 0.3125 Hz.

4.2.7 Passive Testing Considerations

Passive surface wave testing is highly analogous to the active case, however, the problem of defining the dispersion relation is further complicated by the unknown direction and the time dependent statistical nature of passive wavefields. As a result, passive surface wave testing must rely on two-dimensional arrays to monitor wavefields propagating from all directions. Figure 4.6 gives a pictorial representation of passive testing. This limits the range of spatial lags that can be measured due to the added sensors necessary to monitor all possible directions. The main advantage of passive wave sources is the high-energy concentration in the low-frequency range, 0 to 10 Hz, and their existence in the far-field allowing planar wave assumptions. Consequently, the current study strove to utilize a combination of

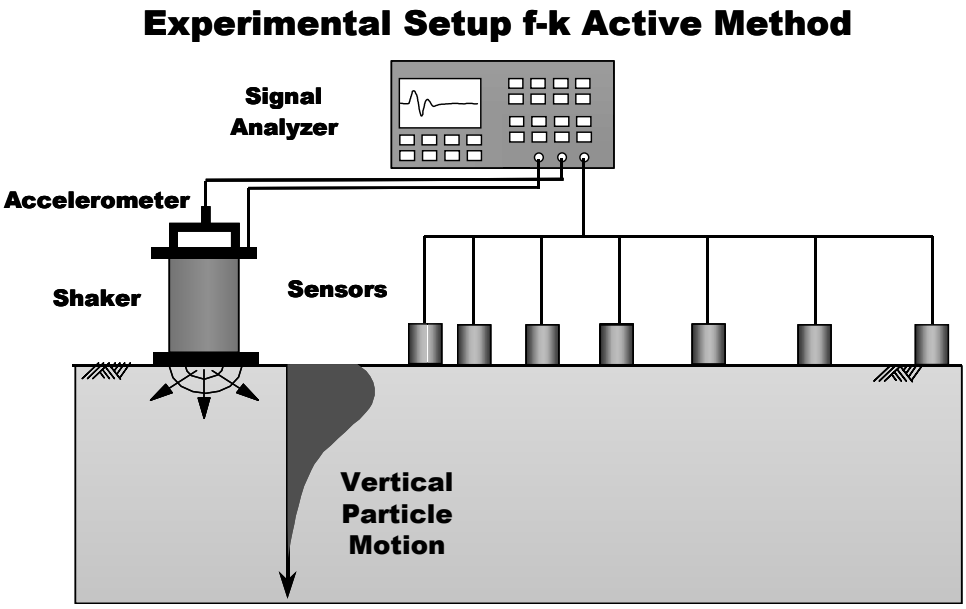

Figure 4.3 Illustration of Active f-k Testing Procedure.

Figure 4.4 Picture of Active f-k Testing Performed in Memphis, TN.

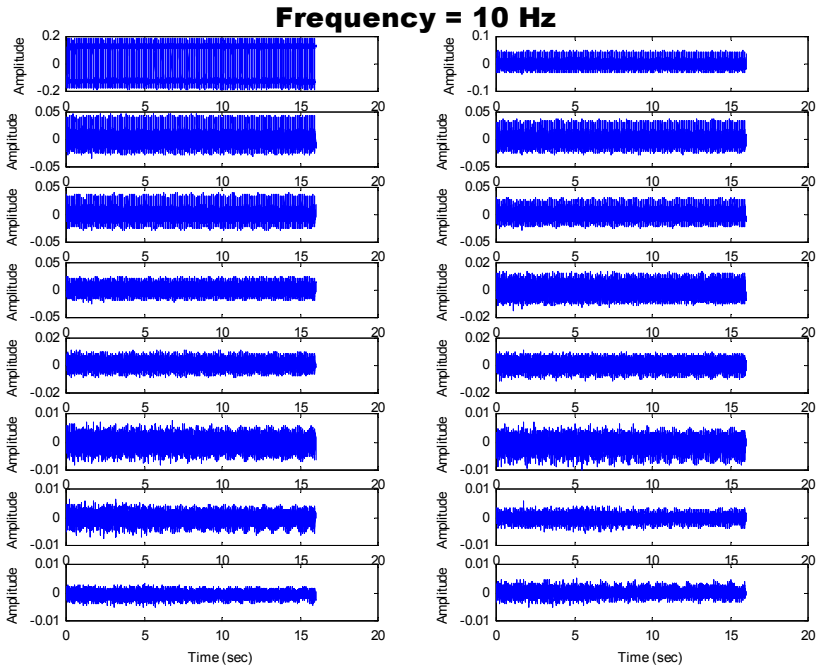

Figure 4.5 Example of a Time Record Plot shown During the Experimental f-k Testing .

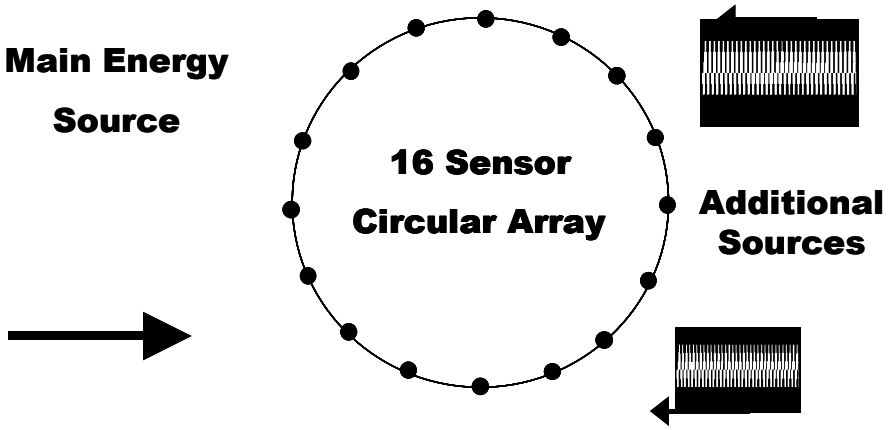

Figure 4.6 Illustration of Passive Surface Wave Testing.

active and passive methods to fully characterize the tested sites. Unfortunately, ambient wavefields do not exist at all site locations, making passive measurements impractical in a number of locations, especially in rural areas.

Zywicki (1999) studied the efficiency of various spatial arrays on passive surface wave measurements and found that a uniformly spaced circular array provides the best results under most circumstances. However, as with linear arrays, two-dimensional spatial arrays can also be optimized by comparing ASF's. Since the direction of wave propagation is unknown and multiple wavefields may exist, a uniform circular array provides equal spatial resolution in all directions. To further increase the level of spatial resolution, several circular arrays of varying radii can be used at each site. As passive measurements are usually conducted to measure long wavelengths, larger-diameter circles are usually preferred. If passive measurements are not to be combined with active measurements, smaller circles must also be used to supplement the large-diameter measurements, so as to adequately define the entire dispersion relation of a site. However, it must be noted that the high-frequency energy of passive wavefields is limited due to the increased attenuation of high-frequency waves with distance. As such, it is not always possible to measure high-frequency dispersion using passive procedures.

4.2.8 Passive Testing Procedures

The array geometry used in the current passive testing consisted of 16 accelerometers placed at equal intervals around a large-diameter circle. It is imperative that the each sensor be placed accurately in the desired location, as small errors in spatial placement would make the task of resolving an unknown passive wavefield prone to significant errors. To minimize spatial placement errors all sensors are placed with respect to a single point, usually the center of the circle. A fast and accurate placement technique was developed by Zywicki (1999), and was used in the current study. Relatively flat and open ground is needed to accurately place and monitor the 16-sensor array. Consequently, the size of the circular arrays implemented was dependent on the various site conditions. During the current testing, the circular arrays ranged in radius from 18 - 27 meters.

The collection of experimental data is significantly simpler than the active case. The main parameters that must be defined to conduct passive tests are the sampling frequency, the blocklength of time domain data, and the number of frequency-domain averages that will be used in the analysis. Once these are defined, the control script can be written to collect the data with the specified parameters and the experimental portion of the testing is complete. In the current study, 65,536 or 2^{16} data points were collected three separate times for each circular array used at a sampling frequency of 320 Hz. If the passive data is to be later combined with active data, then the specified sampling frequency can be lowered to focus the measurements on low frequencies. However, in this research study a relatively high sampling frequency of 320 Hz was chosen to allow flexibility in the subsequent analyses.

4.3 Dispersion Calculations

All dispersion calculations were performed in the frequency domain to allow both the magnitude and the phase to be elegantly and efficiently represented using complex notation. The use of Fourier's theory in frequency-domain calculations requires that the measured signals be both linear and time invariant. The current procedures allow for the use of Fourier's theories, and their use greatly simplifies many of the dispersion calculations. Current dispersion calculations were conducted using a frequency-wavenumber (f-k) procedure. While a number of f-k techniques have been developed throughout the field of array processing, a discussion of various dispersion estimation techniques is not the focus of this report, and the reader is referred to the general discussions presented in Johnson and Dungeon (1993) and a surface-wave-specific discussion presented in Zywicki (1999).

4.3.1 Frequency-Wavenumber Techniques

Frequency-wavenumber spectral techniques are based on the premise of scanning wavenumber space to determine the wavenumber power spectrum for each frequency of interest. In a theoretical case with no external noise and with unlimited time and spatial data, each mode in the propagating wavefield would be seen as a scaled impulse in wavenumber space for each frequency. However, the amount of temporal and spatial data are both limited due to practical constraints, leading to gaps in the temporal and spatial resolution of the measurements. These gaps in resolution lead to energy leakage into wavenumbers that do not correspond to the propagating wavefront, but rather correspond to the geometry of the experimental sampling parameters represented by the sidelobes in an ASF. Additionally, when a Rayleigh wavefront encounters the material interfaces present in heterogeneous and layered media it spawns higher mode surface waves further complicating the wavenumber determination. The ability of the f-k methods to resolve multiple modes is one of the major advantages over traditional methods. The errors induced by traditional estimators only considering the composite, or "effective", wavefront are partially eliminated by the ability to resolve individual modes. The ability to resolve higher modes becomes more important with increasing heterogeneity and for inversely dispersive sites. In depth discussions on multimodal surface wave propagation are given in publications devoted to wave propagation and will not be discussed herein (Kennett, 1983; Gucunski and Woods, 1992; and Tokimatsu et al., 1992a). Additionally, unlike traditional two point methods, the advanced signal and array processing allowed through the use of f-k procedures offer the ability to more accurately and completely consider the effects of external noise, and can be applied to both active and passive measurements.

4.3.2 Spatiospectral Correlation Matrix

The first step in the many f-k dispersion analyses is to form the spatiospectral correlation matrix (R). The R matrix is calculated by combining the cross power spectrum estimates for all spatial lags for a given frequency. To accomplish this the Discrete Fourier Transform (DFT) must be calculated to allow the calculations to be completed in the frequency-domain. The DFT is an application of Fourier theory that allows the application to finite length sequences by implying periodicity outside of the interval of interest (Oppenheim and Shafer, 1999). The DFT is the basis for the Fast Fourier Transfom (FFT) used by most computational programs. The DFT is defined by the relationship given in Equation 4.7:

$$S(\omega) = \sum_{t=0}^{N-1} s[t] \cdot \exp\left(\frac{-j2\pi\varpi t}{N}\right) \tag{4.7}$$

where S(ω) = the DFT of the time data vector s(t), ω = frequency, t = time, and N = number of time-domain samples. The R matrix presents an efficient and optimum way to store and manipulate the phase information contained in the array. Unlike traditional estimators, the f-k methods, through the use of an R matrix, utilize the phase data between all possible pairs of sensors, allowing much more information to be drawn from the array.

To calculate the R matrix, the time domain data from each sensor s(t), of length N, is segregated into B blocks, each of length L = N/B. The DFT of the individual blocks are then averaged, and the cross spectral density between each receiver pair is calculated. The averaging, accomplished using Welch's method, is performed to reduce the variance in the power spectrum estimate (Hayes, 1996). The reduction in variance is achieved in exchange for a reduction in frequency resolution. Welch's method averages the spectra modified with a window weighting vector. For example a Hanning window was used in the current calculations. Windowing the autocorrelation sequence applies smaller weights to the measurements at longer spatial lags, which inherently consist of fewer samples for fixed length data sequences (Zywicki, 1999). The R matrix is then formulated as the collection of cross spectral densities for each test frequency (f) as shown in Equations 4.8 and 4.9 below:

$$R_{i,j}(f) = \frac{1}{B}\sum_{n=1}^{B} S_{i,n}(\varpi) S^{*}_{j,n}(\varpi) \tag{4.8}$$

$$R(f) = \begin{bmatrix} R_{1,1}(f) & R_{1,2}(f) & \dots & R_{1,M}(f) \\ R_{2,1}(f) & R_{2,2}(f) & \dots & R_{2,M}(f) \\ \vdots & \vdots & \ddots & \vdots \\ R_{M,1}(f) & R_{M,2}(f) & \dots & R_{M,M}(f) \end{bmatrix} \tag{4.9}$$

where * denotes complex conjugation, ω = the Fourier frequency, f = the source frequency, and M = the total number of sensors.

4.3.3 Additional Considerations

For impulsive, random noise, and passive sources, where a full range of frequency information is measured simultaneously, it is only necessary to conduct a single set of spatiospectral calculations. However, if each frequency is tested individually, as was done in the current active procedures, it is necessary to combine the frequency domain information from each of the spectral density calculations to form a single composite R matrix. To accomplish this, the calculations are directed by the known frequency of the generated surface wavefield, and only the power corresponding to the frequency of the actively generated surface wave is retained in the R matrix. If the generated wavefield were the only signal monitored by the sensors, the cross power spectrum would exhibit a lone peak at the excitation frequency, f. However, the existence of external noise and ambient wavefields in the measured ground surface may result in large energy contents at frequencies other than those corresponding to the dominant Rayleigh wavefield. The process of selecting the portion of the CSD representative of the generated surface wavefield can be band-limited, allowing the information of the surface wavefront to be extracted from a noisy environment.

This process is performed by selecting the maximum of the cross spectral density over a band-limited range. In the current testing the range of power selections were taken to be 99-101% of the current frequency of wave generation, f. This relative maximum is then considered uniquely corespondent to the generated Rayleigh wavefield. It is important that the point be chosen from a band-limited range and not directly from the input frequency of the active source, because slight variations in frequency might occur during wavefield generation and in the transfer of energy from the source to the ground surface. Each value in the R matrix, $R_{i,j}(f)$, is then representative of a band-limited maximum of the cross power spectrum between two receivers at a particular frequency f. Examples of the band-limited selection are shown for a clean record and a noisy record in Figures 4.7 and 4.8 respectively. It can be clearly seen from Figure 4.8 that excess noise can be significant, and will seriously alter the predicted dispersion relation if not adequately considered. This ability to successfully measure actively produced wavefields in the presence of high levels of noise is one of the main advantages of the current active f-k spectral methods. This concept will be more clearly seen in Chapter 6, where the results of current and traditional surface wave dispersion estimation techniques are compared. A plot showing the selection of the CSD for each point at a particular frequency in the R matrix can be viewed during the R matrix calculations to provide a check of the analysis algorithm. An example of such a plot is shown in Figure 4.9.

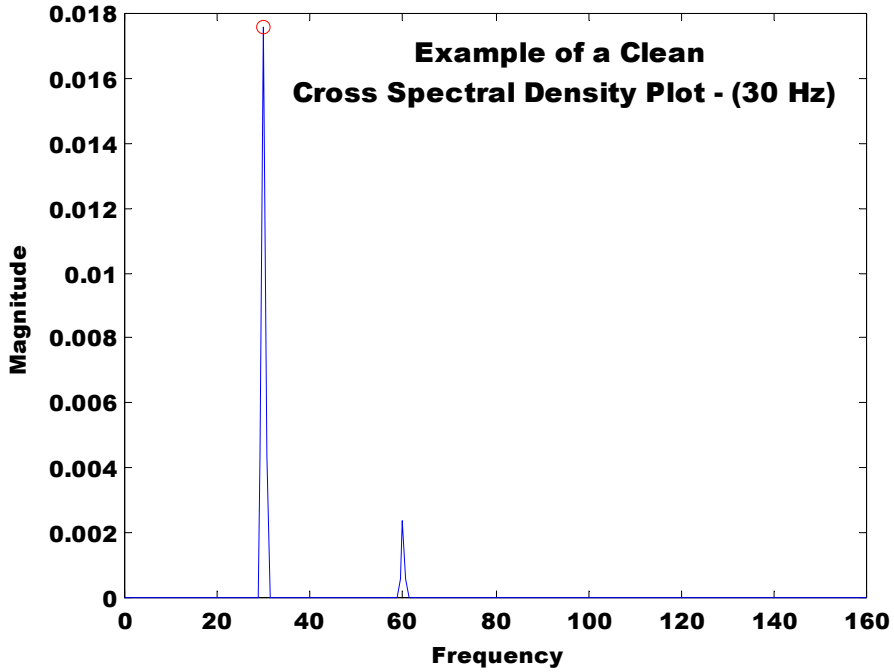

Figure 4.7 Example of a Clean Cross Spectral Density Plot. Source Frequency is 30 Hz.

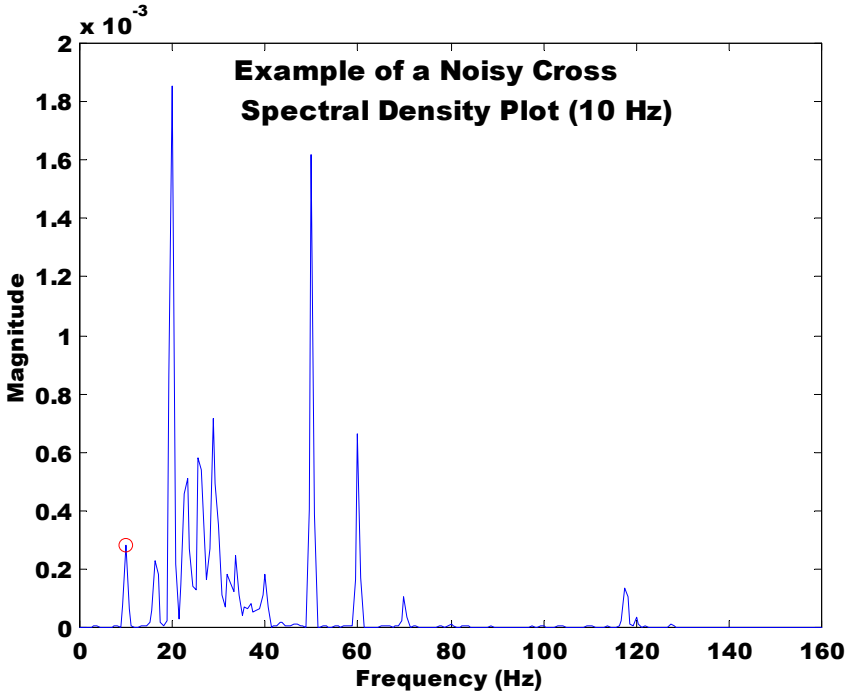

Figure 4.8 Example of a Noisy Cross Spectral Density Plot. Source Frequency is 10 Hz.

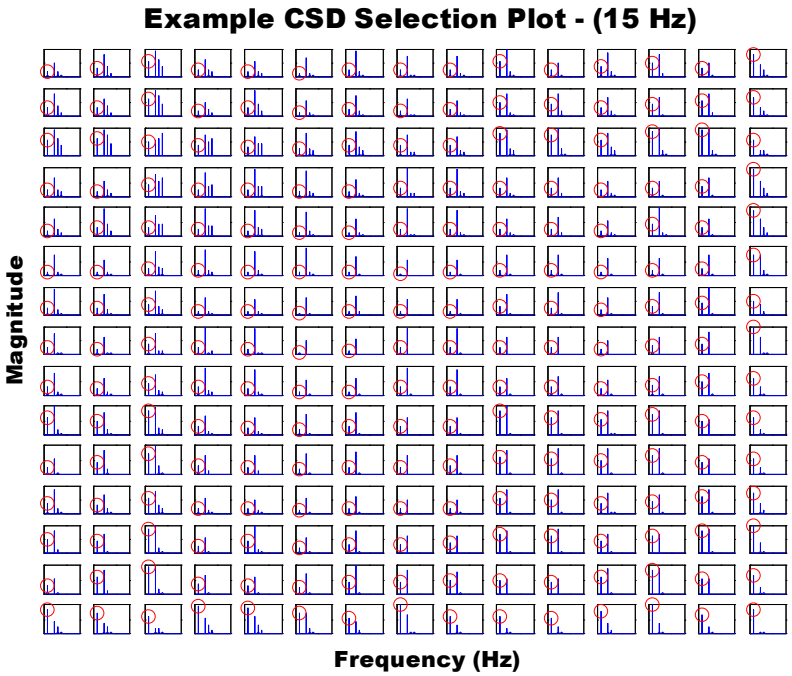

Figure 4.9 Example of a Cross Spectral Density Plot shown During the Experimental f-k Testing .

4.3.4 Beamforming

Once the R matrix has been calculated across the range of desired frequencies, any number of array processing techniques may be used to complete the dispersions calculations. The technique used in the current study is commonly termed a Frequency Domain Beamformer (FDBF) analysis. The mainlobe of an ASF is termed a beam, consequently the term beamformer comes from an array, or algorithm's, ability to focus this beam on a particular direction or wavenumber (Johnson and Dudgeon, 1993). The FDBF technique uses a steering vector to determine the power associated with particular f-k pairs. A steering vector is an exponential phase shift vector whose properties are controlled by a set of trial wavenumbers, which in turn concentrate the power calculation towards a particular wavenumber vector as seen in Equation 4.10:

$$e(k) = \left[e^{-jk \cdot x_1} \;\; e^{-jk \cdot x_2} \;\; \cdots \; e^{-jk \cdot x_S} \right]^T \tag{4.10}$$

where e(k) = phase shift vector associated with a trial k, x_i = the spatial position in the array, and $j = \sqrt{-1}$.

The power in a particular f-k pair is then determined by multiplying the R matrix by the steering vector and summing the total power over all sensors. Furthermore the signals may also be weighted using a diagonal matrix, W(f). Conventional analyses use singular sensor weights, W(f) = I; however, several weighting vectors can be applied to the power calculations to account for the cylindrical geometric spreading of the wavefront with distance from the source. One method is to normalize all of the measured sensor values to eliminate the affects of distance, however a more appropriate weighting vector to account for geometric spreading is shown in Equation 4.11. (Zywicki, 1999)

$$W(f) = \sqrt{\hat{x}}\sqrt{\hat{x}^T} \tag{4.11}$$

where $\hat{x}$ = the vector of sensor positions. The power can then be calculated efficiently using vectors as shown below in Equation. 4.12:

$$P_{FDBF}(f,k) = e(k) W^T(f) R(f) W(f) e^H(k) \tag{4.12}$$

where H denotes the Hermitian transpose of a vector. This calculation results in a single estimate of the power at every f-k pair, and produces a f-k power spectrum across wavenumber space for each calculated frequency. Theoretically, the individual modes of a Rayleigh wavefield would be estimated as scaled impulses at their corresponding wavenumbers. However, due to limitations in spatial and temporal data collection, and the inclusion of background noise, modes are resolved as peaks in the frequency-wavenumber spectra as seen in Figure 4.10.

Peaks in the f-k spectra for each source frequency are used to calculate the Rayleigh phase velocities using the fundamental relationship presented in Equation 4.2. This allows the dispersion estimate to be shown in the traditional form of Rayleigh phase velocity vs. frequency. In the current testing two methods were used to view dispersion estimates. The primary method used, simply presented a dispersion estimate with only the dominant peak represented for each source frequency, as shown in Figure 4.11. In cases where complex modal behavior is present it is often advantageous to view the f-k spectra in three-dimensional space. To accomplish this, the individual f-k spectral estimates at each frequency are normalized to allow the dispersion relation to be accurately viewed as a three-dimensional surface plot in either frequency-wavenumber or frequency-velocity space. Examples of these three dimensional plots are displayed in Figures 4.12 & 4.13 respectively. These three dimensional plots make it easier to follow the trends in multimode dispersion relations, as they allow all of the f-k spectra to be viewed simultaneously. additionally the three dimensional dispersion representations can help to eliminate data irregularities from propagating into the final discrete point dispersion estimate used in the inversion analysis.

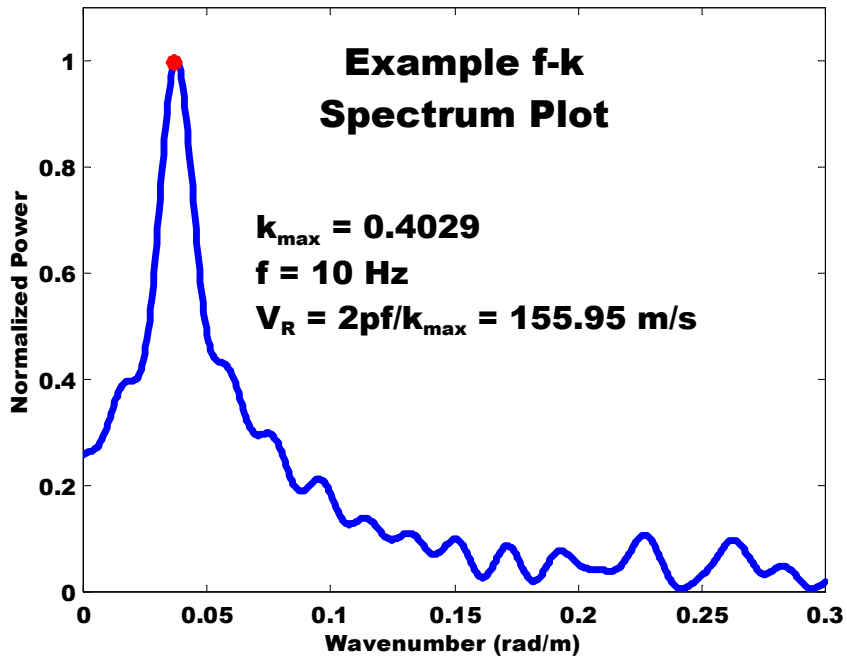

Figure 4.10 Example of an f-k Spectral Plot.

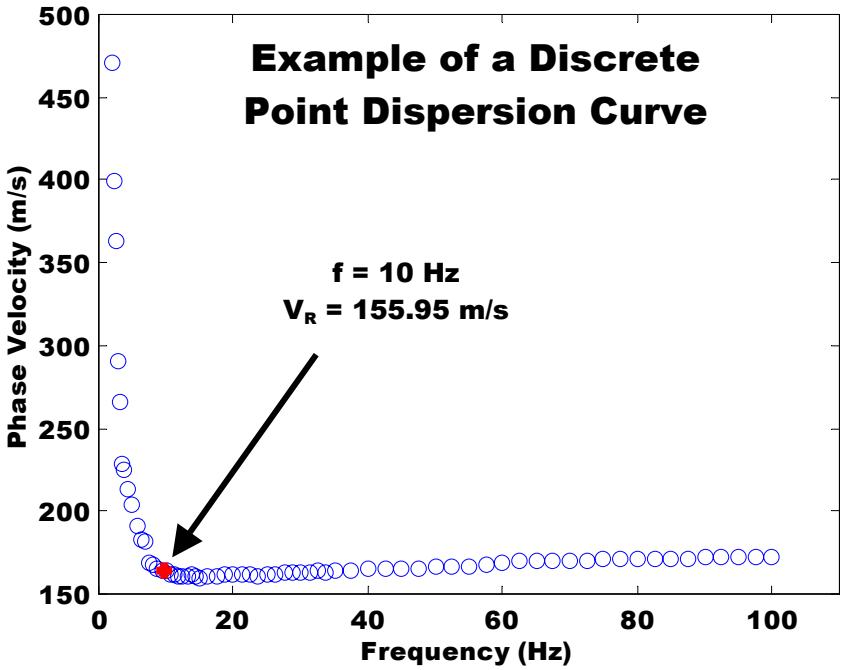

Figure 4.11 Example of a Dispersion Curve.

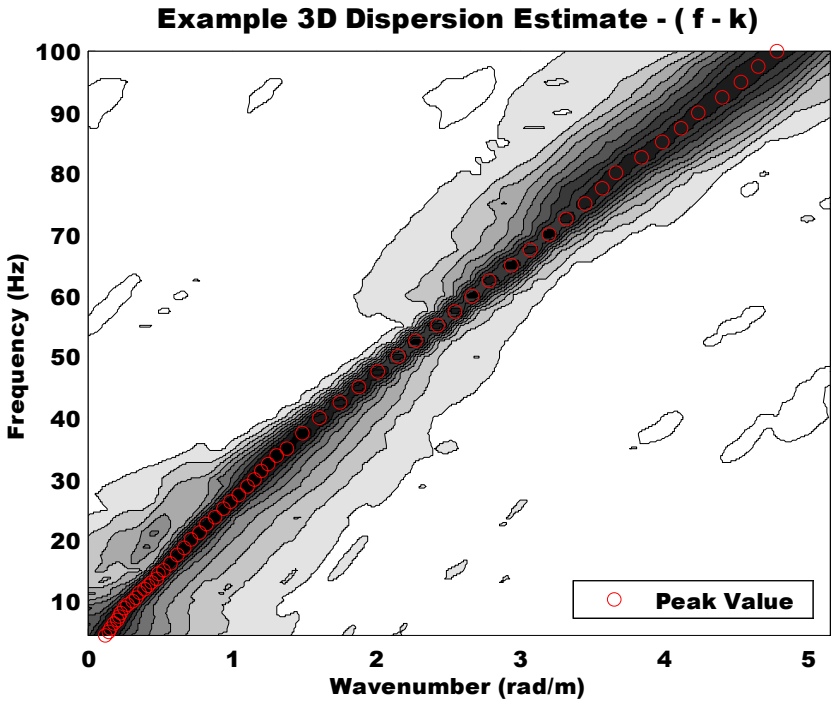

Figure 4.12 Example of an 3-Dimensional Dispersion Curve, Frequency vs. Wavenumber.

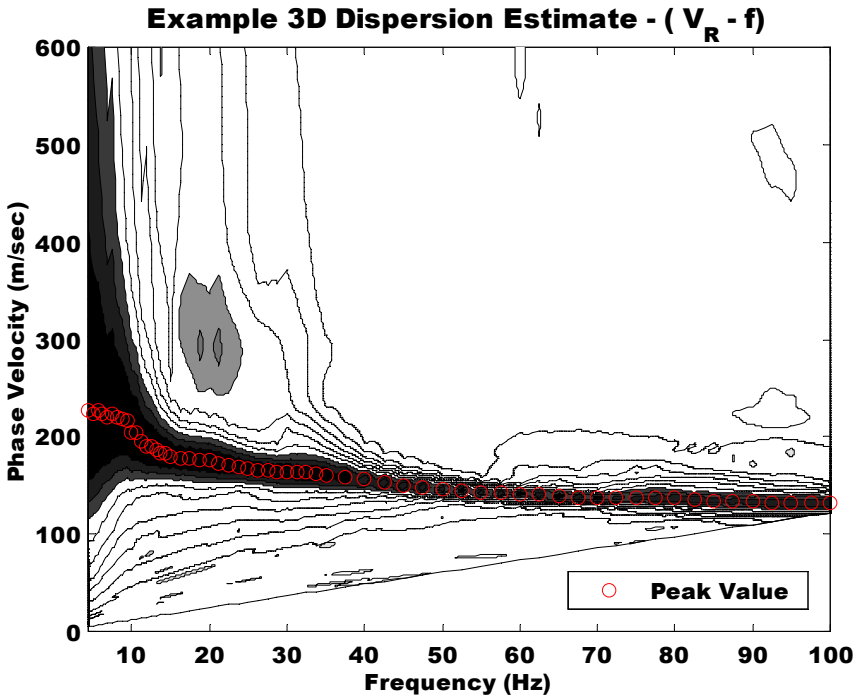

Figure 4.13 Example of a 3-Dimensional Dispersion Curve Rayleigh Phase Velocity vs. Frequency.

Secondary peaks in the f-k spectrum can be representative of lower energy Rayleigh modes, the superposition of Rayleigh modes, manifestations of the ASF sidelobes, or other wavefields present in the monitored surface. The ability to resolve multiple Rayleigh modes is directly related to both the sidelobe height and mainlobe width of the ASF. As such, multiple modes are often only concurrently discernible in f-k spectral plots across a short range of frequencies. An example of the transition of energy content from one Rayleigh mode to another as frequency increases is displayed in Figure 4.14. The subsequent dispersion estimate from these curves is shown in Figure 4.15 to clarify the modal transition. It is often beneficial to identify secondary modes in the f-k spectra and present them as part of the dispersion estimate. However, the resolution of secondary modes, while valuable in the inversion analysis, is practically difficult in most cases. Additionally, it is often difficult to discern which Rayleigh mode is represented by a particular set of secondary peaks, as the energy transfer between modes is not theoretically limited to direct transfer between adjacent modes. As such, it is possible for several intermediate modes to be indiscernible from the f-k spectra. The resolution of multiple modes in surface wave testing provides the ability to more accurately resolve complex stratigraphy and continues to be a topic of current research. However, the focus of the current research was not concentrated in this area, and all of the current analyses employed dispersion curves representative of only the highest energy peak from the f-k spectra at a particular frequency.

4.3.5 Passive Dispersion Estimates

Because passive testing relies on the measurement of ambient wavefields, the separate measurement of individual frequencies is not possible. As such, the subsequent analyses are similar to the procedure described above for impulsive sources and only one set of dispersion calculations is necessary to calculate the spatiospectral R matrix. The number of time domain data points collected experimentally limits the frequency resolution of the dispersion estimate as shown in Equation 4.3. Consequently the selection of the experimental parameters again controls the dispersion analysis procedures, and they must be properly selected based on the objectives of the testing in order to obtain a serviceable dispersion estimate. The frequency content of passive waves is often considered a random distribution across frequency, a white noise signal. However, the distribution of energy is usually shifted towards low frequencies due the increased attenuation of high-frequency surface waves over space, as seen in Figure 4.16. As such, the accurate resolution of passive data is usually restricted to the low-frequency range, and it is often advantageous to combine the application of active and passive tests to define the dispersion relation over the entire relevant frequency range.

The application of the FDBF technique to passive surface wave tests is relatively straightforward, as the calculations are easily expanded to include two dimensional wavenumber space $\hat{k} = (k_x, k_y)$ as seen in Equations 4.13 & 4.14.

$$e\left(k_x, k_y\right) = \left[e^{-j\hat{k}\cdot x_1} \;\; e^{-j\hat{k}\cdot x_2} \;\; \cdots e^{-j\hat{k}\cdot x_S}\right]^T \tag{4.13}$$

$$P_{FDBF}\left(f, k_x, k_y\right) = e\left(\hat{k}\right) W^T(f) R(f) W(f) e^H\left(\hat{k}\right) \tag{4.14}$$

In passive measurements, the weighting vector, W(f), is often used to account for uneven geometric spacings rather than geometric attenuation, due to the possible use of a highly complex array geometry and the limited relative geometric attenuation of far-field planar Rayleigh waves. Passive f-k spectral plots must be represented as three dimensional plots of power shown vertically on two-dimensional $\hat{k} = (k_x, k_y)$ space for each frequency, as seen in Figure 4.17. Dispersion estimates from passive testing must be examined with more scrutiny than those of the current active procedures because the amount of energy

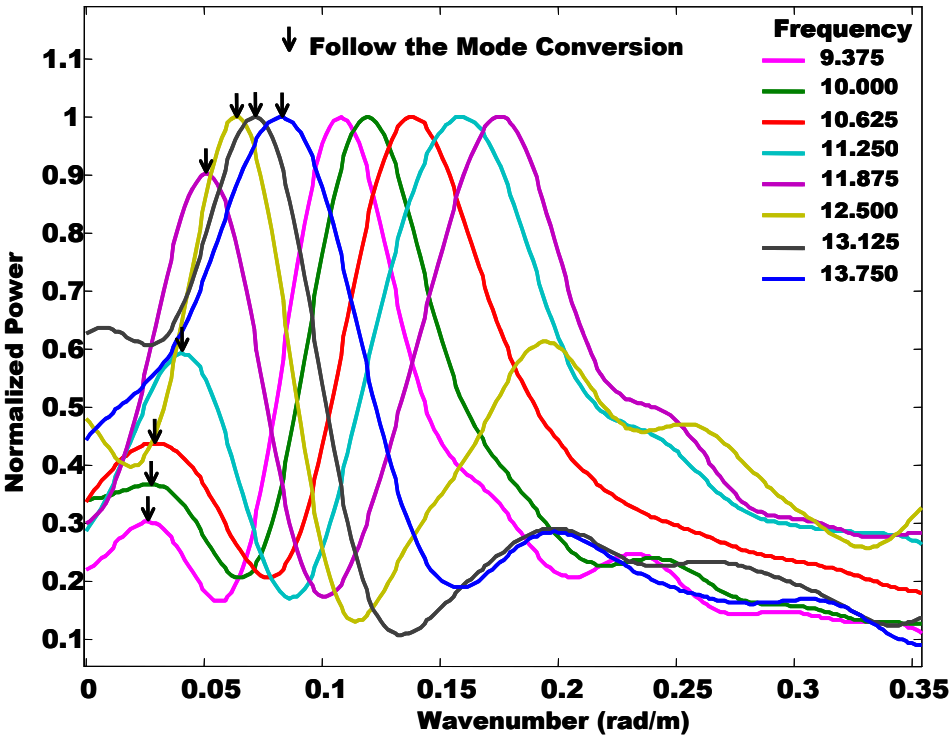

Figure 4.14 Example of Mode Conversion as Seen in f-k Spectral Plots.

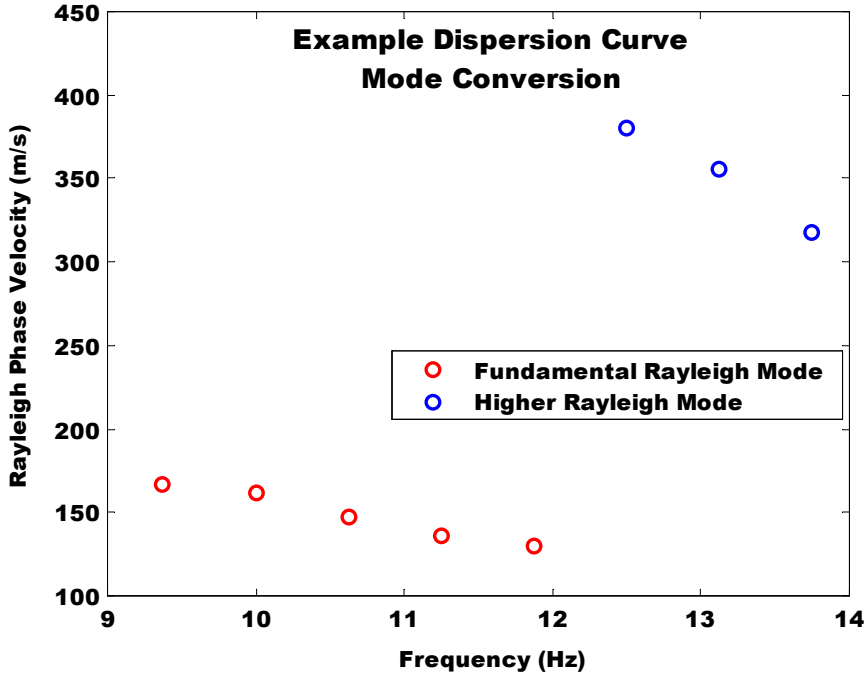

Figure 4.15 Dispersion Points Corresponding to the Mode Conversion Shown in Figure 4.14.

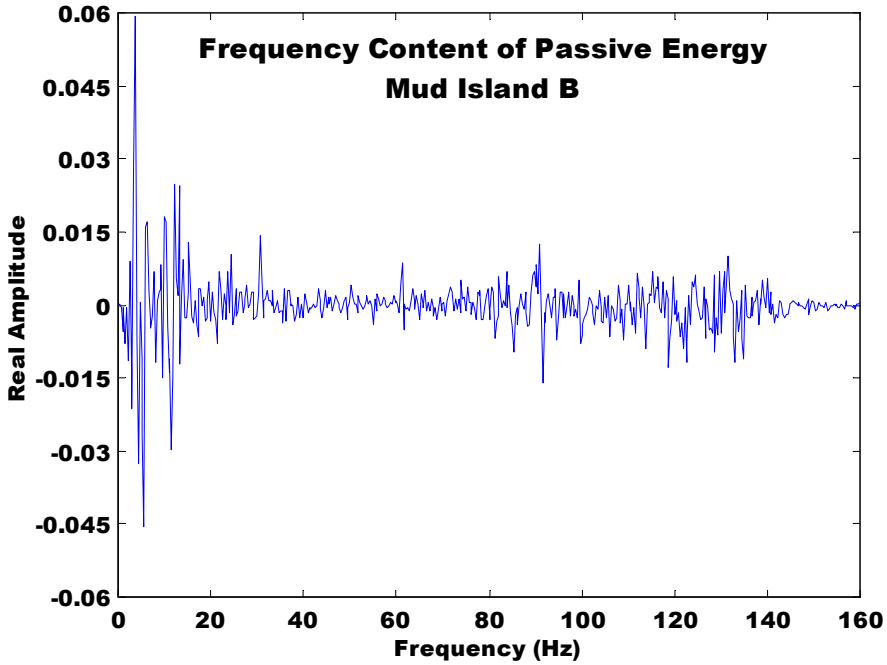

Figure 4.16 Example of Typical Frequency Distribution of Passive Energy Sources.

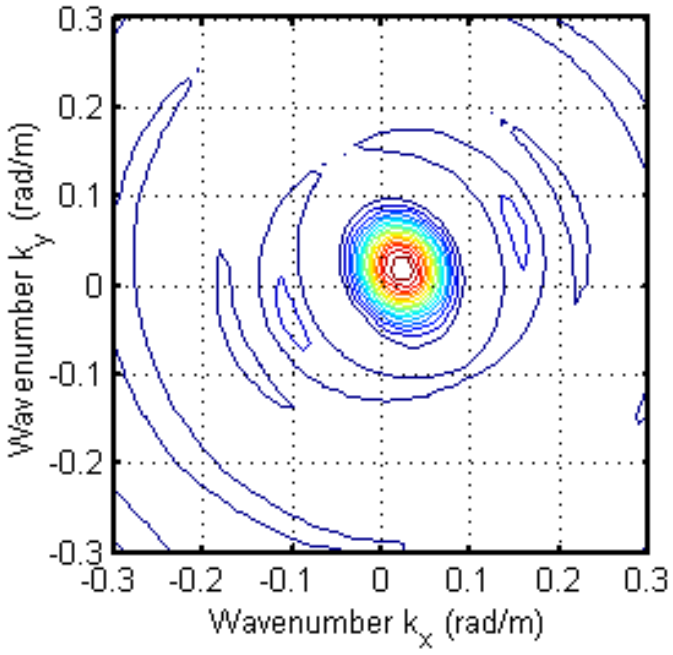

Figure 4.17 Example of a Passive f-k Spectral Contour Plot.

present at individual frequencies in the passive waveform varies considerably. A low energy content at a particular frequency, makes the resolution of the f-k peak correspondent to the Rayleigh propagation increasingly difficult and can result in the misestimation of individual dispersion points. Consequently, the engineer must try to discern the trend of the Rayleigh wavefield amongst several extraneous dispersion points.

The resolution of secondary peaks is further complicated during passive analyses due to the existence of multiple wavefields and the additional dimension of calculation. As such , it is customary to only provide dispersion estimates representative of the primary peak from each f-k spectra. Zywicki (1999) obtained multiple mode dispersion estimates from a limited number of passive tests. The application of this method to the current data did not result in the resolution of additional modes. However, this is most likely the result of only one Rayleigh mode being present in the wavefields of the two sites tested with passive procedures, as the number of modes is theoretically limited at low frequencies (Gucunski and Woods, 1992).

4.4 Rayleigh Wave Inversion

While both shear wave velocity and material damping ratio may be inverted from shear wave velocity data, this report is focused on shear wave velocity measurements and the subsequent discussions of inversion will be limited to this case. Rayleigh wave inversion is the process of fitting a theoretically produced dispersion curve to the experimentally measured dispersion estimate to produce a shear wave velocity profile. This process can be done using either a fundamental or effective approach. The fundamental approach assumes that the dispersion estimate is representative of only the fundamental mode of Rayleigh propagation. This implies that while other modes may be present in the wavefield, the fundamental mode contains the most energy across the range of tested frequencies. While this is usually the case in sites which exhibit normal dispersion and limited stratigraphy, the propagation and superposition of higher modes exhibiting greater energy than the fundamental mode is not uncommon, especially at higher frequencies.

As is the case in most non-linear inverse problems, the Rayleigh inverse problem can result in non-unique or ill-posed solutions. This problem is associated with the limited amount of experimental data that can be collected and the inability to resolve the complete characteristics of a the propagating Rayleigh wavefront, i.e. the accurate resolution of all Rayleigh wave modes. These two problems were addressed separately in the discussions on experimental procedures and dispersion estimators, and carry over directly into the inversion analysis. Since the amount of experimental data is limited, researchers commonly introduce additional information into the inversion by imposing global constraints.

4.4.1 Theoretical Basis

The inversion algorithm used in the current study was proposed by Constable et al (1987), and uses a non-linear least squares algorithm that promotes smoothness and regularity with depth. Lai and Rix (1998) recently developed an updated version of this algorithm which was used in the current study. The requirement of smoothness in the inverted solution eliminates some of the inherent scatter that may be present in the experimental dispersion estimate. Additionally, classic unbounded least squares inversions often yield unreasonable profiles, and the smoothness constraints help to limit possible solutions within the theoretical limits of dynamic soil properties. The roughness, or inverse of smoothness, used in the Constable algorithm may be defined by the expression in Equation 4.15:

$$R_1 = \sum_{k=2}^{nl} \left[V_S(k) - V_S(k-1)\right]^2 \tag{4.15}$$

where *nl* = the number of soil layers and V_S = a vector of length *nl* corresponding to the shear wave velocities of the layers.

The inversion algorithm is an iterative process that looks to minimize the error between the theoretically predicted and experimental measured dispersion curves within the framework of the specified boundary conditions. The least squares error calculated during the Constable inversion algorithm is represented in Equation 4.16:

$$\varepsilon^2 = \left[W \cdot V_{R(\exp)} - W \cdot V_{R(theo)}\right]^H \cdot \left[W \cdot V_{R(\exp)} - W \cdot V_{R(theo)}\right] \tag{4.16}$$

where $V_{R(exp)}$ and $V_{R(theo)}$ represent *nf* length vectors of experimental and theoretical Rayleigh phase velocities respectively, *nf* = the number of frequencies present in the dispersion curves, and W = a *nf* x *nl* x *nl* diagonal matrix as detailed in Equation 4.17:

$$W = diag\left\{1/\sigma_1, 1/\sigma_2, \ldots, 1/\sigma_{nl}\right\} \tag{4.17}$$

where σ = a measure of the uncertainty associated with the experimental data.

Because the solution of the Rayleigh inverse problem is an iterative process, it requires that a prespecified maximum error (ε^2*) be defined to mark the stopping point of the inversion process. The subsequent solution to the Rayleigh inverse problem is a V_S layering that minimizes the roughness R_1 for a profile that meets the error misfit criteria defined by ε^2*. This solution is found through the use of LaGrange multipliers to solve the constrained optimization of the above parameters as outlined in Equation 4.18.

$$V_S = \left[\mu \partial^T \partial + \left(W J_{V_{S0}}\right)^H W J_{V_{S0}}\right]^{-1} \cdot \left(W J_{V_{S0}}\right)^H W \left[J_{V_{S0}} \cdot V_{S0} + \left(V_R - V_{R0}\right)\right] \tag{4.18}$$

where μ = the LaGrange multiplier, or smoothing parameter, ∂ = an *nl* x *nl* matrix that defines the two-point finite difference operator (Constable et al. 1987), V_{R0} = the effective Rayleigh phase velocity obtained through the solution of the Rayleigh inverse problem at $V_S = V_{S0}$, and $J(V_{S0})$ = an *nf* x *nl* Jacobian matrix whose elements are the partial derivatives of the Rayleigh phase velocities with respect to the shear wave velocities of the layers ($\partial V_R/\partial V_S$). The prescribed maximum error (ε^2*) for the current testing was set at ε^2* = 0.5. This value was chosen based on the procedures and conditions present in the current testing, and is not necessarily optimum for all cases. The LaGrangian smoothing parameter (μ) ranges from 1 to 10^{-8}, and provides weights to the individual layer errors to enforce varying levels of smoothness. Once the least squares misfit, the smoothing parameter μ, and the experimental measurement errors are defined, an estimate of the error in each V_S profile can be made. Twenty profiles, each with varying values of smoothness, are calculated for each iteration with the profile exhibiting minimum error selected to continue the inversion. When the maximum prescribed error is met, the smoothest profile meeting the error criteria is chosen as the final V_S estimate. The plots corresponding to the inversion of the continuing example are shown in Figures 4.18 & 4.19. Figure 4.18 shows the match of the theoretical curve, complete with error bars representing the defined σ of 5%. Figure 4.19 shows the inverted shear wave velocity profile, again with the estimated error in each layer velocity shown as error bars, calculated using Equation 4.19.

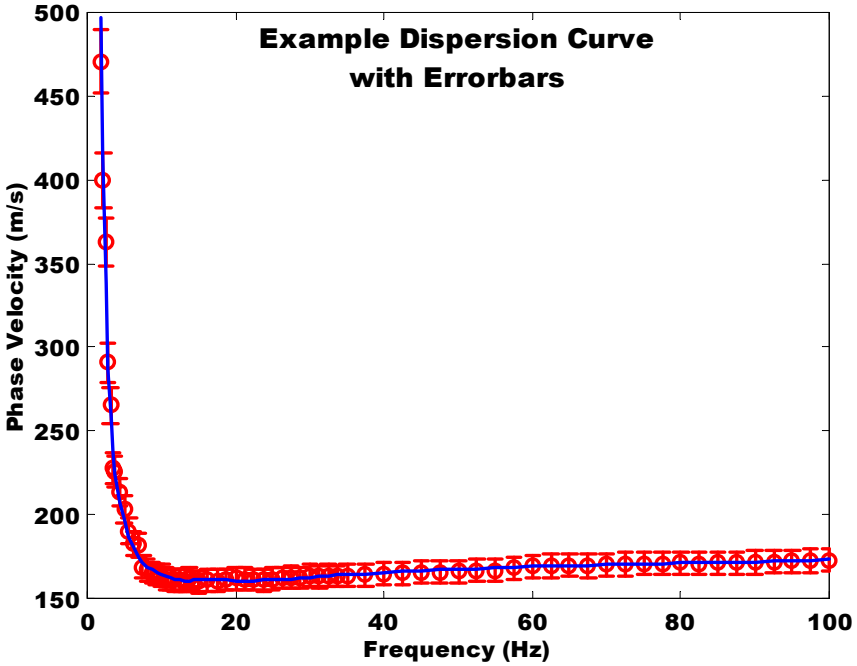

Figure 4.18 Example of a Dispersion Curve Determined using the Current f-k Methods, shown with Errorbars.

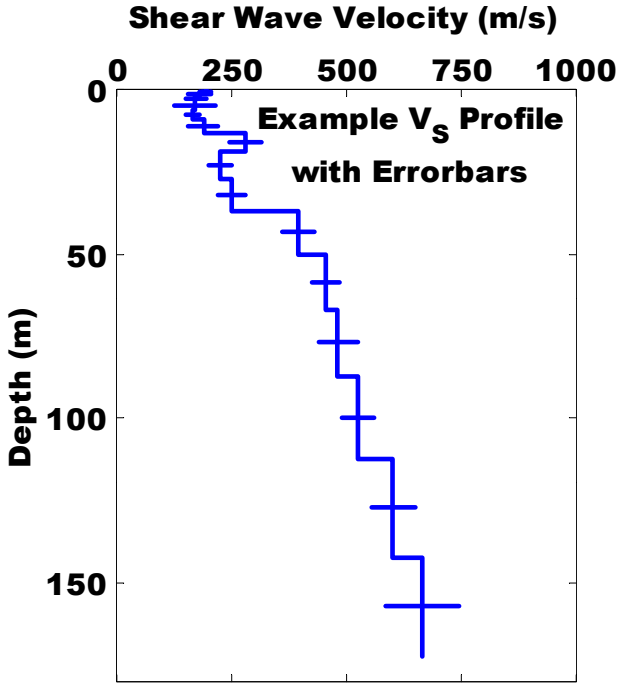

Figure 4.19 Example of a V_S Profile Determined using the Current f-k Methods, shown with Errorbars.

$$Cov(V_S) \approx \left[\left(\mu\partial^T\partial + \left(W_{V_R}J_S\right)^T W_{V_R}J_S\right)^{-1}\left(W_{V_R}J_S\right)^T W_{V_R}\right]\cdot Cov(V_R)\cdot\left[\left(\mu\partial^T\partial + \left(W_{V_R}J_S\right)^T W_{V_R}J_S\right)^{-1}\left(W_{V_R}J_S\right)^T W_{V_R}\right]^T \quad (4.19)$$

The inversion software uses Fortran compiled programs within a matlab interface, which are available at: http://www.ce.gatech.edu/~grix/surface_wave.html#Software (Rix, 1998).

4.4.2 Multi-Mode Effective Phase Velocity

In the current study, the wavenumber with the maximum power at each frequency was extracted and used to produce a discrete point dispersion curve as was seen in Figure 4.11. This curve may contain points from modes other than the fundamental mode of propagation, as the curve simply displays the value of the highest energy at a particular frequency. Theoretically the energy contained in higher modes of propagation will surpass the energy of the fundamental mode at high frequencies in heterogeneous and inversely dispersive profiles. However, it is common for inversion procedures to only consider the fundamental mode of propagation, termed a 2-D analysis. (Roësset et al., 1991) Normally dispersive sites will usually yield satisfactory results with 2-D analysis procedures; however, inversely and highly heterogeneous profiles must be inverted using a 3-D analysis procedure. 3-D analyses are based on numerically reproducing the multi-mode wavefield that would theoretically exist given the specified surface wave test conditions. Conventional 3-D analyses are exact yet they are computationally expensive as they require the solution of a dynamic boundary value problem of elasticity and the numeric calculation of the partial derivatives of the Rayleigh phase velocity with respect to the medium parameters.

Lai and Rix (1999) recently developed a new analytical approach to the 3-D problem. They derived an analytical expression for the three dimensional effective Rayleigh phase velocity that incorporates the simplicity and numeric efficiency of traditional 2-D methods, as shown in Equation 4.21.

$$\hat{V}_R(x,z,\omega) = \frac{2\omega\sum_{i=1}^{M}\sum_{j=1}^{M}\left\{\frac{r_2(z,k_i)r_2(z,k_j)r_2(z_S,k_i)r_2(z_S,k_j)\cos\left[x(k_i-k_j)\right]}{(V_iU_iI_i)(V_jU_jI_j)\sqrt{k_ik_j}}\right\}}{\sum_{m=1}^{M}\sum_{n=1}^{M}\left\{\frac{r_2(z,k_m)r_2(z,k_n)r_2(z_S,k_m)r_2(z_S,k_n)(k_m+k_n)\cos\left[x(k_m-k_n)\right]}{(V_mU_mI_m)(V_nU_nI_n)\sqrt{k_mk_n}}\right\}} \quad (4.21)$$

where (x, z, ω) = the horizontal and vertical directions, and circular frequency respectively, M = the number of propagating modes, V_i = the modal phase velocity, U_i = the group velocity, I_i = the mode dependant first energy integral, k_i = the modal wavenumber, z_s = the depth of the source, and $r_2(z, k, \omega)$ = the vertical displacement eigenfunction (where the frequency dependence of the eigenfunction has been omitted in the above equation to conserve space). Although Equation 4.21 looks highly dependent on a large number of variables, note that the effective Rayleigh phase velocity is only truly dependent on the solution of the Rayleigh eigen problem, as all of the other variables are interrelated. Tokimatsu et al. (1992) show the effects of multi-mode propagation for three examples of typical soil profile types. An example, Tokimatsu Case 2, showing the dominance of higher modes of propagation at high frequencies is shown in Figure 4.20.

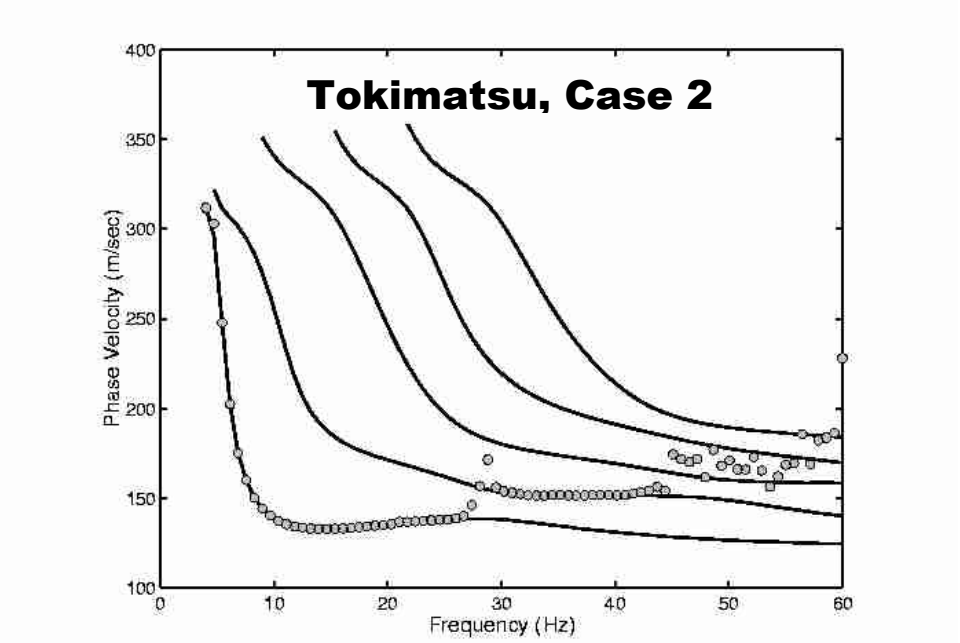

Figure 4.20 Theoretical Example showing the Transition of Energy to Higher Rayleigh Modes with Increasing Frequency. (Tokimatsu et al., 1992a)

While some current inversion algorithms allow for either fundamental or effective mode inversion, many cannot consider more than one mode at a particular frequency. However, the uniqueness of the inverted solution increases as the amount of modal information increases. As such, more modal information increases the confidence and ability to invert dispersion data, especially for sites with complicated stratigraphy. The process of extracting the lower energy modes is not easily automated however, and it may be necessary to manually search for the peaks corresponding to the lower energy modes. For an in depth discussion of multi modal inversion and dispersion estimates, the reader is referred to (Lai 1998, Zywicki, 1999, and Foti, 2000) The experimental dispersion curves for the current eleven test sites are presented in Chapter 5, and a number of these curves serve to highlight unique multi-modal phenomena of dispersion relations.

4.4.3 Shear Wave Velocity Error Estimates

Other current surface wave inversion algorithms make no attempt to accurately quantify the magnitude of the uncertainty in the experimental data. Errors within the experimental data occur as a result of simplifying assumptions and the interpretation of limited spatial and temporal data. While the errors associated with the use of limited measurements may be quantified through statistical Monte-Carlo simulations based on the spatial and temporal sampling parameters, the magnitude of the errors associated with modeling soil stratigraphy as a vertical stack of homogeneous layers are highly site dependent. While soil stratigraphy generally exists in geologic layers; these layers are often not parallel with the ground surface and the soil properties within each geologic layer, including the shear wave velocity, almost always change with depth due to the increase in overburden. Yet, a highly accurate stratigraphic characterization of a site would involve taking samples and running lab tests, thus eliminating most of the advantages of the non-invasive in-situ nature of surface wave testing.

The use of the layered soil model does offer advantages, including the incorporation into many linear and equivalent-linear site response analyses and increased calculation efficiency. As with any geotechnical method, surface wave testing incorporates simplifying assumptions into common practice to achieve relatively accurate solutions. Consequently, the use of the layered soil model in surface wave testing can be justified if an attempt to quantify the errors involved is incorporated into the inversion analysis. As mentioned previously, the model errors are combined with the resolution errors associated with the use of limited spatial and temporal data. However, Monte-Carlo statistical simulations conducted during this research showed that for the current testing parameters the errors resultant to resolution constraints were negligible in comparison to the more prominent modeling errors. While more in depth studies into the error estimation of surface wave testing and inversion should be conducted, the current research used σ = 5% as the standard error of the estimated Rayleigh phase velocities. This was determined to be a conservative bound for use with the current techniques.

4.4.4 Practical Considerations

Some general guidelines were used in the inversion of the current surface wave data. It was considered that the resolvable depth for all data obtained through f-k procedures was equal to:

$$\text{Resolvable Depth} = 2/3 * \lambda_{max} \tag{4.22}$$

where $\lambda_{max} = (V_R(f)/f)_{max}$, which is usually defined by the point of lowest frequency in a particular dispersion estimate. This is increased slightly from the conventional consideration that the resolvable depth is equal to half of the maximum wavelength (Sánchez-Salinero,. 1987). The validity of increasing the resolvable depth from traditional SASW estimates is justified by the increased information that the f-k dispersion estimates are derived from and is explained in detail in Chapter 6. Soil layerings are typically not determined by current inversion algorithms. As such, the layering is commonly chosen based on prior knowledge of the layering obtained from borings or CPT data, or an allowable resolution defined by the number of dispersion points representative of each layer. A recently developed method to chose layer thicknesses strives to achieve equal resolution for all layers, providing equal confidence in the V_S estimates for each layer (Joh, 1996). However, this approach and most other common approaches, are not based on prior knowledge of the soil layering, and make no effort to relate the actual location of the geologic boundaries to the chosen layering. But rather they hope that by defining layers of finite thickness they can approximate the behavior of the soil accurately, even if the layering does not correspond to the actual soil boundaries present in-situ.

The current testing used a combination of techniques to obtain the input layerings for the given profiles. Additionally, all of the chosen layerings were subject to general guidelines prohibiting the resolution of layers defined by inconclusive dispersion data. Where available, previously defined layerings based on borings and CPT profiles obtained at the exact locations of the current testing were used to define the input layers. However, for the most part this information was not available. In most cases the input layerings chosen for each site were determined by analyzing the changes in slope of the dispersion curve. Because the depth represented by each dispersion point increases with increasing frequency, changes in the slope of a single mode dispersion curve are representative of changes in the velocity of the sampled material for layers of moderate thickness. Consequently, an iterative process was used to define the input layering used in the inversion process based on the wavelength corresponding to changes in the slope of the dispersion curve. The author believes that by analyzing the slope of an accurate dispersion estimate one can define the layering of shear wave velocities with a high level of certainty. A potentially useful topic of future consideration could be the generation of a numerical algorithm that analyzes the changes in slope of dispersion curves to determine the soil layering for use in combination with a subsequent inversion analysis.

Chapter 5

Experimental Results

5.1 Introduction

This chapter presents the experimental results from11 sites tested in July 2000 using the seismic surface wave methods described in Chapter 4. Table 5.1 lists the naming convention, and latitude - longitude coordinates for each of the 11 sites tested. Figure 5.1 shows the general spatial locations of the sites.

Table 5.1 Listing of Test Sites: Name, Date, and Coordinates

Test Site Names	Test Date	Latitude Degrees (N)	Longitude Degrees (W)
Shelby Farms - Shooting Range (SR)	7/18/2000	35.1300	89.8392
Shelby Forest	7/19/2000	35.3578	90.0186
University of Memphis	7/20/2000	35.1189	89.9339
Mud Island B	7/21/2000	35.1578	90.0567
Mud Island A	7/21/2000	35.1436	90.0564
Williams 11 (W11)	7/22/2000	35.0725	89.9931
Street 16 (S16)	7/22/2000	35.0294	89.7594
Shelby Farms - Wolf River (WR)	7/23/2000	35.1192	89.8014
Houston Levee Park	7/24/2000	35.0878	89.7389
Powell Road Park	7/24/2000	35.0631	89.6733
Jackson County Landfill, AR	7/25/2000	35.5886	91.0869

The locations of the sites were chosen based on recommendations from Dr. Chris Cramer of the Center for Earthquake Research and Information (CERI) and Mr. Rob Williams of the United States Geological Survey (USGS) both of which are preparing seismic zonation maps of Shelby County, Tennessee. Additionally, many of the site locations coincide with previous measurements allowing comparisons between various in situ seismic techniques. The Jackson County Landfill site in Arkansas was specifically chosen to allow for the comparison of both in situ shear wave velocity and damping ratio measurements previously conducted by Dr. ha ram Pezeshk of the University of Memphis.

5.2 Previous V_S Measurements

Many of the testing sites were chosen to coincide with previous measurements of V_S taken using other methods. Brief descriptions of the specific procedures used to collect the data in these other studies are given below. These descriptions cover the specific testing procedures used by the researchers and are not intended to provide a thorough coverage of each technique. For a more detailed discussion regarding in situ techniques used to determine dynamic material properties refer to Kramer (1996). The previous

Figure 5.1 Map showing the locations of the 11 sites tested in the current study.

studies employed numerous geophysical and geotechnical techniques including seismic refraction and reflection, borehole measurements, and seismic piezocone measurements. V_S comparisons are presented for each site where previous measurement(s) are available. The experimental comparisons show both the advantages and limitations of the current surface wave testing methods. Prior V_S measurements were not used to influence the inversion of the surface wave data, i.e. the V_S comparisons only serve to substantiate the current surface wave methods as reliable and accurate seismic testing procedures.

5.2.1 Seismic Refraction/Reflection

Mr. Rob Williams of the United States Geologic Survey (USGS) used a combination refraction/reflection technique to test a number of sites in the Memphis and Shelby County areas. The results and testing procedures are presented in Williams et al. (1999a), and the procedures are summarized here for convenience. Williams used an adapted seismic refraction/reflection technique that allowed for the detection of inverse layering. Seismic refraction is a surface-based approach that typically uses an impulsive source to measure the travel times of P and/or S waves at an array of sensors located at varying linear distances from the source. The conventional refraction technique typically uses only the first arrivals of the seismic waves (P and/or S), and is unable to detect low-velocity features overlain by higher velocity feature(s). However, the refraction recordings taken by Williams were analyzed using two supplemental analysis techniques to overcome this limitation. The first technique used traveltime skips or terminations in the refracted-phase arrivals and the second technique incorporated information from reflected phases. Data from reflected phases can be used to detect low-velocity features because they represent an average of all overlying materials including any low-velocity layers. These techniques were reliable in determining the existence of low-V_S features; however, they are limited in their ability to determine their exact depth and thickness. (Williams, 1999b) For a more detailed description of these techniques see Williams (1999a & 1999b).

5.2.2 Seismic Refraction

Dr. Ron Street of the University of Kentucky undertook extensive site investigations throughout the Memphis metropolitan area as presented in Street (1999). His study consisted of seismic refraction studies carried out at 54 sites within the Memphis metropolitan area, with a large number of those sites located within Shelby County, Tennessee. The testing consisted of measuring a linear array of either 24 or 48 sensors placed at spacings of either 4 or 6.1 m using a floating point seismograph. The seismic source consisted of an embedded I-beam struck on end with a sledgehammer creating a wavefield rich in horizontally polarized shear (SH) waves. Refraction profiles were generated from the field data using the software package VISTA 7.0 (Seismic Image Processing Ltd., 1993). The refraction analysis software package SIPT2 V-4.1 (Rimrock Geophysics, Inc.) was then used to obtain the V_S profiles (Street, 1999).

5.2.3 Seismic Cone Penetration Tests

All data presented from Dr. Paul Mayne's research group (Schneider, 1999; Casey, 2000; Mayne et al., 2000a; and Mayne et al., 2000b) at the Georgia Institute of Technology were gathered through seismic cone penetration tests (SCPT). Shear wave velocities determined with a seismic cone penetrometer are very similar to data obtained with downhole procedures. The SCPT also allows for the simultaneous measurement of several other geotechnical parameters. The SCPT device is intrusive, limiting its use under certain conditions and locally disturbing the soil around the probe. However, the SCPT provides a direct measure of V_S, and the influence of the penetration disturbance is limited during seismic measurements, making it a useful and reliable seismic in situ method. The data used in the current comparisons was collected using a geophone embedded within the cone penetrometer just above the friction sleeve. Time series recordings of the arrival of surface-generated SH waves were collected at 1-meter intervals

coinciding with the addition of rod lengths. The seismic source consisted of a sledge hammer striking the end of a steel box beam placed under one of the outriggers of the Georgia Tech truck-mounted cone rig. The weight of the truck in combination with the added reaction of twin earth anchors provided adequate coupling with the ground surface. The horizontal striking of the beam created a wavefield rich in vertically propagating SH waves. The V_S values were then determined by dividing the known difference in depth by the calculated travel time difference between adjacent records, $V_S = \Delta z/\Delta t$. The travel time differentials were determined by either visual interpretation or through the use of a cross correlation analysis. Since each V_S value obtained with an SCPT is an independent measurement, the SCPT data are presented as a series of points rather than layered profiles (Mayne et al., 2000c).

5.2.4 Borehole Methods

Borehole V_S measurements were taken by Dr. His-Ping Liu of the USGS at the Shelby Forest test site, and by Dr Shahram Pezeshk of the University of Memphis at the Jackson County Landfill site in Arkansas. Typical near-surface seismic borehole procedures consist of a surface source used to generate SH seismic waves measured by downhole receiver(s) located within a cased borehole. These procedures are commonly known as the downhole seismic technique within the geotechnical community and as vertical seismic profiling within the geophysical community. Borehole V_S measurements are very similar to V_S measurements taken with a seismic cone penetrometer. Measurements are typically taken at short depth intervals to either the bottom of the borehole or until the capabilities of the source are exceeded. The measurements taken at the Jackson County Landfill site were made to allow both the near-surface material damping and V_S profiles to be determined.

5.3 Experimental Results

The main focus of the experimental testing was to conduct active f-k surface wave tests at all 11 test sites in order to substantiate the newly developed experimental and analysis procedures. Additionally, passive tests were conducted at the Mud Island B and Shelby Farms Shooting Range sites, and conventional two-station tests were conducted at the Shelby Forest, University of Memphis, and Shelby Farms Shooting Range test sites. The three sites chosen for conventional testing were chosen to provide a range of ambient noise levels that not only allowed general comparisons between the current and more traditional active techniques but also allowed the noise tolerance of the two methods to be compared over a range of testing conditions. Passive testing was performed to allow for the combination of active and passive dispersion data. The combination of active and passive methods produces a composite surface wave technique with capabilities far superior to either individual procedure. The sites chosen for passive wave testing allowed for the use of a large circular array and were thought to have enough ambient seismic energy to allow passive testing to be successful.

The format of this chapter will be to present the data from each location on a site-by-site basis. A description of the testing location and the experimental parameters used during the active f-k testing will be briefly presented. The active f-k dispersion data is presented followed by a brief discussion regarding site-specific findings and unique features. The inversion procedures and results for the active f-k testing will then be presented. While most of the sites provided minimal difficulties during inversion, a few of the sites demonstrated more complex phenomena that required more careful analyses. Any procedures beyond those introduced in Chapter 4 will be presented for the individual sites for which they were used. Where applicable, the passive testing results will then be presented and discussed. Finally, the current V_S results are compared to those of previous in situ seismic measurements when available. The results and comparisons of the traditional two-station tests are discussed in Chapter 6.

5.4 Mud Island

5.4.1 Site A

The Mud Island A site was tested on July 21, 2000 using only the active f-k surface wave procedures. Figure 5.2 depicts the geographic location of Mud Island and both of the test sites (i.e., Mud Island A and Mud Island B from Table 5.1). Mud Island is a man-made island located just west of downtown Memphis, Tennessee. The island was formed mostly through hydraulic filling, and direct sedimentation from the Mississippi River. As such, the island is composed of very loose sedimentary deposits and is prone to liquefaction and damage in the event of a future large earthquake within the NMSZ (Mayne et al., 2000a). Furthermore, Mud Island has recently seen a dramatic increase in land usage including the Mississippi River Park located at the south end of the island, and numerous residential developments throughout the northern portion of the island. The Mud Island A site was located at the southernmost tip of the island on a small undeveloped section of land. The experimental parameters used during the active f-k testing included the standard array configuration shown in Equation 4.6, and source frequencies spaced at $\Delta f = 0.625$, 1.25, and 2.5 Hz over the respective frequency ranges of 3.75-15, 16.25–35, and 37.5–100 Hz. Figure 5.3 depicts the experimental dispersion estimate along with the theoretical dispersion curve representative of the V_S profile determined for this site as shown in Figure 5.4. The dispersion data show a distinct trend that allowed the V_S profile to be estimated with high confidence. The V_S estimate is consistent with the geologic formation of Mud Island, as the profile approximates a sedimentary deposit as evident through the approximate linear increase in V_S with depth over most of the profile.

Figure 5.2 Map Showing Mud Island Testing Locations.

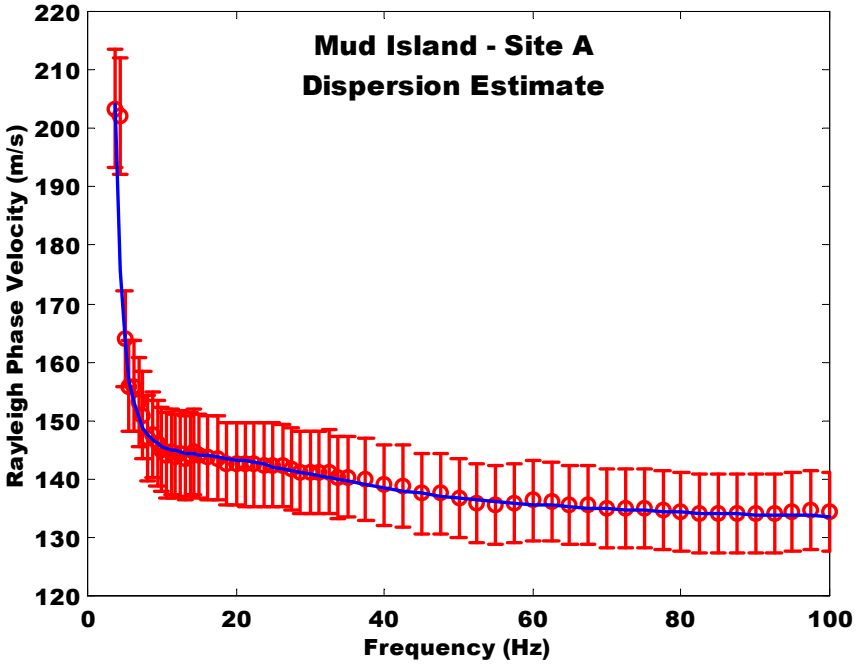

Figure 5.3 Dispersion Estimate from the Mud Island A Site, Active f-k Final Interpretation.

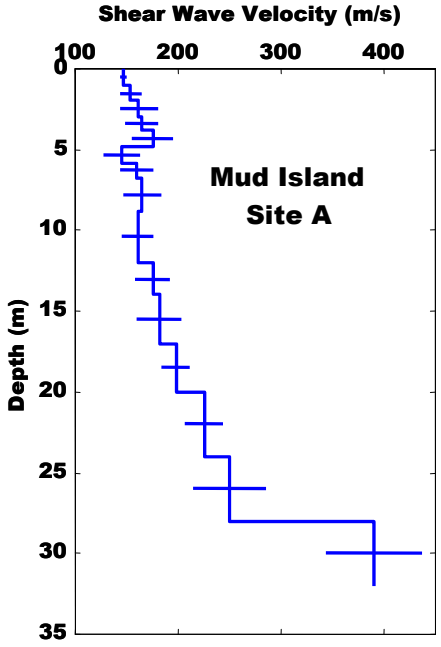

Figure 5.4 Interpreted V_S Profile from the Mud Island A Site.

5.4.2 Site B

The Mud Island B site was tested with the active f-k procedures on July 21, 2000 and passive recordings had been taken by the author on October 21, 1999. This site is located in a large grass field on the west side of South Mud Island Drive, just north of the entrance to the Mississippi River Park, as shown in Figure 5.2. It was believed that the close proximity to Interstate Highway 40, the Mississippi River, and Downtown Memphis would provide sufficient ambient seismic energy to conduct passive tests at this site. The Mud Island B site is one of several sites designated as a USGS test site for the Memphis area. As such, several other researchers had previously conducted measurements at this site allowing for numerous V_S comparisons. The active f-k testing parameters consisted of the standard array geometry shown in Equation 4.6, and source frequencies spaced at $\Delta f = 0.625$, 1.25, and 2.5 Hz over the respective frequency ranges of 3.75-15, 16.25–35, and 37.5–100 Hz. The dispersion estimate from the active testing is shown in Figure 5.5. The data shows a slightly inverse trend from 10 – 100 Hz, and a slight discontinuity at 10 Hz.

The passive testing was conducted using a 16 sensor circular array of radius = 90 ft (~27.4 m). Passive time-domain recordings were collected three separate times at a sampling frequency of 320 Hz. The time domain records were further divided into blocks to allow for frequency-domain averaging to reduce the variance in the signal. The f-k spectral calculations were performed using 256 trial wavenumbers. The frequency resolution corresponding to the above parameters can be calculated as: $\Delta f = f_s/N_f = 320/4{,}096 = 0.0781$ Hz. The maximum wavenumber resolution corresponds to the minimum spatial lag measured by the array geometry, $k_{max} = \pi/d_{min} = \pi/2.09 = 1.504$ (1/m). Passive testing necessitates the use of both positive and negative wavenumbers because of the unknown direction of wave propagation, and as such the maximum wavenumber was used as both the positive and negative limits of the trial wavenumber vector. These parameters correspond to a wavenumber resolution of $\Delta k = k_{max}/N_k = 1.504/128 = 0.0118$ (1/m).

Figure 5.6 shows the passive dispersion estimate for the Mud Island B site over the resolved frequency range. The passive data shows a smooth trend to a minimum frequency of 1.875 Hz, increasing the frequency range defined by the active dispersion data. The nature of passive measurements does not allow for the resolution of dispersion data at frequencies with low passive seismic energy content. The frequency content of the passive seismic energy present at the Mud Island B site during testing is shown in Figure 5.7. The measured passive energy content of the site is concentrated at low frequencies ranging from 1.5 - 15 Hz. Additionally, the experimental sampling parameters limit the range of both the frequency and wavenumber resolution. Consequently the frequency range over which passive dispersion estimates can be accurately resolved is usually limited, as seen in Figure 5.6.

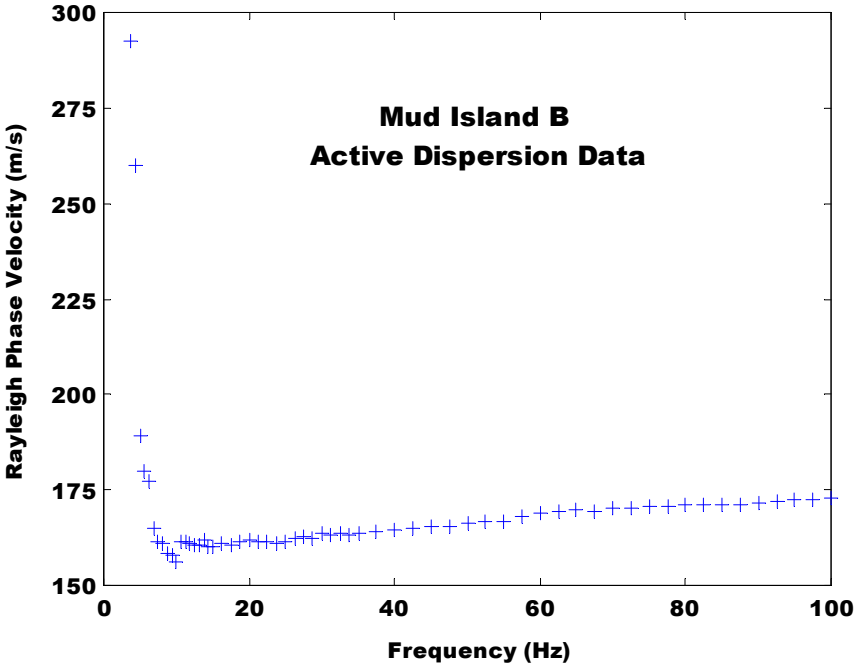

Figure 5.5 Dispersion Estimate from Mud Island B Site, Active f-k Method.

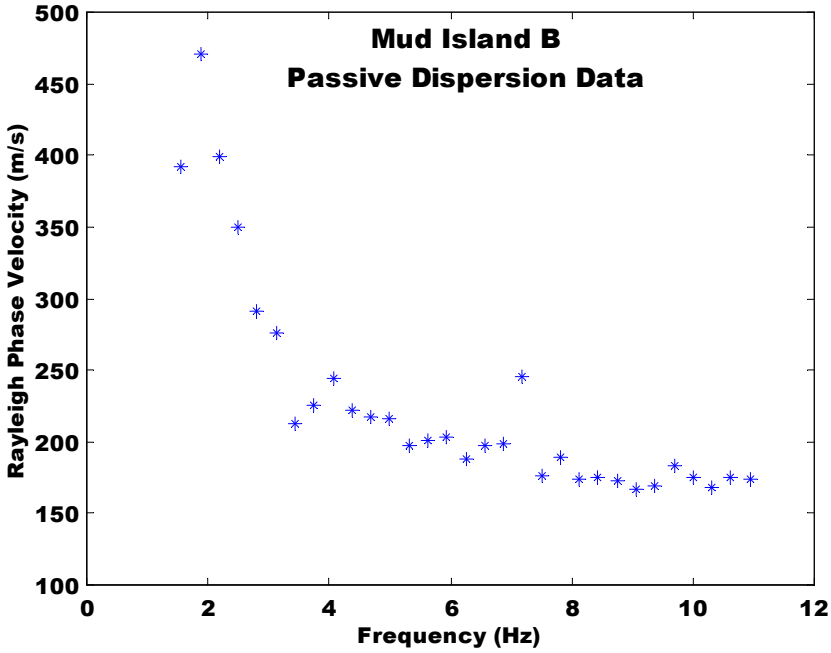

Figure 5.6 Dispersion Estimate from the Mud Island B Site, Passive f-k Method.

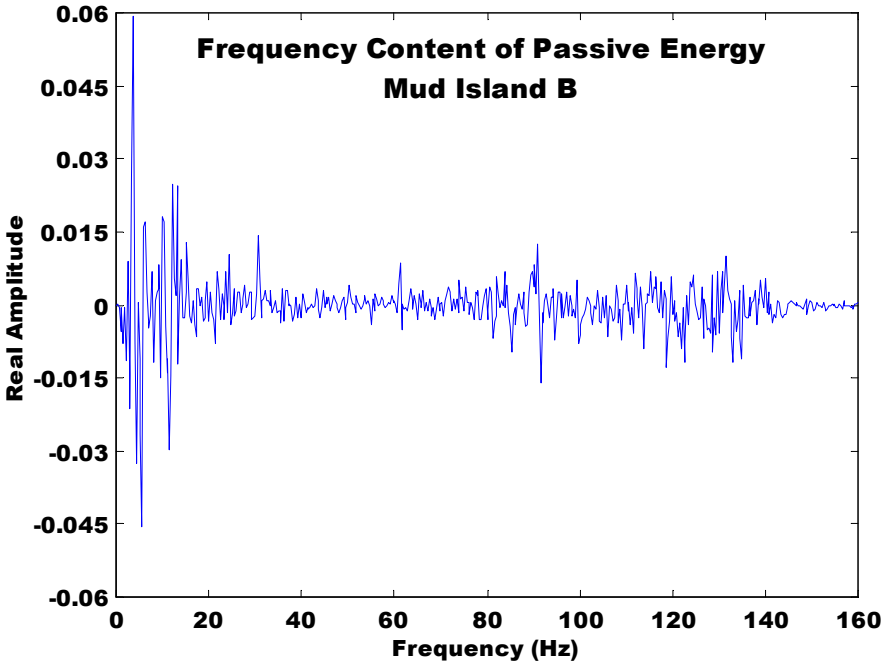

Figure 5.7 Measured Frequency Spectrum from Mud Island B Site at the Time of Passive Testing.

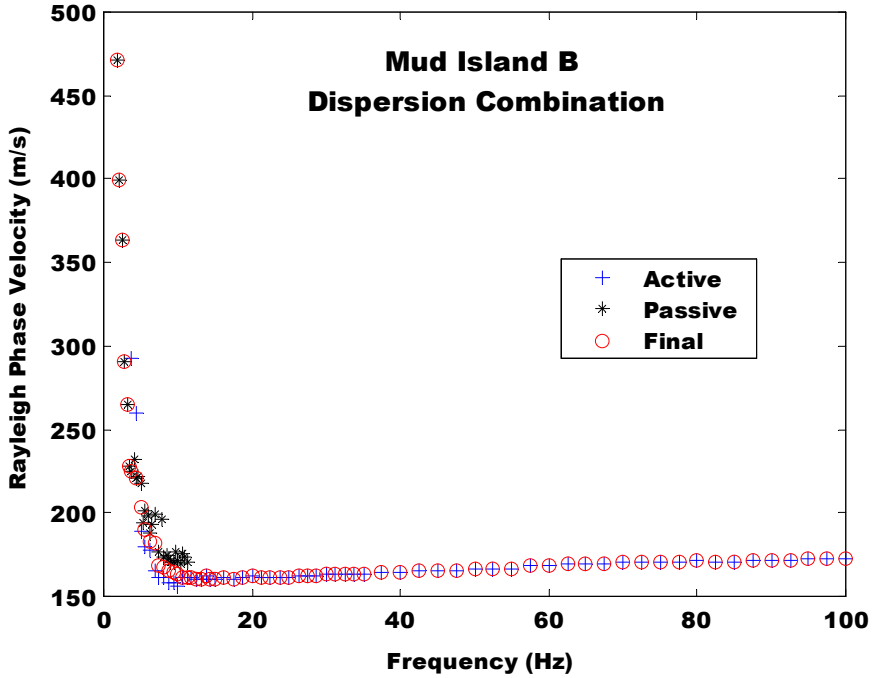

Figure 5.8 Dispersion Data from Mud Island B Site, Active and Passive Combination .

The active and passive dispersion estimates were combined to form a composite dispersion estimate. Ideally the passive and active data would match identically in the frequency range where they overlap, allowing the data to be straightforwardly combined to form a composite dispersion curve. However, the inherent differences and limitations of the two techniques makes this impractical in most cases. Active data may be affected by near field interference and source limitations at very low frequencies, while the passive data may have a low energy content or limited resolution over the coincident range of the dispersion estimates. Figures 5.8 and 5.9 show both the active and passive data across the full range of testing frequencies and over the coincident frequency range, respectively. In order for the V_S profile to be estimated within the confines of an automated inversion algorithm a single dispersion trend must be defined. Additionally, dispersion relationships of surface waves are theoretically required to exhibit a smooth trend unless a modal jump is present. Since multiple modes are rarely present at low frequencies, the disparity between the active and the passive data was not believed to be due to multi-modal phenomena. Subsequently, the slight variation between the passive and active data was believed to be a combination of the above mentioned phenomena as well as measurement and analysis errors of the two estimates. The final dispersion estimate was formed by averaging the active and passive dispersion estimates at points of similar frequency within the transition range of 4.5 – 10.5 Hz as shown in Figure 5.9.

The final composite dispersion curve used in the inversion process is shown in Figure 5.10. The result of the subsequent inversion analysis using this combined dispersion estimate is shown in Figure 5.11. The results of the testing at Mud Island show very low near-surface shear wave velocities on the order of 160 m/s down to approximately 10 m. Both Mud Island sites show gradual increases in shear wave velocity with depth, which corresponds well to the sedimentary nature of the island's formation. Site A is located at an elevation approximately 10 m below that of Site B. This difference in elevation is evident in the depth of the large velocity increase estimated respectively at 28 and 38 m in the two V_S profiles. This increase in V_S is most likely due to a change in the islands sedimentary patterns, or more specifically the limit of the last hydraulic filling operation. The combination of the active and passive test data for the Mud Island B site allowed the depth of resolution to be increased from 52 to 170 m. The successful combination of experimental passive and active surface wave data realizes one of the goals of the current study and creates expanded possibilities for the application of surface wave testing for in situ seismic characterization.

Figure 5.12 shows a comparison of the various V_S studies conducted at the Mud Island B site. These include an SCPT sounding by Mayne et al. (2000a) and refraction surveys by Williams (1999a) and Street (1999). The overall trend of the current estimate matches very well with the other studies, and allowed for resolution to 170 m, 92 m deeper than any other profile. Additionally, the combination of active and passive surface wave data did not limit the near-surface resolution of the V_S estimate. The SCPT method can detect finer features at depth than the current surface wave procedures; however, the capabilities of most conventional cone-rigs limits the testing to a depth of approximately 30 m. The surface wave profile shows a gradual increase in V_S at depth, while the refraction profiles both show thick sharply defined layers with depth. This is due to the encouragement of smoothing incorporated into the inversion algorithm and the ability of surface wave methods to resolve gradual transitions at depth. Additionally, the seismic refraction technique relies on material boundaries to infer the soil properties of the tested material. As such, it is unable to define gradual changes in material properties both at the near-surface and to great depths. The sedimentary formation of Mud Island would most likely result in an approximate linear increase in V_S with depth as depicted by the surface wave profile. The site shows the ability of surface wave techniques to both finely resolve V_S and to detect inverse layering to significant depths through the analysis of dispersive Rayleigh wave propagation.

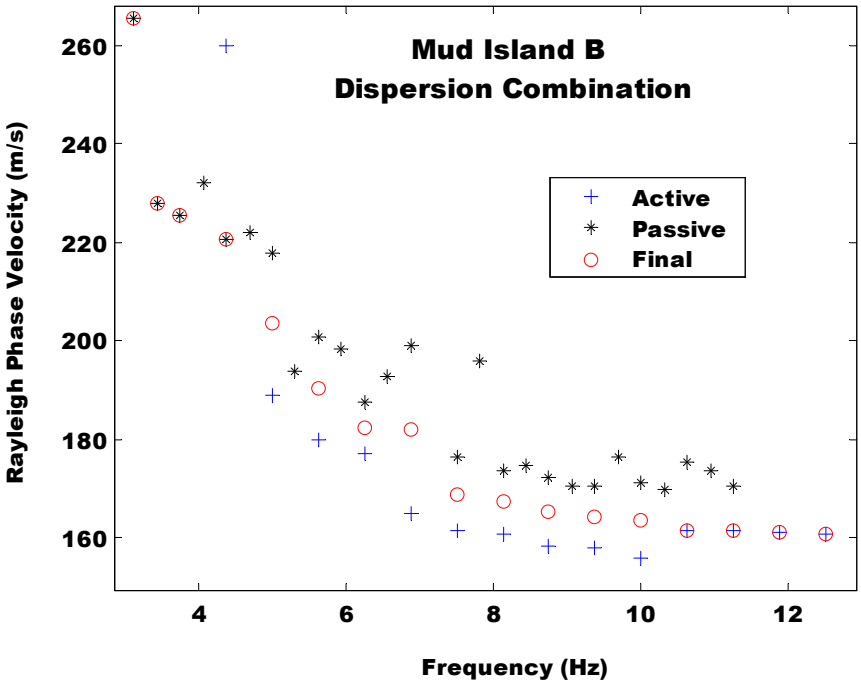

Figure 5.9 Dispersion Data from Mud Island B Site, Active and Passive Combination Over the Coincident Frequency Range.

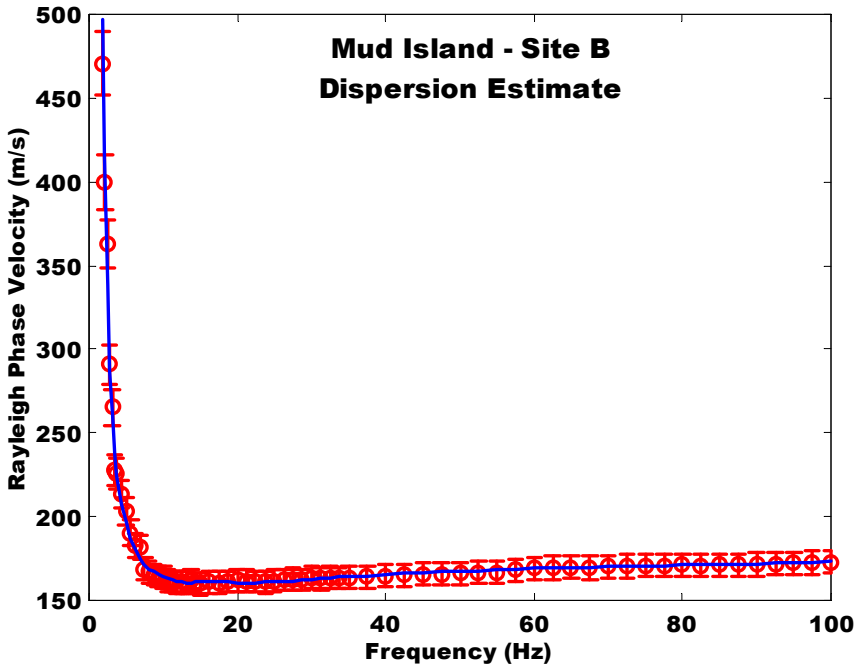

Figure 5.10 Dispersion Data from Mud Island B Site, Active f-k Final Interpretation.

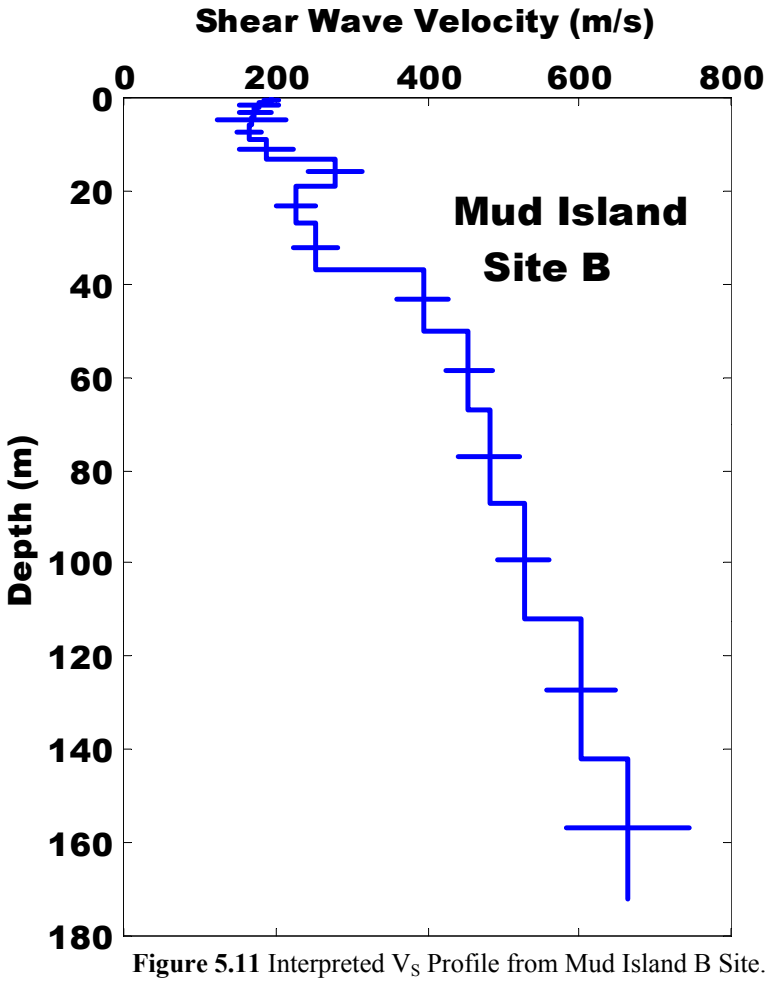

Figure 5.11 Interpreted V_S Profile from Mud Island B Site.

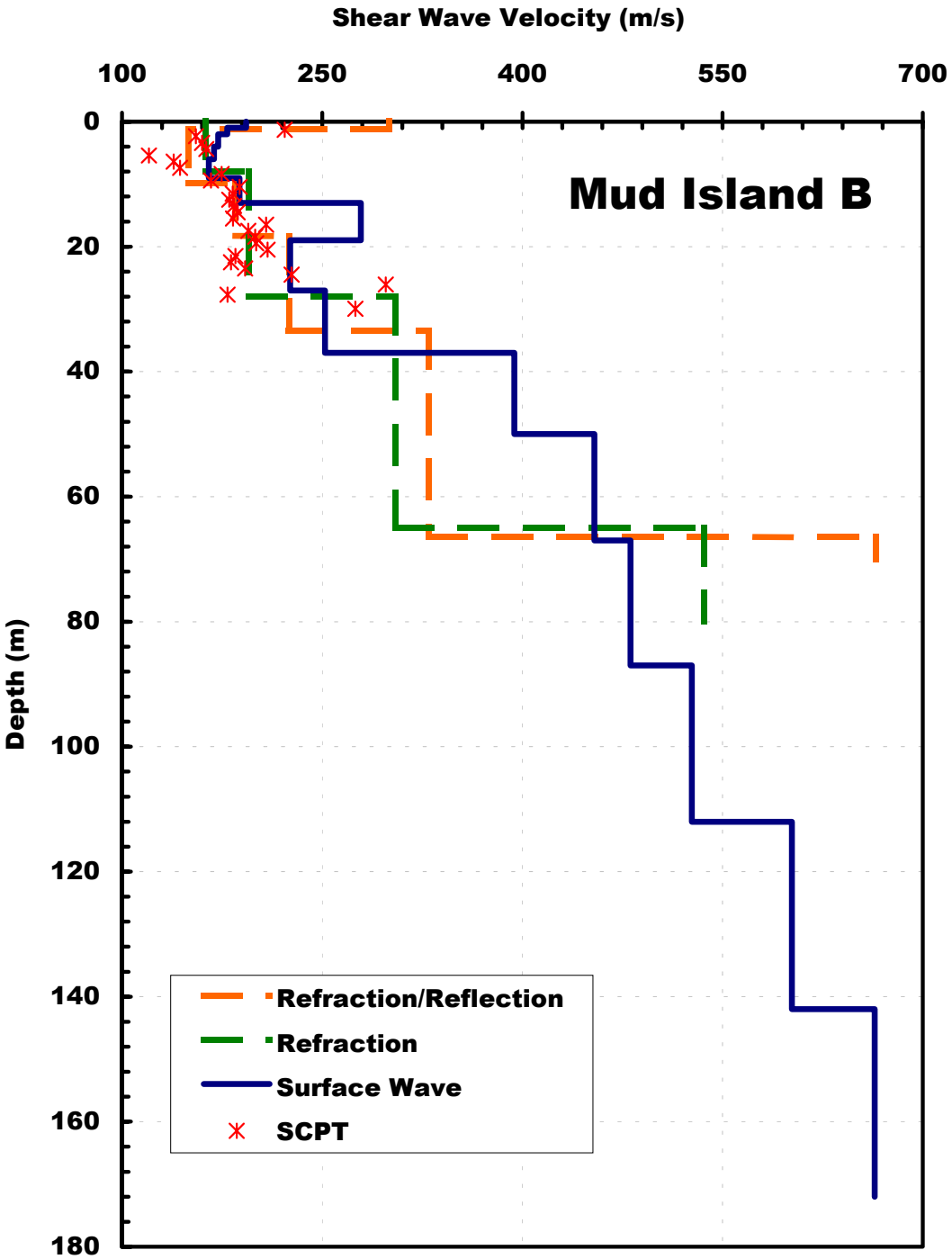

Figure 5.12 V_S Comparisons at Mud Island B Site.

5.5 Shelby Farms

5.5.1 Shooting Range Site

The Shelby Farms Shooting Range Site is located within the Shelby County Recreational Facility known as Shelby Farms. The location of both Shelby Farms test sites is shown in Figure 5.13. The testing was conducted in the grass field between the Shooting Range parking lot to the South and Trap Pond to the North. The ground water table was estimated at 2 m based on the water level in the nearby pond, and confirmed by the results of an SCPT sounding conducted by Schneider (1999). This site is located within a few hundred meters of Walnut Grove Road, a well traveled two-lane road that runs through the middle of Shelby Farms. The proximity to this roadway and the large open testing area made this site one of the two test sites chosen for passive measurements. The Shooting Range site has been designated as a USGS test site, and as such there were several previous V_S profiles available for comparison with the current results. Passive measurements were collected by the author on October 19, 1999, and active testing was performed on July 18, 2000.

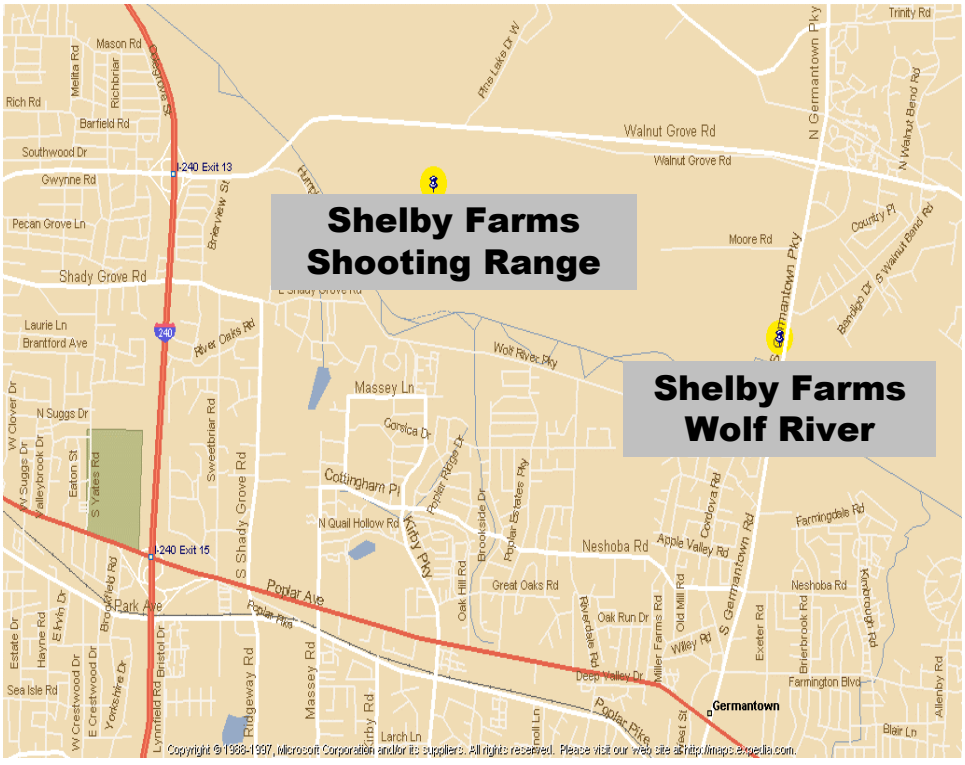

Figure 5.13 Map Showing Shelby Farms and Testing Locations.

The active f-k testing was conducted using the standard array geometry shown in Equation 4.6, and the source frequencies were spaced at Δf = 0.625, 1.25, and 2.5 Hz over the respective frequency ranges of 4.375-15, 16.25–35, and 37.5–100 Hz for a total of 60 excitation frequencies. The active f-k dispersion estimate is shown in Figure 5.14. The variation in the f-k dispersion estimate at high frequencies is most likely due to spatial variation in the near-surface soil. This phenomenon is not unusual in surface wave dispersion curves as near-surface soils are often highly variable due to weathering and site alterations. The remainder of the dispersion curve shows a smooth normally dispersive trend and corresponds to the V_S profile shown in Figure 5.15. The importance of low-frequency dispersion data is highlighted at this site as the resolution of the last two dispersion points allowed for the resolution of the marked increase in V_S at 34 m.

The site conditions did not provide a large enough flat area to use the 90-ft radius circular array used in the passive testing conducted at the Mud Island B site. As such, the passive measurements at the Shooting Range site were conducted using both a 75-ft (~22.9 m) radius and a 60-ft (~18.3 m) radius circular array. The two circles were used in an effort to obtain passive data over a wide range of frequencies. However, the level of passive noise present at the Shooting Range site varied with the level of traffic on the roadway and was lower than the energy measured at the Mud Island site. Figure 5.16 shows a measured frequency spectrum of the passive energy measured at the Shooting Range site. The experimental procedures used to conduct the passive testing were similar to those used at the Mud Island B site. The procedures included the frequency-domain averaging of 8 blocks of 4,096 time domain data points collected at 320 Hz for each set of dispersion calculations. This resulted in a frequency resolution of $\Delta f = 320/4{,}096 = 0.0781$ Hz. The spatial aliasing limits of the circular arrays corresponded to maximum wavenumbers of $k_{max} = \pi/1.741 = 1.805$ (1/m) for the 75-ft circle, and $k_{max} = \pi/1.392 = 2.256$ (1/m) for the 60-ft circle. The maximum resolvable wavenumber was again used to define the positive and negative limits of the trial wavenumber vectors, and resulted in a wavenumber resolution of $\Delta k = k_{max}/N_k = 1.805/128 = 0.0141$ (1/m) for the 75-ft circle, and $\Delta k = k_{max}/N_k = 2.256/128 = 0.0176$ (1/m) for the 60-ft circle.

The calculated dispersion results from four successive passive recordings using the 75-ft radius circular array are shown in Figure 5.17. Each of the tests shows a good deal of variability making it difficult to distinguish a clearly defined dispersion relation. Additionally, the four tests do not all exhibit the same trends, which would indicate that the seismic energy generated by the nearby roadway was nonstationary, limiting the validity of a Fourier analysis. The results of the passive analyses were compared to the active dispersion data as shown in Figure 5.18. The passive dispersion data generally showed higher V_R values than were estimated by the active method over the coincident frequency range. However, some of the passive data does provide an estimate along the same trend as the active dispersion data. In addition to the large variability in the passive data, the low-frequency resolution was limited to approximately 3 Hz, and does not substantially increase the frequency range defined by the active analysis. The relative significance of each point in a dispersion curve increases with decreasing frequency because the depth of influence in the V_S estimate increases. Consequently, it is essential to resolve low-frequency dispersion data with a high level of certainty, because a larger portion of the inverted profile is affected by the misestimation of low-frequency dispersion points. While the passive dispersion data at the Shooting Range site does show a general trend, the selection of any particular trend would be subjective and result in a large uncertainty in the corresponding portion of the V_S profile. Consequently, combining the passive and active dispersion data was not warranted given the current passive dispersion data.

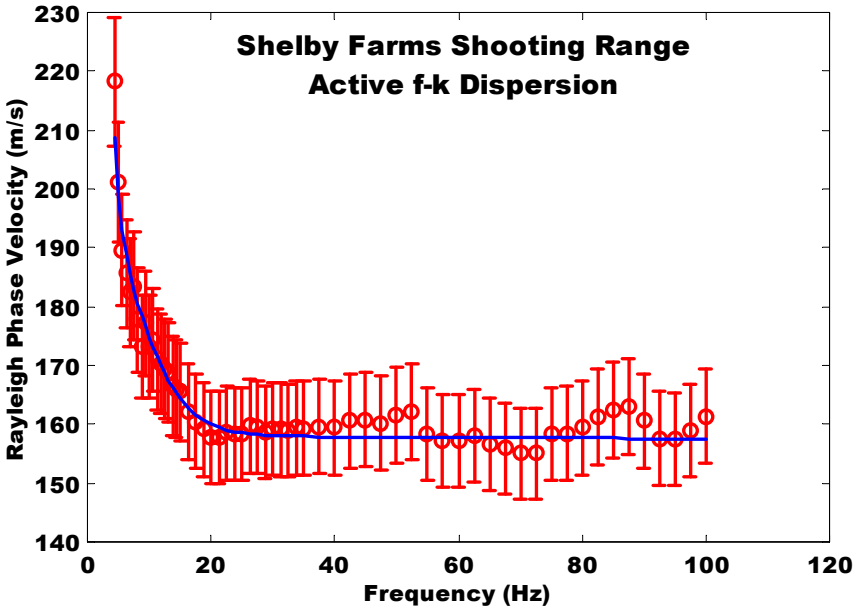

Figure 5.14 Dispersion Data from Shelby Farms Shooting Range, Active f-k Final Interpretation.

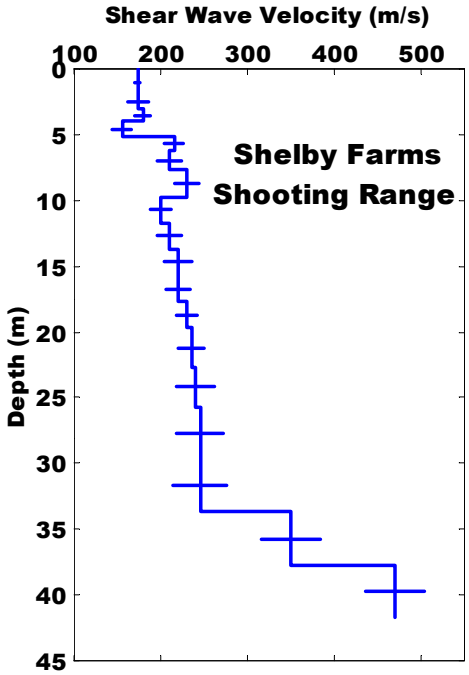

Figure 5.15 Interpreted V_S Profile from Shelby Farms Shooting Range.

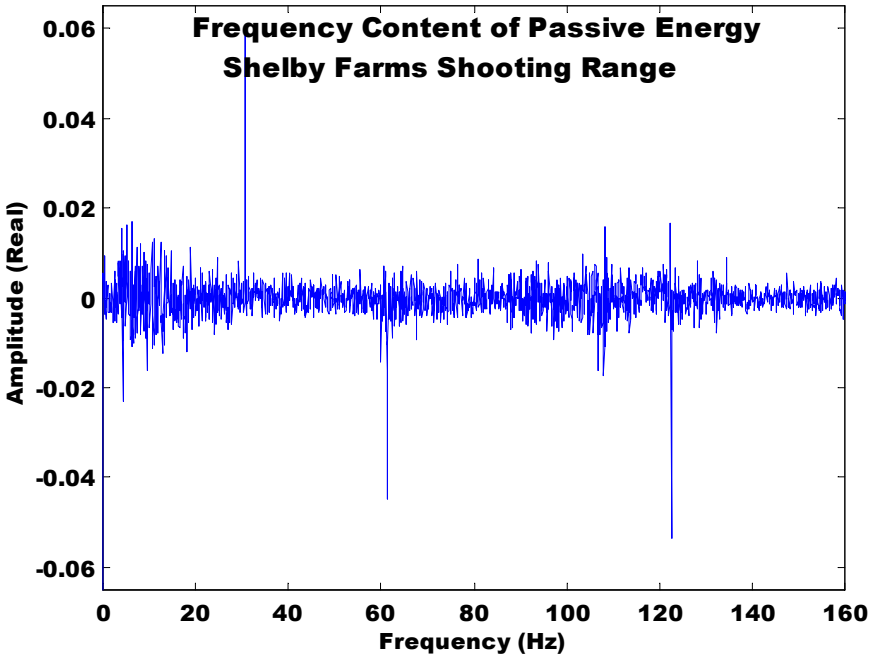

Figure 5.16 Measured Frequency Spectrum from Shelby Farms Shooting Range at the time of Passive Testing.

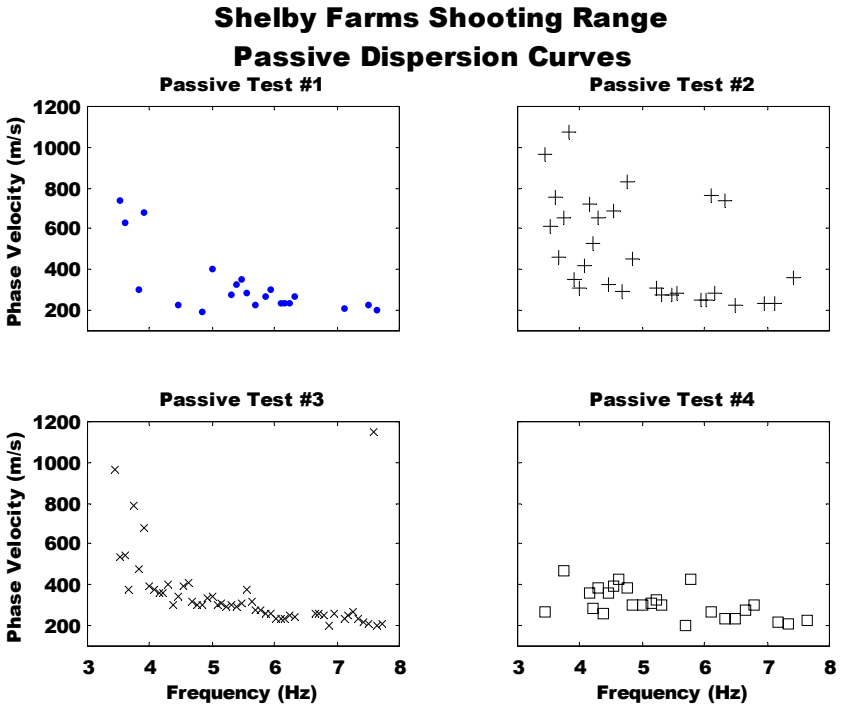

Figure 5.17 Passive Dispersion Estimates from Shelby Farms Shooting Range, Each Plot Represents the Results of a Successive Recording.

Figure 5.19 shows a comparison of the active f-k results with previous V_S measurements taken at the Shooting Range site. The current V_S profile exhibits an excellent correlation with the previous V_S measurements. The current methods were able to resolve the near-surface, low-velocity feature estimated by the SCPT sounding, as well as the large increase in V_S estimated by the refraction survey at approximately 44 m. The surface wave profile allowed for Vs values to be resolved to a depth of 54 m. While this is less than the maximum depth of the refraction survey, the depth of the surface wave profile is adequate for most geotechnical applications.

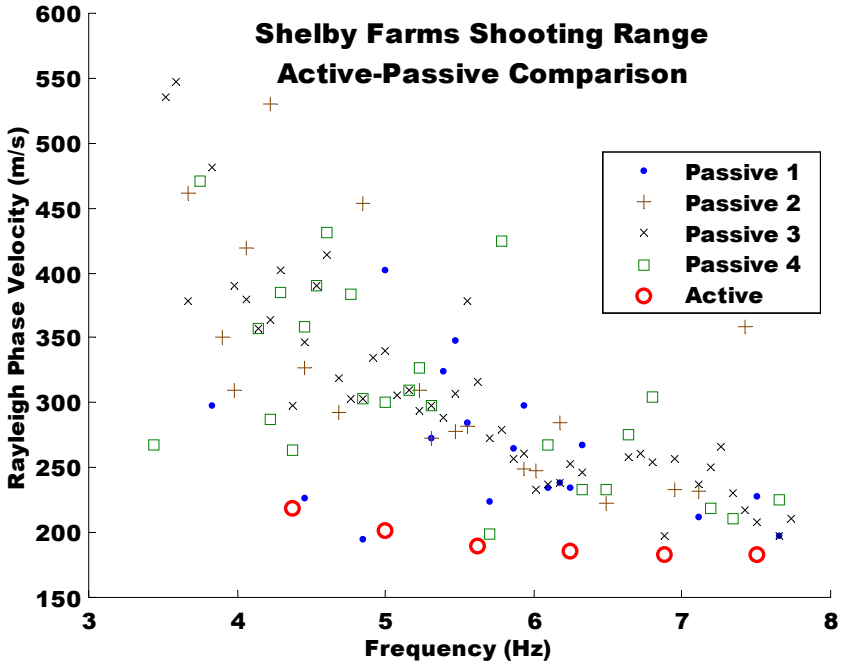

Figure 5.18 Dispersion Data from Shelby Farms Shooting Range, Active and Passive Combination Over the Coincident Frequency Range.

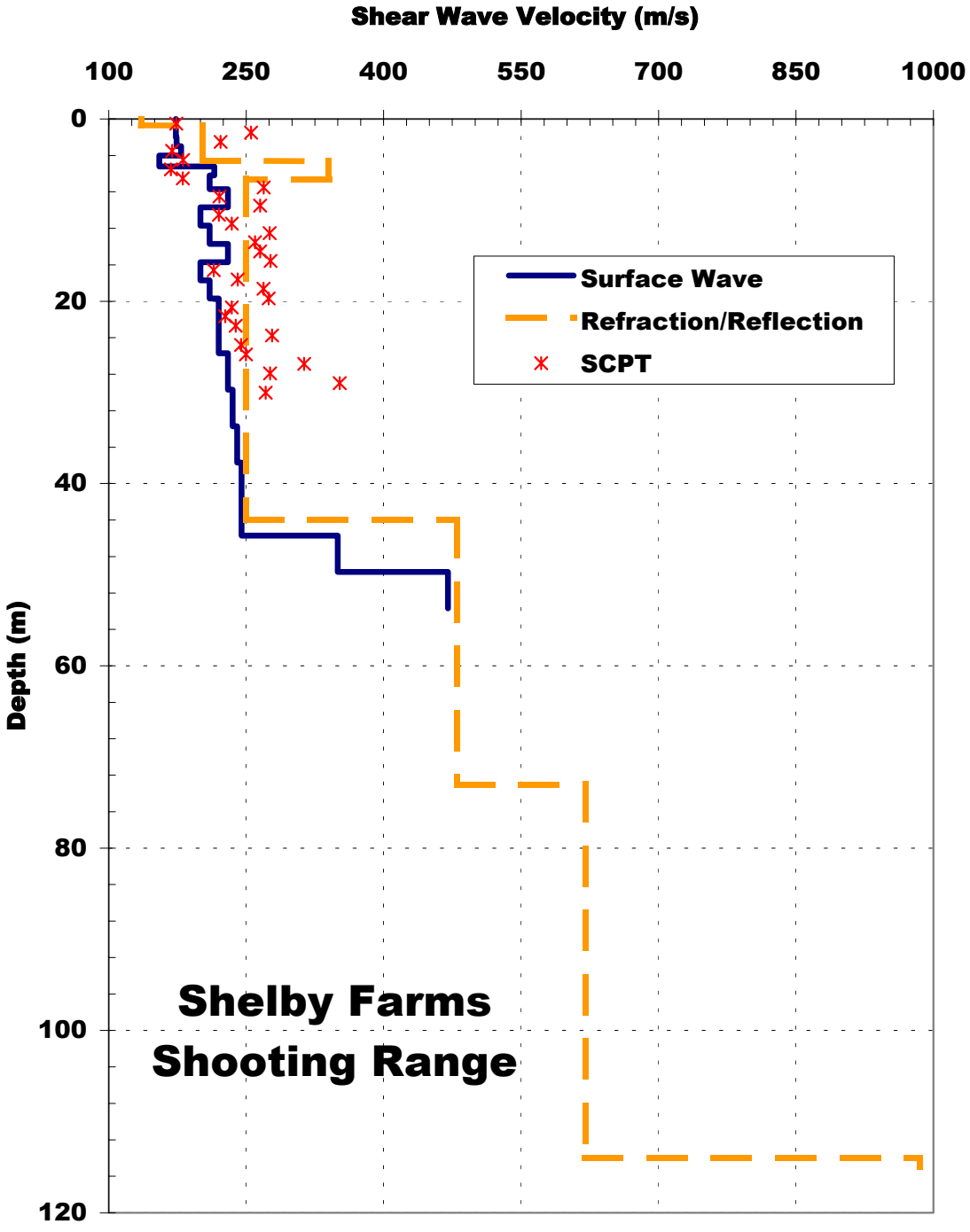

Figure 5.19 V_S Comparisons at Shelby Farms Shooting Range.

5.5.2 Wolf River

The Shelby Farms Wolf River site was located on the eastern limits of the Shelby Farms park lands just north of the Wolf River and to the west of Germantown Parkway as shown in Figure 5.13. The testing was conducted on a triangular strip of grass in between a drainage ditch running alongside Germantown Parkway and a Shelby Farms access road, approximately 30 m from the Wolf River. The surface soils near rivers tend to be sedimentary and have a young geologic age and as such they typically exhibit lower shear wave velocities. The floodplains of the Wolf River had only been sparsely studied at the time of the current testing, and as a result they have been the focus of several recent studies (Mayne et al., 2000b and Schneider, 1999). The current test site coincided with one of the test sites included in the study by Schneider regarding the liquefaction potential of Mid-America, allowing for a V_S comparison.

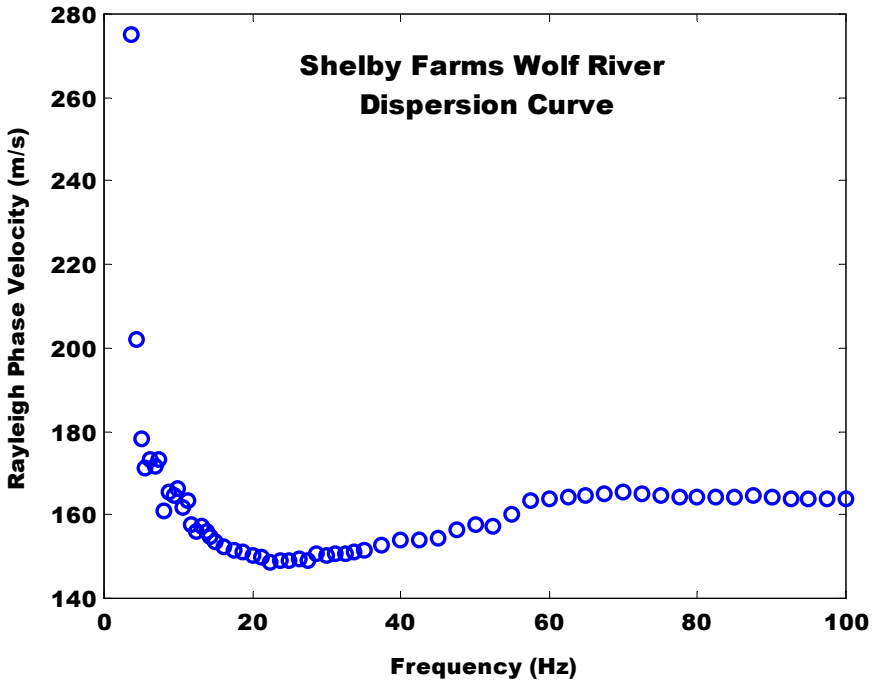

Figure 5.20 Experimental Dispersion Estimate from Shelby Farms Wold River, Active f-k Method.

The active f-k testing was conducted using the array configuration shown in Equation 4.6, and source frequencies spaced at $\Delta f = 0.625$, 1.25, and 2.5 Hz over the respective frequency ranges of 3.75-15, 16.25–35, and 37.5–100 Hz. The experimentally determined dispersion curve for the Wolf River site is shown in Figure 5.20. This curves shows an inversely dispersive trend in the frequency range from 20 – 60 Hz. Inverse dispersion is characterized by decreasing V_R with decreasing frequency. Most sites exhibit normal dispersion, characterized by increasing V_R with decreasing f. Inversely dispersive media have historically caused many difficulties during inversion analyses. These difficulties are caused because most inversion algorithms are written to favor normally dispersive profiles. Favoring normal dispersion not only increases the numerical stability of an algorithm but it also aids in the process of finding the roots of the Rayleigh eigenvalue problem. The V_S inversion of inversely dispersive Rayleigh wave dispersion data is still the focus of continuing research, and a robust and computationally efficient inversion algorithm capable of automatically inverting inversely dispersive sites was not available at the time of this study. It should be noted however, that there are several algorithms available that can generate inversely dispersive theoretical dispersion curves, e.g. Schwab-Knopoff (1972).

In light of the above difficulties a hybrid inverse–forward approach was used to define the V_S layering for the Wolf River site. The dispersion curve was analyzed in two parts starting with the data above 60 Hz. This data approximately corresponds to a homogeneous surface layer due to the approximate constant value displayed in the dispersion curve, as seen in Figure 5.20. This portion of the dispersion curve was inverted using only the frequency points above 60 Hz, allowing the resolution of the top 2 m. Once this was complete the portion of the data below 45 Hz was used to define the remainder of the V_S profile using an iterative forward approach. Figure 5.21 shows the dispersion data below 45 Hz and the theoretical dispersion estimate obtained through the forward analysis. A forward process was used in order to maintain the near-surface layering defined by the first inversion. The forward analysis was performed using an modified version of the inversion algorithm that allowed for the calculation of only the theoretical dispersion curve and the least squares error for a given input V_S profile. The input V_S profile was modified through forward iterations until the theoretical dispersion curve suitably matched the experimental dispersion estimate.

The resultant V_S profile determined for the Wolf River site is shown in Figure 5.22. The small range of inverse dispersion can be seen in the resolved low-velocity layer from 2 – 3.5 m. The top 18 m of the profile exhibit a low shear wave velocity, most likely the result of being within the floodplain of the Wolf River. The remainder of the profile increases steadily to a V_S of over 400 m/s at approximately 40 m. Figure 5.23 shows a comparison between the SCPT sounding performed by Schneider (1999) and the current V_S profile. The two tests show relatively good agreement throughout the depth of the SCPT sounding, although the SCPT results show a significantly higher velocity of the region between 8 and 18 m. Both methods resolve a low-velocity feature near the surface, with the SCPT resolving it slightly deeper and with a lower V_S. The SCPT data is significantly scattered through portions of the sounding, highlighting the independence of individual SCPT data points. The active f-k surface wave method was able to resolve the profile to a depth of 46.5 m, 15.6 m deeper than the SCPT sounding.

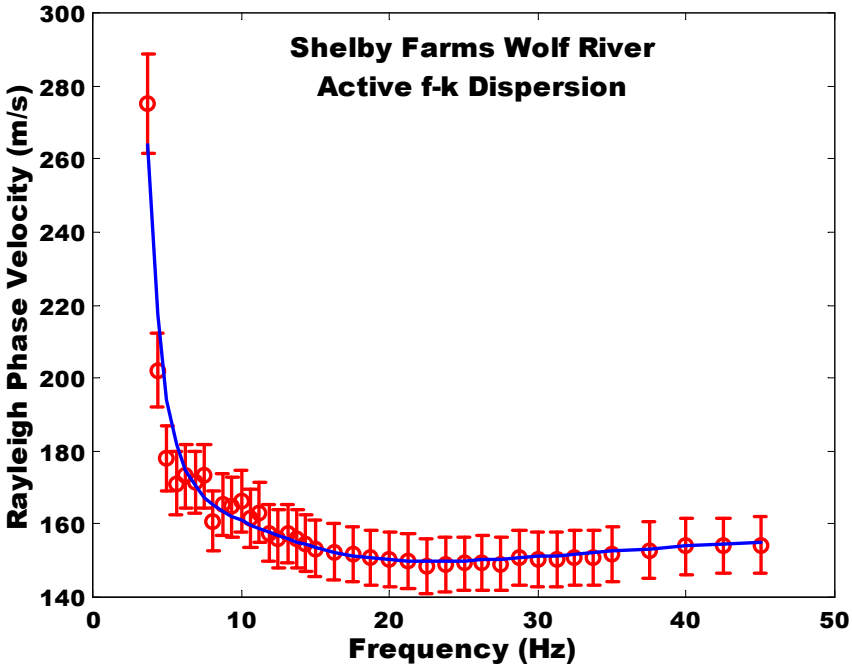

Figure 5.21 Dispersion Data from Shelby Farms Wolf River, Active f-k Final Interpretation.

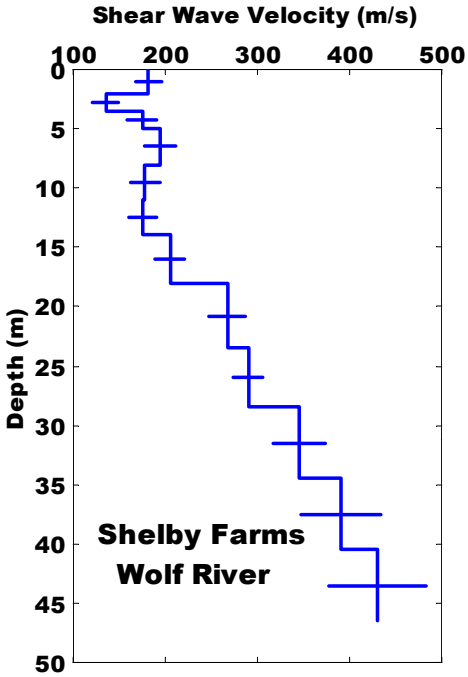

Figure 5.22 Interpreted V_S Profile from Shelby Farms Wolf River.

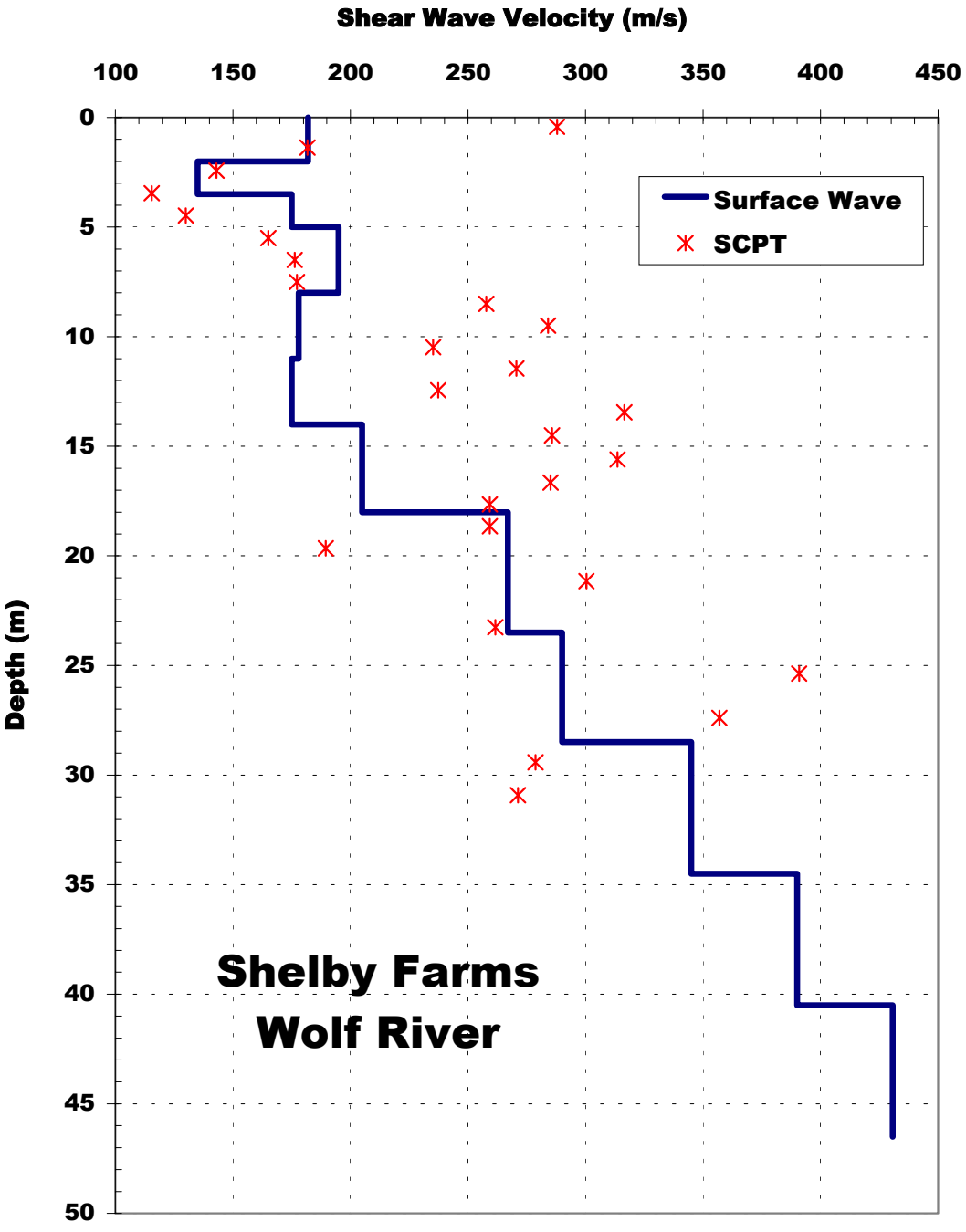

Figure 5.23 V_S Comparison at Shelby Farms Wolf River.

5.6 Shelby Forest

The Shelby Forest site is located in the Meeman-Shelby Forest State Park approximately 15 miles north-northeast of Memphis, as shown in Figure 5.24. The Shelby Forest site is located on the bluffs forming the eastern edge of the Mississippi alluvial plain. The bluffs are composed of Pleistocene loess, Pliocene-Pleistocene alluvial clay and sand deposits, and Tertiary deltaic-marine sediment (Liu et al., 1997). This site has been designated as a USGS test site for the Memphis area because it contains both a deep borehole and a seismic monitoring station. Active f-k testing was performed on July 19, 2000 within close proximity to the CERI borehole to allow for V_S comparisons. The active f-k testing parameters included the use of the standard array configuration detailed in Equation 4.6. The source frequencies were spaced at Δf = 0.625, 1.25, and 2.5 Hz over the respective frequency ranges of 4.375-15, 16.25–35, and 37.5–100 Hz for a total of 60 excitation frequencies.

The active f-k testing resulted in the dispersion estimate provided in Figure 5.25. Upon close examination of the dispersion curve several unique features can be observed. A slight increase in slope can be seen centered at 32 Hz, corresponding to an increase in velocity over this frequency range. A larger, yet similar increase can be seen from 8 – 15 Hz. This second feature shows a significant increase in the slope of the dispersion estimate over a low-frequency range corresponding to a prominent high-velocity feature. The remainder of the low-frequency dispersion data shows a decreased slope indicating that the high-velocity feature is an isolated feature.

Figure 5.24 Map Showing Shelby Forest and Testing Location.

Most conventional inversion algorithms were originally created based on experiences with dispersion curves generated from traditional SASW data. As such, these algorithms tend to smooth out sharp transitions in a dispersion estimate assuming that they are due to experimental measurement error. Consequently, while this site was originally inverted using the constrained least-squares algorithm from Rix and Lai (1998), the final V_S profile was determined through an iterative manual forward process. This process was performed similarly to the process explained above for the Shelby Farms Wolf River site, and allowed for a lower least squares error to be obtained between the theoretical dispersion curve and the experimental estimate. The results of the two analyses modifications can be clearly seen in the comparison of the V_S profiles determined with both the inverse and forward processes seen in Figure 5.26. The trend of the two profiles are very similar, but the encouragement of smoothness with depth implied in the conventional inversion algorithm is very prevalent in the inverted V_S profile.

The velocity features defined in the forward process are more clearly seen in Figure 5.27 showing only the final V_S profile. The dispersion feature centered at 32 Hz was resolved as a high-velocity layer between 2-3 m of depth. The second feature was resolved as a high-velocity layer between 10.5 and 16.5 m. The importance of accuracy in the experimentally determined dispersion estimate can be clearly seen in an examination of the above example. The increased accuracy available with the recent introduction of the current f-k experimental and analysis techniques allows for the resolution of finer features than the more general estimates provided with traditional SASW tests. Additionally, if a feature is known to exist prior to testing, more closely spaced source frequencies can be used in the frequency range of the specific feature allowing for even better V_S estimates.

The Shelby Forest test site had been previously tested by a number of researchers. The previous measurements available for the current V_S comparison consisted of five SCPT soundings conducted by Schneider (1999) and Casey (2000), one seismic refraction/reflection survey conducted by Williams (1999a), and a downhole measurement performed by Liu et al. (1997). A comparison of these V_S results is presented in Figure 5.28. All of the methods show relatively good agreement throughout their respective depth ranges. However, each profile depicts a slightly different V_S stratigraphy. The most prominent feature at this site is the high-velocity layer resolved at varying depths between 10 – 22 m. The current surface wave profile indicates a thicker layer with a lower V_S than most of the other methods. This exhibits one of the limitations of surface based methods, being that the measured increase in dispersion from 8 – 15 Hz could be resolved as either a thin layer with extremely high-velocity or a thicker layer with a less pronounced increase in V_S. Since the current results did not use previous test results to guide the inversion of the V_S profiles, the more conservative estimate of a thicker, lower V_S layer was obtained. The ambiguity in the resolution of such features is demonstrated in Figures 5.29 and 5.30 which compare V_S profiles showing both a thin and thick layer. Figure 5.29 shows the two V_S profiles showing the difference in the resolution of the high-velocity feature. More importantly Figure 5.30 shows the experimental dispersion data, and the theoretical dispersion estimates corresponding to each profile. It can be clearly seen in Figure 5.30 that the two profiles show almost exactly the same dispersion relation and give almost identical least squares errors. While the two profiles represent significantly different layerings, the estimated site response predicted by both profiles is essentially the same. This can be easily shown by comparing the V_{S30} values from each profile: V_{S30} (thick, lower V_S layer) = 232.3 m/s and V_{S30} (thin, higher V_S layer) = 239.8 m/s.

Downhole and SCPT methods are able to resolve finer features due to the direct measurement of each strata. However, the surface wave method was able to resolve the high-velocity, near-surface feature found in a number of the SCPT profiles that both the refraction profile and borehole measurements were unable to detect. This demonstrates that while surface wave methods are able to resolve fine features, the resolution capabilities are decreased with increasing depth due to the nature of Rayleigh wave dispersion. Overall, the results determined using the current surface wave methods show good agreement with previous results from a wide range of in situ seismic methods. This comparison of site characterization methods highlights the inherent differences between the various in situ methods and serves to validate the current active f-k surface wave procedure as a viable in situ seismic technique.

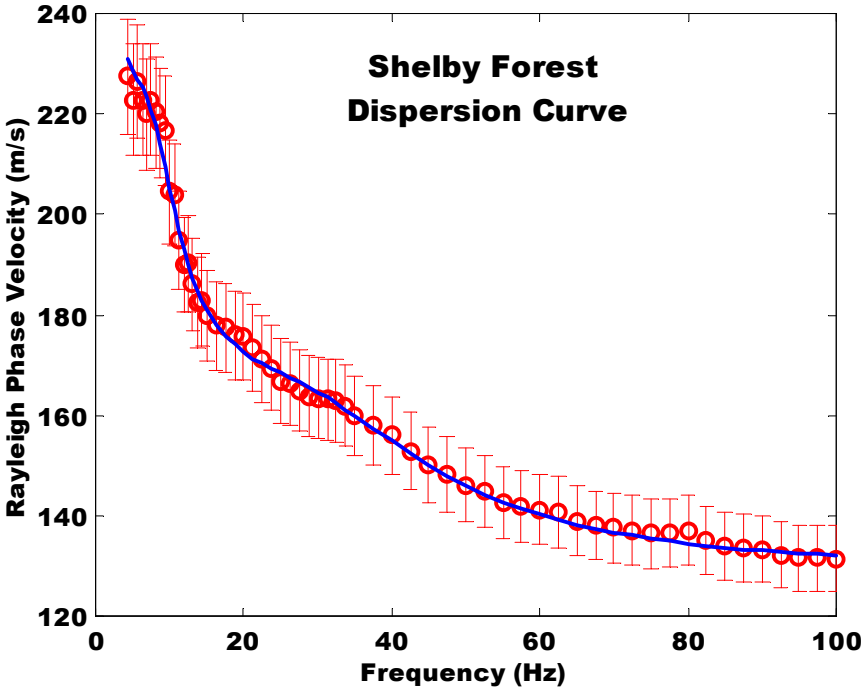

Figure 5.25 Dispersion Data from Shelby Forest, Active f-k Final Interpretation.

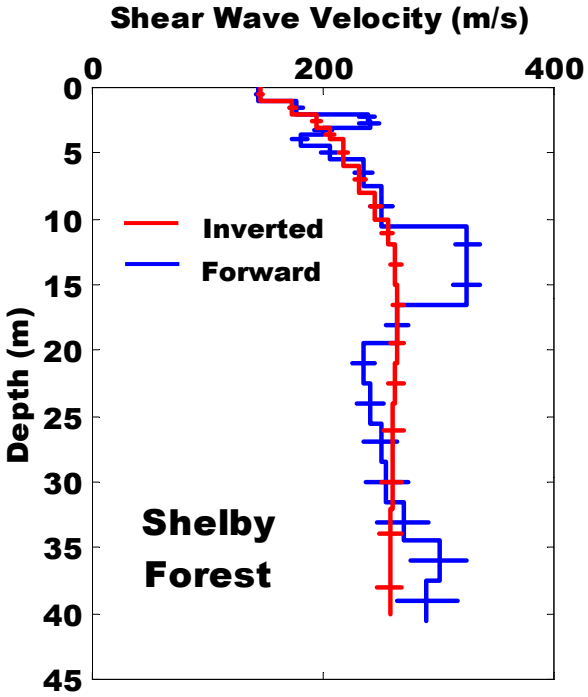

Figure 5.26 V_S Profile Comparison from Shelby Forest, Inverted and Forward Analyses.

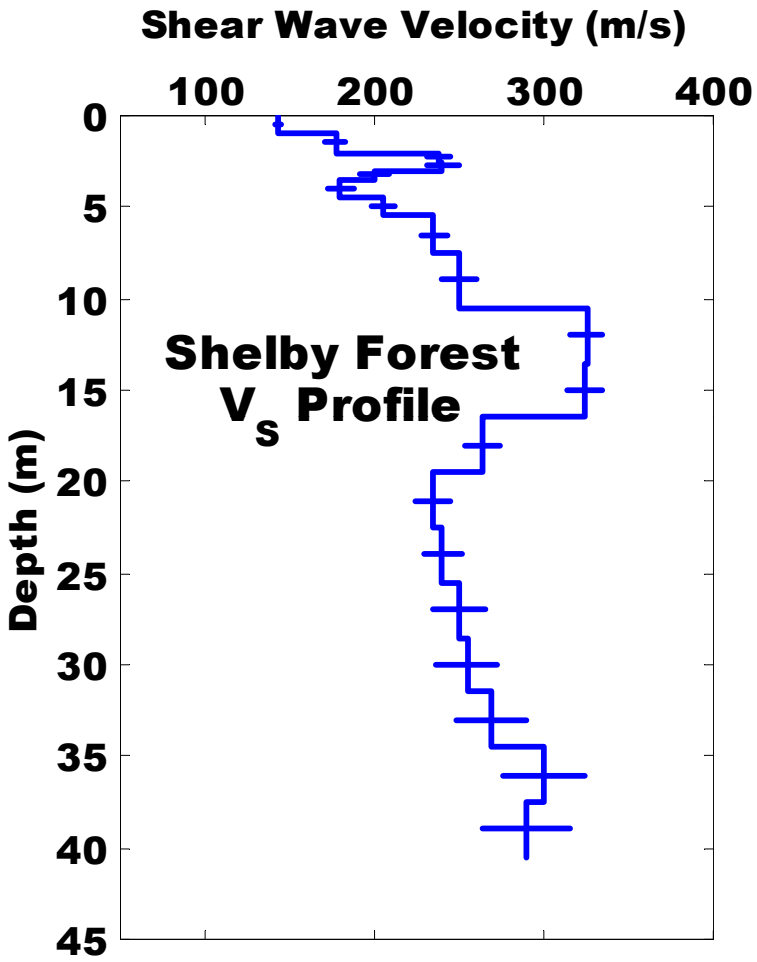

Figure 5.27 Interpreted V_S Profile from Shelby forest.

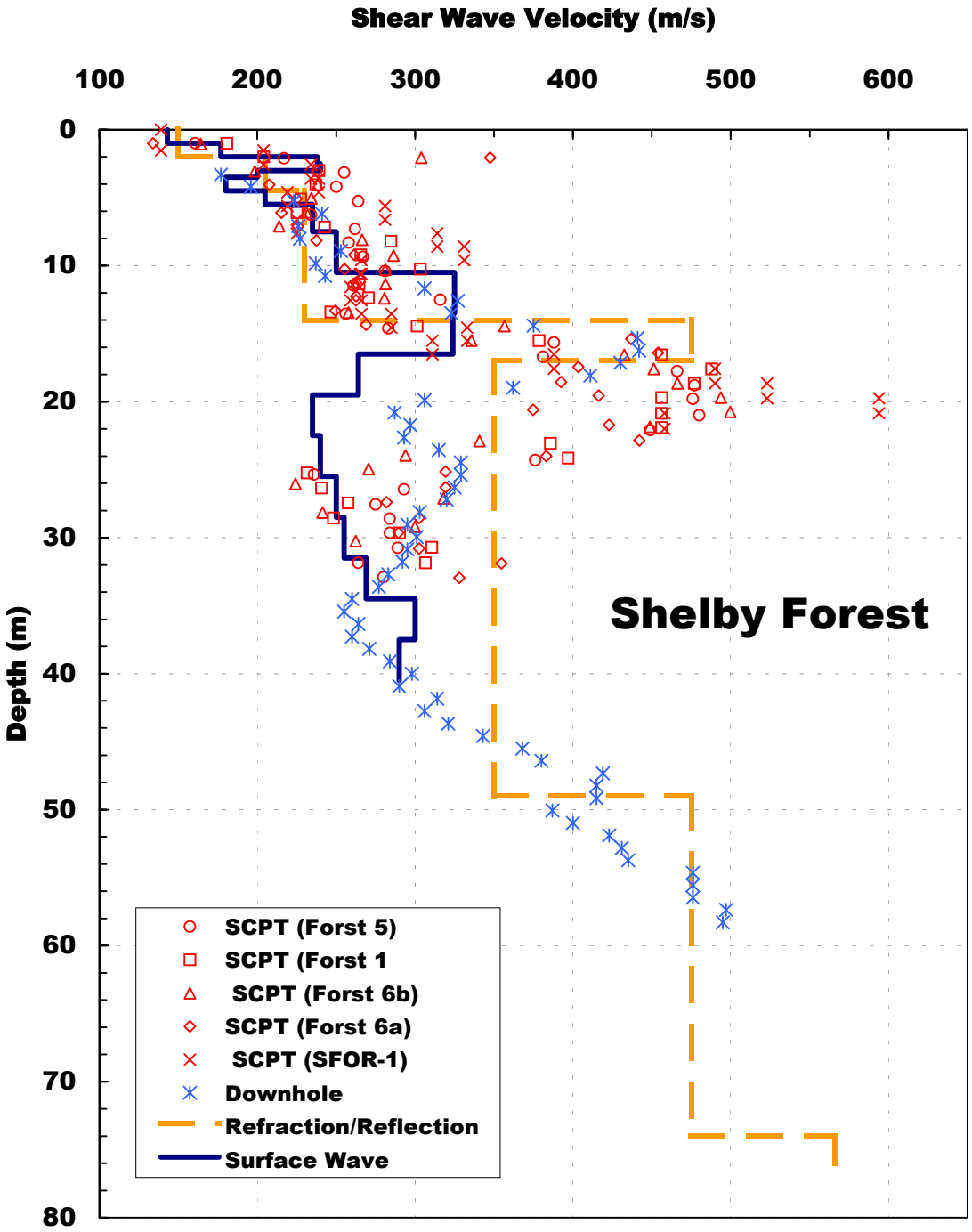

Figure 5.28 V_S Comparisons at Shelby Forest.

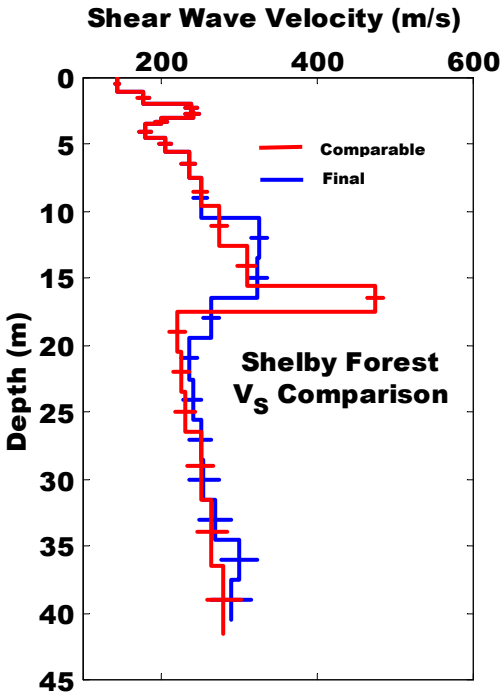

Figure 5.29 V_S Profile Comparison from Shelby Forest, Showing Non-Uniqueness of the Inverted V_S Profile.

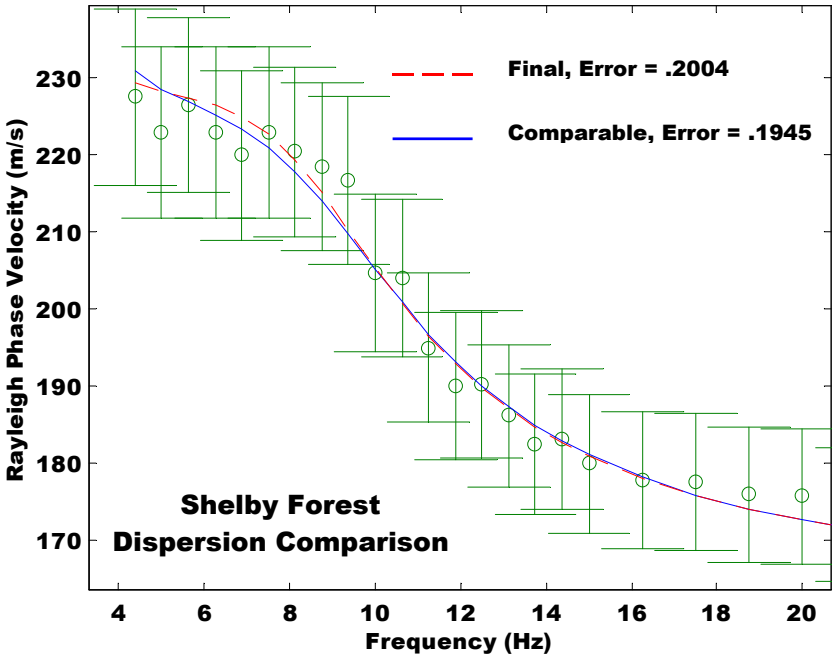

Figure 5.30 Dispersion Comparison from Shelby Forest, Showing the Dispersion Estimates Corresponding to the V_S Profiles in Figure 5.29.

5.7 University of Memphis:

The University of Memphis test site was located in a small grass field to the east of Zach Curlin Drive and across from campus parking lot 53 on The University of Memphis campus, as shown in Figure 5.31. This site is located adjacent to a moderately traveled campus roadway, is within 150 feet of a pumping station and is within a major metropolitan area which combined to create high levels of ambient noise at the test site. Active f-k surface wave testing was conducted on July 20, 2000. The testing was conducted using the standard array geometry outlined in Equation 4.6, with the array placed parallel to the roadway and away from the pumping station. The source frequencies were spaced at $\Delta f = 0.625$, 1.25, and 2.5 Hz over the respective frequency ranges of 4.375-15, 16.25–35, and 37.5–100 Hz for a total of 60 excitation frequencies.

The f-k dispersion curve, shown in Figure 5.32, depicts a dual mode behavior with the modal separation occurring at approximately 12 Hz. The low-frequency data is believed to correspond to the fundamental mode of Rayleigh wave propagation. This assumption is validated by the theoretical dominance of the fundamental mode at low frequencies (Gucunski and Woods, 1992). However, the exact modal number of the high-frequency data can not be accurately estimated. In fact, the large jump in the V_R of the high-frequency data would indicate that the high-frequency data is representative of a much higher mode than the low-frequency data. Additionally, as the modal number increases the tendency for modal superposition increases and the high-frequency data is most likely a combination of multiple modes of Rayleigh wave propagation (Lai, 1998; Gucunski and Woods, 1992).

Copyright © 1988-1997, Microsoft Corporation and/or its suppliers. All rights reserved. Please visit our web site at http://maps.expedia.com.

Figure 5.31 Map Showing The University of Memphis and Testing Location.

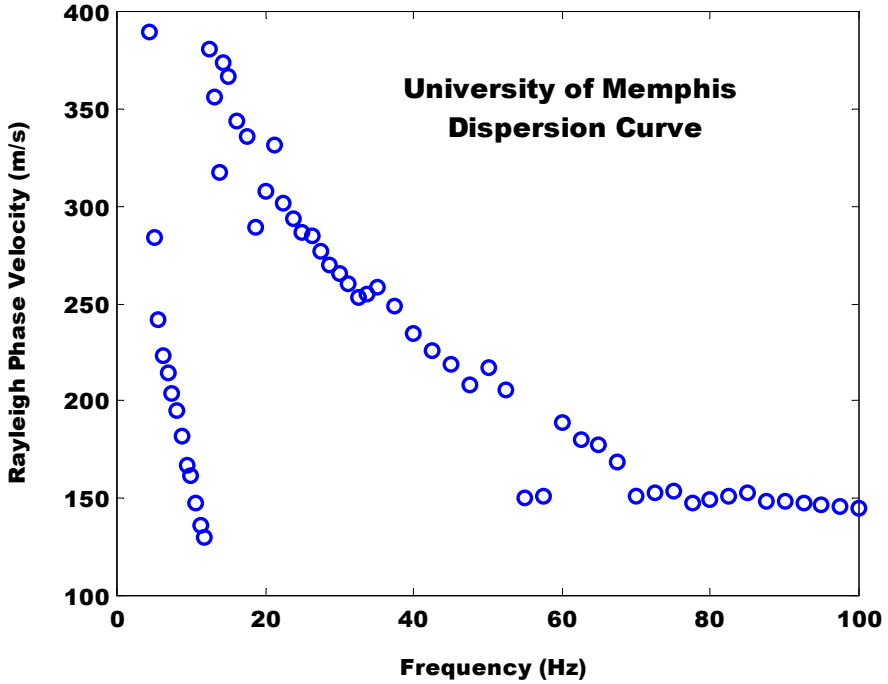

Figure 5.32 Experimental Dispersion Estimate from University of Memphis, Active f-k Method.

As a result of the above considerations it was difficult to use the high-frequency dispersion data within the confines of an automated inversion algorithm. However, the forward portion of the inversion algorithm used in the current study allows for the calculation of the first ten theoretical modes of Rayleigh propagation. As such, the high-frequency dispersion data could be compared to the calculated higher theoretical modes if the algorithm was implemented using a forward approach. A forward analysis was used to match the low-frequency data with the fundamental mode of propagation in conjunction with an attempt to match the high-frequency data with the trends of the higher theoretical modes. Through this process it was determined that the high-frequency data was most likely representative of superposition of several higher modes as seen in Figure 5.33. As can be seen through the analysis of this site, both the resolution and subsequent inversion of higher Rayleigh modes can create numerous complications in the analysis of surface wave data. As such, the fundamental portion of the curve was weighted more heavily than the higher mode data in determining the V_S profile shown in Figure 5.34. This is further justified because the V_S values below 10 m are completely defined by the fundamental portion of the dispersion curve.

The University of Memphis campus had been previously tested by a number of researchers including Mayne et al., Williams, as well as a number of the local seismologists and engineers from both CERI and the University of Memphis. However, the only testing available for comparison was the seismic refraction survey conducted by Williams (1999a). Figure 5.35 shows a comparison of the two V_S profiles. Both methods resolve a similar high-velocity feature within the depth range of 8 – 12 m. While both methods infer a decrease in velocity directly following the high-velocity feature, the surface wave profile estimates that the V_S values return to a much lower velocity of 225 m/s as compared to the 300 m/s estimated by Williams. The surface wave profile shows a gradual increase in V_S from this point, whereas the refraction estimate immediately returns to the V_S of 535 m/s exhibited by the high-velocity layer. This disparity between the two profiles is most likely due to the improved ability of surface wave methods to infer low-velocity features below high-velocity features. The V_S estimates coincide further from 32 –40 m, after which the surface wave profile continues to exhibit a gradual increase in V_S to a depth of 60 m.

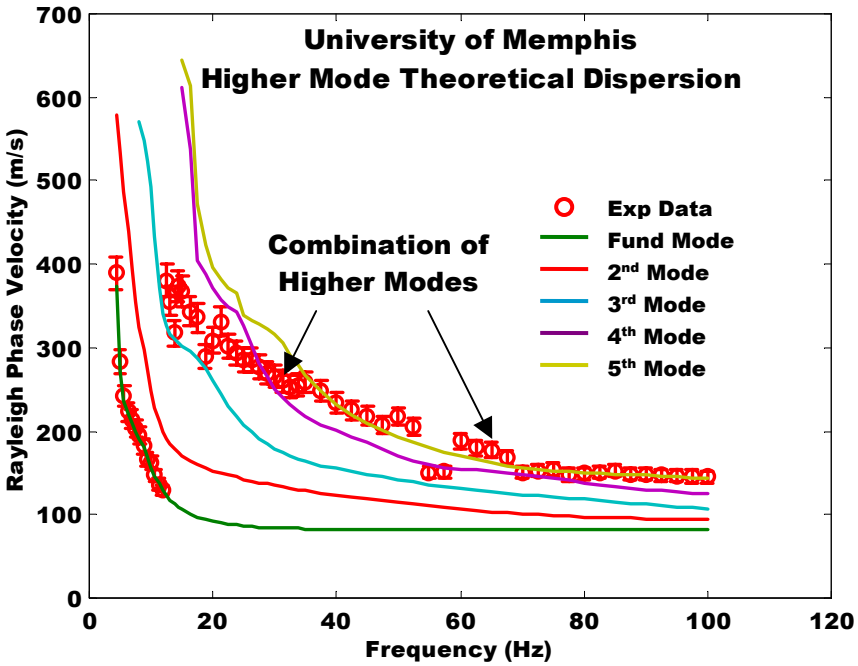

Figure 5.33 Dispersion Estimate from University of Memphis, Active f-k Final Interpretation.

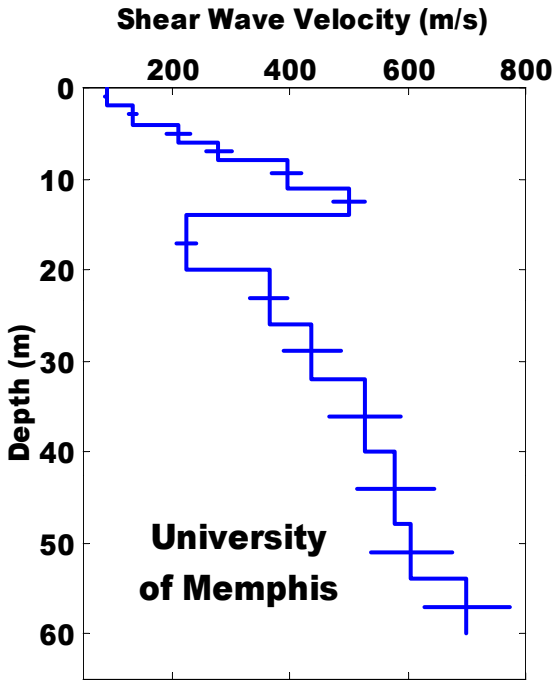

Figure 5.34 Interpreted V_S Profile from University of Memphis.

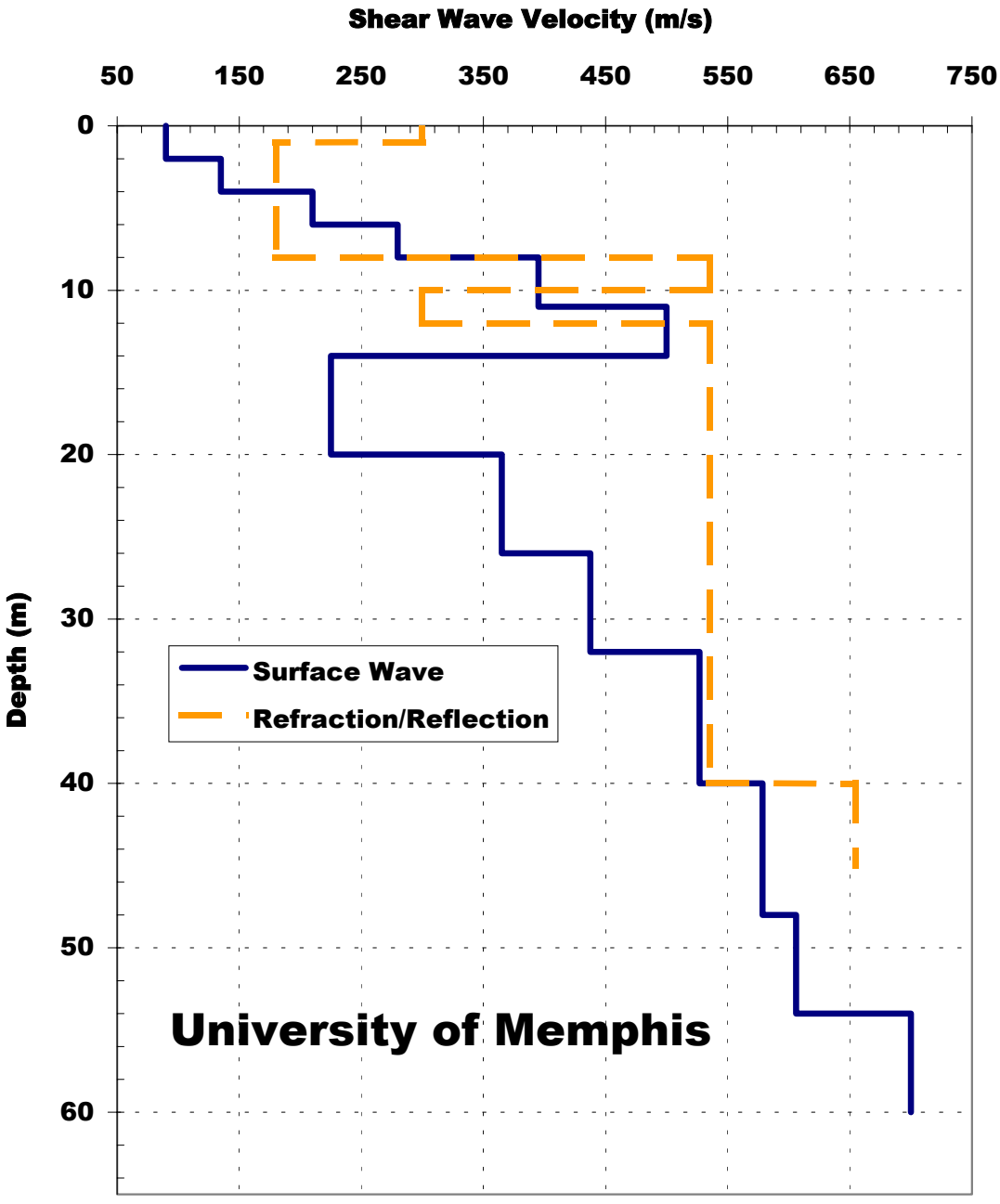

Figure 5.35 V_S Comparisons at University of Memphis.

5.8 Street 16:

The site designated as Street 16 is based on the CERI seismic zonation map (http://www.ceri.memphis.edu/usgs/hazmap_old/geotech/index.html) naming convention. This site was chosen as a test site in the current study to determine if the high-velocity layer found at the near-surface by Professor Ron Street of The University of Kentucky could be confirmed. The location of Street's testing was given as GPS coordinates and the site used in the current testing was located as close as possible to those coordinates. The surface wave testing was performed in the large open area at the northeast corner of the intersection of Nonconnah Parkway and Forest Hill Irene Road as shown in Figure 5.36. The site was located approximately 100 m to the south of Nonconnah Creek. Active f-k surface wave testing was performed at this site on July 22, 2000. The experimental testing parameters included the standard array geometry stated in Equation 4.6 and source frequencies spaced at Δf = 0.625, 1.25, and 2.5 Hz over the respective frequency ranges of 3.75-15, 16.25–35, and 37.5–100 Hz.

The resultant experimental dispersion curve can be seen in Figure 5.37. The two points shown with a "+" in the figure fell too far out of trend to be included in the inversion calculations. The dispersion relation used in the final analysis is shown in Figure 5.38. The dispersion estimate shows slight scatter in the high-frequency range above 90 Hz, however this scatter is believed to be the result of the severe cracking present in the surface clays of the test site. Secondly, the dispersion curve shows a decrease in slope between 6 – 10 Hz. This decrease in slope of the dispersion estimate corresponds to a low-velocity feature. The subsequent inversion of the dispersion estimate resulted in the V_S profile shown in Figure 5.39. The V_S profile shows a near constant velocity of approximately 190 m/s in the upper 6 m, followed by a steady increase in V_S to a value of 375 m/s at 11 m. A low-velocity feature, corresponding to the decrease in the slope of the dispersion estimate from 6 – 10 Hz, was resolved from 18 – 22 m with a V_S of ~ 180 m/s. The V_S increases slightly to a depth of 27 m, where the profile exhibits a large increase in V_S to ~ 450 m/s. The V_S continues to increase to a value of ~750 m/s at 60 m from the surface.

The refraction study by Street in the area had found a layer with a V_S = 974 m/s from 6-20 m of depth. The exact location of the test site used by Street was unavailable at the time of testing, although the current site is within 150 m of the given GPS coordinates. The current study was conducted at this site in an effort to determine if the high-velocity feature in the near-surface determined by Street could be confirmed. The current testing site was within the floodplain of Nonconnah Creek, indicating that the surface soils were of a young geologic age and were unlikely to exhibit high V_S values (Van Arsdale, 2000b). While moderately high-velocity layers were found at depths ranging from 8 - 18 m, the layer of extremely high-velocity found by Street was not detected in the current study. Figure 5.40 shows a comparison of the two V_S profiles and clearly depicts the large variation in the two profiles below 6 m. The dispersion estimate of the current testing does show a break at 6 m, however the increase in V_S is much less significant than that detected by Street. While the current study does not rule out the possibility of a high-velocity, near-surface layer in the area, it does reduce the likelihood especially with respect to the local geology.

Figure 5.36 Map Showing the Street 16 Testing Location.

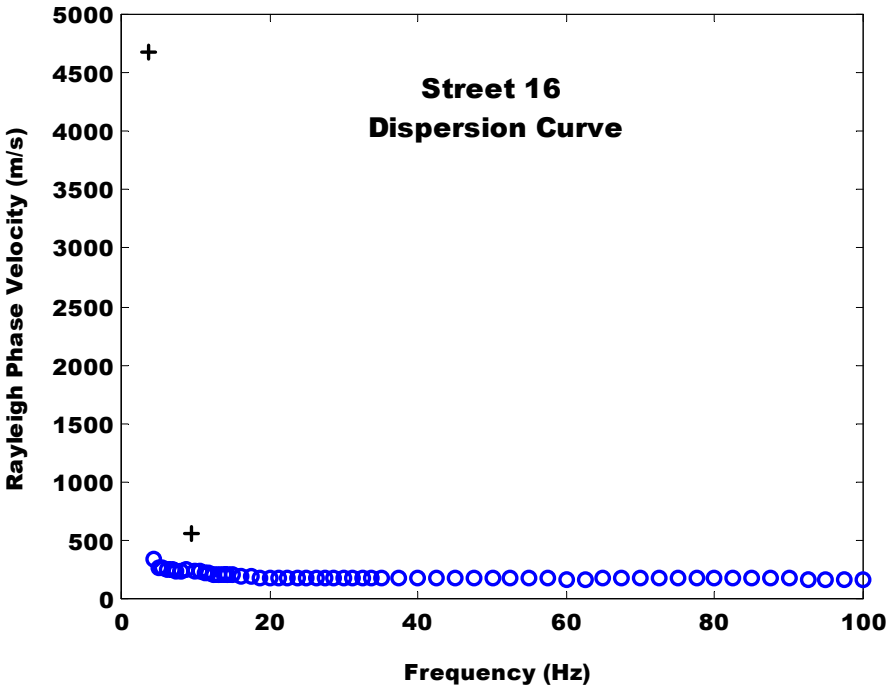

Figure 5.37 Experimental Dispersion Estimate from Street 16, Active f-k Method. "+" Symbols Indicate Points Not Used in the Final Analysis.

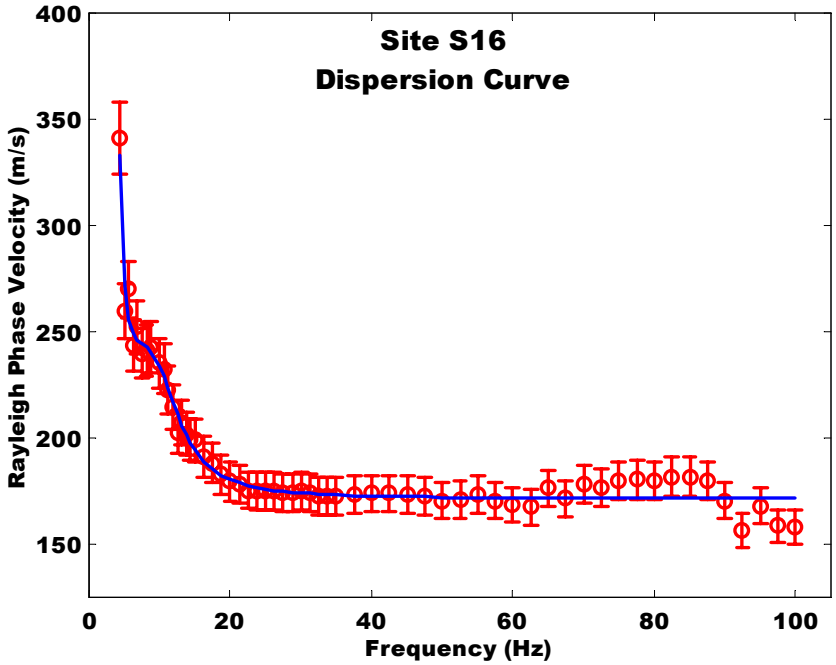

Figure 5.38 Experimental Dispersion Estimate from Street 16, Active f-k Final Interpretation.

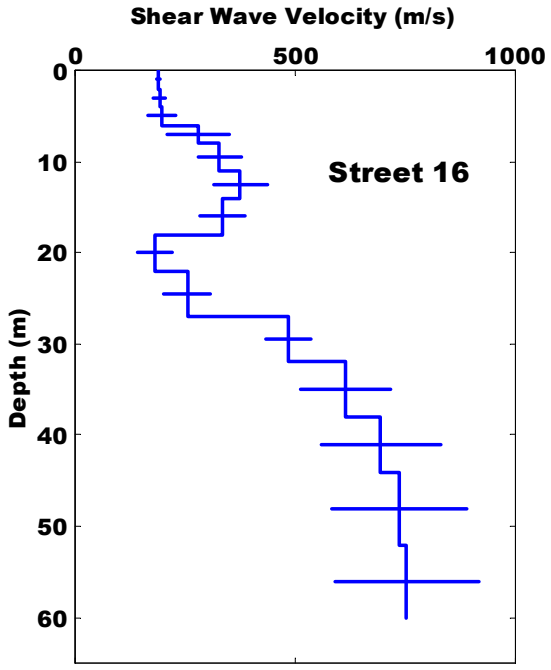

Figure 5.39 Interpreted V_S Profile from Street 16.

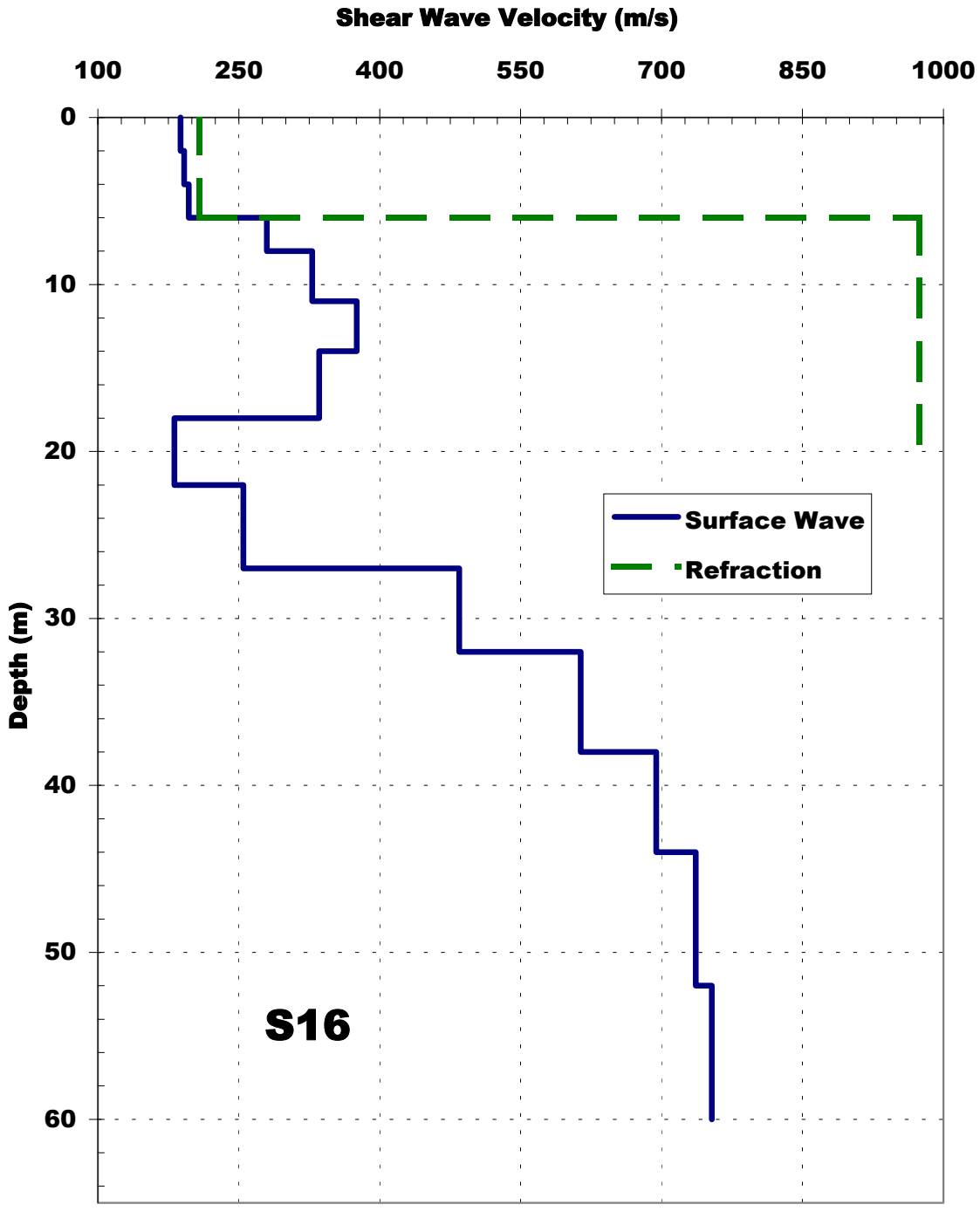

Figure 5.40 V_S Comparison at Street 16.

5.9 Williams 11

This site also refers to a site used in the CERI seismic zonation map, and was also tested to see if the high VS layer found by Rob Williams of the USGS could be confirmed (Williams et al., 1999a). This high-velocity layer is found throughout the Memphis metropolitan region and is representative of the conglomerate terrace formation. The terrace formation consists of fluvial sands and gravels that have become cemented and conglomerated in some portions of the formation creating very high-velocity features as discussed in Chapter 2. Through personal communication with Mr. Williams, the location of his testing was determined to be along a strip of grass behind the Johnson Controls building off of Nonconnah Boulevard in southern Memphis, Tennessee. The current testing was conducted at the same location shown in Figure 5.41. The test site was located approximately 10 m above and about 20 m to the north of Nonconnah Creek. The close proximity of this site to the Memphis International Airport resulted in a good deal of low-frequency interference. Additionally, the test site was located directly below high voltage power lines resulting in additional electrical noise at approximately 60 Hz.

Active f-k testing was conducted at this site on July 22, 2000. The experimental testing used the standard array geometry shown in Equation 4.6, and source frequencies spaced at $\Delta f = 0.625$, 1.25, and 2.5 Hz over the respective frequency ranges of 3.75-15, 16.25–35, and 37.5–100 Hz. The resultant experimental dispersion curve is shown in Figure 5.42. The point of lowest frequency (3.75 Hz), shown with a "+" in the figure, was not included in the final dispersion estimate because it falls too far out of trend to warrant consideration. The low-frequency interference from the large planes traveling overhead may have resulted in the misestimation of this point. Figure 5.43 shows the dispersion points used in the final estimate, along with the fundamental and second theoretical modes of dispersion related to the estimated V_S profile. As this site is slightly inversely dispersive, the problem of accurately determining the roots of the Rayleigh eigenvalue problem caused the slight variations seen at high frequencies in the theoretical dispersion curves.

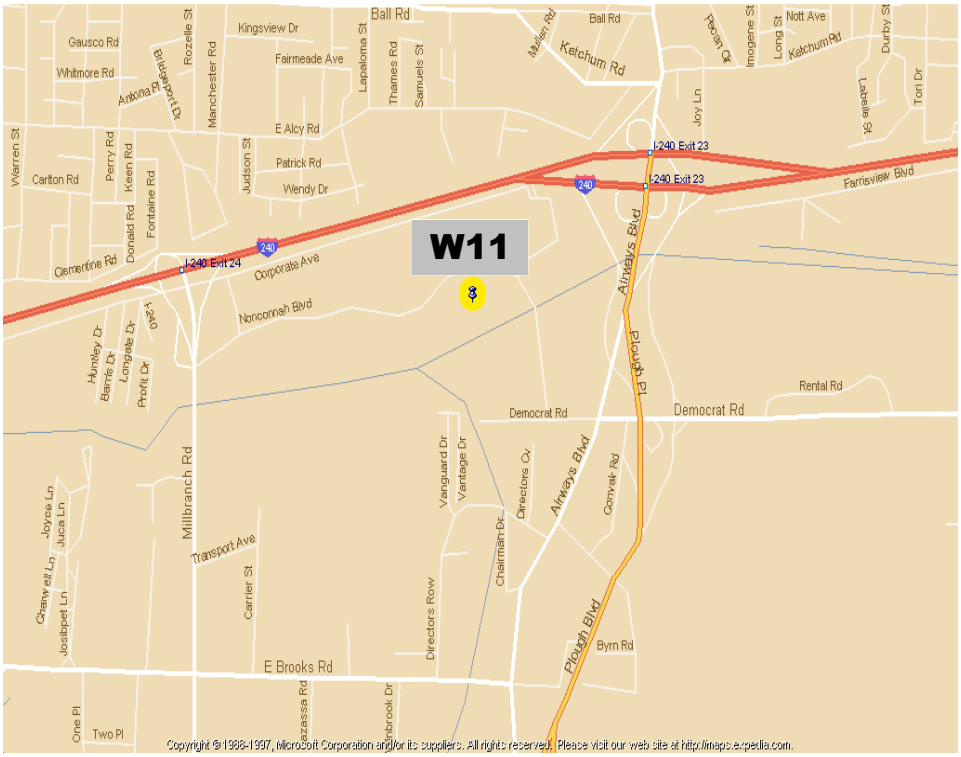

Figure 5.41 Map Showing the Williams 11 Testing Location.

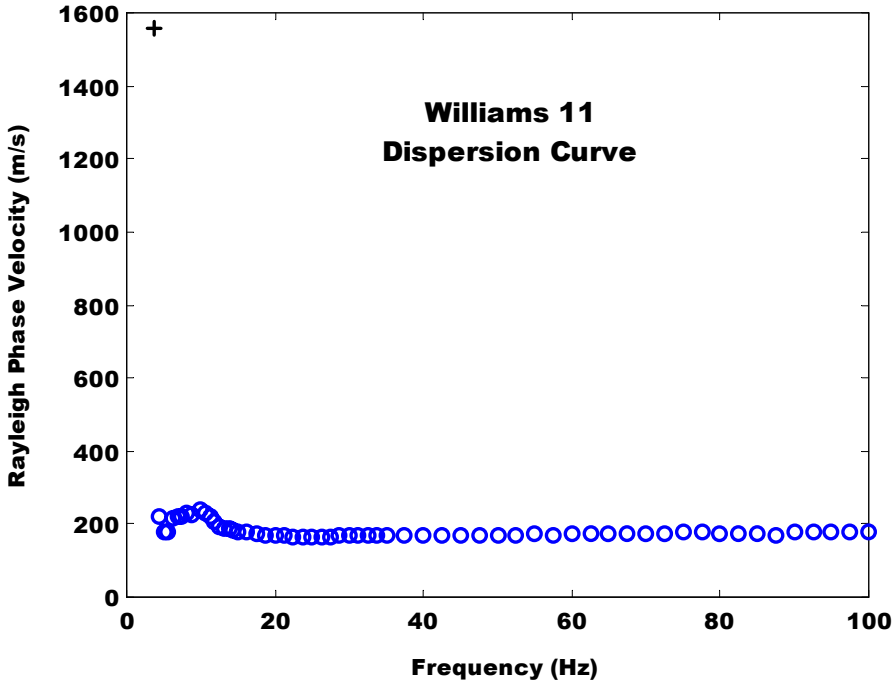

Figure 5.42 Experimental Dispersion Estimate from Williams 11, Active f-k Method. "+" Symbol Indicates a Point Not Used in the Final Analysis.

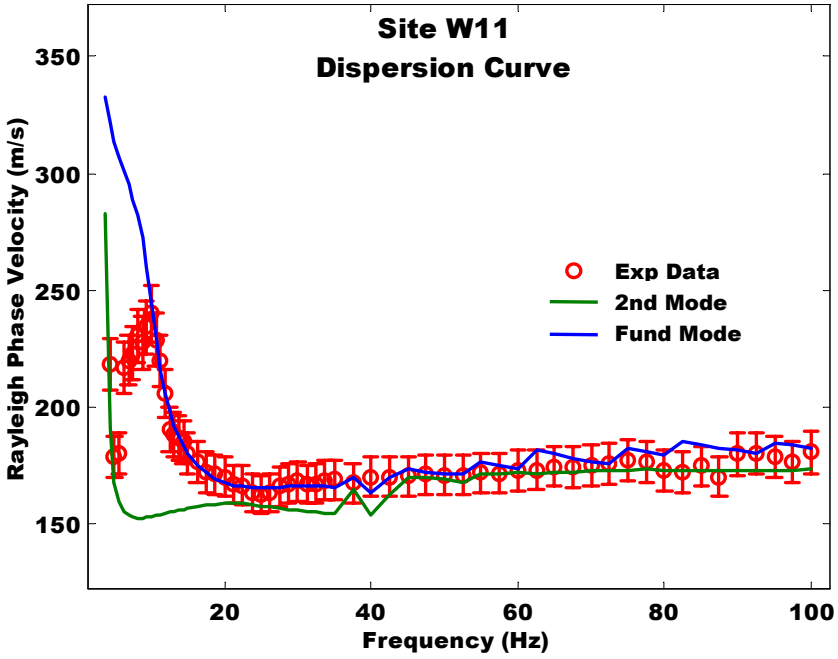

Figure 5.43 Experimental Dispersion Estimate from Williams 11, Active f-k Final Interpretation.

The prominent hump seen at low frequencies is representative of a very high-velocity layer surrounded by layers of lower velocity. Tokimatsu et al. (1992b) provide a theoretical example of this phenomena in their example of a simple four layer soil system. The calculated dispersion estimate found through their theoretical analysis of the layering properties shown in Table 5.2, is shown in Figure 5.44.

Table 5.2 Input Material Properties, Tokimatsu et al. (1992) - Case 3

Layer Number	Thickness H (m)	Density (Mg/m^3)	V_P (m/s)	V_S (m/s)
1	2	1.8	300	80
2	4	1.8	1000	180
3	8	1.8	1400	120
4	Half Space	1.8	1400	360

This theoretical example shows how dispersion estimates are affected by isolated high-velocity layers, especially the effect of higher Rayleigh modes. As such, the dispersion estimate of the current study would indicate the existence of a similar high-velocity layer. A portion of the example dispersion estimate is representative of the 2nd mode of propagation rather than the fundamental mode. This phenomena was also seen in the analysis of the current site as seen in Figure 5.43, and is due to a large portion of the incident wave being reflected from the high-velocity layer as a result of the large velocity gradient at the layer interface.

Because of the above phenomena, the dispersion relation in Figure 5.43 was difficult to invert with an automated inversion procedure. Consequently, as was done with certain previous sites, the V_S profile was determined through an iterative forward process matching both the fundamental and 2nd theoretical modes to the experimental dispersion estimate. The result of this process can be seen in the V_S profile shown in Figure 5.45. The V_S profile determined in the current study estimates a high-velocity feature (V_S = 1100 m/s) from 20 – 21.25 m. The high V_S layer is most likely representative of the conglomerate terrace deposit found in various locations throughout the region. The V_S values at depths above this layer were resolved below 200 m/s which correlates well with the floodplain geology of the region. Because of the complicated stratigraphy present at this site, the subsequent accuracy in the V_S profile should be considered lower than that of the simpler sites presented in this study. The increased uncertainty is the result of the increased complexity in analyzing dispersion estimates of complex stratigraphy which are often characterized by more than one mode of propagation.

Figure 5.46 shows a comparison of the current V_S estimate with that determined by Williams (1999a). While both studies resolve a high-velocity inclusion, the depth, thickness, and velocity of the resolved inclusions is significantly different in the two profiles. This difference is not entirely understood even after discussions with Mr. Williams regarding the discrepancy between the two profiles. The profiles do show good agreement in the upper 12 m, and the inconsistencies in the estimation of the high-velocity layer serve to highlight the difficulty in exactly defining such features using surface based methods.

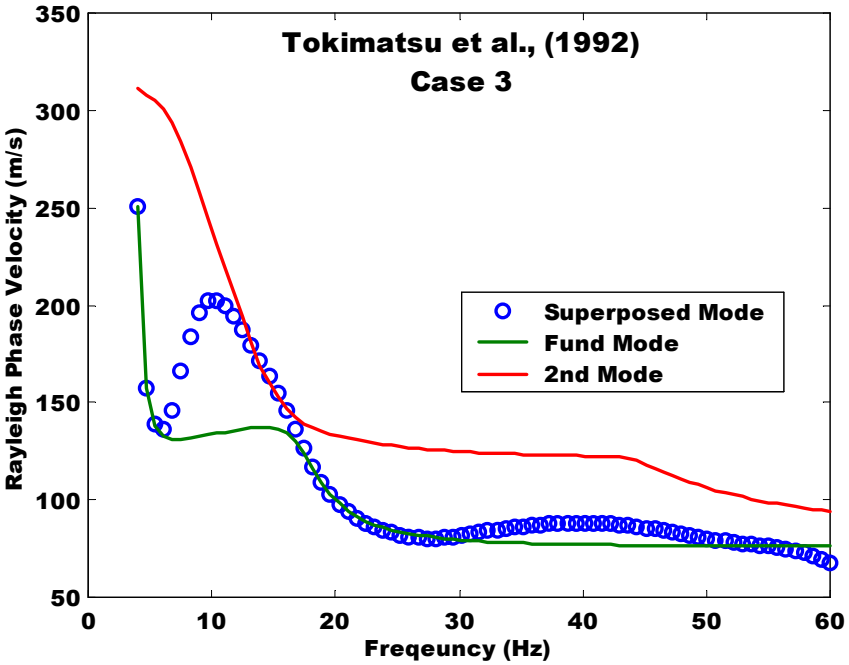

Figure 5.44 Theoretical Example Showing the Effect of High-Velocity Layers (Tokmatsu et al., 1992b).

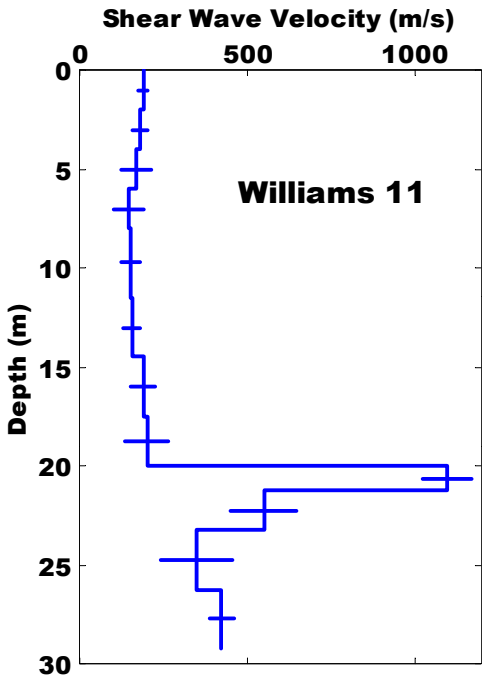

Figure 5.45 Interpreted V_S Profile from Williams 11.

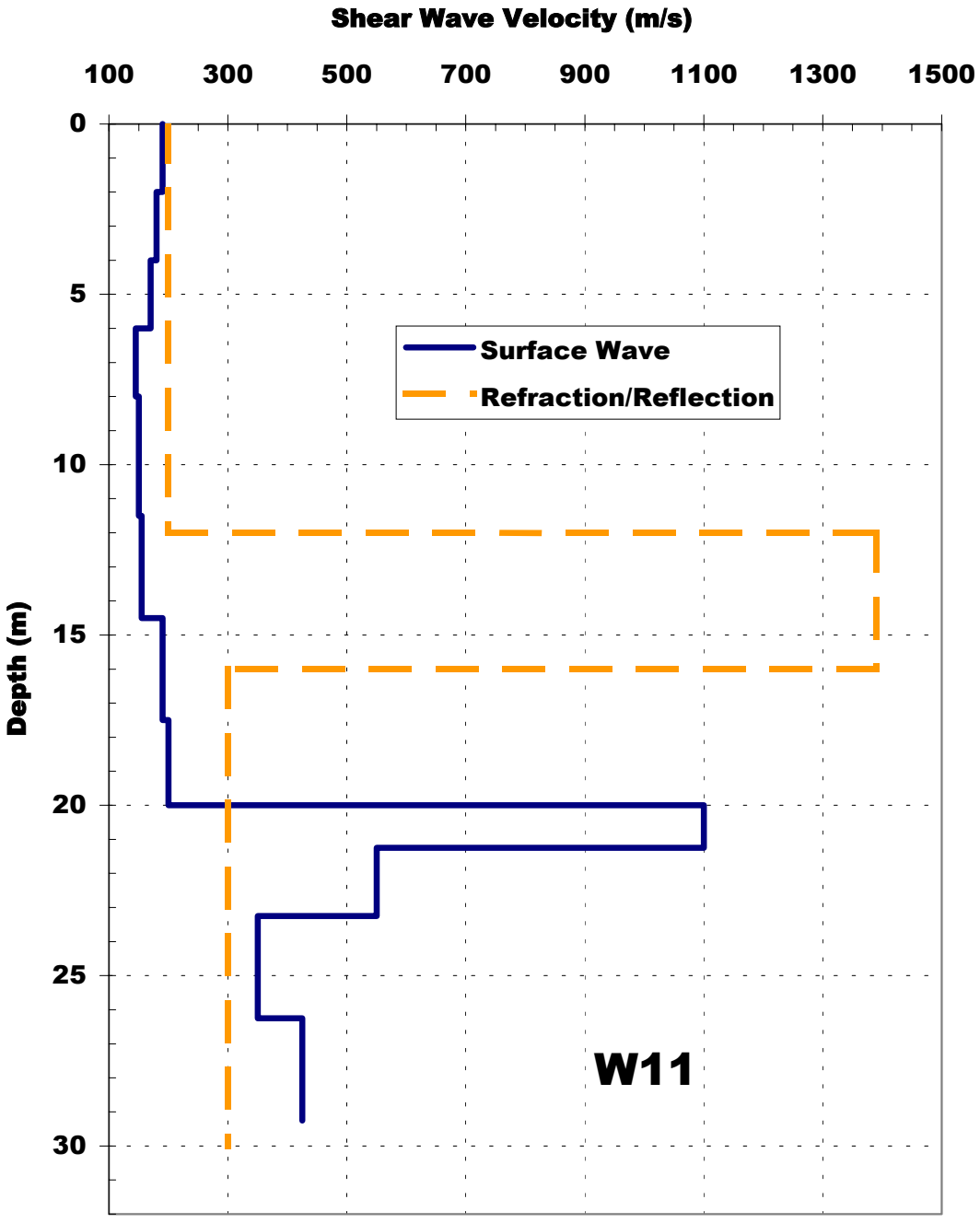

Figure 5.46 V_S Comparison at Williams 11.

5.10 Houston Levee Park:

The Houston Levee Park site is located on a strip of grass to the northwest corner of the western baseball field behind Houston Levee High School in Germantown, Tennessee as seen in Figure 5.47. The two park sites located in eastern Shelby County were tested to broaden the extent of V_S measurements into the eastern regions of Shelby County. Additionally, these sites were used to determine the presence and/or extent of the high-velocity conglomerate terrace formation in the area. The terrace formation thins eastward away from the Mississippi River and disappears entirely in the eastern regions of Shelby County. Additionally, the depth of the soil deposits over the underlying Paleozoic bedrock decreases extending away from the Mississippi River to the east (Van Arsdale, 2000). Consequently, the geologic formations and subsequently the soil properties tend to be less variable over larger spatial areas. The current investigation of the two sites in eastern Shelby County was aimed at classifying the general trend in the dynamic soil properties of the region as they extend away from the Mississippi River.

Figure 5.47 Map Showing Houston Levee Park and Testing Location.

Active f-k testing was performed at this site on July 24, 2000. The experimental testing was conducted using the standard array configuration outlined in Equation 4.6, and source frequencies spaced at Δf = 0.625, 1.25, and 2.5 Hz over the respective frequency ranges of 3.75-15, 16.25–35, and 37.5–100 Hz. The results of the f-k active testing are shown in the dispersion estimate of Figure 5.48. The four points of lowest frequency, shown with "+" symbols, were not included in the dispersion curve used in the inversion procedure. These four points exhibit an oscillatory behavior making it difficult to determine an accurate trend over their frequency range. The lowest (3.75 Hz) and third lowest (5 Hz) frequency points deviate too far from the other points to warrant their inclusion. A large gap between low-frequency dispersion points results in the resolution of large depth ranges based on a limited amount of dispersion data. For example, the inclusion of the two points of lowest frequency would correlate to a maximum measured wavelength of $\lambda = V_R/f$ = [545.8 m/s / 4.375 Hz] = 124.75 m, as compared to the maximum wavelength of the points actually used, λ_{max} = [288.8 m/s / 6.25 Hz] = 46.21 m. As such, this would correlate to an additional 52 m of resolvable depth, as per the procedure described in Equation 4.22. Subsequently, the uncertainty in the properties determined from low-frequency dispersion points offset from the trend is significantly increased from that typically acceptable in surface wave measurements and the inclusion of such points is not warranted.

The second and fourth lowest frequency points (4.375 and 5.625 Hz) were also not included because they do not show a clear trend and any subsequent interpretation would result in an increased uncertainty over this region. The final dispersion curve used in the inversion analysis is shown in Figure 5.49. The inverted V_S profile was subsequently resolved to a depth of 35 m as shown in Figure 5.50. The profile shows a low near-surface velocity with a gradual but rapid increase to a constant V_S of approximately 340 m/s for the remainder of the profile with a small decrease in V_S resolved from 11 to 14 m.

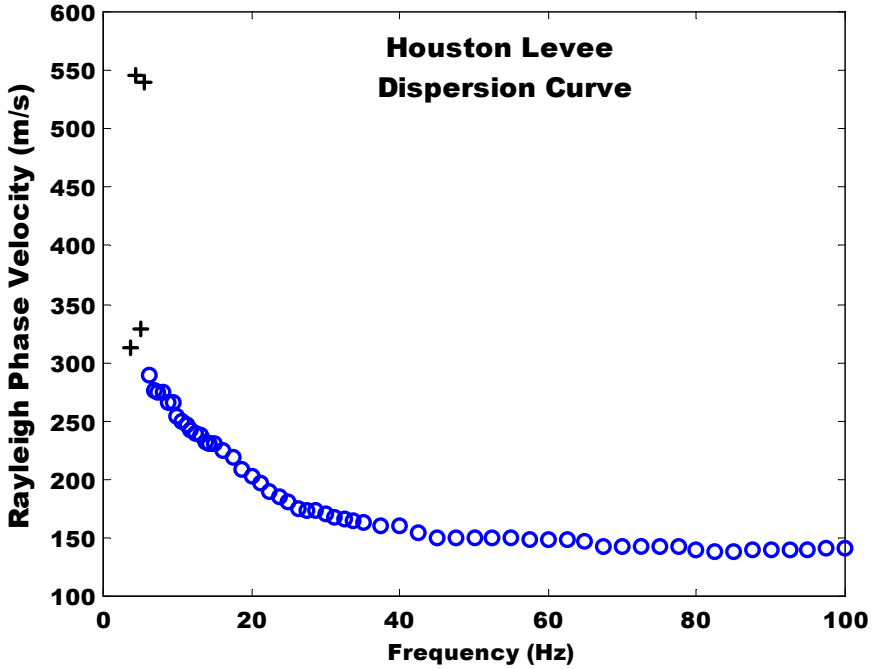

Figure 5.48 Experimental Dispersion Estimate from Houston Levee Park, Active f-k Method. Plus Symbols Indicates Points Not Used in the Final Analysis.

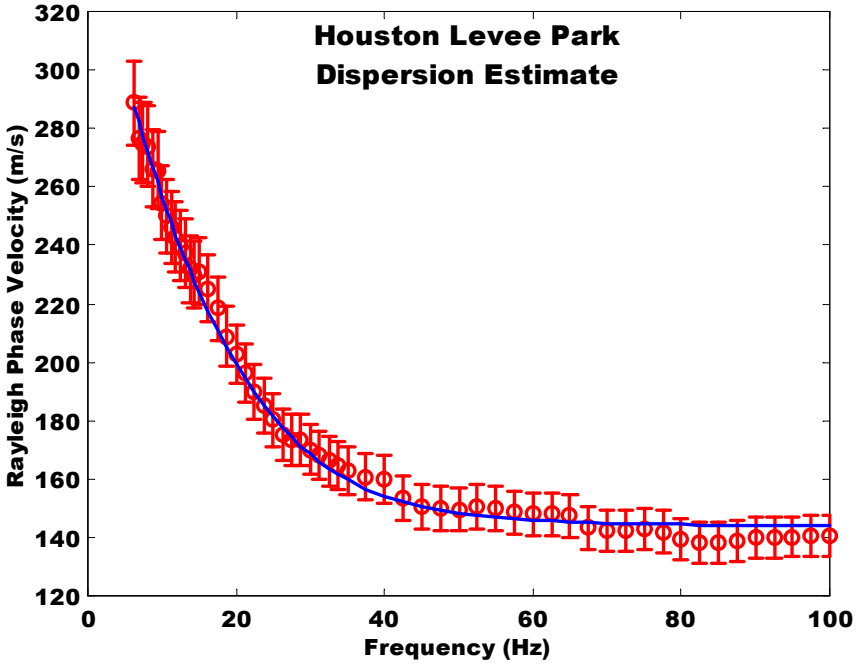

Figure 5.49 Dispersion Estimate from Houston Levee Park, Active f-k Final Interpretation.

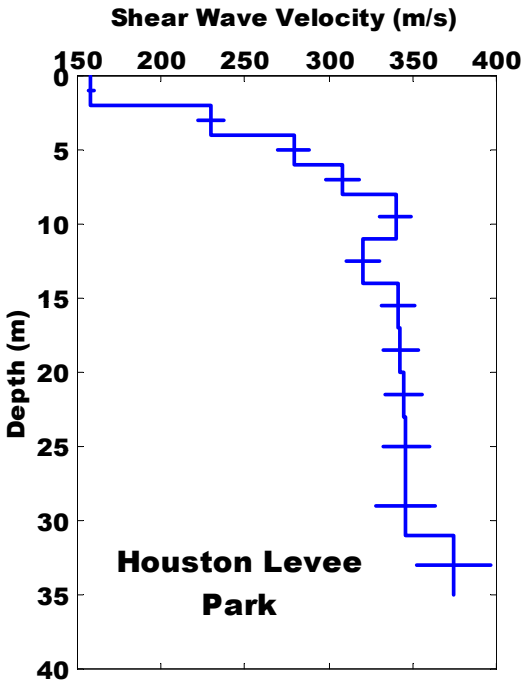

Figure 5.50 Interpreted V_S Profile from Houston Levee Park.

5.11 Powell Road Park

Powell Road Park is a large recreational facility of the City of Collierville in Shelby County, Tennessee. The test site was located on the park grounds to the northeast of the tennis facilities and directly south of a small trail exercise station as shown in Figure 5.51. The site was tested with the active f-k method on July 24, 2000. The experimental parameters used at this site consisted of the standard array geometry shown in Equation 4.6, and source frequencies spaced at $\Delta f = 0.3125$, 1.25, and 2.5 Hz over the respective frequency ranges of 3.75-15, 16.25–35, and 37.5–100 Hz. The results of the testing are seen in the experimental dispersion estimate shown in Figure 5.52. The point of lowest frequency was excluded from the V_S determination because of the criteria explained previously. The final dispersion estimate used to determine the V_S profile is shown in Figures 5.53. The estimated V_S profile for this site is shown in Figure 5.54.

The two sites in eastern Shelby County, Houston Levee Park and Powell Road Park, were located approximately 4 miles apart, with the Powell Road site located southeast of the Houston Levee site. The variation in V_S across this spatial distance was investigated by comparing the results from these two sites. Figure 5.55 shows a comparison of the experimental dispersion data, while Figure 5.56 shows the two V_S profiles. The dispersion estimates are very similar, however the Powell Road estimate shows a more prominent decrease in slope between 8 –12 Hz, corresponding to the more prominent low-velocity feature between 17 – 23 m resolved in the Powell Road Park V_S profile. These direct comparisons show very little spatial variation over this distance. This served to strengthen the hypothesis that the soil properties became less variable eastward from the Mississippi River. The importance of accurate low-frequency data is also highlighted by the increased resolution depth of the Powell Park site.

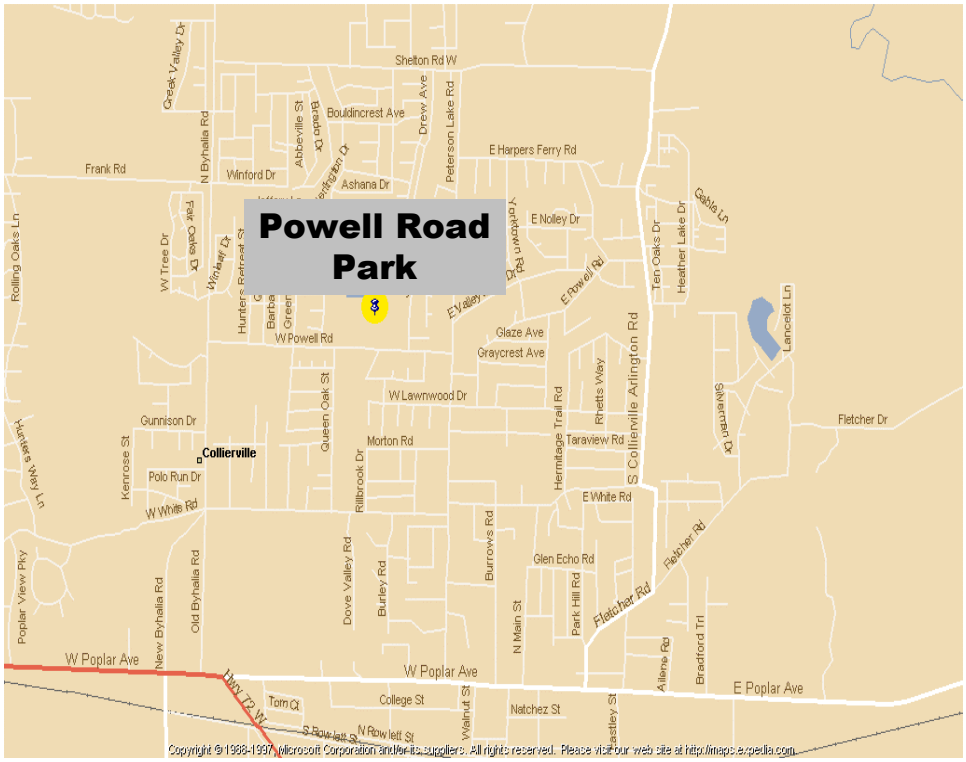

Figure 5.51 Map Showing Powell Road Park and Testing Location.

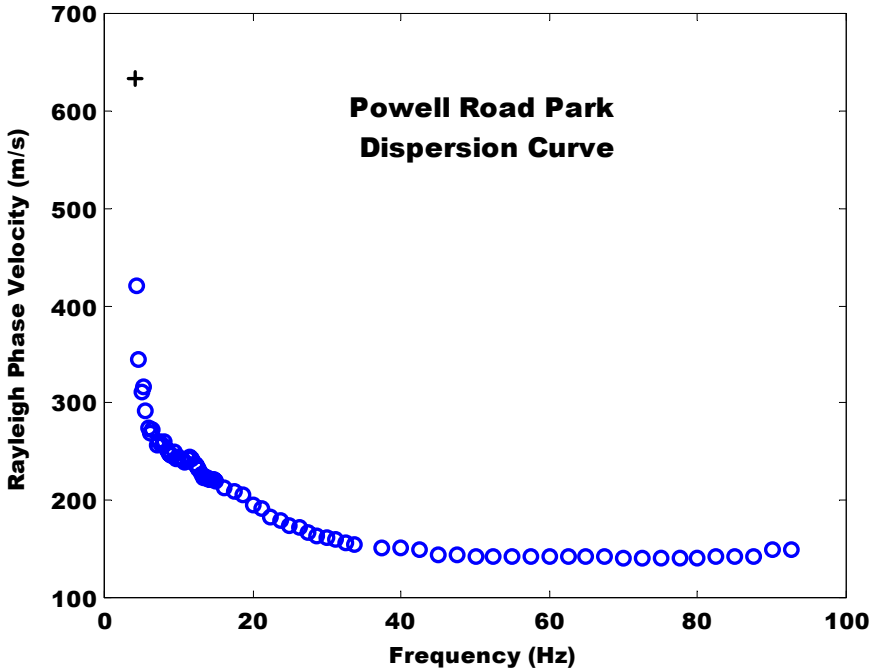

Figure 5.52 Experimental Dispersion Estimate from Powell Road Park, Active f-k Method. Plus Symbols Indicates Points Not Used in the Final Analysis.

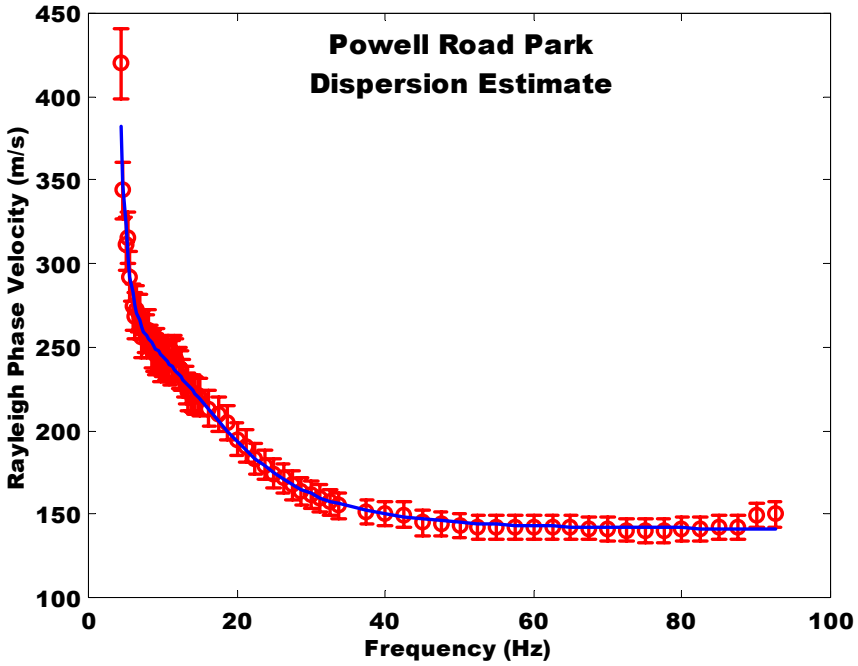

Figure 5.53 Dispersion Estimate from Houston Levee Park, Active f-k Final Interpretation.

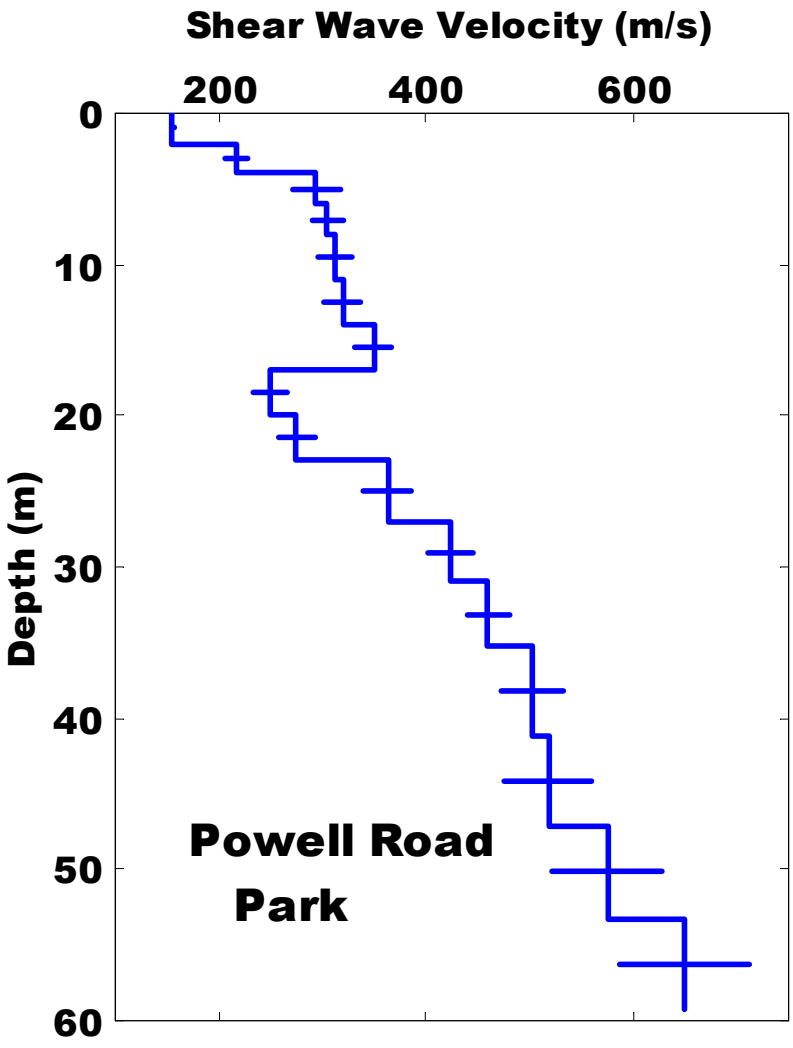

Figure 5.54 Interpreted V_S Profile from Powell Road Park.

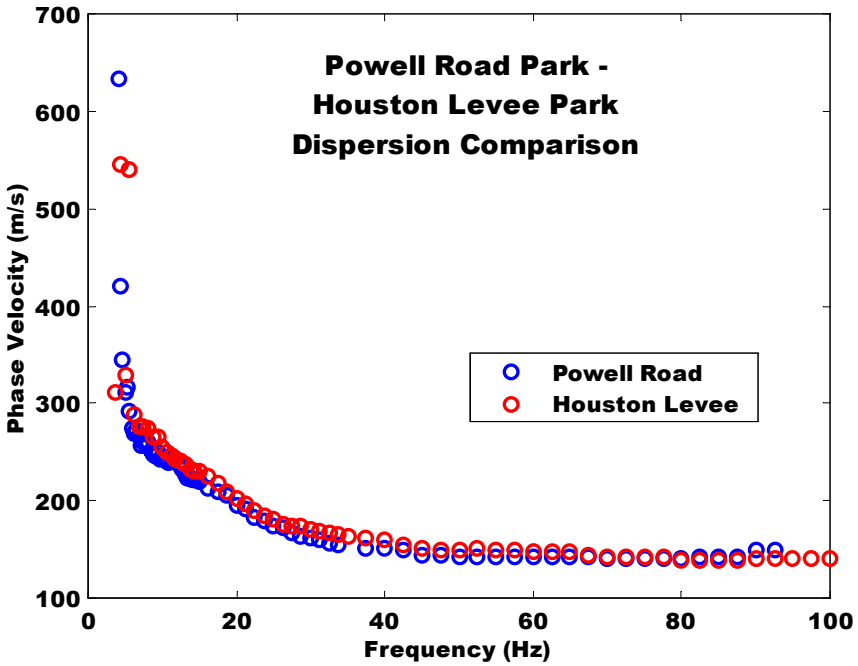

Figure 5.55 Dispersion Comparison of Houston Levee and Powell Road Parks.

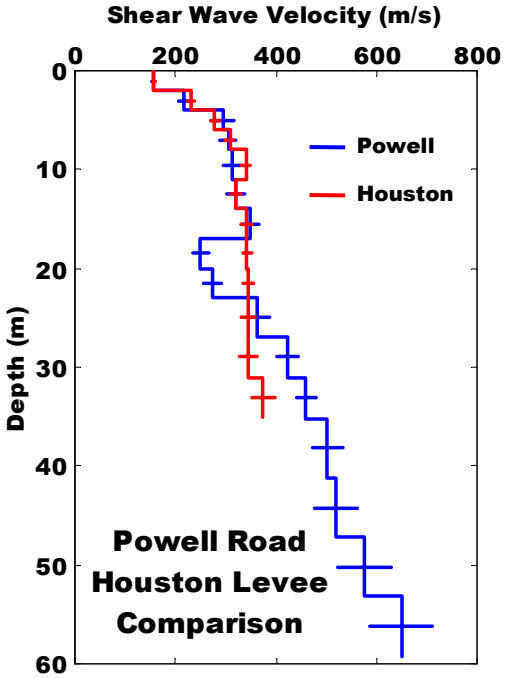

Figure 5.56 V_S Profile Comparison of Houston Levee and Powell Road Parks

5.12 Jackson County Landfill

The final site tested was located on the property of the Jackson County Landfill in Arkansas. Figure 5.57 shows the location of the test site off of local Route 14 near Amagon, Arkansas. The site was chosen for testing because previous downhole measurements by Dr. Shahram Pezeshk of the University of Memphis had been made to determine both V_S and material damping profiles of the site. The landfill site was the only site available for direct material damping comparisons, and it was subsequently tested with the active f-k procedures on July 25, 2000. The available testing areas near the borehole used in the previous measurements were limited. The ground conditions consisted of very stiff surficial clay that had become severely cracked due to the dry summer conditions. Additionally, the testing was conducted parallel to a drainage ditch, approximately 2 m in depth and a lateral distance of 4 m from the linear array configuration. The fissured nature of the surface clay, combined with the interference generated by reflections from the drainage ditch served to complicate the surface wave testing of the Jackson County Landfill site.

Active f-k testing was conducted using the standard array geometry shown in Equation 4.6, and source frequencies spaced at Δf = 0.156, 0.625, and 2.5 Hz over the respective frequency ranges of 3.75 – 8.125, 8.75 – 20, and 22.5 – 95 Hz. The experimental dispersion estimate derived from the f-k dispersion analysis is shown as Figure 5.58. The presence of the ditch is thought to have caused the extremely high V_R estimates at frequencies above 60 Hz. Reflections from the drainage ditch propagated back towards the array at a non-parallel angle of incidence. Because the active f-k analysis assumes a source colinear with the receiver array, waves traveling at any non-parallel angle away from the source are interpreted with a higher apparent velocity than motions traveling parallel to the array geometry. As such, the velocity of the reflections would be interpreted as much faster than the generated Rayleigh wavefield traveling parallel to the array configuration. Data corresponding to reflections can not be used within the framework of the current active f-k analysis procedures. Consequently, the information above 60 Hz was not used in determining the V_S profile due to the above-mentioned complications regarding the reflections from the drainage ditch and the cracked nature of the surface clay. The exclusion of this data was not significant, as the excluded points correspond to only the top 2 m of the site.

The assumed modal properties of the dispersion estimate can be seen in Figure 5.59. The higher V_R trend from 25 – 60 Hz seen in the dispersion estimate was assumed to be representative of a higher surface wave mode and not further reflections from the nearby ditch. The resultant V_S profile was determined using a combination of forward and inverse techniques as done for several previous sites. An inversion process was first completed using the dispersion points corresponding to the fundamental mode of propagation. A forward process was then used to more accurately match the portion of the dispersion estimate between 25 – 60 Hz consisting of higher modal behavior. This analysis resulted in the determination of the V_S profile shown in Figure 5.60. The incomplete high-frequency resolution makes the upper portion of the V_S estimate subjective. However, all but the upper 2 m of the profile were resolved using the experimental dispersion data and should be considered accurate. The current profile was resolved to a maximum depth of 40 m. Figure 5.61 shows the V_S comparison of the current profile with the downhole measurements completed by Pezeshk. The two profiles show minor disagreement over the top and bottom portions of the surface wave profile. However, the agreement over the remainder of the profile is very good. The material damping calculations of the current data have not yet been completed and a comparison of those results will be presented in a later publication.

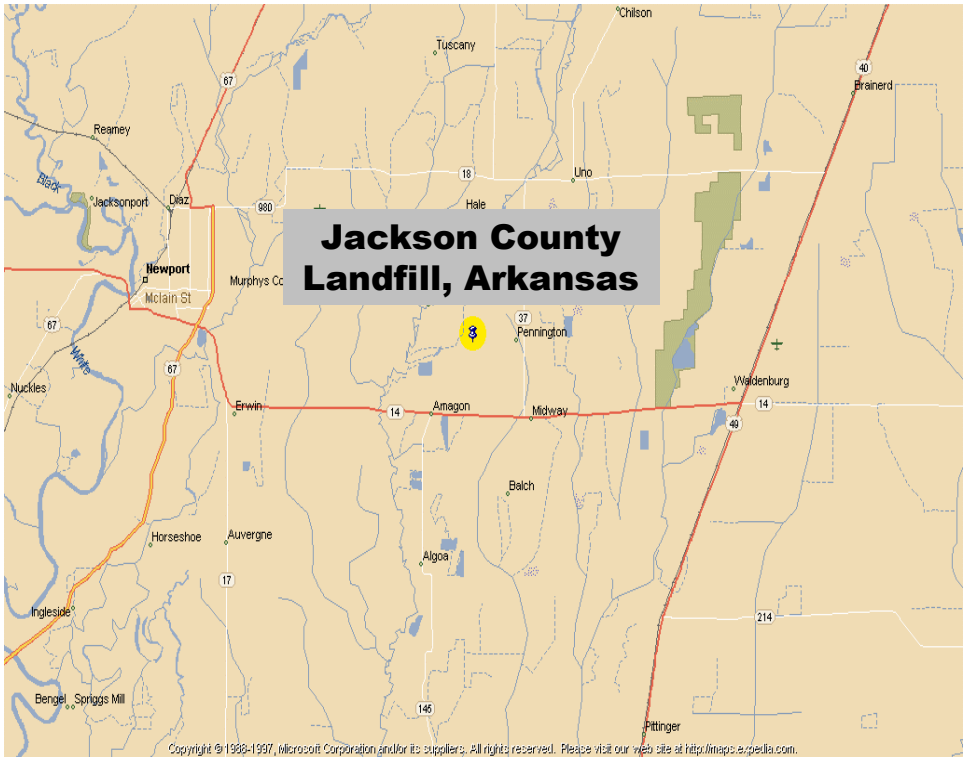

Figure 5.57 Map Showing Jackson County Landfill and Testing Location.

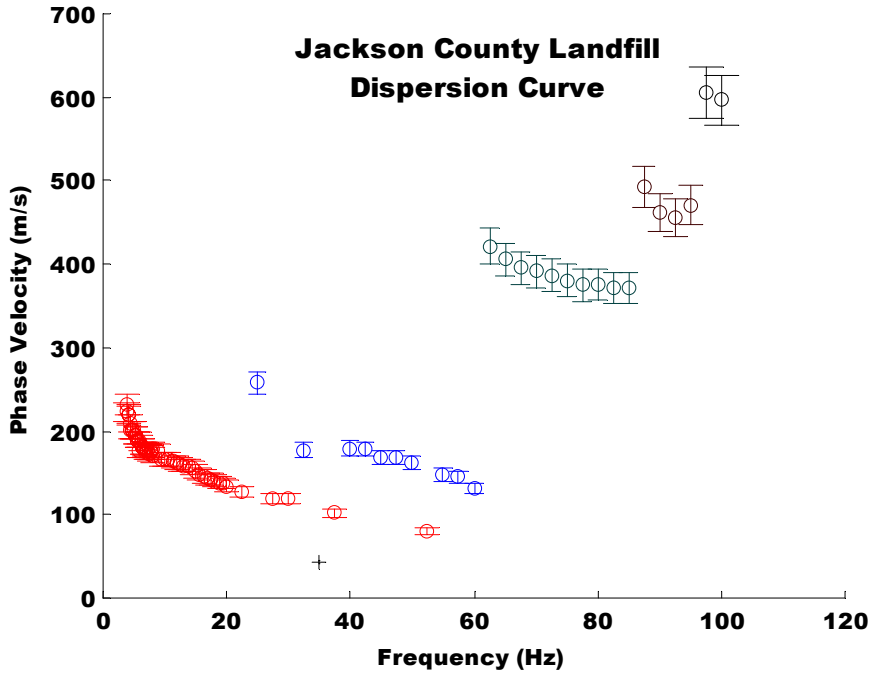

Figure 5.58 Experimental Dispersion Estimate from Jackson County Landfill, Active f-k Method.

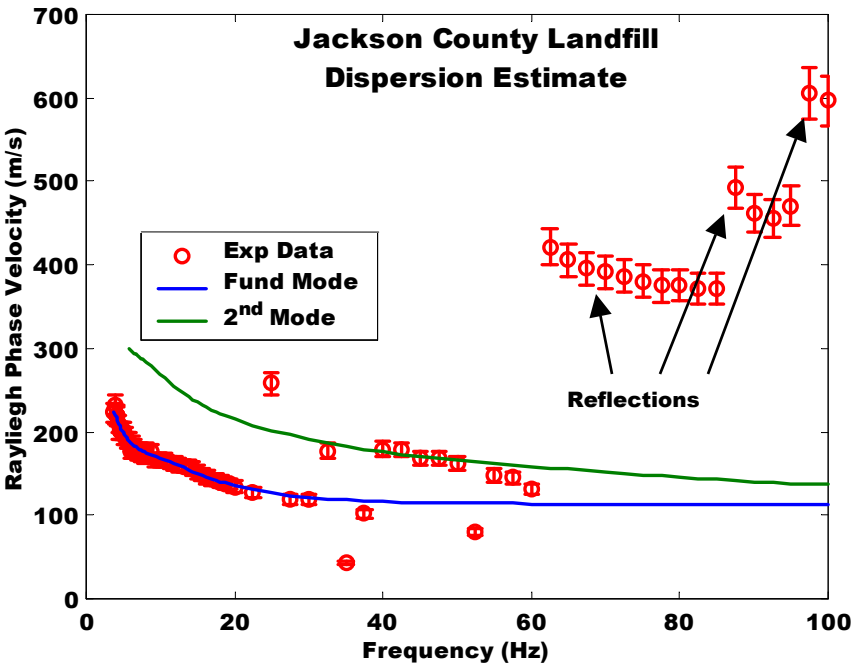

Figure 5.59 Dispersion Estimate from Jackson County Landfill, Active f-k Final Interpretation.

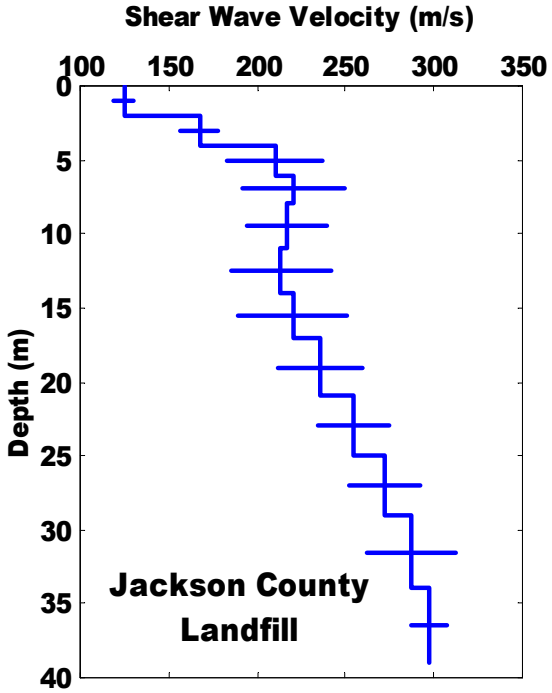

Figure 5.60 Interpreted V_S Profile from Jackson County Landfill.

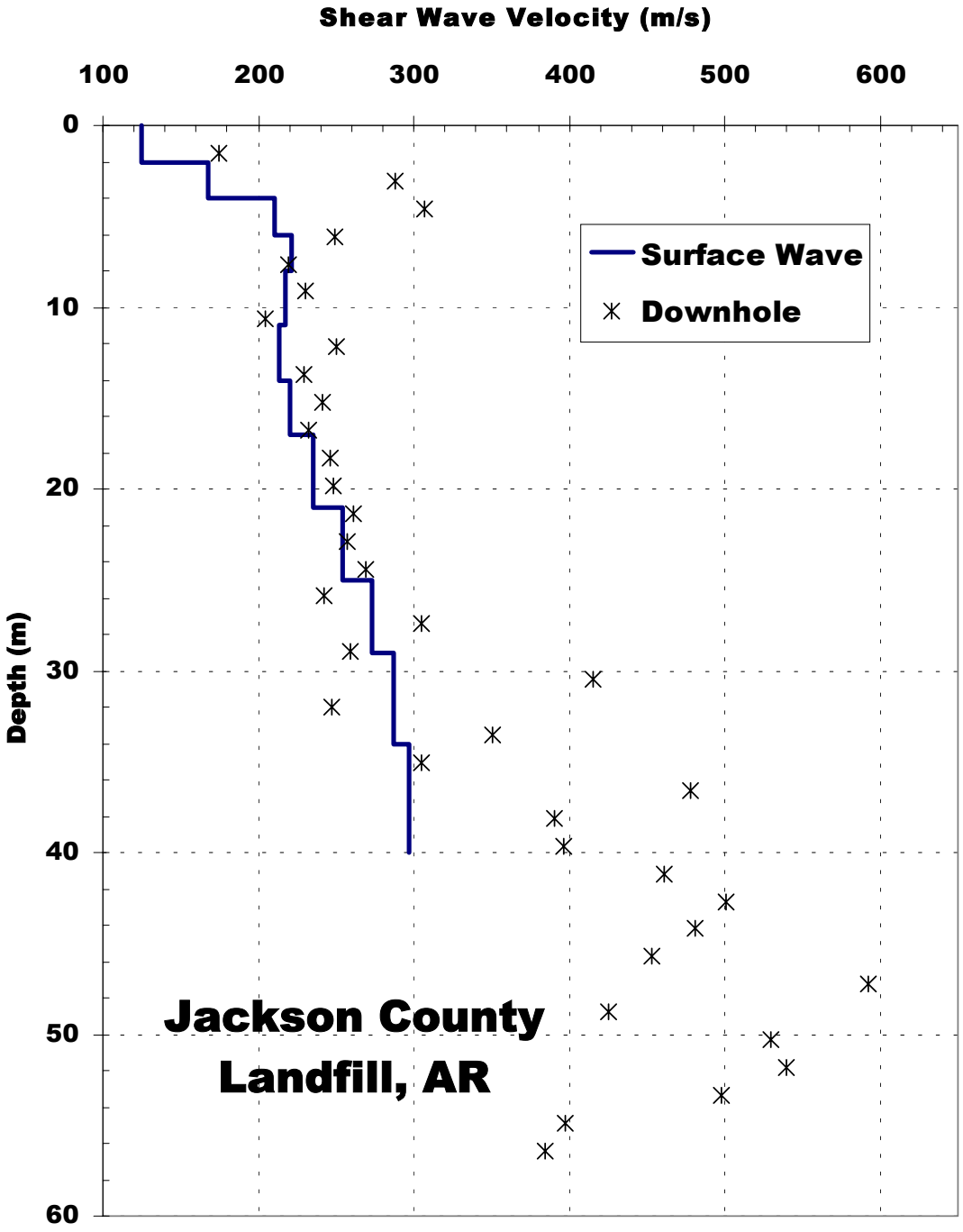

Figure 5.61 V_S Comparison at Jackson County Landfill.

5.13 Site Classification

V_{S30} is the primary National Earthquake Hazard Reduction Provisions (NEHRP) site class parameter and is used to define the local ground amplification effects of a site (FEMA, 1997). This parameter is not a direct average of the shear wave velocities in the top 30 m, rather it is calculated based on travel times as shown in Equation 5.3:

$$V_{S30} = \frac{\sum_{i=1}^{n} d_i}{\sum_{i=1}^{n} \frac{d_i}{V_{Si}}} \tag{5.3}$$

where V_{si} = the shear wave velocity, d_i = the thickness of a given layer i, and n = the number of layers from 0-30 m. The V_{S30} values from the current testing are seen in Table 5.3. Dr. Chris Cramer of CERI and Mr. Rob Williams of the USGS made suggestions regarding the selection of the current sites to allow for more complete spatial coverage of V_S estimates throughout Shelby County, Tennessee. Additionally, some of the sites were tested to provide additional measurements at sites that showed abnormal phenomena in previous tests, e g. the W11 and S16 sites. The results from the current testing have been added to the CERI, USGS, and MAE center data bases of near-surface V_S data for Shelby County and will aid in the production of future seismic zonation maps.

Table 5.3 V_{S30} Values Calculated from the Current V_S Profiles

Test Site Names	V_{S30} (m/s)
Shelby Farms - Shooting Range	186.85
Shelby Forrest	232.28
University of Memphis	241.69
Mud Island B	229.72
Mud Island A	184.82
Williams 11	213.77
Street 16	251.28
Shelby Farms - Wolf River	193.80
Houston Levee Park	292.47
Powell Road Park	281.87
Jackson County Landfill, AR	193.23

Chapter 6

Comparison of Traditional SASW and Frequency-Wavenumber Surface Wave Tests.

6.1 Introduction

Active frequency-wavenumber (f-k) methods were developed to improve upon traditional SASW surface wave testing. Many of the drawbacks of the traditional test methods and the improvements made through the implementation of the current f-k methods were presented in Chapters 3 and 4. This chapter begins by briefly summarizing the improvements and requirements of the current f-k methods with respect to the traditional SASW methods. A comparison of the two methodologies is then shown through the experimental results obtained at three test sites (Shelby Forest, Shelby Farms – Shooting Range, and The University of Memphis) where both active surface wave methods were used. These sites were chosen to represent a range of testing conditions based predominantly on the level of ambient noise present at each site. The comparisons of the two methods are based on both the ergonomics of the experimental testing procedures and on the ability of each method to accurately resolve the dispersion relationship of each site.

6.2 Requirements and Improvements of the Current f-k Method

Traditional SASW surface wave testing procedures are limited by several drawbacks including: no multi-mode resolution, frequency dependent dispersion calculations, limited noise removal capabilities, limited attenuation estimation possibilities, poor quality dispersion estimates, limited low-frequency resolution, substantial near-field interference, and the possible need for manual phase interpretation (Zywicki, 1999). The current frequency-wavenumber methods were developed to alleviate some of these drawbacks as explained in Chapter 4 and summarized below. The use of array-based measurements decreases the effects of near-field interference, increases the accuracy of the dispersion estimate, allows for greater coverage of spatial lags, and allows for both multi-mode resolution and attenuation estimation. The better spatial coverage of the f-k method was seen in the comparison of array smoothing functions shown in Figure 4.2. The use of multiple sensors also provides simultaneous measurements limiting external influences, and allowing for tremendous increases in the quantity of phase data available for dispersion calculations. External influences mainly consist of spatial variability, ambient wave energy present in the measured ground surface, and apparent phase velocity differences over space (Lai, 1998). However, electronic noise generated from the experimental equipment, as well as any other interfering signals can hinder the experimental measurements.

Frequency-wavenumber methods require the use of more sophisticated testing equipment than used in traditional SASW testing. Multiple sensors, 16 in the current procedures, and a compatible data acquisition system capable of handling the high speed temporal sampling and added receivers are fundamental components of the current procedures. Additionally, while array measurements can be conducted using an impulsive source, the current active procedures make use of a harmonic source. The harmonic source is needed to conduct the stepped-sine testing which allows for band-limited frequency-

domain calculations. Band-limited calculations dramatically increase the ambient noise level tolerance, attributing to the improved accuracy and low-frequency resolution of the f-k dispersion calculations. The improvements of the f-k method over traditional engineering surface wave procedures are clearly shown in the dispersion comparisons presented below, especially for the sites containing large levels of ambient noise.

6.3 Experimental Comparisons

The experimental comparisons are presented in order of increasing ambient noise level, starting with the rural Shelby Forest site, continuing through to the Shelby Farms – Shooting Range site, and finishing with the urban University of Memphis test site. Figure 6.1 shows frequency spectra measured during the f-k testing from the three experimental sites, and clearly depicts the different ambient noise levels present at each location.

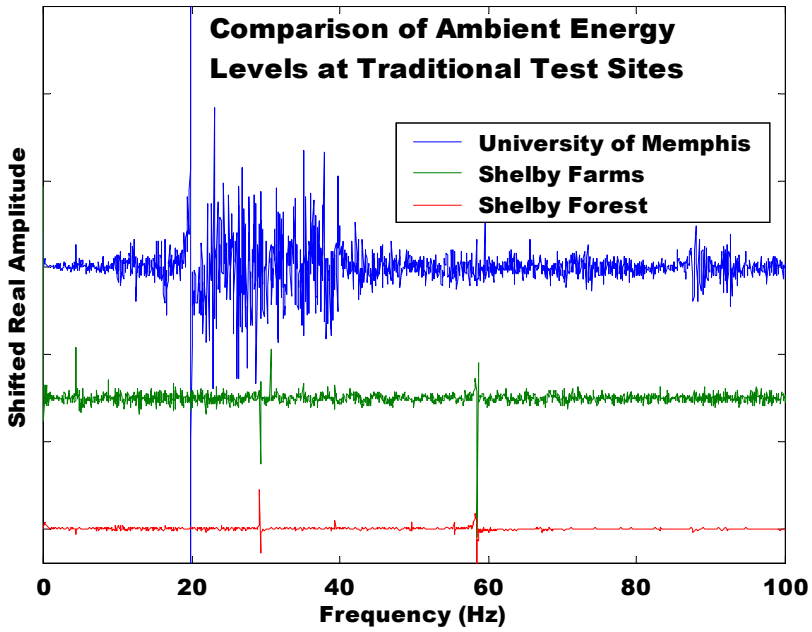

Figure 6.1 Frequency Spectra Depicting the Ambient Noise Levels at Each of the Three Sites Used in the Comparison of Active f-k and Traditional Surface Wave Methods.

Each of the three sites was tested using the same experimental and analysis procedures for both the active f-k and traditional SASW tests. All tests were conducted using the Wilcoxon 731A seismic accelerometers placed at the following distances from the source, (8, 10, 12, 15, 18, 22, 28, 34, 42, 50, 60, 70, 80, 95, 110 ft) for the active f-k method as shown in Equation 4.6. The traditional measurements utilized the f-k receiver positions to maintain similar testing conditions for both methods. The traditional testing used four receiver pairs at the following distances from the source: (8, 15), (15, 34), (28, 60), and (60, 110), providing spatial lags of: 7, 19, 32, and 50 ft respectively. The digital signal analyzer used for the f-k

testing was the HP 1432A 16-channel analyzer described in Chapter 4. While the traditional measurements were taken using an HP 3562A 2-channel analyzer and following the procedures for the cross power spectrum method using a harmonic source and the common source array configuration as outlined in Chapter 3. The receivers were not altered in any way between tests, and the same harmonic source and frequency range were used for both testing methods, allowing for focused comparisons of the two methods. The method developed by Rix (1988) for forming an average dispersion curve from traditional SASW data was used as explained in Chapter 3. This process was utilized when necessary to allow the traditional data to be represented as a single curve, providing more direct comparisons between the two methods. The experimental comparisons are based on the ability of each method to accurately determine the dispersion relationship of each site. Previous V_S results from each of the three sites were presented in Chapter 5, and will be used to demonstrate the accuracy of the dispersion estimates.

6.4 Shelby Forest

The Shelby Forest test site is located within a state park providing very low levels of ambient noise as seen in Figure 6.1. The stratigraphic features are also well known due to the numerous previous V_S measurements taken at this site, presented in Figure 5.28. As such, this site was chosen to allow the improved capabilities of the f-k method to be observed under ideal active surface wave testing conditions. The traditional two-station measurements were performed according to the procedures outlined above. The collected phase data from each of the four sensor spacings is given in Figure 6.2. The sharp well defined trend of the phase records confirms the assumption of limited ambient noise at the secluded Shelby Forest test site. The traditional phase data was used in its entirety except for the small portion of the 50-ft spacing data that shows two adjacent phase wraps. The phase records were analyzed using Equation 2.8 which relates the phase change at a particular frequency and spatial lag to an estimate of apparent wavenumber. This analysis led to the individual dispersion estimates shown in Figure 6.3. The individual dispersion records overlap in some portions of the frequency range as is typical in traditional SASW analysis. The individual curves show large deviations at 20 and 35 Hz, as well as throughout the high-frequency range. The deviations at 20 and 35 Hz are most likely due to the high-velocity features resolved at these points in the analysis of the f-k method presented in Chapter 5. In order to define a single trend to be compared with the f-k dispersion estimate, the individual curves were averaged to form the average curve shown in Figure 6.4.

The f-k phase records are presented in Figure 6.5 and show similar clarity to those determined using the traditional methods. The dispersion estimate determined using the f-k method is shown in Figure 6.6 and shows a fairly regular dispersive trend over the entire range of resolvable frequencies. Figure 6.7 shows an overlay of the f-k dispersion estimate with both the composite and average traditional dispersion curves. While both methods define the same general trend over a wide span of frequencies, the f-k method clearly displays a smoother, more accurate trend. The large variations throughout the traditional estimate only allow the general dispersive trend to be determined and limit the resolvable depth of a subsequent inversion analysis. Both methods were tested over the same frequency range from 4.375 – 100 Hz. However, the f-k method was able to resolve the dispersion relation to f_{min} = 4.375 Hz, while the traditional method was only able to resolve to f_{min} = 8.75 Hz. The added low-frequency resolution of the f-k method increased the maximum resolvable wavelength, λ_{max}, to 52 m from the 25.7 m resolved by the traditional method. This increases the resolution depth of the V_S profile an additional 17.5 m using the criterion given in Equation 5.2. The increase in low-frequency resolution of the f-k method shows the decreased near field interference encountered when using array-based measurements. The large number of receivers and the use of a developed wavefield allow for the resolution of surface wave dispersion closer to the source than typically allowed using traditional techniques (Zywicki, 1999).

The large variability of the traditional estimate over the entire dispersion estimate does not allow for the resolution of any fine layering features based on trends observed in the dispersion estimate. Any variations in the traditional dispersion estimate must be considered to be representative of test errors due to the poor resolution over the entire frequency range. However, the regular trend of the f-k dispersion estimate does allow for the resolution of fine features. This is shown in the resolution of the high-velocity features shown at 12 and 32 Hz in the f-k dispersion estimate. The improved accuracy of the f-k method is further validated by the existence of high-velocity features at the corresponding depths as seen in the previous V_S results shown in Figure 5.28. The above comparison shows that even for a site with ideal testing conditions, the use of the f-k methods provides a significantly more accurate dispersion estimate over a larger range of frequencies. The more accurate f-k estimate allows a deeper and more finely defined V_S profile to be determined. As a result of the limited external influences at the Shelby Forest site, the improved dispersion estimate is directly related to the benefits of array-based testing described above. The added improvements of the f-k procedure regarding the negation of ambient noise will be seen in the remaining two comparisons.

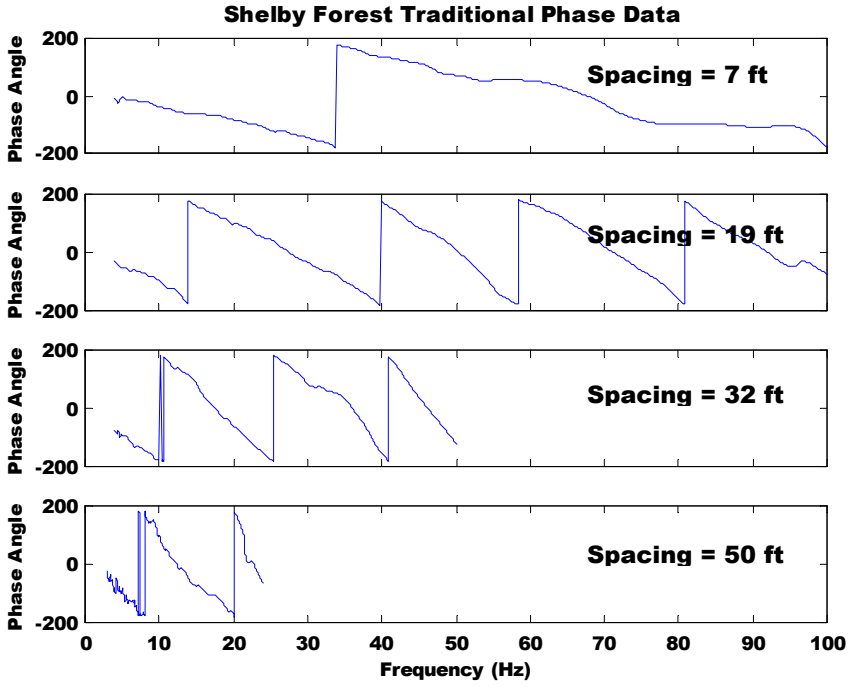

Figure 6.2 Traditional Phase Data From the Shelby Forest Test Site.

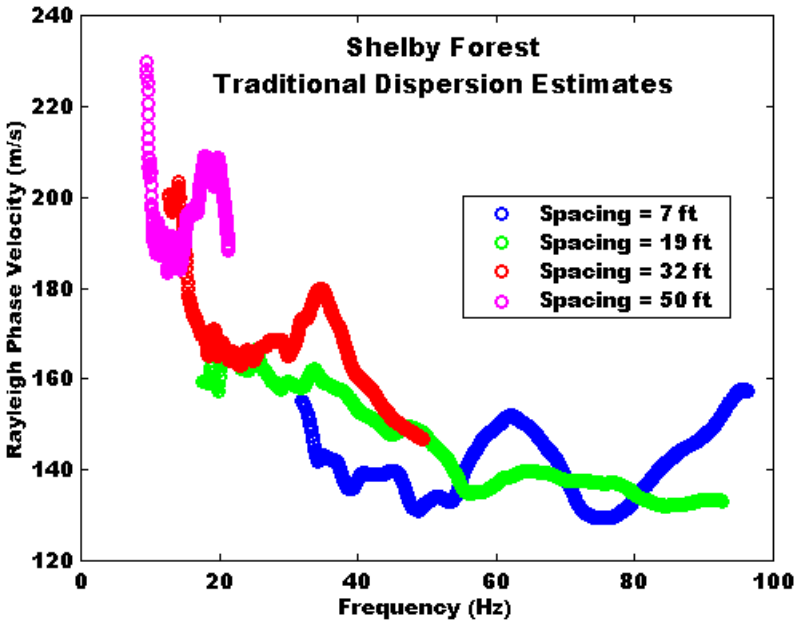

Figure 6.3 Individual Dispersion Estimates From Traditional SASW Testing Conducted at the Shelby Forest Test Site.

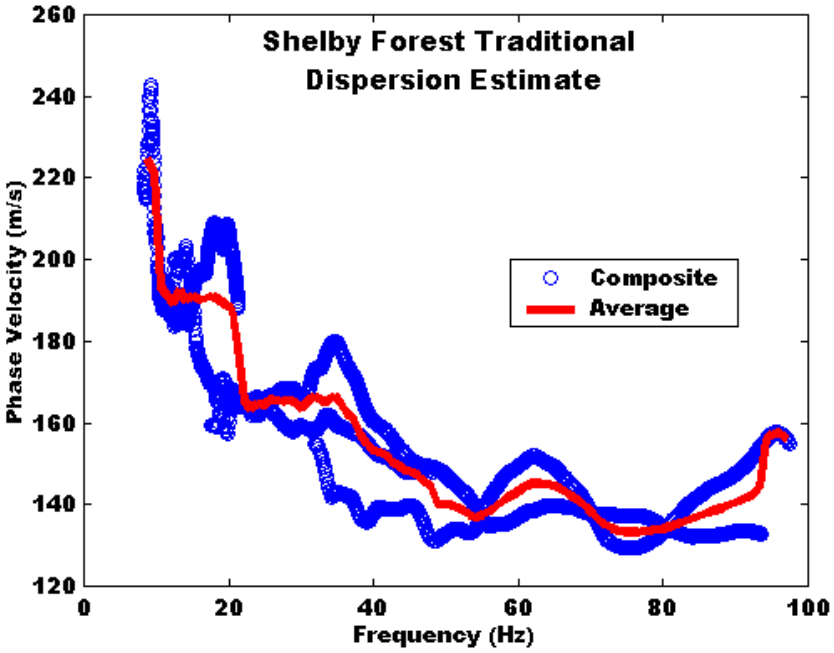

Figure 6.4 Composite and Average Dispersion Estimates From Traditional SASW Testing Conducted at the Shelby Forest Test Site.

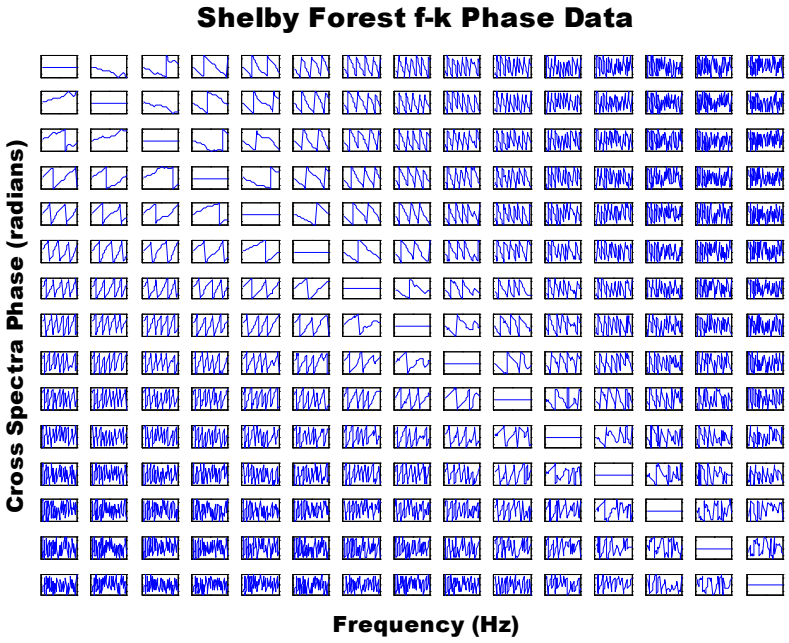

Figure 6.5 F-k Phase Data From the Shelby Forest Test Site.

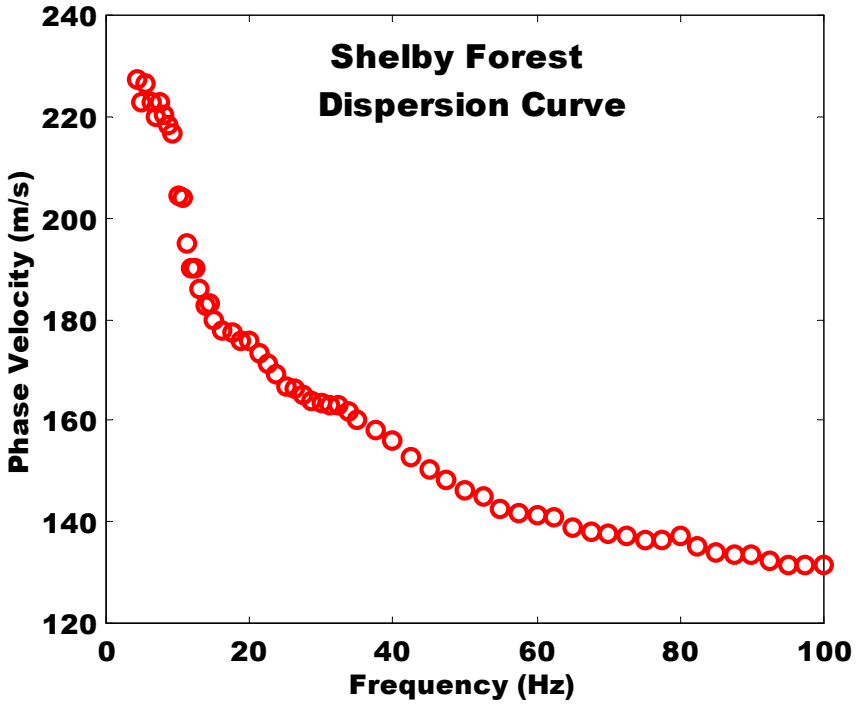

Figure 6.6 Dispersion Estimates From f-k Active Testing Conducted at the Shelby Forest Test Site.

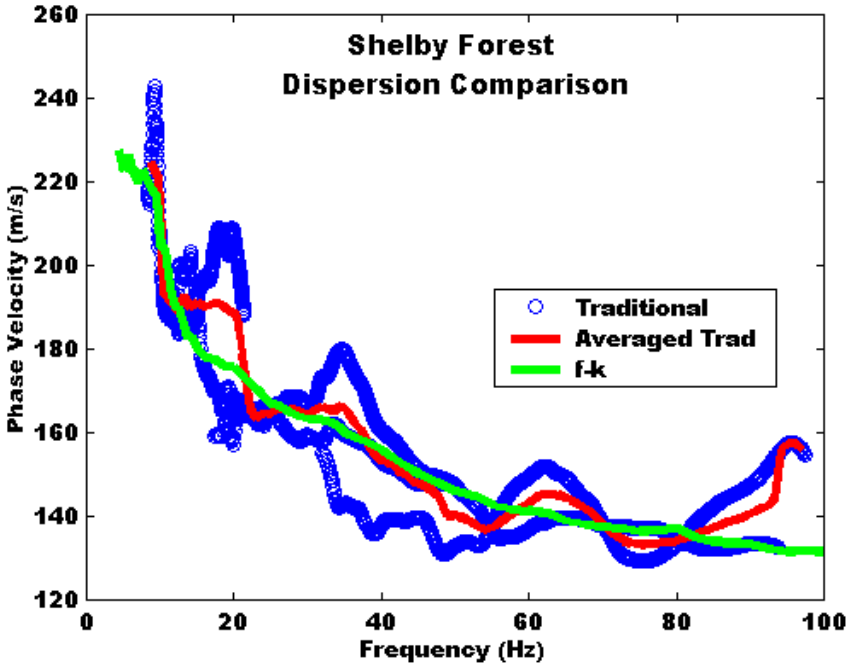

Figure 6.7 Comparison of f-k and Traditional Dispersion Curves For the Shelby Forest Test Site.

6.5 Shelby Farms – Shooting Range

The Shelby Farms Shooting Range site is located within the large Shelby County land preserve known as Shelby Farms. Because the site is still an active shooting range it is located in a secluded section of the preserve. The testing was conducted on a day when the range was not in service; however, there is a major roadway running east to west located approximately 500 m to the north of the Shooting Range. The traffic energy from the roadway resulted in medium levels of ambient noise larger than those found at Shelby Forest, but not at the levels found within highly urbanized areas as seen in Figure 6.1. The traditional SASW testing was conducted as described above for the Shelby Forest site and resulted in the phase estimates shown in Figure 6.8. The phase data is relatively clean except for the slight corruption at high frequencies in the 19-ft spacing and at low frequencies in the 50-ft spacing. Corruption of phase data is defined by large variations in the trend over a short frequency range. Data of this type is not theoretically possible and results from the misestimation or aliasing of the phase over the corrupted frequency range. Individual portions of a phase record can be corrupted without compromising the other portions of the record as each phase point is calculated independently. Manual estimation of corruption is completed and any portions of the phase records deemed corrupted by the testing engineer are not used in the subsequent dispersion analysis.

Dispersion calculations were completed on the uncorrupted portions of the phase data and resulted in the individual dispersion estimates shown in Figure 6.9. The dispersion estimate corresponding to the 7-ft spacing was calculated well below the trend of the other spacings within the frequency range of 30 – 70 Hz. The 7-ft phase record shows slight variations over this frequency range which may have resulted in the low V_R estimates. The individual dispersion estimates again show a large amount of variability over the entire range of resolved frequencies. Averaging the individual dispersion estimates resulted in the average curve shown in Figure 6.10. Traditionally, the average curve may have been further altered around 50 and 70 Hz to allow for a smooth transition at these frequency ranges which represent the transition between the individual dispersion estimates. While further smoothing of the average curve would lead to a more feasible V_S profile, it highlights the increased need to manually interpret both the phase and dispersion data using the traditional procedures.

The f-k data shown in the phase plots of Figure 6.11 and the dispersion estimate of Figure 6.12 also shows some corruption and variability, especially at higher frequencies. The high-frequency variability shown in the dispersion estimates of both methods is partially due to the near-surface soil at the Shooting Range consisting mainly of manmade fill and waste materials. Placed fills are sometimes highly variable over short distances and resulted in the noticeable variability of the high-frequency dispersion estimates of both methods. Figure 6.13 shows the comparison of the traditional and f-k dispersion estimates for this site. The f-k estimate provides a smoother overall curve resolved beyond the traditional estimate to both higher and lower frequencies. The significant increase in low-frequency resolution, relates to an increase in the longest resolved wavelength of $\Delta\lambda = \lambda_{max(f\text{-}k)} - \lambda_{max(trad)}$ = [218.3 (m/s) / 4.375 (Hz)] - [176.6 (m/s) / 10.5 (Hz)] = 49.9 – 16.8 = 33.1 m. The additional low-frequency dispersion data provided through the use of the f-k method allows the V_S profile to be resolved an additional 22 m as per Equation 5.2. The f-k method not only provided more low-frequency dispersion data allowing for deeper V_S estimates, but it also provides a much more accurate dispersion relation over the full range of tested frequencies.

The benefits of the f-k method in the presence of increased external influences are again apparent in the above comparison. The f-k method was able to remove the low-frequency influences of the traffic energy from the nearby roadway through the use of stepped-sine testing and band limited dispersion calculations which calculate each frequency independently. Additionally the simultaneous measurement of the increased number of spatial lags using array-based measurements allowed the f-k method to average the highly variable near-surface data of the Shooting Range site, providing an easily invertable dispersion estimate. Whereas the high-frequency estimate provided with the traditional method would have to be manually altered before it could be used in an automated inversion procedure. Again the higher accuracy and confidence of the f-k dispersion estimate allows for easier inversion and less manual interpretation of the data. The accuracy of the f-k method was shown by the agreement with previous V_S measurements in Figure 5.19.

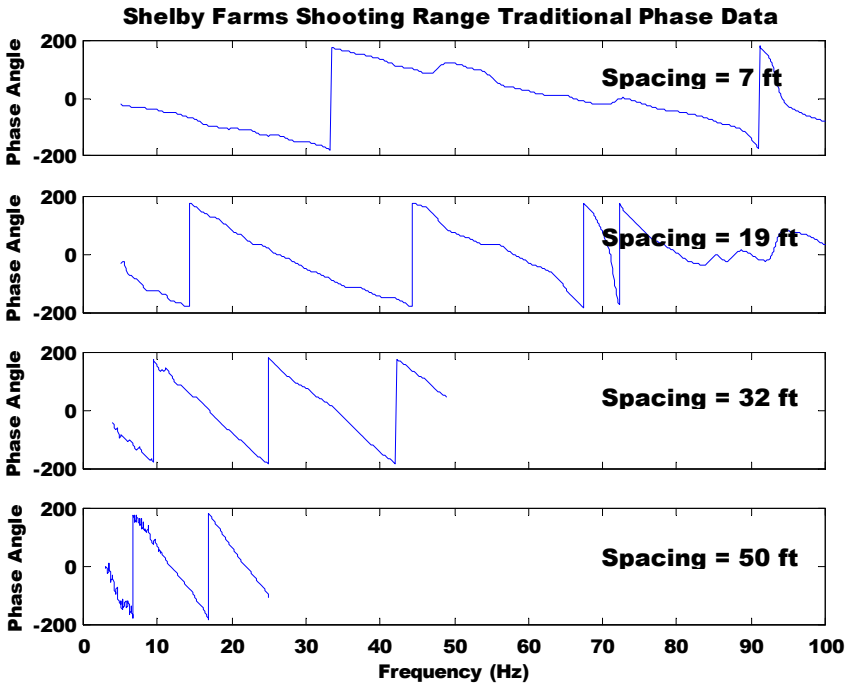

Figure 6.8 Traditional Phase Data From the Shelby Farms Shooting Range Test Site.

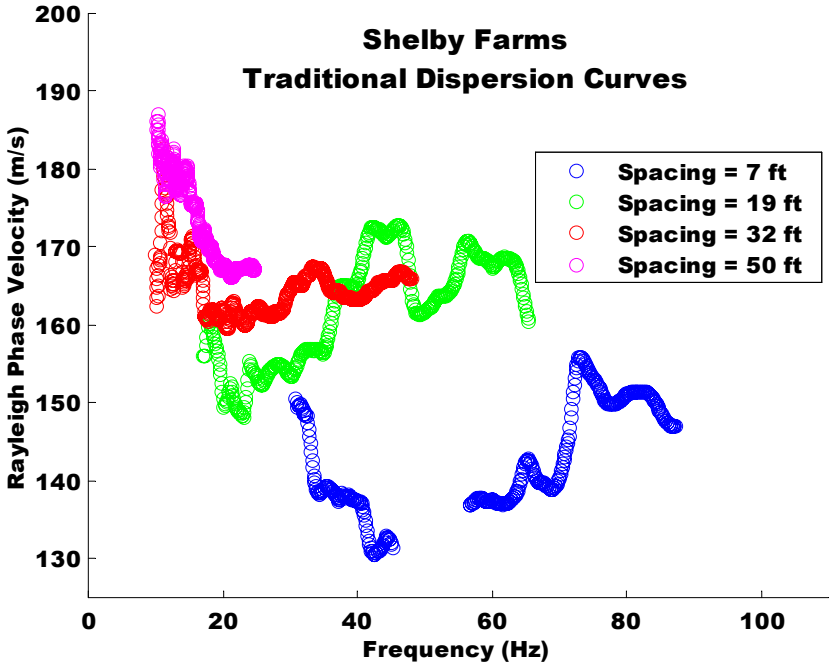

Figure 6.9 Individual Dispersion Estimates From Traditional SASW Testing Conducted at the Shelby Farms Shooting Range Test Site.

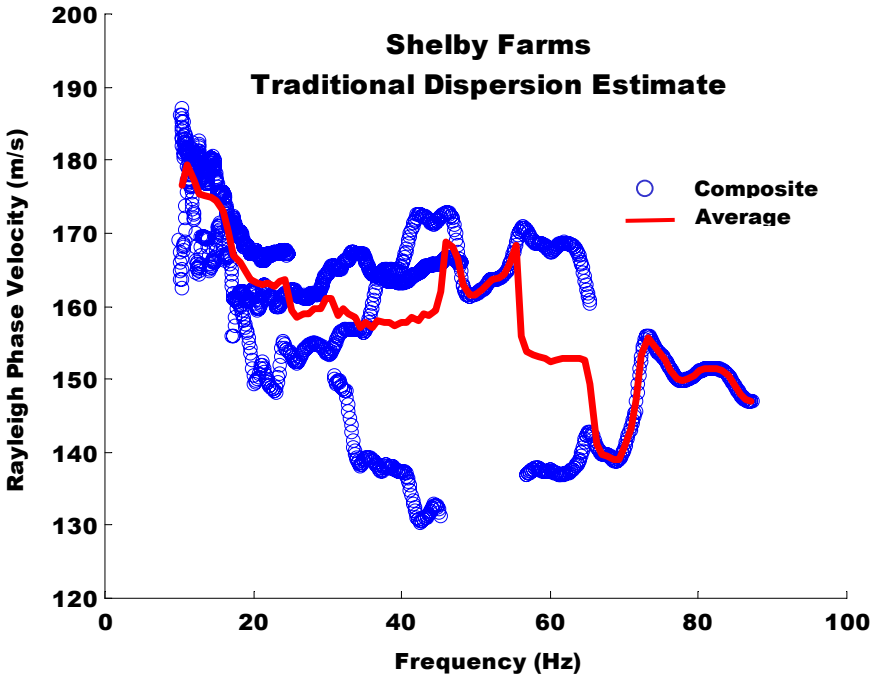

Figure 6.10 Composite and Average Dispersion Estimates From Traditional SASW Testing Conducted at the Shelby Farms Shooting Range Test Site.

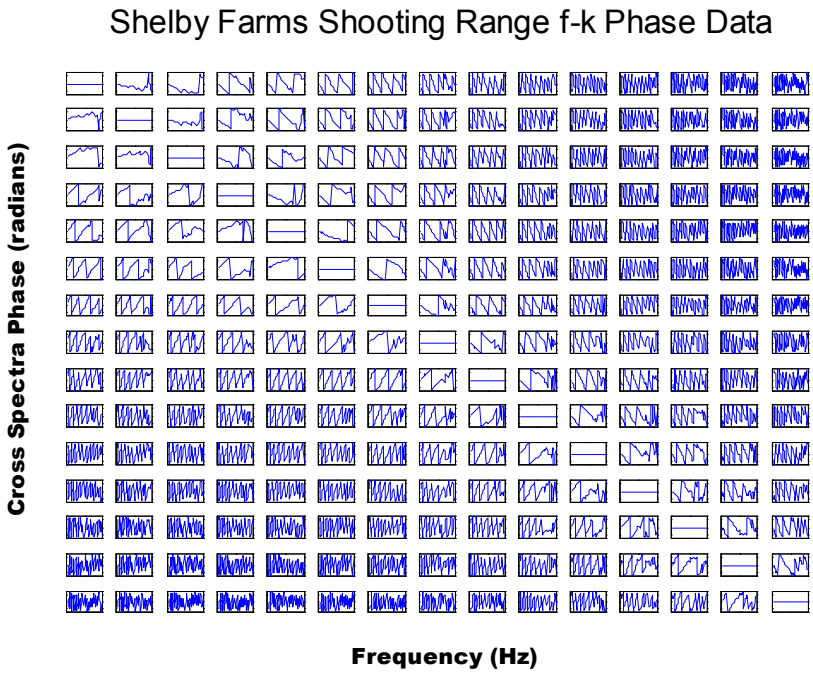

Figure 6.11 F-k Phase Data From the Shelby Farms Shooting Range Test Site.

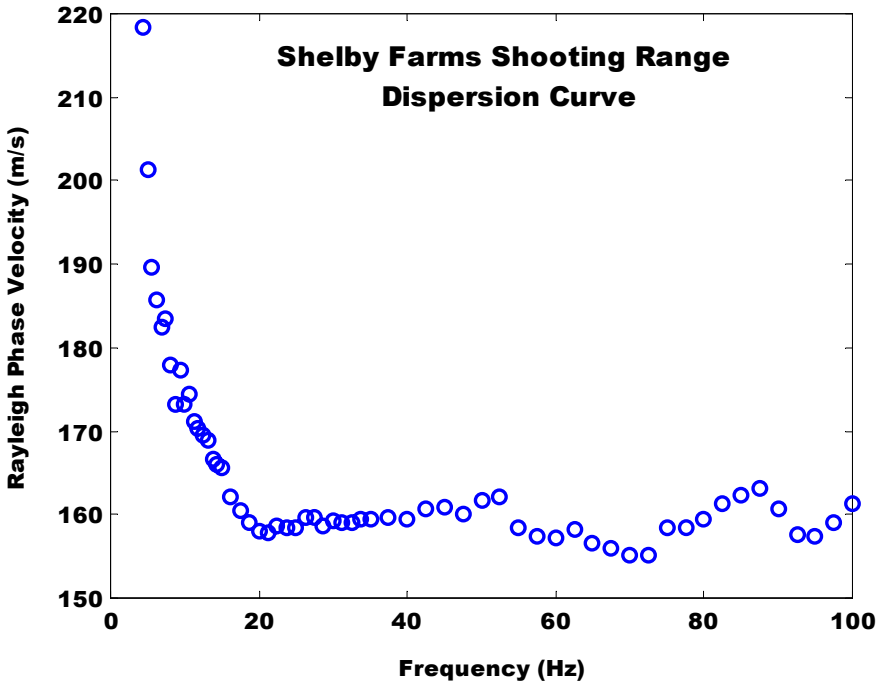

Figure 6.12 Dispersion Estimates From f-k Active Testing Conducted at the Shelby Farms Shooting Range Test Site.

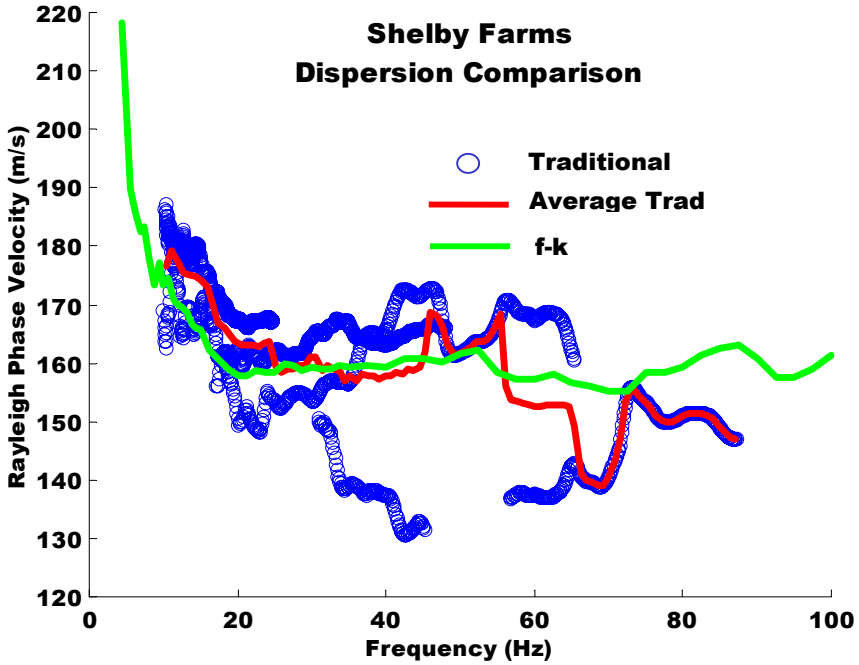

Figure 6.13 Comparison of f-k and Traditional Dispersion Curves For the Shelby Farms Shooting Range Test Site.

University of Memphis

The University of Memphis test site is located within a moderately urbanized area and directly adjacent to a campus roadway and a small operational pumping station. These factors made this site prone to high levels of nonstationary external noise across a large range of frequencies. The roadway provided low-frequency interference, the overhead power lines and the pumping station provided intermediate frequency interference, and the urban location provided additional high-frequency noise to further inhibit the testing conditions. These high levels of ambient noise present in the ground were shown in Figure 6.1, and significantly influenced the traditional phase records as seen in Figure 6.14. The noise levels were sufficient to fully corrupt the data collected at the 50-ft spacing, and resulted in the corruption of the low-frequency data of both the 19- and 32-ft spacings. The portions of the phase data that showed corruption were not used in the dispersion calculations and resulted in the limited range of the individual dispersion estimates seen in Figure 6.15. Because the individual dispersion curves only coincide over a limited number of frequencies they were not averaged to form a single curve as done previously. An investigation of the traditional dispersion data requires the engineer to make some judgements about the quality and interpretation of the data. Either the data from the 32-ft spacing can be entirely ignored as being misestimated, or the data from the shortest two spacings must be considered to be representative of higher modal phenomena. In either case it would be difficult to justify resolving more than an approximate shallow V_S estimate due to the poor quality of the traditional dispersion data.

The f-k data also shows some corruption from the high levels of interfering external noise, as shown in the phase records of Figure 6.16. However, the f-k technique was able to resolve a dispersion estimate over the full range of tested frequencies, as shown in Figure 6.17. The f-k dispersion estimate shows some of the features of the traditional estimate, although it is defined over the entire range of frequencies allowing the higher mode nature of the high-frequency data to be more clearly defined. As was

discussed in Chapter 5, dispersion data representative of higher modes is often resolved as a superposition of several modes and may represent an effective Rayleigh phase velocity. The unknown modal nature of higher mode dispersion data can make their interpretation in subsequent inversion analyses more difficult. In cases such as this one, where the higher mode data apparently skips over several modes, it is often difficult to use an automated inversion analysis, and an iterative forward procedure must be used.

Figure 6.18 shows a comparison of the dispersion curves determined by the two active methods. By overlaying the dispersion estimates of the two methods, it becomes clear that the traditional data representative of the 32 foot spacing is most likely a continuation of the mode depicted by the low-frequency portion of the f-k data. Additionally, the higher mode points from both procedures show fairly good agreement over their coincident range. However, the traditional data by itself, without the added information provided by the f-k data, allows for almost no confident V_S interpretation and the use of such data would be highly subjective to the bias of the testing engineer. Furthermore, the f-k dispersion data shows a consistent trend over the entire range of calculated frequencies, allowing an experienced analyst to accurately determine the near-surface site characteristics. While the f-k method still estimates a complex multi-modal dispersion estimate, it does allow for a justifiable V_S estimate to be made as seen in the procedures outlined in Chapter 5, and the V_S profile shown in Figure 5.35. The comparison at this site, representative of adverse testing conditions, shows the increased capability of the f-k method to limit the effects of external influences. Specifically, this comparison highlights the traditional drawbacks of frequency interdependence and limited noise removal capability, which severely hampered the low-frequency resolution of the traditional procedure.

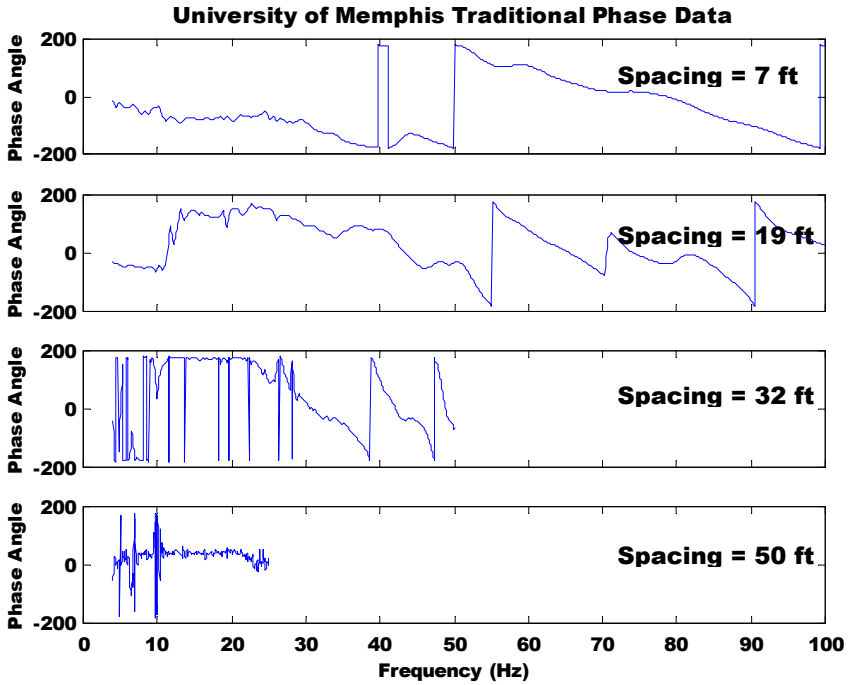

Figure 6.14 Traditional Phase Data From the University of Memphis Test Site.

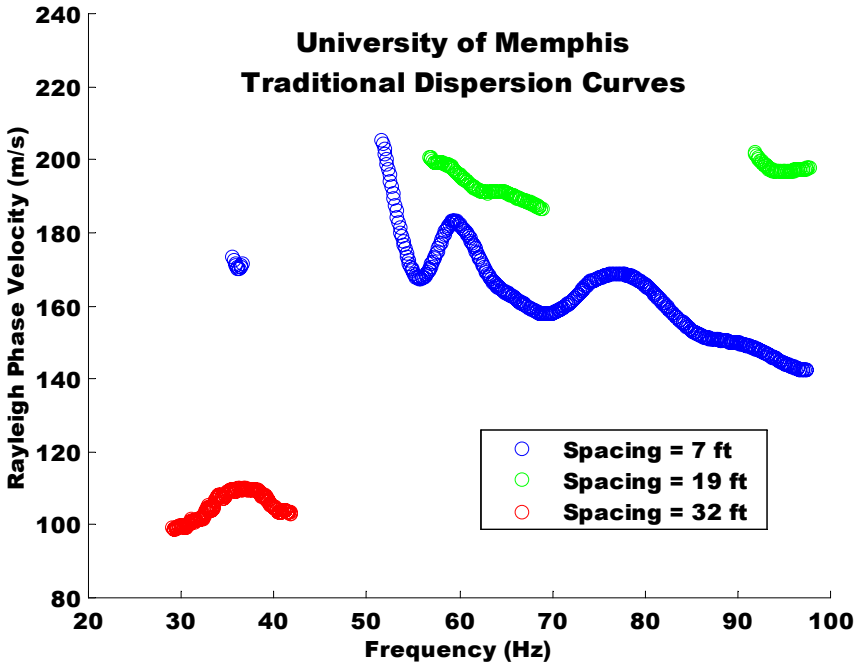

Figure 6.15 Individual Dispersion Estimates From Traditional SASW Testing Conducted at the University of Memphis Test Site.

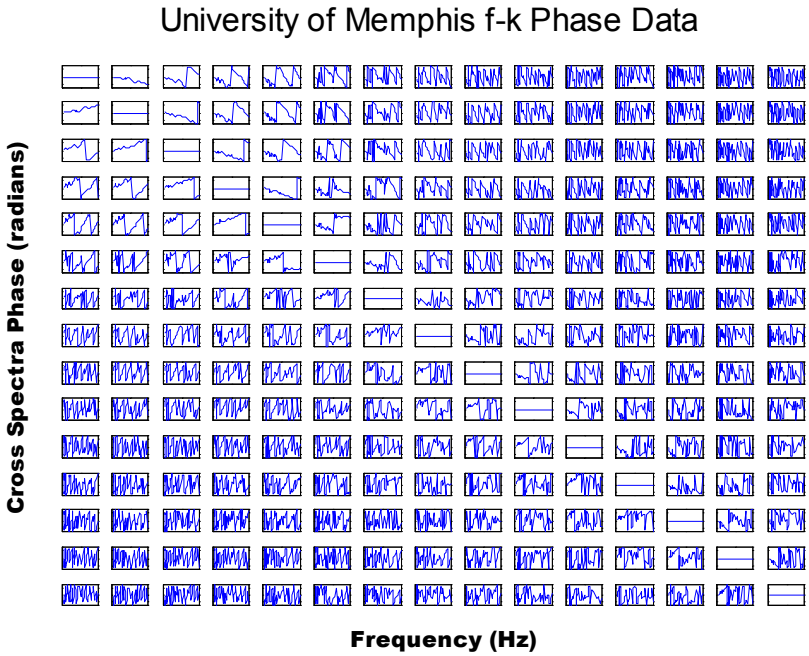

Figure 6.16 Dispersion Estimates From f-k Active Testing Conducted at the University of Memphis Test Site.

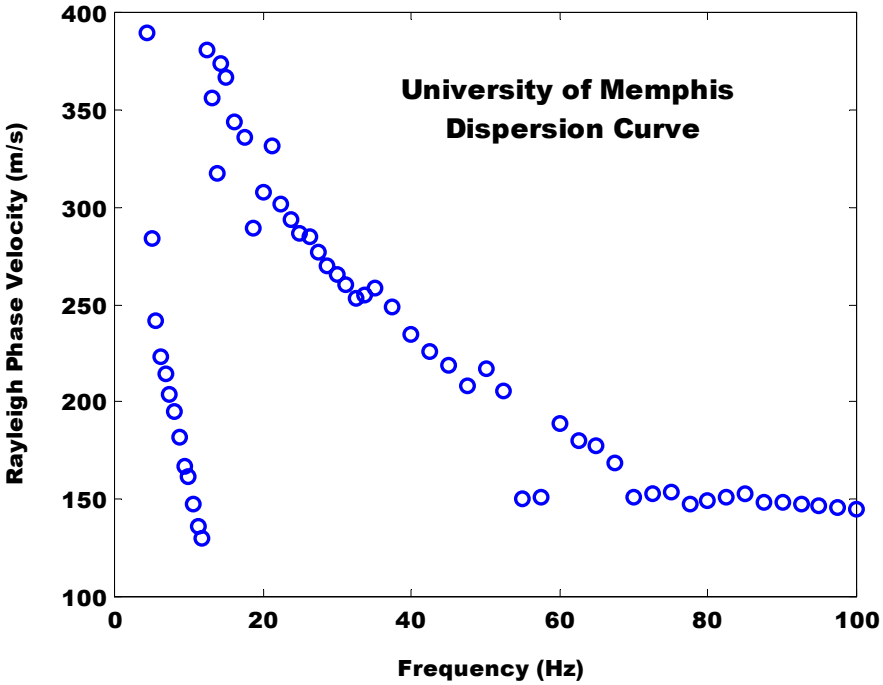

Figure 6.17 F-k Phase Data From the University of Memphis Test Site.

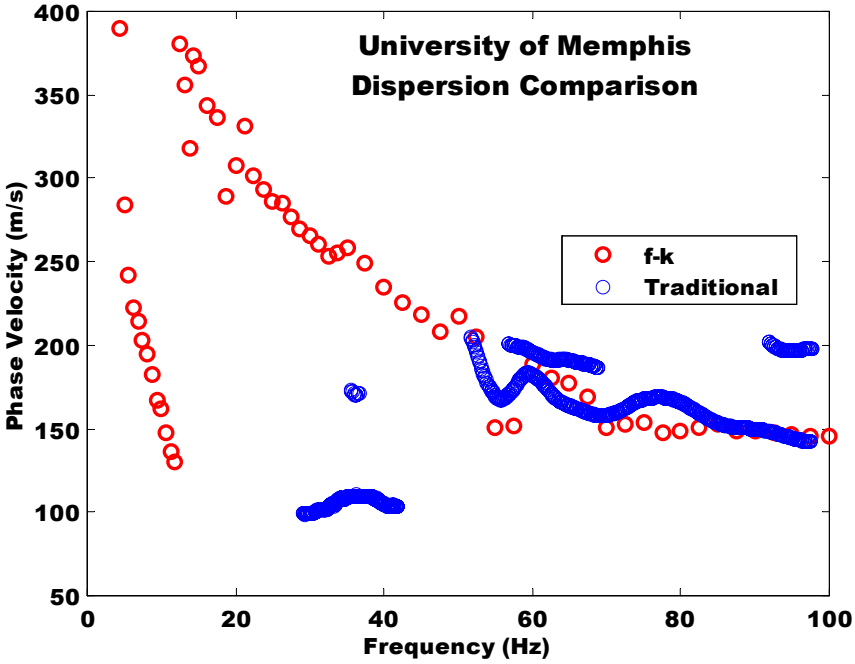

Figure 6.18 Comparison of f-k and Traditional Dispersion Curves For the University of Memphis Test Site.

6.7 Conclusions

The above experimental comparisons show the increased capabilities of the f-k method over traditional SASW procedures. Most notably the f-k dispersion estimates provided smoother dispersion estimates to lower frequencies in all cases. This not only increases the accuracy of any resultant V_S profiles, but also greatly increases the depth to which they can be resolved. Additionally, the current f-k method provides an estimate of the error in the dispersion estimate, as presented in Chapter 5, that allows the accuracy of the dispersion and V_S inversion to be quantified. This is important because it provides a limit to guide the resolution of the V_S profile, which before was left entirely to the discretion of the testing engineer. The decreased variability of the f-k dispersion estimates allows for the justifiable resolution of thin features, and allows the soil stratigraphy to be approximately defined by variations in the dispersion estimate. Additionally, more accurate dispersion estimates eliminate the need for highly experienced personal to manually interpret the dispersion data, providing a testing method more conducive to implementation in professional practice.

Another important improvement is the significant increase in the ability to limit the effects of external influences, mainly ambient noise and spatial variability, on the accuracy and frequency range of the dispersion estimate. The progressive increase in the quality of the f-k dispersion estimates over the traditional estimates as the level of ambient noise increased not only highlights a major drawback of traditional testing, but it also serves to show the broad range of applicable testing conditions serviceable by the f-k method. Traditionally, the applicability of surface based methods has been limited in urban and other areas with high ambient noise levels. The effectiveness of the current procedures in a wide range of testing conditions extends the applicability of surface wave testing by allowing both deeper resolution and testing in the midst of higher ambient noise levels. Additionally, the possible concatenation of active and passive f-k dispersion data as shown in Chapter 5 provides further improvement over traditional surface wave procedures. The use of more receivers, as well as sophisticated digital signal analysis and source equipment make the capital investment necessary to conduct the current f-k testing substantially higher than that of the traditional methods. However, the advantage of obtaining more accurate and inclusive dispersion estimates and the increased flexibility of experimental parameters, including the ability to conduct passive measurements, validates the increased cost of the testing equipment. Overall, the improved capabilities of the current f-k method seen in the above examples serve to validate the use of the current f-k method as not only a viable active surface wave technique, but also a reliable in situ seismic testing method.

Chapter 7

Conclusions and Recommendations

7.1 Summary

Traditional engineering analysis of surface waves suffers from several limitations, restraining the accurate determination of shear wave velocity profiles. This study was aimed at implementing and improving the array-based experimental and dispersion analysis methods for seismic surface wave testing developed by Zywicki (1999) using advanced digital signal and spatial array processing. The current study refined the methods developed by Zywicki by defining experimental testing parameters and procedures to optimize the implementation of active and passive surface wave methods. The improvements developed in the current study include the use of stepped-sine harmonic testing, band-limited dispersion calculations, and the combined use of active and passive methods. The refined methods were evaluated by performing surface wave tests at 11 sites in the Memphis/Shelby County, TN area. The experimental results presented in Chapters 5 and 6 demonstrated the successful implementation of the current procedures, and provide support for the use of the current methods. The improvements of this study were motivated by the need for cost effective and timely methods capable of producing accurate site characterizations for seismic zonation applications in Mid-America. These improvements included the development of improved testing and analytical procedures for use with array-based surface wave methods, and the combination of active and passive dispersion results.

7.2 Conclusions

7.2.1 Array-Based f-k Testing

Traditional engineering surface wave techniques only use two sensors to estimate the wavenumber characteristics of the measured surface wavefield. This is analogous to the impractical estimation of temporal frequency using only two temporal samples. Additionally, the traditional procedure of combining several two-sensor measurements taken at different times introduces time dependant errors into the dispersion estimate. The use of array techniques in the current study allowed for reduced testing times and time dependant errors, allowed dispersion estimates to be resolved from a far greater amount of spatial data, provided better spatial resolution, and improved noise removal capabilities. Frequency-wavenumber analysis procedures allow for the calculation of power across both time and space. This provides an additional dimension of analysis over traditional two-sensor testing, and greatly enhances the ability to resolve Rayleigh wave propagation in the midst of external influences. The improved dispersion estimates determined through the use of the current testing methods, as seen in the comparisons of Chapter 6, are predominantly due to the use of array-based f-k testing and analytical methods. This is substantiated because all of the other testing parameters, including: receiver type, position, and coupling; source type and frequency range; as well as test location and ambient noise level were not altered between tests. Overall the dispersion estimates determined using the array-based methods were less variable, resolved to lower frequencies, better able to resolve multiple modes, and allowed for the resolution of finer features.

7.2.2 Stepped-Sine Harmonic Testing

Most traditional SASW testing has been conducted using impulsive sources which allow for the testing of a large frequency range with a single measurement. However, harmonic sources have been used since the inception of surface wave testing, and their use has been shown to increase the signal to noise ratio (SNR) over traditional impulsive sources, thus providing better dispersion estimates (Rix, 1988; Spang, 1995) As such harmonic sources were used in all of the active testing conducted in this study. Traditional testing using harmonic sources is typically conducted using swept-sine harmonic inputs controlled by a digital signal analyzer with a built in filtering algorithm.

The multi-channel digital signal analyzer used in this study does not provide a built in algorithm to adaptively perform the signal processing over multiple sensors in real-time, limiting the use of swept-sine inputs with array-based techniques. The inability to perform adaptive signal processing over a large number of sensors in real-time necessitates the use of post-measurement signal processing methods. Consequently, in order to fully achieve the increased benefits available using array-based f-k techniques, stepped-sine testing and analysis algorithms were developed and implemented. The use of stepped-sine testing allows for the development of a steady-state wavefield at each frequency. Measuring steady-state wavefields allows post-measurement signal processing and averaging to be implemented into the dispersion calculations.

The current techniques implemented frequency domain averaging and band-limited frequency-domain dispersion calculations. The use of stepped-sine harmonic testing and subsequent band-limited dispersion calculations in the active f-k procedures reduced near-field effects, allowed for improved SNR, permitted flexibility in the post-measurement signal processing, allowed for the complete development of multiple modes allowing for the resolution of more complete dispersion estimates, and greatly reduced the effects of ambient noise and spatial variability through frequency-domain averaging and filtering. Previous array-based measurements conducted without the use of stepped-sine testing and band-limited dispersion calculations were much less successful than the those conducted with the current procedures. Additionally, the high quality of the current experimental results shown in Chapters 5 and 6 demonstrated the effectiveness of the current methods over a wide range of testing conditions.

7.2.3 Active and Passive Combination

This study strove to expand the applicability of surface wave testing by combining active and passive methods to allow for more complete site characterization. The combination of active and passive dispersion estimates was evaluated through the analysis of two test sites. One of the sites, the Shelby Farms Shooting Range site, did not provide enough passive energy at the time of testing to allow for the accurate resolution of a passive dispersion estimate. However, the Mud Island B site provided ample passive energy to accurately resolve the dispersion relation over a range of frequencies. The subsequent concatenation of the active and passive dispersion results from the Mud Island B site was effective in producing a combined dispersion curve representative of a fuller frequency range. The two methods provided similar estimates at overlapping frequencies and necessitated very little manual interpretation to form the combined dispersion estimate. As such, the decreased influence of near-field effects using the f-k active procedures was shown through the agreement of the low-frequency active dispersion data with the passive plane wave dispersion data. Overall the possibilities presented through the combination of active and passive surface wave testing methods are quite encouraging, and offer the possibility of significantly expanding the application of engineering surface wave testing.

7.2.4 Near-Surface Characterization in Memphis / Shelby County, TN

The current study was partially motivated by the need for near-surface site characterization over large spatial areas in Mid-America in order to accurately quantify the effects of a future damaging earthquake in the region. By developing improved and more easily implemented surface wave testing procedures, the near-surface characterization of Mid-America could be more efficiently accomplished. The current experimental testing program displayed the ability of the current methods to accurately characterize the soils in Mid-America. Additionally, the results of the current testing will aid in the seismic zonation of Memphis/Shelby County, TN. Specifically the current testing extended the near-surface site characterization into untested portions of eastern Shelby County, helped to better define the near-surface V_S properties of the densely populated metropolitan Memphis region, and provided a measure of the near-surface V_S properties of northwest Arkansas.

7.3 Recommendations

Through the development and implementation of the current f-k surface wave testing and analytical methods several recommendations have been formulated concerning the choice of experimental testing parameters and areas for future study. The recommendations concerning the implementation of the current procedures were developed through the experiences of the experimental testing program and hopefully serve as a basis for the selection of testing parameters in future implementations of the current methods. The recommendations for future work are presented as possible avenues of research that the author feels will either benefit or extend the applicability and functionality of seismic surface wave testing.

7.3.1 Experimental Testing Parameters

The current experimental parameters were chosen in an effort to provide general site characterization using the current testing equipment. In a post analysis of the testing procedures and results some minor refinements would be made for future tests. Practical constraints limited the active f-k testing to 60 source frequencies using the current sampling parameters. The distribution of frequency data would have been more effective if weighted more heavily towards the low-frequency limits of the active source. In order to achieve more accurate low-frequency resolution without increasing the amount of data collected, the high-frequency dispersion data would be collected at a larger frequency spacing. Additionally, varying the temporal sampling frequency based on the requirements of the source frequency was only minimally used in the current testing and could result in further computational savings, especially at low frequencies.

The passive measurements were conducted at a sampling frequency of 320 Hz to allow for flexibility in the analysis of the results. However, the practical application of passive measurements is often restricted to a low-frequency range and the temporal sampling frequency should be chosen based on more site specific criteria, e.g. the minimum spatial resolution, the maximum frequency present in the passive energy at the site, etc. Additionally, more testing needs to be conducted regarding the combination of active and passive surface wave methods to better define optimum testing and analysis parameters for the efficient combination of dispersion data.

7.3.2 Passive Testing Criteria

The use of passive surface wave methods is inherently restricted in locations with low passive energy content and insufficient spatial testing area. However, there exists no quantitative criteria to quickly evaluate the suitability of a site for conducting passive surface wave measurements. The author

recommends that either a theoretical and/or experiment study be undertaken to formulate standard easily measured criteria for estimating the effectiveness of subsequent passive measurements at a particular location. These criterion would typically include a minimum passive energy content within the frequency range desired, and the specification of optimum temporal and spatial testing parameters based on the characteristics of the observed source(s), e.g. temporal sampling frequency, array geometry, etc.

7.3.3 V_S Profile Determination

The current study used an V_S inversion algorithm originally developed for use with traditional SASW data. The use of a traditional SASW inversion algorithm necessitated the use of a number of manual interpretations in order to accurately invert the V_S profile at a number of the current test sites. While some of the manual interpretations involved the interpretation of complex multi-modal behavior, manual interpretations were also necessary at some sites showing dominant fundamental mode dispersion. Traditional SASW inversion algorithms were designed based on the accuracy of the dispersion estimates from traditional SASW testing. As such, many of the resultant inversion programs incorporate significant smoothing to account for the large variability present within traditional dispersion estimates, as seen in Chapter 6. The higher accuracy of the dispersion estimates produced using the current f-k methods allows for the finer resolution of features than typically available using traditional dispersion estimates. Consequently, the application of a traditional inversion algorithm to the dispersion results of the current study often resulted in the unnecessary smoothing of clearly defined features in the dispersion estimates. This is validated through comparison with previous V_S results as seen in Chapter 5, and the discussion regarding Figure 5.28.

As such, the author feels that the modification of traditional surface wave inversion algorithms to allow for the resolution of finer features would eliminate the need for manual interpretation of dispersion results in most cases, and would facilitate the use of surface wave testing by less experienced personnel. In addition to the refinement of traditional surface wave inversion algorithms to allow for finer V_S resolution, the author believes that the methods currently used for determining the thickness of layers in inverted profiles can be significantly improved. While the selection of layers based on borings, CPT results, or other direct means will still be effective, this information is not available for most sites tested using surface wave techniques. The common procedures currently used to define the layering in cases with no a priori knowledge of the site stratigraphy are extremely arbitrary and are not necessarily based on the dispersion estimate, but rather an estimate of the allowable V_S resolution. The choice of arbitrary layers not based on the trends of the dispersion data is one of the main reasons traditional inversion algorithms are unable to accurately match the fine features resolved in the current dispersion data.

Unfortunately, the non-uniqueness of dispersion estimates makes the simultaneous inversion of both layer thickness and V_S numerically unstable. Additionally, the simultaneous inversion of an entire V_S profile is fundamentally flawed since the estimate of the low-frequency dispersion is dependent on the estimation of higher frequencies. For example, if the high-frequency portion of a theoretical dispersion curve is estimated at a lower V_R than the experimental dispersion data, the remainder of the theoretical dispersion curve will be estimated at a V_R higher than experimentally measured in order to compensate for the misestimation of the low-frequency data. Consequently, the author believes that the formulation of an iterative V_S/layering inversion algorithm would be beneficial. Such an algorithm would resolve portions of the V_S profile starting with the high-frequency data. The algorithm would invert the current portion of the experimental dispersion data within some pre determined error criterion, and then that portion of the profile would be fixed for the remainder of the inversion. The inversion would then continue by analyzing the next lower frequency portion of the curve. This type of procedure would reduce the computation requirements of the algorithm by focusing on smaller portions of the dispersion data, and by eliminating unnecessary iterations that contain poor high-frequency estimates

Appendix A

Matlab Control Scripts

A.1 Frequency-Wavenumber Analysis Script

```
%%%%%%%%% Frequency-Wavenumber - Active Surface Wave Analysis %%%%%%%%%

% This script calculates a dispersion curve using frequency-wavenumber
% (f-k) methods. This version uses previously measured data instead of
% acquiring data as part of this file.

% Define sampling parameters
global blocklength; blocklength = 512;
global numavgs; numavgs = 10;
blocksize = blocklength*numavgs;

% Input the temporal sampling parameters (2.56 = Analyzer aliasing
criterion)
span = 125;
global fs; fs = 2.56*span; %Temporal sampling frequency

% Generate a column vector of time values
delta_t = 1/fs;
time = (0:delta_t:(blocksize-1)*delta_t)';

% Define a maximum velocity used for scaling plots
max_velocity = 3000;

% Set plotting flag (1=Yes; 0=No)
plot_flag = 0;

% Define the receiver positions [x1 y1 ; x2 y2 ; ... ; xn yn]
position = [8 0; 10 0; 12 0; 15 0; 18 0; 22 0; 28 0; 34 0; 42 0;...
50 0; 60 0;70 0; 80 0; 95 0; 110 0];
[numchannel n] = size(position);

% Define the frequencies for stepped-sine testing
frequency = [3.75:0.3125:15 16.25:1.25:35 37.5:2.5:100];

% Loop through the frequencies
for j = 1:length(frequency)   %if mod(frequency(j),0.625) == 0;

   % Show the calculation frequency if plotting is turned off
   if ~plot_flag
      disp(['Frequency = ', num2str(frequency(j)),' Hz ']);
   end
```

```
% Load experimental time histories
filename = strcat('d:\shfst\shfstdata',num2str(j));
load(filename);
% Remove the data corresponding to the sensor monitoring the
% harmonic source
data = data1(:,2:16);

% Plot the time histories
if plot_flag
h1 = figure;
suptitle(['Frequency = ', num2str(frequency(j)),' Hz ']);
for k = 1:numchannel
   subplot(floor((numchannel+1)/2),2,k)
   set(gca,'FontSize',6);
   plot(time,data(:,k));
   ylabel('Amplitude','FontSize',6);
   if k > numchannel-2
      xlabel('Time (sec)','FontSize',6);
   end
   drawnow;
end
end

% Calculate and plot the cross-spectra between each pair of
% receivers
plot_flag = 1;
if plot_flag
   h2 = figure;
   suptitle(['Frequency = ', num2str(frequency(j)),' Hz ']);
end


for m = 1:numchannel
   for n = 1:numchannel

      [P,freq] = csd(data(:,m),data(:,n),blocklength,fs,'linear');
      index = find(freq > 0.99*frequency(j) &...
      freq < 1.01*frequency(j));

      [max_value max_index] = max(P(index));
      % Form the spatiospectral matrix (R)
      R(m,n,j) = P(index(max_index));

      if plot_flag
         subplot(numchannel,numchannel,numchannel*(m-1)+n)
         plot(freq,abs(P),freq(index(max_index))...
         ,abs(P(index(max_index))),'ro');

         set(gca,'FontSize',6,'XLim',[0 max(freq)]);
         if n == 1
            ylabel('Magnitude','FontSize',6);
         end
         if m == numchannel
            xlabel('Frequency (Hz)','FontSize',6);
```

```
            end
            drawnow;
         end
      end
   end

   if plot_flag
      close(h1);
      close(h2);
   end
   end
end

% Plot the cross-spectra phase as a function of excitation frequency
h3 = figure; hold on;
for m = 1:numchannel
   for n = 1:numchannel
      subplot(numchannel,numchannel,numchannel*(m-1)+n)
      plot(frequency,angle(squeeze(R(m,n,:))));
      set(gca,'XLim',[0 max(frequency)],'YLim',...
      [-pi pi],'XTickLabel','','YTickLabel','');

      if n == 1 & m == fix(numchannel/2)
         ylabel('Cross Spectra Phase (radians)','FontSize',12);
      end
      if m == numchannel & n == fix(numchannel/2)
         xlabel('Frequency (Hz)','FontSize',12);
      end
      drawnow;
   end
end

% Calculate and plot the f-k spectrum for a linear array
[P ktrial] = beamformer(position,frequency,R);

% Normalize the f-k spectrum to allow for 3D plotting
% Select the maximum value at each frequency for single point
dispersion estimate
for j = 1:length(frequency)
   Pnorm(:,j) = P(:,j)/max(abs(P(:,j)));
   [max_value,max_index] = max(abs(P(:,j)));
   kmax(j) = ktrial(max_index);
end
vmax = 2*pi*frequency./kmax;

% Plot the 3-D f-k spectra
h4 = figure;
[fr wave] = meshgrid(frequency,ktrial);
contourf(wave,fr,Pnorm);
gray_map = gray(64);
gray_map = gray_map(64:-1:1,:);
colormap(gray_map);
xlabel('Wavenumber (rad/ft)');
ylabel('Frequency (Hz)');
```

```
% Plot the 3-D dispersion curve
h5 = figure;

velocity = 2*pi*fr./wave;
contourf(fr,velocity,Pnorm);
colormap(gray_map);
set(gca,'YLim',[0 max_velocity]);
xlabel('Frequency (Hz)');
ylabel('Phase Velocity (ft/sec)');
```

A.2 Beamformer Analysis-Script

```
%%%%%%%%%%%%%  Frequency Domain Beamformer Analysis  %%%%%%%%%%%%%

% This function uses a precalculated spatiospectral matrix (R) to
% calculate the power in f-k space using the conventional
% 1D frequency domain beamforming technique
% (This program is used in conjunction with "fkanalysis"

function [P,ktrial] = beamformer(position,frequency,R)

% Define the number of trial values of wavenumber
numk = 1024;

% Assign the x coordinates of position to a local vector
x = position(:,1);

% Define the maximum wavenumber to avoid spatial aliasing
kalias = pi./min(abs(diff(x)));

% Define a vector of trial wavenumbers
ktrial = linspace(0,kalias,numk);

% Calculate the f-k spectrum (e) = steering vector, (P) = power
for j = 1:length(frequency)
   for k = 1:numk
      e = (exp(i*ktrial(k)*x));
      P(k,j) = (e'*R(:,:,j)*e);
   end
end
```

A.3 Two-Dimensional Beamformer Analysis-Script

```
%%%%%%%%%%%%  2D Frequency Domain Beamformer Analysis  %%%%%%%%%%%%

% This function uses a precalculated spatiospectral matrix (R) to
% calculate the power in f-k space using the conventional
% 2D frequency domain beamforming technique
% (This program is used in conjunction with "Rpest")

function [P,ktrialx,ktrialy] = beamformer2D(position,frequency,R)

% Define the number of trial values of wavenumber
numk = 256;

% Assign the x coordinates of position to a local vector
x = position(:,1);
y = position(:,2);

% Define the maximum wavenumber to avoid spatial aliasing
kaliasx = pi./min(abs(diff(x)));
kaliasy = pi./min(abs(diff(y)));

% Define a vector of trial wavenumbers
ktrialx = linspace(-kaliasx,kaliasx,numk);
ktrialy = linspace(-kaliasy,kaliasy,numk);

% Calculate the f-k spectrum (e) = steering vector, (P) = power
for j = 1:length(frequency)
   for kx = 1:numk
      for ky = 1:numk
         e = (exp(i*[ktrialx(kx) ktrialy(ky)]*position'));
         P(kx,ky,1) = (e*R(:,:,j)*e');
      end
   end
   [kxval kxind] = max(P(:,:,1));
   [kyval kyind] = max(kxval);
   kx1 = ktrialx(kxind(kyind));
   ky1 = ktrialy(kyind);
   k(j) = sqrt(kx1^2 + ky1^2);
   vel(j) = frequency(j)*2*pi/k(j)
end
% Only keeps the value of maximum power at each frequency to conserve
% memory. To obtain full f-k spectral plots solve for each frequency
% individually or if resources allow replace P(_,_,1) with P(_,_,j)

figure;
% Plot the dispersion curve in f-k space
plot(frequency,k,'o');

figure;
% Plot the dispersion curve in f-v space
plot(frequency,vel,'o');
```

A.4 Spatiospectral Matrix Calculation Script

```
function [R,freq,DATA] = rpest(data,fs,B,BL,N,W)
%Rpest - Estimate R(omega) from N channels of temporal data
%   Rpest estimates the spatiospectral correlation from N
%   channels of temporal data, collected at sampling frequency
%   fs.
%
%   Input:
%   data = matrix of experimetal temporal data, in the format
%          of column vectors for each channel, i.e.
%          [ (channel 1)  (channel 2) ... (channel N) ].
%   fs = sampling frequnecy used during acquisition
%   B = number of blocks to average in R(omega) estimate
%   BL = block length of each block B (in number of samples)
%   N = number of sensors/channels conatined in data
%   W = vector of sensor specific calibrations (form as a
%       column vector of length N)
%
%   Output:
%   R = spatiospectral correlation matrix estimate with shape
%       ( N x N x length(freq) )
%   freq = vector of temporal frequecies clacluated from
%          processing characteristics
%
%   Example:
%   10240 temporal samples have been collected with 16 channels
%   at a fs = 256 Hz.  An example input to Rpest is
%   [R,freq] = rpest(data,256,20,512,16,W) where the temporal
%   measurements for each sensor are in the columns of data and
%   W must be loaded into memory manually or from another file.

% Author: Daren J. Zywicki, 11/1/99
% Copyright (c) 1999


global num;

data1 = data(1:B*BL,:);
data2 = reshape(data1,BL,B,N);
data2 = data2-repmat(mean(data2),[BL 1 1 ]);
DATA = fft(data2,2*length(data2));
freq = (0:(length(DATA)-1)).*fs./(length(DATA));
for lll = 1:length(freq);
   Rsum = zeros(N);
   for nn = 1:B;
      Ra = squeeze(DATA(lll,nn,:))*squeeze(DATA(lll,nn,:))';
      Rsum = Rsum + Ra;
   end;
   WeightingMatrix = W*W';
   R(:,:,lll) = (W*W').*(Rsum./B);
   lll
end;
```

References

Aki, K. and Richards, P.G., (1980), *Quantitative Seismology, Theory and Methods*, Vol. 1 W.H. Freeman & Co., New York.

Anderson, J.G., Lee, Y., Zeng, Y., and Day, S. (1996), "Control of Strong Motion by the Upper 30 Meters", *Bulletin of the Seismological Society of America*, Vol. 86, No. 6, pp. 1749-1759, December 1996.

Achenbach, J.D. (1984) *Wave Propagation in Elastic Solids*. North-Holland, Amsterdam, Netherlands, pp. 425.

Bodin, P. (1999) Personal Communication, (Center for Earthquake Research Institute).

Borcherdt, R.D. (1994), "Estimates of Site-Dependent Response Spectra for Design (Methodology and Justification)", *Earthquake Spectra*, Vol. 10, No. 4, pp. 617-653.

Brekhovskikh, L.M. (1960) *Waves in Layered Media*. Academic Press, New York, NY.

Casey, T. J. (1999), "*Shear Wave Data Collection in Mid-America Using an Automated Surface Source During Seismic Cone Testing*." Master's Thesis, School of Civil and Environmental Engineering, Georgia Institute of Technology, Atlanta, GA, December, 212 pp.

Casey, T.J., McGillivray, A.V., and Mayne, P.W. (1999), *Results of Seismic Peizocone Penetration Tests Performed in Memphis, Tennessee*, GTRC Project E-20-E87.

Clarke, (2000) Personal Communication, (Mid-America Earthquake Center).

Clay, F. (1986) *A Century on the Mississippi, A History of the Memphis District, U.S. Army Corps of Engineers (1871-1981)*, U.S. Army Corps of Engineers – Memphis District, June.

Constable, S.C., Parker, R.L., and Constable, C.G. (1987) "Occam's Inversion: A Practical Algorithm for Generating Smooth Models from Electromagnetic Sounding Data." *Geophysics*, Vol. 52, pp. 289-300.

Cramer, C. (2000) Personal Communication, (Center for Earthquake Research Institute).

Ewing, W.M., Jardetzky, W.S., and Press, F. (1957) *Elastic Waves in Layered Media*, McGraw-Hill, New York, NY.

Graff, K.F. (1975) *Wave Motion in Elastic Solids*, Dover Publications, Inc., New York, pp. 649.

Gucunski, N. and Woods, R.D. (1992) "Numerical Simulation of the SASW test." *Soil Dynamics and Earthquake Engineering,* Vol. 11, pp. 213-227.

Foti, S. (2000) "Multistation Methods for Geotechnical Characterization using Surface Waves." Ph.D. Dissertation, Politecnico di Torino.

Haskell, N.H. (1953), "The Dispersion of Surface Waves in Multilayered Media." *Bulletin of the Seismological Society of America*, Vol. 43, pp. 17-34.

Hayes, M.H. (1996) *Statistical Digital Signal Processing and Modeling*, John wiley and Sons, Inc., 608 pp.

Heisey, J.S., Stokoe, K.H., Hudson, W.R., and Meyer, A.H. (1982) 'Determination of In Situ Shear Wave Velocities from Spectral-Analysis-of-Surface-Waves." *Research Report No. 256-2,* Center for Transportation Research, The University of Texas at Austin.

Horike, M. (1985) "Inversion of Phase Velocity of Long-Period Microtremors to the S-Wave Velocity Structure Down to the Basement in Urbanized Areas", *Journal of Phys. Earth*, Vol. 33, pp. 59-96.

Heukelom, W., and Foster, C.R. (1960) "Dynamic Testing of Pavements." Journal of the Soil and Foundations Division, ASCE, Vol. 86, No. SM1, pp. 1-28.

Ishihara (1996) *Soil Behavior in Earthquake Geotechnics*. Oxford University Press, Inc., New York, NY, pp. 350.

Jacob, K.H. (1991), "Seismic Zonation and Site Response: Are Building Code Soil-Factors Adequate to Account for Variability of Site Conditions Across the US?" *Proceedings, 4th International Conference on Microzonation*, Earthquake Engineering Research Institute, Stanford University, Palo Alto, California, Vol. 1, pp. 695-702.

Joh, S.H., (1996) "Advances in the Data Interpretation Technique for Spectral-Analysis-of-Surface-Waves (SASW) Measurements." Ph.D. Dissertation, The University of Texas at Austin, pp. 241.

Johnson, D.H., and Dudgeon, D.E. (1993) *Array Signal Processing – Concepts and Techniques*, PTR Prentice Hall, Inc., pp. 533.

Johnston, A.C., and Nava, S.J. (1985) "Recurrence Rates and Probability Estimates for the New Madrid Seismic Zone." *Journal of Geophysical Research*, Vol. 90, pp. 9737-6753.

Johnston, A.C., and Kanter, L.R. (1990) "Earthquakes in Stable Continental Crust." *Scientific American*, Vol. 262, p. 68-75.

Johnston, A.C. (1996) "Seismic Moment Assessment of stable Continental Earthquakes, Part III: 1811-1812 New Madrid, 1886 Charleston and 1755 Lisbon." *Geophysical Journal International*, Vol 126, pp. 314-344.

Johnston, A.C., Schwieg, E.S. (1996) "The Enigma of the New Madrid Earthquakes of 1811-1812," *Annual Review of Earth and Planetary Sciences*, Vol. 24, pp. 339-384.

Jones, R. (1962) "Surface Wave Technique for Measuring the Elastic Properties and Thicknesses of Roads: Theoretical Development." *British Journal of Applied Physics*, Vol 13.

Jongmans, D. and Demanet, D. (1993) "The Importance of Surface Waves in Vibration Study and the use of Rayleigh Waves for Estimating the Dynamic Characteristics of Soils." *Engineering Geology*, Vol. 34, pp. 105-113.

Kennett, B.L.N. (1983) *Seismic Wave Propagation In Stratified Media*, Cambridge University Press, 342 pp.

Knopoff, L. (1952) "On Rayleigh Wave Velocities" *Bulletin of the Seismological Society of America*, Vol 42, pp. 307-308.

Kramer, S.L. (1996), *Geotechnical Earthquake Engineering*, Prentice Hall, Upper Saddle River, NJ, 653 pp.

Lai, C.G. (1998) "Simultaneous Inversion of Rayleigh Phase Velocity and Attenuation for Near-Surface Site Characterization" Ph.D. Dissertation, Georgia Institute of Technology, pp. 370.

Liu, H.P., Hu, Y., Dorman, R., Chang, T.S., and Chiu, J.M. (1997), "Upper Mississippi Embayment Shallow Seismic Velocities Measured In Situ." *Engineering Geology*, Vol. 46, pp. 313-330.

Mayne, P.W., Liao, T., Zavala, G. Camp, B., and McGillivray, A.V. (2000a), *Results of Seismic Piezocone Penetration Tests Performed in Memphis, Tennessee*, GTRC Projects E-20-F47/F34.

Mayne, P.W. et al. (2000b), Seismic CPT Soundings at Wolf River in Memphis, Tennessee (July 2000), http://www.ce.gatech.edu/~geosys/Faculty/Mayne/Research/summer2000/wolf/wolf.htm.

Mayne, P.W. (2000c), USGS-CERI Memphis-Shelby County Seismic Hazard mapping Project: Site Response Data, http://www.ceri.memphis.edu/usgs/hazmap_old/geotech/index.html.

Mayne P.W. et al. (2000) Personal Communication, July, (Georgia Institute of Technology).

Nazarian, S. (1984) "In Situ Determination of Elastic Moduli of Soil Deposits and Pavement Systems by Spectral Analysis of Surface Waves Method." Ph.D. Dissertation, The University of Texas at Austin.

Nazarian, S. and Stokoe, K.H. II, (1984) "Use of Surface Waves in Pavement Evaluation." *Transportation Research Record*, Vol. 1070, pp. 132-144.

NEHRP Recommended Provisions for the Development of Seismic Regulations for New Buildings, Part 1 – Provisions (1997), Prepared by Building Seismic Safety Council for the Federal Emergency Management Agency, Washington, D.C.

Oppenheim, A.V. and Schafer, R.W. (1989) *Discrete-Time Signal Processing*, Prentice Hall, Inc., pp. 879.

Park, C.B., Miller, R.D., and Xia, J. (1999) "Multimodal Analysis of High Frequency Surface Waves." *The Symposium on the Application of Geophysics to Engineering and Environmental Problems*, Conference Proceedings, March 14-18, Oakland, CA, 115-121.

Purser, J.L. and Van Arsdale, R.B. (1998), "Structure of the Lake County Uplift: New Madrid Seismic Zone." *Bulletin of the Seismological Society of America*, Vol. 88, No. 5, pp. 1204-1211.

Rayleigh, Third Baron (Strutt, John William) (1885), "On Waves Propagated Along the Plane Surface of an Elastic Solid," *Proceedings of the London Mathematical Society*, Vol. 17, pp. 4-11.

Richart, F.E Jr., Hall, J.R. Jr., and Woods, R.D. (1970) *Vibrations of Soils and Foundations*, Prentice Hall, Inc., New Jersey.

Rix, G.J. (1988) "Experimental Analysis of Factors Affecting the Spectral-Analysis-of-Surface-Waves Method." Ph.D. Dissertation, The University of Texas at Austin, pp. 315.

Rix, G.J., and Lai, C.G. (1998) "Simultaneous Inversion of Surface Wave Velocity and Attenuation" Geotechnical Site Characterization, Edited by P.K. Robertson and P.W. Mayne, Vol., 1, pp. 503-508, *Proceedings of the First International Conference on Site Characterization* – ISC '98, Atlanta, Georgia, 19-22 April.

Rix, G. J., C. G. Lai, S. Foti, and D. Zywicki (1998) "Surface Wave Tests in Landfills and Embankments," *Geotechnical Earthquake Engineering and Soil Dynamics III*, ASCE Geotechnical Special Publication No. 75, Dakoulas, P., Yegian, M., and Holtz, R.D., Eds., pp. 1008-1019.

Rix, G.J., Lai, C.G., and Spang, A.W. Jr. (2000) "In Situ Measurement of Damping Ratio Using Surface Waves." Journal of Geotechnical and Geoenvironmental Engineering, Vol. 126, No. 5, pp. 472-480.

Rix, G.J. (2000) Site Characterization Using Surface Waves. Short Course Notes.

Roësset, J.M., Chang, D.-W., and Stokoe, K.H. II (1991) "Comparison of 2-D and 3-D Models for Analysis of Surface Wave Tests." *Proceedings of the 5th International Conference on Soil Dynamics and Earthquake Engineering*, pp. 111-126.

Romero, S., and Rix, G.J. (2000) "Recommended Reference Profile for Memphis, Tennessee, http://mae.ce.uiuc.edu/Research/GT-1/Obsolete/RRP.htm

Romero, S. and Rix, G.J. (2001), "Regional Variations in Near Surface Shear Wave Velocity in the Greater Memphis Area", *Engineering Geology* – Special Volume on Seismic Hazard Mapping Issues in the Central U.S., Accepted for Publication.

Romero, S. (2001) "Seismic Zonation of Soils Susceptible to Ground Motion Amplification." Ph.D. Dissertation, Georgia Institute of Technology.

Sànchez-Salinero, I. (1987) "Analytical Investigation of Seismic Methods Used for Engineering Applications." Ph.D. Dissertation, The University of Texas at Austin, pp. 401.

Schneider, J.A. (1999), *Liquefaction Response of Mid-America Soils Evaluated by Seismic Cone Tests*, Master's Thesis, School of Civil and Environmental Engineering, Georgia Institute of Technology, Atlanta, GA, August, 273 pp.

Schwab, F., and Knopoff, L. (1972) "Fast Surface Wave and Free Mode Computations." *Methods of Computational Physics*, Vol. 11, Ed. Bolt, B.A., Academic Press, New York , NY pp. 87-180.

Seed, H.B., Romo, M.R., Sun, J.I., Jaime, A., and Lsymer, J. (1988), "The Mexico Earthquake of September 19, 1985 – Relationships between Soil Conditions and Earthquake Ground Motions." *Earthquake Spectra*, Vol. 4, No. 4, PP. 687-729.

Seed, R.B., Dickenson, S.E., Rimer, M.F., Bray, J.D., Sitar, N., Mitchell, J.K., Idriss, I.M., Kayen, R.E. Kropp, A., Harder, L.F. Jr., and Power, M.S. (1990), *Preliminary Report on the Principal Geotechnical Aspects of the October 17, 1989 Loma Prieta Earthquake*, UCB/EERC-90/05.

Silva, W. J. (1988) "Soil Response to Earthquake Ground Motion." *EPRI Report NP-5747*, Electric Power Research Institute, Palo Alto, CA.

Spang, A.W., (1995) "In Situ Measurements of Damping Ratio Using Surface Waves, Master's Thesis, School of Civil and Environmental Engineering, Georgia Institute of Technology, Atlanta, GA, September.

Stokoe, K.H. II, Wright, S.G., Bay, J.A., and Roësset, J.M. (1994), "Characterization of Geotechnical Sites by SASW Method" in Geophysical Characterization of Sites, Edited R. D. Woods, International Science Publisher, New Hampshire

Stover, C.W. and Coffman, J.L., (1993), "Seismicity of the United States, 1568-1989 (Revised)", United States Geological Survey Professional Paper # 1527, US Government Printing Office, Washington, DC.

Street, R., and Nuttli, O. (1984) "The Central Mississippi Valley Earthquakes of 1811-1812," in *Proceedings of the Symposium on "The New Madrid Seismic Zone*," U.S. Geological Survey Open-File Report 84-770, p. 33-63.

Street, R. (1999), "Shear Wave Velocities of the Post-Paleozoic Sediments in the Memphis, Tennessee, Metropolitan Area" Final Technical Report U.S. Geological Survey National Earthquake Hazards Reduction Program, Award Number 1434-HQ-98-GR-0014, US Government Printing Office, Washington, DC, August 15.

Street, R. (2000), USGS-DERI Memphis-Shelby County Seismic Hazard mapping Project: Site Response Data, http://www.ceri.memphis.edu/usgs/hazmap_old/geotech/index.html.

Thomson, W.T. (1950), "Transmission of Elastic Waves Through a Stratified Solid," *Journal of Applied Physics*, Vol. 21, pp. 89-93.

Tokimatsu, K. Tamura, S., and Kojima, H. (1992a) "Effects of Multiple Modes on Rayleigh Wave Dispersion." *Journal of Geotechnical Engineering*, Vol. 118, No. 10, October, pp. 1529-1543.

Tokimatsu, K. Shinzawa, K., and Kuwayama, S. (1992b) "Use of Short Period Microtremors for V_S Profiling." *Journal of Geotechnical Engineering*, Vol. 118, No. 10, October, pp. 1544-1558.

Tokimatsu, K. (1995) "Geotechnical Site Characterization Using Surface Waves." *Proceedings, First International Conference on Earthquake Geotechnical Engineering IS-Tokyo '95*, Tokyo, Balkema, Rotterdam, pp. 1333-1368.

Tuttle, M.P. (1999) "Late Holocene Earthquakes and their Implications for Earthquake Potential of the New Madrid Seismic Zone, Central United States." Ph.D. Dissertation, University of Maryland, College Park, 250 pp.

Van Arsdale, R.B. (2000) Personal Communication, December, (University of Memphis).

Van Arsdale, R.B. and TenBrink, R.B. (2000) "Late Cretaceous and Cenezoic Geology of the New Madrid Seismic Zone." *Bulletin of the Seismological Society of America*, Vol. 90, No. 2, pp. 345-356, April.

Viktorov, I. (1967) *Rayleigh and Lamb Waves: Physical Theory and Applications*, Plenum Press, New York, NY.

Vucetic, M.L., and Dobry, R. (1991) "The effects of soils plasticity on cyclic response." *Journal of Geotechnical Engineering*, Vol. 117, No. 1, ASCE, pp. 898-907.

Williams, R.A., Odum, J.K., Stephenson, W.J., and Worley, D.M. (1999a), "Surface Seismic-Reflection/Refraction Measurements of P- and S-Wave Velocities in the Memphis, TN, region." *Seismological Research Letters*, V. 71, No. 1, p. 113.

Williams, R.A., Stephenson, W.J., Odum, J.K., and Worley, D.M. (1999b), "Comparison of P- and S-Wave Velocity Profiles From Surface Seismic-Reflection/Refraction and Downhole Data." *Seimological Research Letters*, V. 71, No. 1, p. 126.

Williams, R. (2000a), USGS-DERI Memphis-Shelby County Seismic Hazard mapping Project: Site Response Data, http://www.ceri.memphis.edu/usgs/hazmap_old/geotech/index.html.

Williams, R. (2000b) Personal Communication, (United States Geologic Survey).

Yaun, D., and Nazarian, S. (1992) "Automated Surface Wave Method: Inversion Technique." *Journal of Geotechnical Engineering*, Vol 119.

Zywicki, D.J. (1999) "Advanced Signal Processing Methods Applied to Engineering Analysis of Seismic Surface Waves." Ph.D. Dissertation, Georgia Institute of Technology.

Zywicki, D.J., and G.J. Rix (1999) "Frequency-Wavenumber Analysis of Passive Surface Waves," *Proceedings*, Symposium on the Application of Geophysics to Engineering and Environmental Problems, pp. 75-84, Oakland, CA.